Ultrafast Energy and Charge Transfer in D$_2$O/Ru(0001)

im Fachbereich Physik der Freien Universität Berlin eingereichte Dissertation

Juraj Bdžoch[1]

December 2010

[1] bdzoch@zedat.fu-berlin.de

This work was done between July 2006 and August 2010 in the group of Prof. Dr. Martin Wolf at the Physics Department of the Freie Universitt Berlin.

Berlin, December 2010

There is a theory which states that if ever anybody discovers exactly what the Universe is for and why it is here, it will instantly disappear and be replaced by something even more bizarre and inexplicable.
There is another theory which states that this has already happened.

Douglas Adams

Man sagt, der Mensch erfahre seine Welt. Was heißt das? Der Mensch befährt die Fläche der Dinge und erfährt sie. Er holt sich aus ihnen ein Wissen um ihre Beschaffenheit, eine Erfahrung. Er erfährt, was an den Dingen ist.
Aber nicht Erfahrungen allein bringen die Welt dem Menschen zu.

Martin Buber

Jedna z najťažších vecí v živote je správne rozpoznať, kedy nám vlastne Boh dáva, kedy berie a kedy nás skúša.

Slovenská múdrosť

Abstract

Thin D_2O layers on a Ru(0001) surface experiencing energy transfer from the photoexcited metal and charge confinement after UV illumination were studied with surface–sensitive optical techniques and in a time–resolved manner to gain a microscopic understanding of the fundamental processes within this system.

The surface of ice is a highly relevant medium in atmospheric science [Sol90, Ber09, Lu10] and astrophysics [Jen94, Jen96], being involved in many chemical processes of vital importance. The water–metal interface and interaction are of interest for corrosion and electrode processes, future applications involve e.g. sustainable energy generation and storage based on hydrogen economy, employing the dissociation of water (the largest convenient natural hydrogen reservoir) on a metal surface as a key step [Mae10].

The intrinsically interface–sensitive sum frequency generation (SFG) vibrational spectroscopy is employed to investigate the surface structure of an ice film grown on the Ru(0001) substrate with different thickness and thus with different interaction strength with the metal. The vibrational signatures of thicker ice samples show characteristic differences between the surfaces of amorphous and crystalline ice, but the structure of the wetting layer is significantly influenced by the metal and distinctly different from that of ice, which leads to the pronounced hydrophobic properties of the first water adlayer [Kim05, Haq07]. The number of hydrogen bonds between this wetting layer and further multilayers is shown to be considerably limited, which most probably gives rise to the Stranski–Krastanov growth mechanism.

The surface of ice is of special interest also due to its ability to stabilize an excess charge on a minute timescale [Bov09]. In the present work, the reason for this stabilization is consistently explained. After an electron is excited from the metal into the (D_2O) ice layer by an intense, ultrashort UV (4.66 eV) laser pulse and stabilized at its surface, the SFG vibrational spectrum in the OD stretch region is changed dramatically. Electron injection resonantly enhances the SFG signal up to a factor of 10^3, particularly in the frequency range of vibrations involved in hydrogen bonding. The signal from the ice surface is simultaneously overwhelmed by the contribution from the bulk. The observed changes do not spontaneously reverse back to the original state on a timescale of several hours and strongly depend on the D_2O structure, since no change in the sum–frequency spectra of thin amorphous ice layers can be observed under otherwise identical conditions.

The proposed explanation for this phenomenon is based on partial *ferroelectric alignment* of water molecules experiencing large electric fields, which results in a net dipole moment of the D_2O layer. Such a reorientation converts ice to a medium that is not centrosymmetric anymore and SFG becomes dipole–allowed also in the inner part of ice, which gives rise to the observed tremendous SFG signal enhancement.

The screening occurs on a timescale faster than $\sim$100 fs and its dynamics is strongly dependent on the water isotopologue (D_2O vs. H_2O) used. Confinement mechanisms that *do not* involve the movement of molecular center–of–mass, like the OD flip, are consistent with our observations and are feasible in the defect–rich structure of Ru(0001)–supported ice even at low temperatures.

The ultrafast desorption dynamics of the D_2O wetting layer on Ru(0001) after optical excitation were followed to obtain a deeper insight into the energy transfer mechanism between

the substrate and adsorbate. Based on a simple model that treats the substrate electrons and phonons and the adsorbate as coupled heat baths, this process was found to be non–adiabatic, mediated to a large degree by the hot substrate electrons, although the participation of excited lattice vibrations could not be excluded. A reaction mechanism involving multiple electronic transitions from the ground state into a repulsive excited state (DIMET) is strongly supported by our results and it may account for the significant fraction ($\sim$50 %) of desorbing molecules that break their bond to the surface within the first 2 ps after the excitation. Simultaneously, it explains the recorded high translational energy of the desorbing species that is much higher than the corresponding temperature in the phonon heat bath.

Deutsche Kurzzusammenfassung

Die vorliegende Arbeit leistet wichtige Beiträge zum Verständnis der fundamentalen Prozesse innerhalb des D_2O-Ru(0001) Adsorbat–Substratsystems und beschäftigt sich mit den Ladungs– und Energietransfermechanismen zwischen der Eisschicht und dem Metall.

In einer Vielzahl von atmosphärisch relevanten Prozessen spielt die Oberfläche von Eispartikeln eine bedeutende Rolle und ist von entscheidender Relevanz für das Studium der aktuellen Umweltprobleme, wie z.B. Ozonschichtzerstörung [Sol90, Ber09, Lu10]. Die Grenzfläche zwischen Metall und Wasser ist viel mehr als nur der Ort, wo Korrosion oder Elektrolyse in einer wässrigen Lösung stattfindet – es ist auch ein höchst interessantes Medium für zukünftige Energiespeicherungsanwendungen, die auf der Wasserspaltung basieren [Mae10]. Der Energietransfer zwischen einem Substrat und dem adsorbierten Wassermolekül stellt dabei einen der wichtigsten Zwischenschritte dar.

Die intrinsisch oberflächenempfindliche Methode der Summenfrequenzerzeugung aus zwei Laserpulsen – einem Sichtbaren und einem Infraroten in Resonanz mit ausgewählten Schwingungen im System – bietet sich als hervorragend geeignete Methode an, um die Eisgrenzflächen (sowohl Eis/Vakuum als auch Wasser(Eis)/Metall) zu untersuchen. Mit dieser Spektroskopieart wurden D_2O Eisschichten auf Ru(0001) mit unterschiedlicher Dicke – und somit auch mit unterschiedlich starker Wechselwirkung mit dem Substrat – untersucht und ein wichtiger Einfluss der Metallsubstratstruktur auf die äußere D_2O Bilage entdeckt: Obwohl die Eis/Vakuum Grenzfläche durch ein abruptes Ende der Volumenperiodizität und aufgrund der großen Zahl von unterkoordinierten Molekülen die Ordnung charakteristisch für das Volumen verlieren sollte, findet man jedoch auf der Oberfläche der dicken kristallinen und amorphen Eisschichten die für die jeweilige Struktur charakteristischen Unterschiede. Bei kleineren Bedeckungen, besonders wenn die Wassermoleküle direkten Kontakt zum Metall haben, ist die Eisschicht noch stärker durch das Substrat beeinflusst und weist hydrophobe Eigenschaften auf [Kim05, Haq07]. Dies manifestiert sich unter anderem durch die signifikant reduzierte Wasserstoffbrückenbindung zwischen der ersten und den weiteren Eislagen, was mit großer Wahrscheinlichkeit zu einem Stranski–Krastanov–artigem Wachstum führt.

Darüber hinaus ist die Eisoberfläche auch aufgrund ihrer Fähigkeit, Überschussladungen (Elektronen) zu stabilisieren, von speziellem Interesse [Bov09]. Der Grund für dieses Verhalten ist in dieser Arbeit aus der Sicht der Wassermoleküle konsistent erklärt. Elektronen werden durch die UV–Bestrahlung des Metalls in die Eisschicht injiziert. Nach der Lokalisierung dieser Überschussladungen, die fast ausschließlich an der Oberfläche stattfindet, steigt die SFG Intensität dramatisch an, in der Frequenzregion der vollkoordinierten OD–Streckschwingungen sogar um Faktor 10^3. Gleichzeitig überdecken die, an der Intensität gewinnende, in–Phase symmetrischen und antisymmetrischen Resonanzmoden die Oberflächensignaturen von Eis. Die beobachteten Änderungen in der Eisschicht sind besonders stabil und bleiben auch nach Wartezeiten von mehreren Stunden bestehen, was auf eine dauerhafte Strukturänderung hindeutet. Zusätzlich ist eine starke Abhängigkeit dieser Änderung von der Morphologie der präparierten Eisphase zu beobachten: Das SFG Spektrum von amorphem Eis bleibt auch nach UV Bestrahlung gleich und ausschließlich von dem Oberflächenbeitrag dominiert.

Die Erklärung dieser Phänomene beruht auf einer (partiellen) ferroelektrischen Reorien-

tierung der Wassermoleküle, die über eine relativ weite Distanz von der Überschussladung beeinflusst werden. Eine Struktur, die ein permanentes Dipolmoment besitzt, ist nicht mehr zentrosymmetrisch, wodurch der signifikante Volumenbeitrag zur SFG Intensität zustande kommt. Die Umordnung in der Schicht findet auf sehr kurzen Zeitskalen statt. Konsistent mit den zeitaufgelösten und isotopenselektiven Messungen ist ein Szenario, das ein Umklappen von OD–Oszillatoren in der defektreichen Wasserstruktur berücksichtigt.

Die ultraschnelle Desorptionsdynamik der D_2O–Moleküle von der aus dem thermischen Gleichgewicht durch eine Photoanregung gebrachten Ru(0001)–Oberfläche wurde untersucht, um den Mechanismus des Energietransfers in diesem System zu finden. Anhand eines Modells, das die Elektronen und Phononen des Festkörpers sowie auch das Adsorbat als gekoppelte Wärmebäder betrachtet, wird gezeigt, dass die Desorption ein nicht–adiabatischer Prozess ist und die Energie überwiegend durch die Kopplung des Adsorbates an die heißen Substratelektronen übermittelt wird. Jedoch kann auch ein Beitrag der Gitterschwingungen nicht vollständig ausgeschlossen werden. Die diskutierten Ergebnisse unterstützen einen Desorptionsmechanismus, der auf mehrfacher elektronischer Anregungen beruht, da ein signifikanter Anteil ($\sim$50 %) der Moleküle innerhalb der ersten 2 ps desorbiert und ihre Translationstemperatur die des phononischen Subsystems bei weitem übersteigt.

Contents

List of Figures

Introduction

A catalyst, an electrode, a blood cell, a solar cell. Just four examples out of a plethora of cases where the interface is not just the end of the bulk, but far more the place, where the most interesting processes take place. In a catalyzed reaction, the reactants experience only the surface of the catalyst and therefore supported materials are widely employed. At an electrode, the redox reactions (like corrosion) lead to a charge exchange at the electrode surface. The surface of a haemocyte is able to bind and transfer oxygen in our bodies and at the surface of a solar cell is the place, where the sunlight is absorbed and converted into electricity.

There is an interface of special relevance for nearly all areas of scientific research and of vast importance for the everyday life: the surface of water in its solid and liquid form. Responsible for impressive (lightning) and environmentally important (participation in the ozone layer depletion) phenomena, it has attracted a lot of interest in the past. However, the knowledge about its structure and properties gathered up to now is still not satisfactory.

In many cases, the interfacial water molecules are strongly influenced either by the order or disorder in the bulk *and* by forces exerted on them by the second medium at the interface – e.g. by the support on which the water layers grow, or by the surface of an electrode in a water solution. This interaction might open new energy and charge transfer channels relevant for catalysis, it can play a decisive role in the future energy storage applications, or support a molecular order that facilitates the charge (ion) stabilization.

The impact of these phenomena is at least as large as their complexity. To understand them better, we investigated the simpler, model system $D_2O/Ru(0001)$, allowing us to obtain reliable results that are still valid in the more complicated, real case. The present thesis contributes to our knowledge by offering answers to three very fundamental questions (see Figure 0.1):

(i) What is the structure of the topmost ice layer at the ice/vacuum interface and how is it influenced by the ordering in the lower lying layers or by the direct interaction with the substrate atoms?

(ii) How is the energy, deposited in the substrate via an ultrashort laser pulse, subsequently exchanged between the metal and the adsorbed ice layer? What kind of mechanism and which timescales can describe this process?

(iii) In which way do water molecules react to an excess charge localization, how fast is their adaptation to the new local environment and what is the role of the supporting material and of the actual ice structure in the evolving layer transformation?

To be particularly sensitive to the ice surface, we employ an intrinsically interface–sensitive type of vibrational spectroscopy, based on the nonlinear process of sum frequency generation (SFG) in environments with broken centrosymmetry. Using a (spectrally narrow) visible and an ultrashort infrared laser pulse, one can measure the spectrum of the SFG signal generated at the boundary between two centrosymmetric media. This is resonantly enhanced, if the original IR frequency matches the vibrational frequency of the system (i.e. the frequency of an molecular
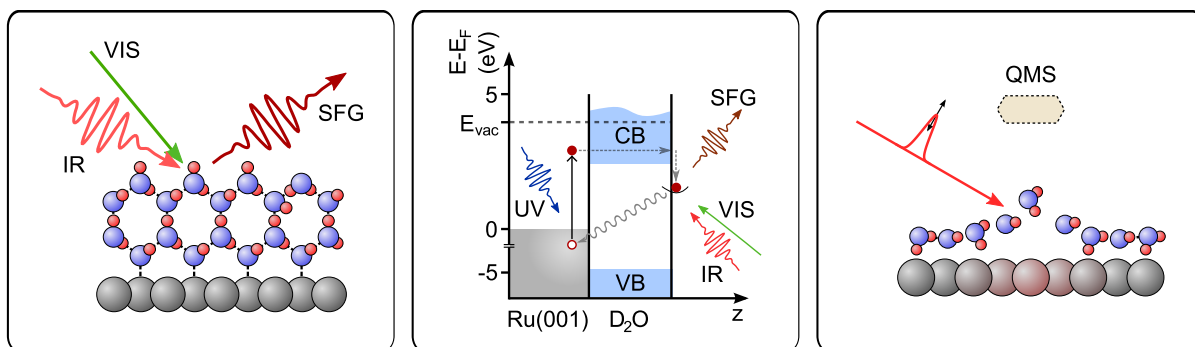
Figure 0.1.: An outline of the three fundamental questions addressed in the present thesis and the approach to solve them: Using SFG vibrational spectroscopy, the interfacial structure of supported ice of various structure and thickness is investigated (left) and the response of the water layers to excess charge localization is probed (middle). Apart from the charge transfer process, the energy transfer from the substrate metal into the water layer is investigated after the system is brought out of the thermal equilibrium by an intense, femtosecond laser pulse, which results in the molecular desorption (right).

oscillator or the frequency of the collective lattice oscillations). As many of the crystal classes do posses a center of inversion (and ice belongs to such a class), the nonlinear phenomena of an even order are (in the dipole approximation) symmetry forbidden and can not arise in their volumes. Nevertheless, at interfaces the inversion symmetry is always broken and this allows to investigate them *without* any contribution from the bulk. Sum frequency generation as a second–order nonlinear process benefits from these circumstances.

Equipped with this powerful method, we have investigated one of the longest studied (and most controversially disputed) model systems for water–metal interaction, the $D_2O/Ru(0001)$. The main difficulty that has contributed to the long–lasting discrepancies between theory and experiment is the combination of the large interaction strength between this metal and the directly adsorbed water molecules, the complexity of the hydrogen bonded network, the particularly sensitive adsorbate structure (prone to dissociation) and the inability of most of the structure–determining methods to exactly find the position of the hydrogen atoms.

We started our investigations on thin crystalline and amorphous ice multilayers and elucidated the influence of the order (or disorder) in the inner ice layers on the topmost, interfacial D_2O sheet. The problem of surface melting of ice dates back to the times of M. Faraday, who has first described the tendency of two blocks of good, Wenham–lake ice to freeze into one if brought together, but the question whether this thin, liquid–like layer at the surface should be independent on the structure of the bulk has not been addressed experimentally so far. Existing theoretical results predict a significant disorder in the topmost layer due to the tendency of the undercoordinated water molecules at the interface to maximize the number of engaged hydrogen bonds, but are the molecules adsorbed below 160 or below 60 K still mobile enough to reorient in this way? Our findings are presented in Chapter 4.

Only if the structure of molecularly intact ice multilayers on Ru(0001) is known, one has a reference, which can be used to trace the changes in the molecular arrangements in the ice layers closer and closer to the surface. Approaching the first, wetting layer, the overall signal becomes very low and it is only due to the many significant improvements in the formerly employed optical setup that we are able to make reliable conclusions about its structure. For a long time,

the SFG results were not compatible with other available experimental data, but in the present work we can finally offer a picture consistent with the experiments of different other groups and restore the agreement with the – in the meanwhile published and accepted – water adlayer model. Moreover, we can also provide an insight into the seemingly paradoxical, *hydrophobic* behavior of the wetting ice layer and demonstrate the influence of this property on the growth of the further ice multilayers on this substrate. These results are presented in the Chapter 4 as well.

Water is an excellent solvent of polar molecules. This property is given by the high energy a system can gain if single ions are surrounded by water dipoles and in many cases this energy is larger than the dissociation barrier of the solute. The charged particles are coordinated by the molecules in a solvation shell and this screens them very efficiently from their surrounding. Water can also stabilize an excess electron that can freely diffuse through the liquid. However, its lifetime of several µs is much shorter than in ammonia, the other well known electron solvent. The unique properties of the ice surface are responsible for generation of much stabler electron states, though.

Recent photoemission studies have detected excess charges on top of the crystalline ice on Ru(0001) with lifetimes on a minute timescale [Bov09]. This is 15 orders of magnitude larger than the longest–lived electron state in amorphous ice is populated and thus the question arises: what is the mechanism of such an perfect screening – in a *solid* water and *below* $60\,\mathrm{K}$ – and how relevant is it for stabilization of other, atmospherically relevant compounds like chlorofluorocarbons? Chapter 5 discusses the experiments performed to address this question. The process is also related to the heterogeneous electron transfer across interfaces, which represents an essential step considered in all nanoscale electronic devices, where a molecule is connected to a conducting electrode, but is equally important in the biological transport systems.

However, the properties of the localized excess *electron* are less in the focus of this work, much more effort is put into the understanding of the microscopic *molecular response* to its presence in the ice layer. Is the stabilization a surface phenomena or are the molecules in the bulk involved as well? What is the substrate influence on the screening process and which role does the order or disorder in the subsurface water layers play in creating the highly effective trapping sites for an excess charge? These are not only fundamental questions, but also problems of vivid interest e.g. for atmospheric science (or astrophysics), as the surfaces of ice particles (interstellar bodies) are formed under different conditions and their reactivity (viscosity, evaporation rate of comets) could be crucially dependent on the ice modification they contain.

The larger picture is rounded with a detailed examination of the *mechanism* of the D_2O response to the charge injection. To this end, time–resolved SFG experiments are presented and combined with results of measurements on isotope substituted water molecules. In this way, the relevant degrees of freedom, activated even at low temperatures and essential for electron confinement can be deduced. Together with other new insights and explanations, those results are presented in the Chapter 5.

The charge transfer between the metal and the adjacent water layer is not the only important aspect of this system. For many applications, the *energy transfer* could be an interesting phenomenon. Under our conditions, such a process can lead to a simple surface reaction: to the desorption of D_2O from the metal surface, accompanied with the bond breaking between the water and the metal. The potential energy surface (PES), describing the molecular movement in the atomic potential (and thus any reaction) is usually derived in the framework of the *adiabatic*, Born–Oppenheimer approximation that presumes no interaction between the nuclear motions and the electronic degrees of freedom. However, at metal surfaces, where the PESs involved in

the reaction significantly approach each other and are coupled by a continuum of the electron–hole pair excitations, also *non–adiabatic* coupling becomes important. Best demonstrated is this fact by the creation of electron–hole pairs in silver upon gas adsorption [Ger01]: The energy gained in the bond forming process (involving the approaching of the nuclei) is not dissipated in the lattice vibrations (phonons), but is transferred into the electronic subsystem of the substrate solid. Equally, the reversed reaction – energy transfer from the metal into the adsorbate – can proceed either adiabatically, or be driven by the coupling of hot (energetically rich) electrons to the nuclear degrees of freedom.

To distinguish between these two pathways is virtually impossible if the system is in thermal equilibrium. However, this can be disturbed by an intense, ultrashort laser pulse that transiently increases the temperature of the electron subsystem to values of several thousand degrees Kelvin above that of the lattice. Coupling of these hot electrons to the adsorbate degrees of freedom can either considerably enhance the process taking place in equilibrium (if electron mediated) or open completely new reaction channels. However, it is also possible that the reaction is very well described within the Born–Oppenheimer approximation and the increased temperature plays only a role as far as it heats the phonon subsystem on longer timescales as well. Chapter 6 discusses the possible scenarios of energy transfer between the metal and the adsorbed water layer and offers a deeper insight into its desorption mechanism (DIMET vs. DIET picture). It is also a suitable starting and reference point for further spectroscopic investigations of the water desorption, as it reveals its temporal aspects after the intense photoexcitation.

The present work is organized as follows:

Chapter 1 introduces the most important properties of water that connects all parts of this thesis into one, homogeneous whole. Further discussed are here the different cases, where the water interaction with an excess electron leads to its localization and the state–of–the art overview of the electron localization in ice/Ru(0001). To the basic theoretical concepts of this work belong the energy transfer mechanisms between a metal and an adsorbate as well, treated in detail in the last Section of the first Chapter.

Many of the results presented here would be not achievable without numerous improvements and important innovations in the experimental setup described in the Chapter 3. They form a group of tools employed to observe the phenomena described earlier and therefore are put in context with the experimental methods that allow to investigate them.

In the following Chapter 2, the complex experimental setup combining an ultrafast laser and ultra high vacuum conditions is introduced.

Chapters 4, 5 and 6 discuss the experimental results concerning interfacial structure of water, electron localization in ice and photoinduced D_2O desorption, respectively. Each Chapter starts from the current research status (where earlier works exist) and integrates the thoroughly discussed experimental findings into a larger frame provided by similar investigations and models developed by other authors.

1. Concepts and models

Many instruments used throughout this work are indeed much lighter than their manuals. Another come in boxes that would really impress the people who set up Stonehenge. Arranged in complicated setups, they not only create a novel form of life (which usually decides to "die" regularly at the least appropriate point), but allow to discover even more complex phenomena as well. To guide the reader through the fascinating ideas worth spending such an effort without a need for the famous label »Don't panic« on the cover of this work is the aim of the following chapter.

It introduces the investigated species – water and its interaction with metal surfaces. Is devoted to energy and charge transfer mechanisms, that play a crucial role in many important processes in nature or technology and discusses the most interesting theories, models and ideas, that help to understand many of its relevant aspects as well as the methods capable to explore its unique behaviour. Typically, structure and properties of any system are closely connected, therefore water itself and several types of networks it is able to create are reviewed as well. The many references that are simultaneously offered should fulfill the requirement that the thesis must in any case weigh less than its author.

1.1. Physical properties and structure of solid water

Three atoms make up the probably most studied and the most essential compound for the man in the known universe[1]. What makes this compound so special, is not only the molecule itself – it is rather its ability to form stable networks in its liquid and solid phase. Water and ice dramatically influence our environment (like through the in the footnote mentioned ozone hole [Sol90, Lu10]), therefore to understand its structure, especially at the surface that is in contact with other media, is of vast importance [Sie10a]. Many studies are focused particularly on the solid form of water, mainly due to the more regular arrangement of molecules, although emerging research activities are focused on the liquid water interfaces as well, because of their importance for chemistry and biology [Smi07, Dzu05, All00].

The present work deals with the solid water in its several different phases, attempts to provide a model for its interface and investigates its interaction with a metal surface. Largest part is devoted to explanation and discussion of the phenomenon of excess charge stabilization in ice, as will be discussed later. The goal of this Section is thus to introduce all relevant forms of ice that one can expect to be formed under ultra high vacuum conditions[2]. Defects and aspects in

---

[1]At this place, the author wished to be more poetic. However, as so often, someone else was faster and did it much better, therefore, only a citation is offered to the reader to be and to stay impressed [Gro07]: "Ice is arguably one of the most important solids in the universe. In interstellar space, the surface of ice is a veritable chemical factory and is of major importance to the composition of comets. Closer to *terra firma*, generation and interparticle transfer of charges on ice particles are responsible for most lightning storms. In the stratosphere, ice surfaces play a key role in enabling and catalyzing reactions that are responsible for the now famous ozone hole. Throughout the troposphere, ice and aqueous particles transport and cycle countless species as well as provide a staging site for reactions that are either forbidden or very slow in the gas phase. The world would literally be a different place without this marvelous solid."

[2]This is not far from the top research topics in other areas like astrophysics: different forms of solid water and their mutual transitions are, of course, studied on Earth ($\approx$ *terra firma*) as well as in the 'unholy emptiness' of

ice structure relevant for electron stabilization are also discussed, as they can play an important role in charge confinement in amorphous ice and help to understand the way the water molecules arrange to compensate for a vacancy of a specific kind. Since deuterated ice (D_2O) has been investigated for reasons explained later, all values and facts in the following parts apply to this molecular species.

1.1.1. Water and hydrogen bonding

Water molecule

The perfection of the water molecule lies in its simplicity: the oxygen atom forms, in the LCAO (Linear combination of atomic orbitals) approximation, four molecular sp^3 hybrid orbitals with tetrahedral symmetry. Two of them overlap with the corresponding hydrogen orbitals and contribute to the single σ–bond, the remaining both form two lone pairs, each occupied by an electron pair. This symmetry is similar to the symmetry of carbon in saturated aliphatic organic compounds and similarly gives rise to a plethora of possible structural conformations. The dimensions of a single, free water molecule together with the induced electrostatic potential around its center are depicted on the left side of the Figure 1.1. Different to most organic
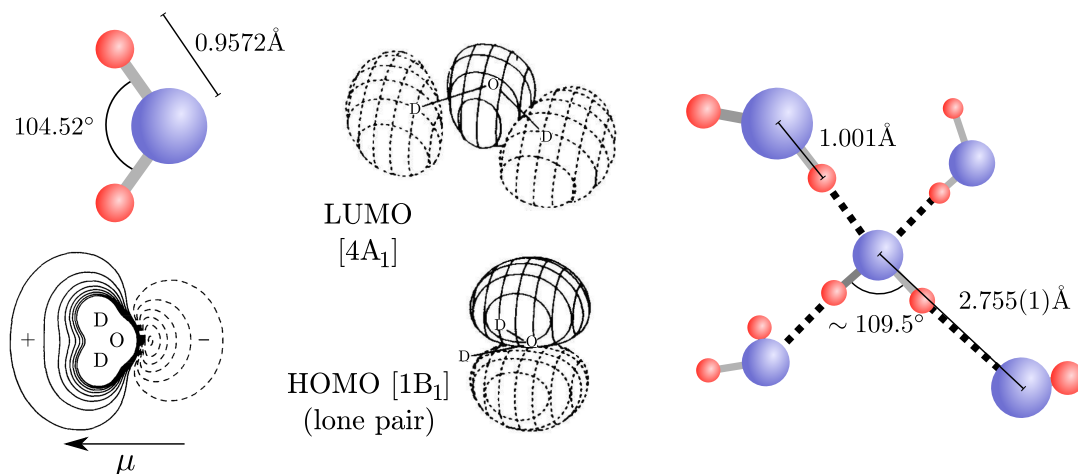
Figure 1.1.: Structural parameters of a free water molecule and a molecule embedded in a hydrogen–bound network as in ice I$_h$ at 123 K. The single D_2O has a total dipole moment of 1.8558(21) D^3 [Clo73], slightly higher than the H_2O. The probability density in HOMO and LUMO orbital is shown to illustrate the molecule's predisposition to form hydrogen bonds. Data taken from [Kuh08, Pet99, Thi87, Ows58].

compounds, water is polar, which determines its applicability as an excellent solvent of other polar or ionic molecules, since its interaction energy with charged particles is consequently large.

The first electronic excitation in water occurs upon irradiation with at least 7.5 eV (165 nm) light and the corresponding higher lying state has a linear configuration [Pet99]. Absorption of a photon with this energy can also lead to the photodissociation of the molecule. Nevertheless, this molecular value remains unchanged also in ice [Kob83], which means that none of the laser pulses with energies up to 4.6 eV that are used in the present experiment is capable of destroying the intact sample and all can be expected to be transmitted without a loss to the substrate.

---

the outer interstellar space [Jen94, Jen96].

Possible vibrational transitions in water will be treated in a separate Section 1.1.4, as they are of particular importance for this work.

Hydrogen bond

Very interesting are also the non–bonding HOMO and anti–bonding LUMO orbitals of the water molecule. As shown in Figure 1.1, the highest occupied orbital is composed mainly of the lone pair located on the oxygen atom, whereas the probability density of the LUMO extends beyond the deuterium atoms in the O–D direction. Such an arrangement, together with the electrostatic interaction, favors the formation of a weak intermolecular bond between the water molecules called the *hydrogen bond*. The partial filling of the anti–bonding LUMO weakens the binding between the oxygen and the deuterium atom belonging to the same molecule, so that each D, although still chemically bonded to an oxygen, is shared between two adjacent O–atoms, while the tetrahedral symmetry of this molecular aggregate is preserved. As it is illustrated on the right side in the Figure 1.1, in result the O–D bond length becomes larger as compared to a free D_2O. Another consequence of this 'deuterium–sharing' is e.g. the extraordinarily high (and fast) electrical conductivity in aqueous acid solutions, as the protons here do not need to physically move and the current can flow via forming and breaking of already existing hydrogen bonds. Similar type of intermolecular interactions is generally expected to play a significant role in compounds, where a hydrogen atom lies between two of the highly electronegative atoms like F, O or N.

The typical strength of the hydrogen bond is $\sim 20\,\mathrm{kJ\,mol^{-1}}$, which corresponds to approximately $200\,\mathrm{meV}$ per bond. If two molecules are engaged in the hydrogen bonding, the one that provides the hydrogen is called a 'proton donor', the other, bonded via its oxygen lone pair, a 'proton acceptor'. In a bulk solid, usually all molecules are fully coordinated, so that this distinction is not very useful (all molecules are double donors and simultaneously double acceptors). This situation may, however, change at the water or ice surface.

To visualize the nature of hydrogen bonding, the potential energy curve of a hydrogen, co-valently bonded to one oxygen and in a close proximity to another, suitably oriented water molecule, is often used and is drawn in Figure 1.2 (left) in comparison with that of the single water molecule (i.e. a species with the hydrogen bond partner in infinite distance). The different equilibrium position of the 'shared' deuterium atom was already explained above, what can be seen more from this picture is a second local minimum that corresponds to the $[D_3O]^+[OD]^-$ configuration[4] and a significant widening of the potential well. The latter leads to a lower energy difference between the molecule's vibrational levels and consequently to a correlation between the strength of the hydrogen bond (expressed as the relative distance between the two oxygen atoms) and the O–D vibrational frequency.

The hydrogen bonds in ice are quite uniform and the distances defined by the lattice constant, so this dependence seemingly plays a little role as well. Nevertheless, this perfect periodicity is again broken at the ice surface. Not only are the molecules here unable to reach the full coordination as stated above, but from the thermodynamical point of view the free energy of an ice surface can be lowered by converting its upper layer from solid–like to liquid–like [Kro92][5]. This behavior is reported for many substances (like lead or aluminum) well below their melting

---

[3]$1\,\mathrm{D}$ (Debye) $= 3.335\,641 \times 10^{-30}\,\mathrm{C\,m}$ [Lid07].

[4]As in the liquid water always a certain amount of molecules exists, with an energy sufficient to overcome the barrier to the ionic state, under normal conditions a concentration of $10^{-7}\,\mathrm{mol\,dm^{-3}}$ of both H_3O^+ and OH^- species is present in pure water, giving rise to the pH scale.

[5]In this context, liquid–like layer denotes a layer, that is not perfectly organized as in a solid, but maximizes the number of hydrogen bonds (and hence decreases its free energy) by its restructuring. Even a surface (or
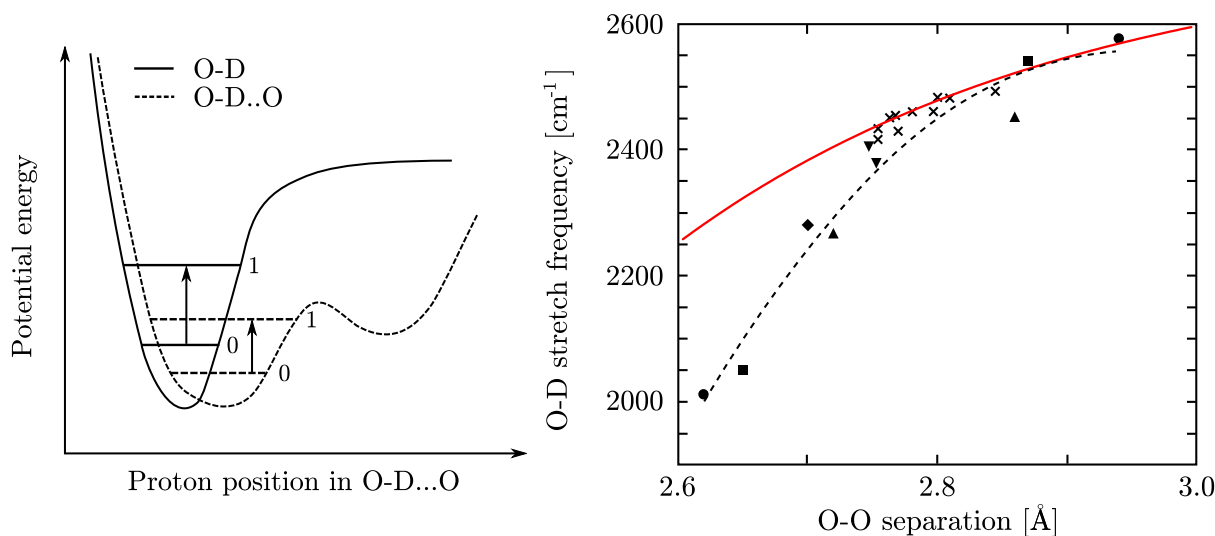
Figure 1.2.: (Left) Potential energy curve for a hydrogen bond. Solid curve shows the potential energy of a free water molecule, the dashed line shows the potential curve if another water molecule is positioned suitably oriented at a fixed distance corresponding to a typical hydrogen bond length from the first one. In the later case, the broadening of the potential well brings the vibrational levels of the molecule closer, which leads to a correlation between the O–D vibrational frequency and the strength of the hydrogen bond (right). The red curve represents the fit to experimental values taken from 82 different solid hydrates, points represent results of various calculations. Largest deviations between theory and experiment is observed when one interaction partner is a fully dissociated water molecule (lower circle and lower square). Taken from [Thi87, Mik86, Fei04].

point [Das89]. For ice, the most precise studies show the existence of a quasiliquid layer with ordering different to that expected for perfect crystalline ice down to 200 K at ambient pressure [Wei01b, Wei02].

Obviously, this offers a challenge and new opportunities for a surface–sensitive vibrational spectroscopy like SFG (introduced in Section 3.1.2) to study in a fine–resolved way the interface processes like surface melting of ice or its phase transitions at low temperatures, as usually they are accompanied with a change of the surface structure as well. Even more complex phenomena can be investigated – like ion solvation [Par00, Kim07a], or excess charge confinement. The different structural properties of the ice interfaces and its inner part allow to make conclusions about the actual place, where those processes occur and this in situations, where such information is hard to obtain by other means – e.g. in thin films. Due to its large sensitivity to smallest changes in the intramolecular distances and geometry, the O–D vibrational frequency is a particularly convenient marker for any geometrical rearrangement.

1.1.2. Solid forms of water

The thermodynamically most stable modification of all solid compounds (although sometimes kinetically inaccessible) is the crystalline form. While many compounds posses a single crystalline phase, up to now 15 different polymorphs of crystalline ice are known [Mal09, Zhe06].

---

more generally interface) of liquid water has a molecular arrangement that is clearly different from its bulk 'organization' [Fan09, Wer04].

Most of them exist only under high pressures, which results in denser packing of molecules as compared to the hexagonal ice modification that is the stablest form of ice at normal and low pressures. Additionally, ice can form several distinct amorphous structures [Loe06, Fin02], characterized mainly by their packing density, a property that has been first discovered in ice and named polyamorphism. A closer examination of those structures could shed light on many of the characteristics of solid water that is in the focus of this thesis.

Solid state and order   In general, a crystalline solid is thought to consist of periodically repeating patterns formed by its atoms or molecules, i.e. to possess a translational symmetry (long–range order) in all directions. An amorphous solid, in contrast, does not exhibit this symmetry. On a microscopic scale, this leads to a highly ordered lattice in the crystalline case, producing well defined diffraction pattern (a definition, which includes also quasicrystals), in amorphous case, the (dis)order is a matter of ongoing discussion, although it is clear that no long–range ordering exists here. A schematic illustration of both states is offered in the Figure 1.3. On the left side, the regularity of a crystalline lattice is depicted, together with the
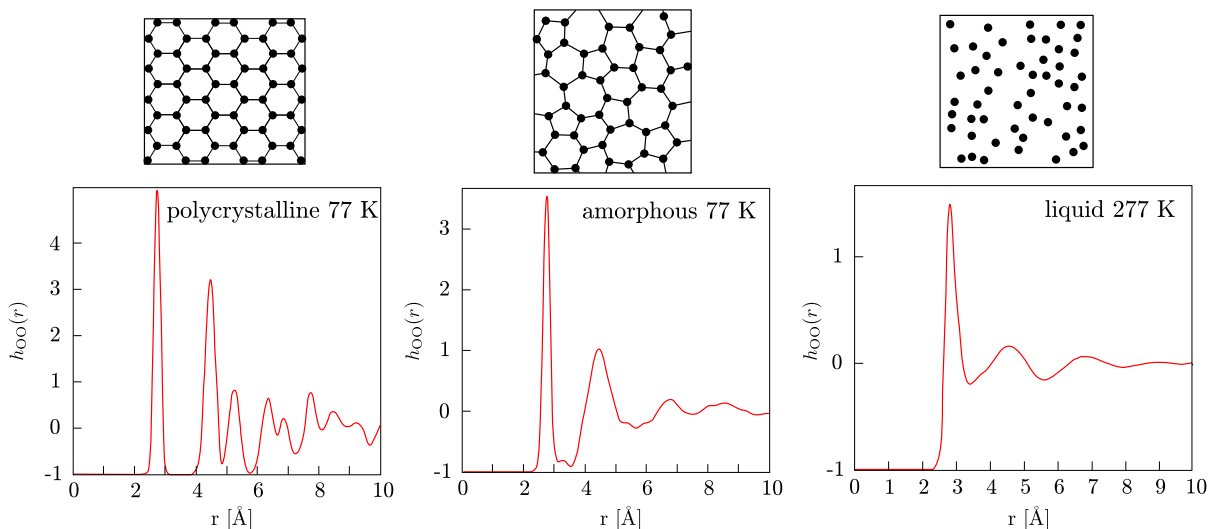
Figure 1.3.: The distinction between an amorphous and crystalline solid. A microscopic arrangement is shown on the top, graphs below represent the radial distribution function (pair correlation). For explanation see text. Modified from [Nar76, Zal98].

radial distribution function (RDF, or pair correlation) of crystalline ice below. The curve shows the variation of the atomic density depending on the radial distance from one particular atom. A clear first maximum can be observed at the position corresponding to the nearest neighbor distance and distinct maxima appear also for larger distances. Note that if the distance becomes too large, the radius of a thought circle drawn around the central particle increases and even in a perfect structure almost always borders on one of the other lattice partners, which naturally leads to RDF flattening. In amorphous ice, the radial distribution function does not show pronounced features on long–range scale. However, the positions of atoms (molecules) are not random. Their equilibrium positions marked by the black circles show that each atom (molecule) possess the same amount of nearest neighbors at a *nearly* equal distance, the bond angles are also *nearly* equal. In crystalline solid those parameters are *exactly* equal leading to a long–range order, here the atoms (molecules) exhibit a high degree of short–range ordering or local correlation. It is important to stress this difference to gas or liquid, where the atom

positions are random and change, so that in the corresponding picture in Figure 1.3 the black circles show only the instantaneous snapshot of atom positions and this distribution evolves further uncorrelated. One can consider an amorphous solid as in a metastable state, where the atoms (molecules) were condensed too fast and their diffusion to the optimal lattice positions was hindered, which in fact corresponds to the most frequently used procedure of creating this kind of solids.

Bernal–Fowler–Pauling rules   Regardless of its modification, molecules in the bulk ice always attempt to achieve the configuration with the highest number of hydrogen bonds. This has been realized first by Bernal and Fowler [Ber33] and later reformulated by Pauling [Pau35] in form of 'ice rules':

(i) There are two hydrogens adjacent to each oxygen and the DOD bond angle is similar to the gas molecule.

(ii) The orientation of each water molecule is such that its two hydrogen atoms are directed approximately toward two of the four oxygen atoms which surround it tetrahedrally, forming hydrogen bonds.

(iii) The adjacent water molecules are oriented in a way that one hydrogen atom lies approximately along each oxygen–oxygen axis.

(iv) Under ordinary conditions the interaction of non–adjacent molecules is not such as to appreciably stabilize any one of the many configurations satisfying the preceding conditions with reference to the others.

Until today they represent the basis for discussions concerning ice structure and its defects. It is important to note that consistent to those rules, tetrahedral D_2O networks are preserved in amorphous ice as well, although slightly distorted.

The last of the Pauling statements has an interesting consequence regarding the crystallinity of several ice modifications. Taking into account the most general definition of crystalline solid as a modification producing a regular diffraction pattern, in a classical X–ray experiment crystalline states would be identified that do not possess perfect translational symmetry. The electron density on the deuterium is namely far too low to be detected by this method[6] and even in a identical arrangement of oxygen atoms the hydrogens can occupy several equivalent positions, which always make up a perfect hydrogen network. This fact leads to a non–zero entropy[7] at $0\,\mathrm{K}$ and the usually resulting proton disorder additionally increases the stability of water networks, which leads e.g. to a higher melting temperature of ice [Ric05]. Some of the very fruitful controversies arose also recently in the literature that are connected to stability, formation and relevance of perfectly ordered ice modifications [Ied98, Whi99, Cow99], as they are formed for most of the known crystalline ice phases [Mal09]. Some of those issues will be also illustrated on the following examples of water modifications expected to form at low temperatures under ultra high vacuum conditions.

Ice I_h

The hexagonal form of ice I is the crystalline modification present in nature under normal conditions. Its structure and unit cell are displayed in Figure 1.4. It belongs to the isotropic

---

[6]Neutron diffraction is used instead, that allows to discover order or disorder in hydrogen/deuterium positions as well [Jac97].

[7]The value of the residual entropy of ice was calculated by Pauling as $S = k_B N_A \ln \frac{2}{3} = 3.371\,\mathrm{J\,K^{-1}\,mol^{-1}}$.
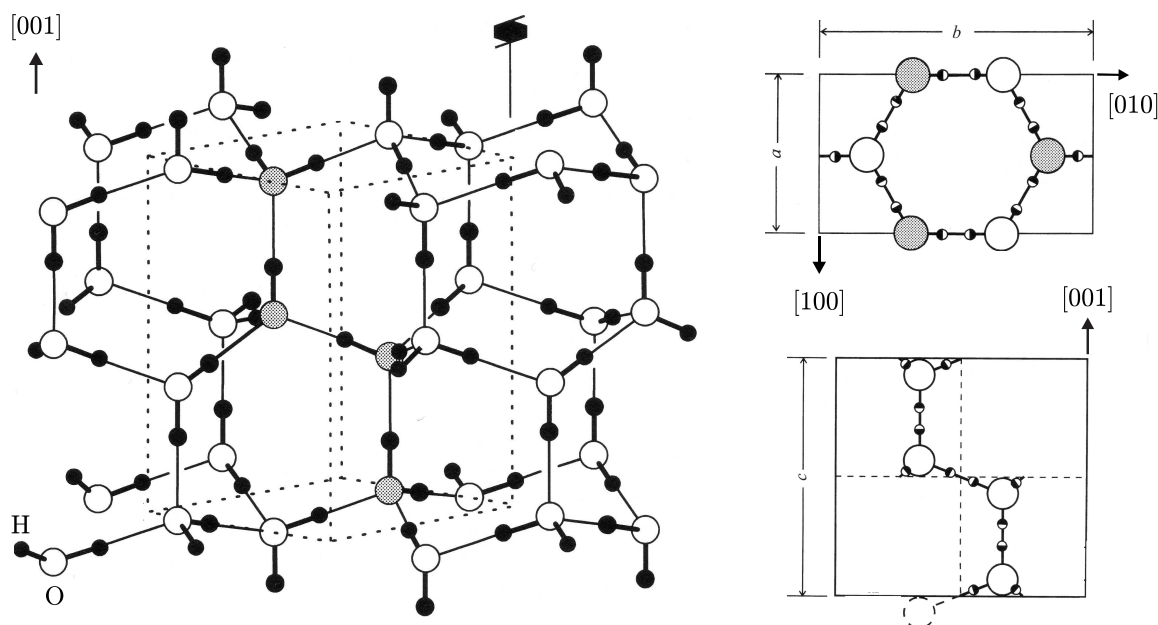
Figure 1.4.: The crystal structure of ice I_h. (Left) The unit cell marked by the dashed lines, the four oxygen atoms contained within it are shaded. (Right) Top view on the hexagonal ice plane, below the side view of the unit cell. Possible proton positions allowed by ice rules are represented by half–filled circles. Modified from [Pet99].

(centrosymmetric) symmetry group D_{6h} and represents one of the proton–disordered ice forms following the Bernal–Fowler–Pauling rules. For this reason, one usually deals with its 'averaged structure' as plotted here. One of the remarkable water anomalies is connected to the density of ice I_h, that is lower at $276.97\,K$ (triple point temperature) as the density of the liquid phase under identical conditions (1.0177 versus $1.1055\,g\,cm^{-3}$ [Lid07]). The deviations from perfect tetrahedral symmetry in this modification are negligible in D_2O ice, as can be seen from parameters shown in Figure 1.1.

Due to the thermodynamical stability (lowest chemical potential) under normal conditions, ice I_h is not difficult to prepare. Older works, e.g. the famous papers about ice written by M. Faraday, simply use 'pieces of good Wenham–lake ice' [Far59]. Nevertheless, the methods to prepare the well defined single crystalline ices are not much more sophisticated: they employ either crystallization from the liquid held slightly below the triple point using crystallization seeds, or from a capillary that serves as a nucleation bulb [Pet99]. Ice I_h can be also prepared by evaporation on a solid support under reduced pressure at temperatures not too far below the triple point.

Ice I_c

When ice is prepared by the latter method at a very low temperature (of about $150\,K$[8]), another closer packed modification of ice can be formed. The structure of this metastable cubic ice I is shown in Figure 1.5. Consistent with the ice rules, the tetrahedral hydrogen bond coordination is preserved, cubic ice differs from its stable hexagonal counterpart only in the stacking of the

---

[8]This temperature is still sufficiently high to not hinder the molecular diffusion into the positions determined by a crystalline lattice.
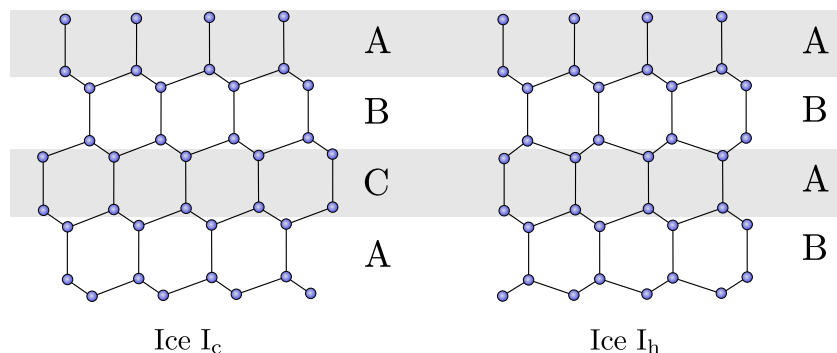
Figure 1.5.: The structure of cubic ice I_c in comparison with the hexagonal ice I_h. To simplify the stacking pattern, pairs of identical adjacent layers have been graphically merged (the 'correct' stacking pattern for ice I_h is AABB).

hexagonal layers. Instead of simple ABABAB–sequence typical for hexagonal unit cells, ice I_c possess an ABCABCABC sequence, whereas the deuterium atoms are disordered exactly as in I_h. The difference between those two phases is indeed very subtle and they are not distinguishable in interface sensitive spectroscopy as it is used in the present work due to the identical surface structure as shown in Figure 1.5.

Ice I_h never transforms to I_c on cooling. This metastable phase can be prepared by heating of the amorphous water layer vapor–deposited on a substrate below 120 K. Between 130 and 150 K the amorphous structure changes to cubic I_c and the same is formed if water vapor is dosed on a support with a temperature in this range. Between 150 and 170 K the cubic and hexagonal phases can coexist in thicker layer, above this temperature ice I_h is definitely formed [Bla58, Pet99]. Experiments aiming to prove the phase transition temperatures at ambient pressure as listed here, however, differ slightly. The neutron diffraction findings offer values cited above, X–ray diffraction [Bur35, Zhe06, Mal09] report the existence of the cubic ice form up to 183 K. The difference in transition temperatures between D_2O and H_2O is about 4 K, which is caused by the lower D_2O vapor pressure.

There is also a lack of experimental data that would allow to unambiguously determine whether the lattice of very thin ice (several layers) formed in the temperature range between 130 to 160 K under ultra high vacuum conditions is cubic or hexagonal. Recent measurements [Mat95], however, favor the latter, therefore (and due to the limited relevance for this work) this structure will be addressed in the following discussions.

Ice XI

A deep truth, giving rise to the third law of thermodynamics, could be inspired by a very intuitive suggestion: namely that for any substance, given the system is in the thermodynamic equilibrium, one structure is the most stable and is adopted close to 0 K [Bra99, Bje52]. The disordered ice I_h, with its large number of quasi–randomly distributed deuterium positions is clearly not such a structure, as many energetically equivalent configurations can be found here, resulting in a high entropy of such a system. One particular structure of ice I_h, assigned to it already by Bernal and Fowler is the perfectly proton ordered ice XI[9]. Due to the low amount of

---

[9]Although ice XI is a valid form of ice I_h, it is practically never formed spontaneously. Following the argument of Pauling [Pau35], only two (up and down) out of $\left(\frac{3}{2}\right)^N$ possible configurations have all protons oriented in one

identical structural configurations (and thus low entropy), it is one of the possible candidates for the ice modification at the low temperature limit[10] [Whi99].

Ever since this structure (see Figure 1.6) has been predicted theoretically, numerous attempts have been made to prepare this 'philosopher's stone', but they failed, or inadvertently discovered another phenomena [Den64, Cub67, Ied98]. Ice XI is kinetically inaccessible upon cooling, as the diffusivity of water molecules below the glass transition ($\sim$136 K) is significantly limited. One way to enhance the proton mobility considerably, is to dope ice with alkali hydroxides, as OH^- ions create defects in the ice structure that remain sufficiently mobile even at low temperatures [Kaw97]. Cooling the doped ice I_h below 76 K reveals a new phase transition [Kaw72, Hen79, Taj84, Jac95], which in a neutron–diffraction study shows peaks attributed fully proton ordered modification [Jac97].

Another way to prepare ice XI is to exploit a specific substrate for vapor deposition that
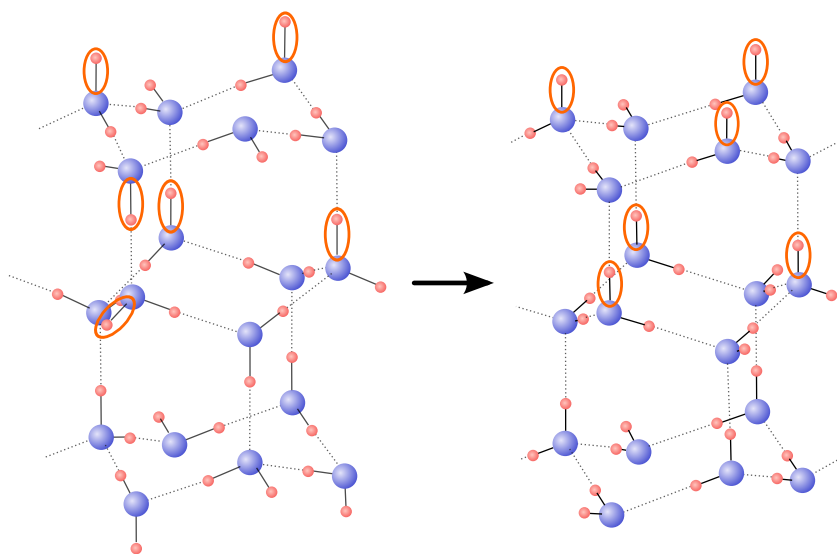
Figure 1.6.: Schematic view of the phase transition between ice I_h and ice XI.

forces the water molecules to adsorb with a preferential orientation (template surface). After one proton–ordered ice layer is grown, it may act as a nucleation core and if the ice rules are not broken, e.g. by the presence of a defect, it should be theoretically possible to grow the ferroelectric ice XI. Using Pt(111) as the template, a successful preparation of this structure has been reported [Su98]. The thin ice films have been investigated by the SFG vibrational spectroscopy (see Section 3.1.2), which is intrinsically sensitive only to interfaces or, more generally, media with broken centrosymmetry. Ice XI belongs to the C_{6v} symmetry group and the inversion symmetry is broken in the crystal. Therefore the amplitude of the observed signal from ice XI is expected to grow rapidly with increasing ice layer thickness, which was confirmed.

Unfortunately, in neither case is it clear, how much of the hexagonal ice undergoes proton ordering. This information could be, in principle, derived from the neutron–diffraction data of doped ice (the authors claim to see 37 % of ice transformed), however, the presence of hydroxyl ions complicates the evaluation and allows a different interpretation of results. In the second case the evaluation of work function changes upon adsorption reveals that not more than 0.6 %

---

direction, so the appearance of ice XI in normal ice is very unlikely. Additionally, the strong repulsion between the layers and the huge overall dipole moment of the structure would most probably lead to its disintegration.

[10]The real structure at $T \to 0$ K could be also antiferroelectric in principle.

of the dipoles are actually aligned [Ied98].

It is more than surprising that the crystalline ice grown on a nearly ferroelectric template looses this property already in a thin film. As the structure of perfect ice does not allow any proton reorientation due to the large energy barrier of such a process, specific defects (deviations from Bernal–Fowler–Pauling ice rules) must exist in the ice structure and promote its structural reorganization. However, at low temperatures the point defects in ice lattice (discussed later on page 16) are extremely rare and are not likely to be responsible for the large degree of structural change. Theoretical calculations of thin ice layers attribute this role to the dangling free O–D bonds that would point uncoordinated towards vacuum in the ferroelectric case [Wit99, Buc98]. Their flip leads to a much better coordination and substantial energy gain in the system, which is the same phenomena as discussed for the surface melting of ice above. Sandwich–like structures are formed upon ice relaxation in the model, where the O–D bonds of a layer above the template one 'dive ' into the structure interior and create stable layers by simultaneously compensating the net dipole moment of the first layer.

Probably the most exciting question that can be asked about ice XI is, whether this structure is the one that is thermodynamically stable at the low temperature limit. Experiments that dope the ice with OH^- ions are hard to interpret in this direction, especially because the dopant can have a large influence on the weak long–range interactions in pure ice that play a decisive role at $T \to 0$ [Ric05, Buc98]. Theoretical models predict a preference of the antiferroelectric phase (with no net dipole moment), although the results of the intermolecular interactions are still quite dependent on the potential model used [Ric05].

The reason why ice XI might be a very important species relevant for processes in the nature and space is due to the probably general response of water molecule to electric field exerted most notably by ions. On electrode interfaces, at surfaces of aqueous solutions and in all similar situations, the water dipoles align to screen the field and this can be studied among others also by the sum–frequency generation, where the corresponding vibrational amplitudes are expected to grow due to symmetry breaking induced by the field, which makes this method extremely sensitive to such changes [Sch99, Sch00, All00, Buc07, Shu02].

Supercooled liquid water – "Water A"

So far, crystalline forms of water have been examined. In the twilight between the glass transition of water at 124–136 K [Fis95], where all movement (diffusion) of water molecules is frozen, and the onset of crystallization to cubic or hexagonal ice at ∼150 or 160 K, respectively, a range of temperatures exists, where the water is mobile and exist in a form of a metastable quasi–liquid. Its measured diffusivity is 6 orders of magnitude larger than the extrapolated diffusivity of ice, as can be shown by isotope labeling of upper water layer deposited at lower temperatures and its consequent heating [Smi97, Smi99]. This enhanced mobility can not be attributed to defect diffusion that sets on before the glass transition and possess a much lower overall value, therefore a new liquid–like phase of water, denoted as 'water A', was proposed to exist under these conditions, which is supported by theoretical calculations.

In the present thesis, isotope mixed experiments – like vibrational characterization of the D_2O ice covered by thin H_2O layer – were performed as well and at about 120 K the intermixing of both isotopes could be also observed (for details see Section 4.2.2). Similar amounts of H_2O were discovered to desorb together with all D_2O layers (except of the layer bound directly to the substrate, that desorbs as nearly pure D_2O), although the H_2O was initially dosed only on top of this system. Consistent with this finding, whenever the D_2O surface signal should be spectroscopically 'quenched' without influencing the hydrogen bonded system of the substrate,

the H_2O overlayer was dosed below $100\,K$.

Amorphous solid water

There is much more to say about amorphous ice than to give the widespread statement that it is a form of frozen liquid existing as a metastable phase below $110\,K$. Some general aspects regarding amorphous state have been already discussed in the introduction and should be now related to water more specifically, while stressing only aspects relevant for the present work. For a more detailed review the reader is referred to [Loe06, Mal09, Zhe06].

Amorphous ice can not be prepared by cooling water, because the crystallization occurs first[11] [Pet99]. Nevertheless, under large pressure ($1.2\,GPa$) and low temperature ($\approx 77\,K$) the structure of ice I_h mechanically collapses and forms an unique amorphous phase of high density, the *high density amorphous* ice. If this phase is allowed to relax, its density is lowered by heating to the glass transition ($136\,K$) and the *low density amorphous* ice is formed. Pressurizing ice at $\sim 165\,K$ leads to ice of even larger density – this has been named *very high density amorphous* ice. When water vapor condenses at a substrate below $110\,K$, the phase named *amorphous solid water* (ASW) is formed, which is probably the most common modification of amorphous ice in the universe [Ste99, Lof03, Jen94, Jen96]. It is structurally similar to the low density amorphous ice and is examined in the next parts as the prototype for amorphous water, which can be prepared in our experiment[12]. There is a good argument to be aware of the many high density phases of ice: recent studies show that the deposits on cold metal substrates usually considered as crystalline might in fact contain a large amount of high density amorphous and crystalline ices together [Nil10].

Mobility in amorphous ice A picture of amorphous water as a system where all motion is frozen is unjustified. Already before the water reaches the glass transition, different degrees of freedom become active, so that the molecules can reorient and attain more energetically favorable orientations, although no diffusion takes place. Interesting is the consequence of this fact on the water morphology investigated by inert gas co–adsorption [Ste99]: if the D_2O is dosed at temperatures as low as $20\,K$, a simple ballistic deposition model applies. This assumes a simple 'hit–and–stick' behavior of adsorbing species and hence proposes a very porous structure, when the deposition angle (between the molecule's flight direction and surface normal) is large. Regions that are initially thicker by random chance have higher growth rates in this case and shadow the regions behind, which leads to a formation of a porous film. As the vapor adsorption from the background gas is composed of cosine distribution of all angles, porous films are expected also upon dosing via this method adopted in our setup. Regardless of the deposition angle, if the substrate temperature is higher, the amorphous film porosity reduces and at about $90\,K$ the structure is compact. As a result, one has to state that the water molecules obviously do possess significant mobility also well below $136\,K$, which might be due to defects in its structure as will be explained later [Zha90].

In the present work the structure of both amorphous morphologies was investigated. Consistent with the work cited above, the porous ASW is adsorbed at $\sim 50\,K$ and compact amorphous ice was prepared at $120\,K$.

---

[11]One exception is the *hyperquenched glassy water* that is formed when very fine droplets of liquid water are deposited at supersonic speed onto a substrate at $77\,K$.

[12]The reason, why water exhibits polyamorphism can be probably found in the double well potential of the hydrogen bond as shown in the Figure 1.2. Particle with a low energy can be trapped in any of the minima of the interatomic potential, which gives rise to an additional phase transition [Fra01].

Surface of amorphous ice The question might arise, whether a surface of amorphous and crystalline ice should be spectroscopically distinguishable, especially if one takes into account the loss of the translational order at the surface as mentioned above. This question is of central interest for atmospheric science, as the answer should help to understand e.g. the surface catalytic properties of ice particles in the polar stratospheric clouds. Experiments employing acetone co–adsorption on top of a thick crystalline and amorphous ice layer show a clear difference between the surfaces of the two phases [Sch94]. The more ordered ice interior is presumably more supportive of regular molecular arrangements of outermost molecules, possibly with alternating free O–D bonds that should point towards vacuum if ideal structure would be preserved. This could be the reason, why the intensity of the corresponding IR spectral signature is low in the crystalline case [Sch94] and the surface of crystalline ice rather nonpolar [Ada66]. In contrast, amorphous ice surface contains more free O–D oscillators in one of the directions, which results in its larger polarity. Also its roughness in nanocrystallites might be larger, although this finding does not apply to ASW films [Buc96].

Due to the lower structural stiffness (and hence lower energy required for bond rearrangement), the outer part of amorphous ice might be also the place, where the creation of crystallization nuclei preferentially occurs [Bac04]. This is important especially for small particles or thin films, where the surface/volume ratio is not negligible. Unfortunately, this effect is highly interface–specific and e.g. the crystallization of thin amorphous water layers on Ru(0001) is initiated by the random nucleation in the bulk [Kon07]. Although templating effect from the substrate would be expected, the interaction between the interface and the nucleation grain adds to the total free energy of the system and increases the corresponding crystallization barrier. This can be also confirmed by the observation of a delayed onset of crystallization at this interface upon heating [Kon07].

Electronic structure of ASW The large energy needed to reach the first excited state in water is similar for amorphous and crystalline ice and their electronic structure resembles the behavior of a semiconductor with a large band gap. As stated above, the excited states of water can not be reached in our setup due to much lower photon energies used, but the range within the band gap has to be examined very carefully. The lack of translational symmetry in amorphous ice and the degree of randomness in defect position give rise to the Anderson localization: the missing periodicity leads to 'diffuse' Brillouin zone boundaries and the sharp features in the density–of–states diagram valid for crystalline phase are smoothed as indicated in the Figure 1.7. Moreover, localized states arise in the band gap, indicating large potential energy minima in the potential energy surface, as the kinetic energy of a localized electron is large due to the Heisenberg's uncertainity principle.

In the largest part of this work the stabilization mechanism of an electron in ice is studied and the states in its band gap might provide a relevant channel either for its decay after excitation from the metal substrate or for its short time localization. Their importance will be obvious from the discussion of the results later in Chapter 5.

As a summary of the preceding parts, the phase transition data are compiled into a flowchart shown in the Figure 1.8. It should help the reader to find the orientation between the low–pressure phases of ice that might be relevant for the further discussions and serve as a quick reference in later sections.
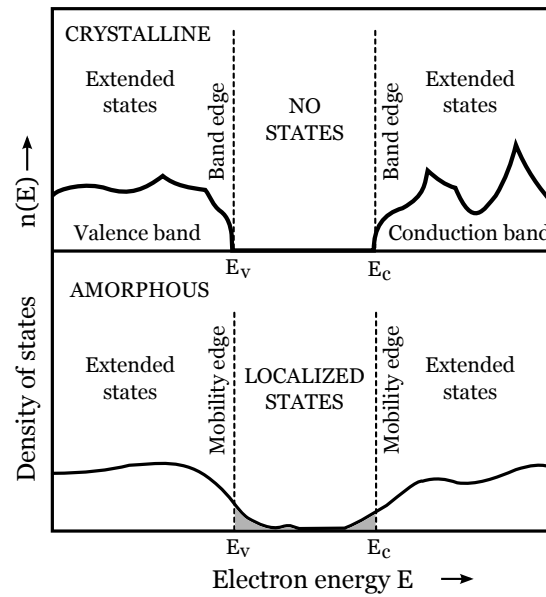
Figure 1.7.: Band structure of amorphous and crystalline solid. The less sharp Brillouin zone boundaries in the amorphous case result in a smoother density–of–states curve, the Anderson localization gives origin to localized states in the band gap. Adopted from [Zal98].
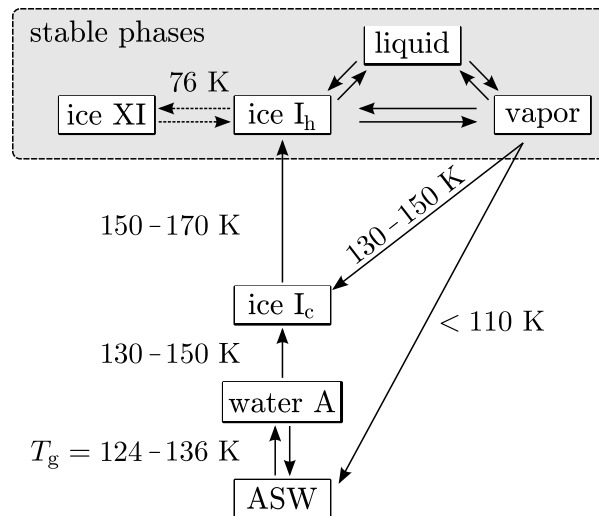
Figure 1.8.: Phase diagram of water at low temperatures. Inspired by [Pet99].

Point defects in ice structure

Along this Section, there have been many places, where the ice rules were broken. It has been mentioned that they are definitely not fulfilled at the surfaces or interfaces of ice and that the double–well potential might be a source of another type of defect produced by water autodissociation. Although their concentration is fairly low, they have a large influence: as an example, a perfect ice should be an electrical insulator, but in fact its conductivity is estimated to be $0.01\,\mu\mathrm{S\,m^{-1}}$ [Pet99]. Point defects are also responsible for transitions between different hydrogen configurations within the ice $\mathrm{I_h}$ phase and from a large part also for the mobility of the

ice films below the glass transition. Additionally, having in mind the subject of this work, the places where the structural periodicity of ice is disturbed are potential traps for excess charges, as they cause fluctuations in the potential energy surface and may create conditions discussed in the previous paragraphs.

Although the ice rules are locally broken, the point defects do not change the oxygen atom lattice considerably. The most relevant of them can be therefore envisaged as in the Figure 1.9. *Ionic defects* arise, if a proton has sufficient energy to overcome the barrier ($\sim 1.4\,\mathrm{eV}$) in the
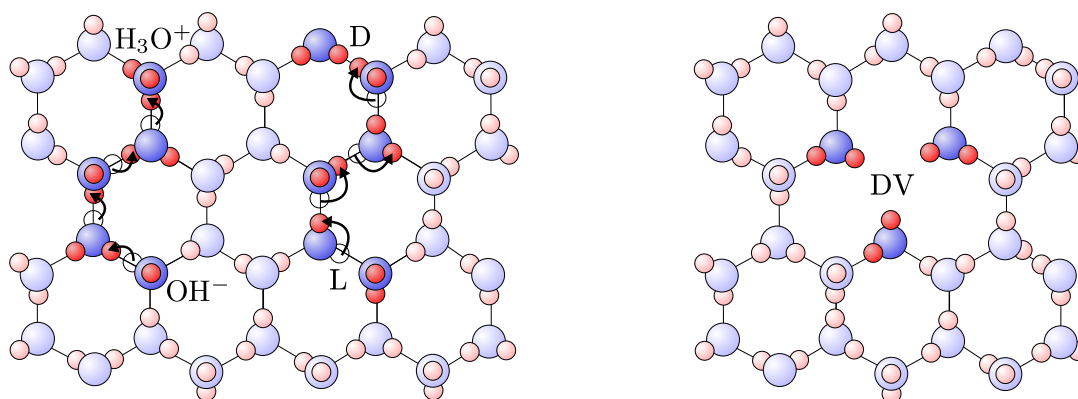
Figure 1.9.: Illustration of different types of defects in ice. From left to right ionic and Bjerrum defect next to a dressed vacancy.

double well potential and the pair $[\mathrm{D_3O}]^+[\mathrm{OD}]^-$ is formed. Initially, such a complex is unstable, but once the $\mathrm{D_3O}^+$ ion has been created, the protons can move through the lattice from site to site very fast, as the activation energy of this motion is close to zero [Pet99]. An oxygen with one or three deuterium atoms clearly violates the first ice rule.

The third rule is broken in the so–called Bjerrum defect [Bje52]. Here, a molecule reorients in such a way that along one of the O–O axes a deuterium is missing, but on another axis two protons face each other. Similarly, a reorientation of the lattice neighbors leads to a defect diffusion. The undercoordinated, empty (German: "leer") axes are called L–defects, the doubly occupied (German: "doppelbesetzt") sites D–defects.

The different types of imperfections in ice can be combined, e.g. in a dressed vacancy shown on the right side in the Figure 1.9, one $\mathrm{D_2O}$ molecule is missing in the lattice. However, adding it to the vacant place would yield a L– or D–defect, so this structure represents a combination of vacancy with a Bjerrum defect.

1.1.3. Water on metal surfaces

The importance of interaction of water with a metal surface does not need to be stressed: catalysis, weathering, processes at electrode surfaces or dissociation of water as a possible way to store energy are ubiquitous phenomena relevant not only for specific fields of chemistry or physics, but also often discussed in public.

Despite of the variety of metal surfaces, there has been a classical picture developed for this interaction, which can be summarized in four points [Thi87]:

(i) Water bonds to the surface *through the oxygen atom.* Hydrogen bonds with the surface are rare. This is similar to coordination compounds in chemistry or clusters, where the bonds are formed via the O–atom as well.

(ii) Bonding is accompanied by net *charge transfer to the surface.* This manifests itself in the usually negative work function change upon adsorption.

(iii) The internal bond angle, bond lengths and vibrational frequencies of the molecule are only *slightly perturbed* from the gas phase values by the interaction with the substrate.

(iv) Formation of *hydrogen–bonded clusters* is common, even at very low coverages, because hydrogen bonding between two or more D_2O molecules is often energetically competitive with the molecule–substrate bond (e.g. for Ru(0001) typically 0.2 eV/bond versus 0.4 eV/bond, respectively [Mic06, Mic03]).

Such a structure of water overlayer is schematically depicted in the Figure 1.10. Due to the
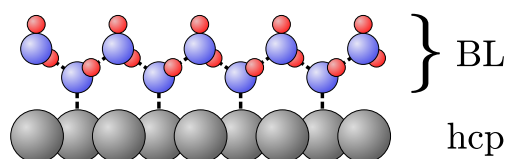
Figure 1.10.: A classical water bilayer.

buckled geometry of hexagonal ice layers, the wetting layer is conventionally termed "bilayer" (BL), as the vertical distance between the two oxygens belonging to the same hexagonal plane in ice is rather large (0.91 Å). The cited list of rules is especially expected to be obeyed in close–packed structures of d–metals (hcp – hexagonal close packed and ccp – cubic close packed), because the lattice mismatch between the metal surface and an ideal ice structure is very low.

The classical picture is also aware of the fact that the strong interaction between the metal and water can even lead to its dissociation, which should be accompanied with a work function *increase*, since the charge would be transferred from the metal into the partially vacant antibonding 1π orbital of the hydroxyl ion OH^-. In terms of potential energy surfaces, the situation could be illustrated as in Figure 1.11. A water molecule approaching the metal sur-
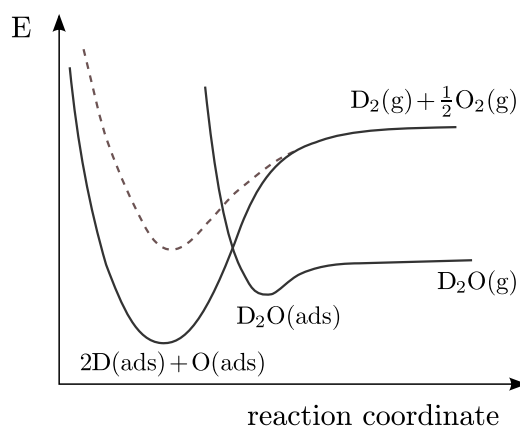
Figure 1.11.: Interaction potential between water and its dissociation products at the metal surface. Taken from [Thi87].

face could be first trapped in a minimum corresponding to the intact adsorbate. This could be thermodynamically metastable as in the situation marked with the solid line (the dissociation products possess a lower energy), or thermodynamically stablest state (dashed line). Note that

in the example above the configuration with lower chemical potential could also be inaccessible, because the barrier for desorption is lower than the dissociation energy. It is therefore hard to predict the actual adsorption behavior of water on many surfaces from a simple consideration and there is a need for experimental data, although in some cases a definitive resolution of this problem remains difficult despite of numerous investigations [Men02b].

Thermal desorption spectroscopy (TDS; introduced in Section 3.2.1) is probably the most straightforward method to study the strength of the water–metal interaction and hence the depth of the potential curve in Figure 1.11. Its interpretation, however, needs to be very cautious. First important information can be deduced from the shape of the spectra: desorption of whole water layer at a single temperature indicates that the bond strength between the molecule and the substrate is actually lower than the strength of hydrogen bonds (observed e.g. for Cu, Al, Au and Ag). Nevertheless, for most metals the desorption of the first water bilayer takes place at a higher temperature than of the multilayer, indicative of stronger metal–water bond. Early studies proposed a correlation between the ice–metal lattice mismatch and the bond strength (and thus the desorption temperature of a bilayer) [Thi87], but a later reexamination of the data after additional points became available revealed no such direct relation between those two characteristics [Den03a].

Another factor is the presence of impurities or coadsorbed molecules: water adsorbed on a surface covered by a low amount of oxygen in some cases can show three peaks in TDS that are identical to water dissociated by electron impact [Doe82, Hen02, Far05]. Despite of this, water remains intact on the surface and the coadsorbed oxygen only disrupts the hydrogen network interacting strongly with water and influencing up to 8 neighboring molecules. Moreover, even a dissociated water layer could recombine upon desorption, which only stresses the importance of a careful examination of the TDS data.

Challenge of the classical picture: substrate's influence on water overlayers

The substrate's influence on the structure of adjacent water layers can be surprisingly large. Studies of crystallization kinetics of mesoscopic ice films reveal that bulk–like properties of a water layer are established only after about 30 BL [Lof03, Smi96], which is in striking contrast with the rule (iii), stating only slight effect of substrate on the ice films that cover it. The adsorption of H_2O on Pt(111) shows a preferential ordering of water molecules induced by this surface comparable to that in ice XI with a similar decay length of 30 BL [Su98].

Ice layer on Pd(111) and Pt(111) are even more interesting: the bonding to the metal leads to a fully coordinated configuration, which makes the first water layer *hydrophobic*. As a result, next molecules adsorb on top of it in the form of crystallites more than 45 BL high and ∼14 nm or more separated [Haq02, Kim05, Kim06, Kim07b, Wal08].

Despite of the mentioned serious deviation from the classical picture, the biggest challenge has been the theoretical prediction of Feibelman [Fei02] that a water molecule *must* dissociate in order to wet a surface: the calculated sublimation energies were significantly lower than adsorption energies otherwise. Although being initially proposed for Ru(0001), number of other metals possess a similar structure and the ice layers in contact with them yield the same LEED patterns, so that this behavior seemed to be more general. Even though this idea has proven to be wrong, as will be discussed later, in certain sense it was extremely useful and led to a significant change ("out with the old" [Men02b]) in the view on water layers. Reexamination of water–metal interaction on surfaces led to a suggestion of hydrogen bonding between the metal and oxygen on Pt(111) and the discovery that oxygen must not necessarily bind strongly to the metal [Oga02] (see Figure 1.12). Also the charge transfer was found occur from the metal to
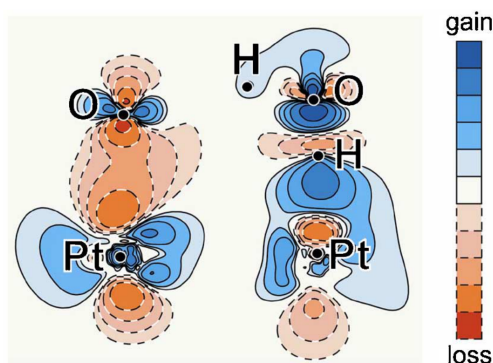
Figure 1.12.: Charge density difference plots for Pt–O (left) and Pt–HO (right) bonding species. Adopted from [Oga02].

the water (breaking the rule (ii)), which makes a simple picture of work function changes upon adsorption questionable. The motivation is therefore high to understand, what from the initial set of ice rules and metal–water interaction schemes is applicable to the system studied in the present thesis.

Water on Ru(0001)

Among other metals, the water adsorbed on Ru(0001) has had a special position probably due to their interaction strength: according to a compiled set of TDS data, the water molecules desorb from this metal at highest temperature [Thi87, Den03a]. The lattice mismatch between ice (2.5989 Å) and Ru(0001) (2.7059 Å) leads to a slight expansion of the hydrogen bonded lattice, nevertheless, the hexagonal symmetry is preserved and at low coverages hexamers are formed, as can be shown by STM (Figure 1.13) [Nor09]. The interaction strength can
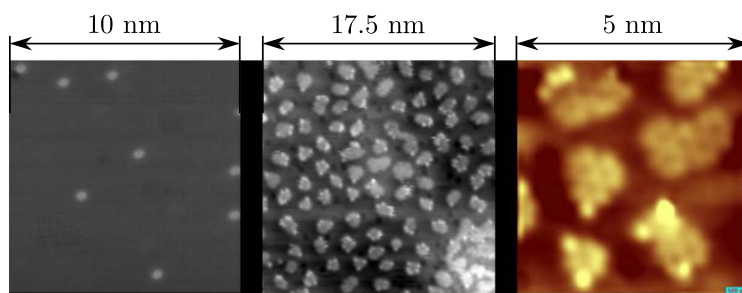
Figure 1.13.: STM image of water clusters on Ru(0001) at various coverages (from [Nor09]).

be anticipated also from early LEED (low energy electron diffraction) studies, showing that the vertical distance between the oxygen atoms in the ice unit cell is reduced from 0.91 to 0.1 Å [Hel94, Hel95a, Pui03]. Dipole–mirror dipole attraction and a large charge–transfer to the metal are proposed there as possible explanations for the compression of the ideal bilayer structure, which can not be explained by the influence of the lattice mismatch between Ru(0001) and ice. To prevent water dissociation upon electron impact, the LEED system used in the cited work was optimized for very low total doses of electron irradiation ($\sim$3 to 9 electrons/molecule). As this compressed structure very much resembles the structure of water partially dissociated

on the surface [Fei02], XPS (X–ray photoelectron spectroscopy) studies were performed aiming to find the OH^- signature in the oxygen $1s$ core–level spectrum, but provided contradicting results [Wei04, And04, Fei05b], probably due to the unexpectedly large cross–section for electron beam damage that has been later estimated to be as low as $10^{-15}\,cm^2$ (i.e. $1\,electron/molecule$ converts $50\,\%$ of D_2O molecules) [Far05].

The SFG vibrational spectroscopy was also employed, since there was a dangling OD vibration oscillating free towards the vacuum expected in an intact structure (as in Figure 1.10). The data revealed that the signature attributed to this species vanishes at coverages below $1\,BL$, but another one, belonging to fully coordinated water molecules (absent in the calculated data for the dissociated case) is present even in a much thinner adlayer [Den03b]. Therefore, a D–down structure has been proposed (shown in Figure 1.14). This is also consistent with the other
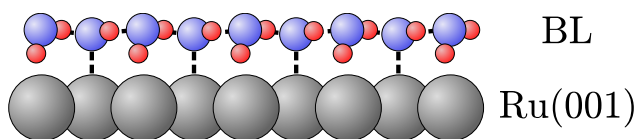
Figure 1.14.: A side view on the D–down structure.

findings – a very sensitive TDS spectrum (measured with an angle averaging mass spectrometer, see [Feu80]) does not show desorption of fragments attributable to dissociation products of D_2O and if the layer is co–doped with H_2, no isotopic exchange takes place upon desorption, which would be expected for a dissociated layer [Den03c]. Although this work provided very reasonable arguments favoring intact D_2O overlayer on Ru(0001), several weak points led to a further debate: First, it is hard to conclude about the structure based on the fact that a predicted peak is missing – using a larger supercell in the calculations, the fully–coordinated feature can be found theoretically as well, even for the dissociated case [Fei04]. Unfortunately, the measured SFG spectrum suffered a significant intensity loss (due to the CO_2 absorption in air) exactly in the region, where the discussed feature should appear, which complicated the data fitting especially for coverages below one bilayer.
The second point concerns the compatibility between the LEED data (if the measured structure would be not dissociated) and the D–down configuration: assuming the on–top site for water adsorption, the Ru–O distance $(2.23\,Å)$ would be too small to accommodate a deuterium atom if pointing directly towards the metal [Fei04]. Moreover, the vibration mode for the D–down stretch was not found, although predicted clearly in the measured range [Men04, Men02a].
Nevertheless, the DFT calculations proposing partial dissociation of the water adlayer [Fei02, Mic03] also do have weak points: the work function change, one of the main indicators of a correct overlayer structure, is greatly underestimated in their results. Also the van der Waals interactions are not modeled reliably [Men02b], although their poor treatment might be not sufficient to completely invert the theoretical prediction [Fei05a]. Still, the question whether the thermodynamically stablest partially dissociated state is also kinetically accessible (see also Figure 1.11) remained unanswered.
Theoretical studies of Meng et al. could show that the latter is not the case and for D_2O the activation barrier for desorption is lower than that for the dissociation [Men02a]. Simultaneously they could explain the absence of D–down OD stretch frequency in the SFG data: the value for work function change that matches the experimental one can be evaluated from a model, where the adlayer is composed of equal amounts of D–up and D–down oscillators, which would resemble the structure of disordered ice I_h and lead to cancellation of the free OD signal in the

previously cited work [Men05]. It is probably not necessary to add that neither this support was completely convincing: it is not intuitively clear, why the vibrational frequency of a D–down oscillator should match the frequency of its D–up counterpart, which in the previous work of the same authors was clearly different [Men02a]. The present thesis will hopefully fill the missing stone to this extremely complex mosaic in Chapter 4.

While the more and more controversial debate continued, the group of A. Hodgson actually solved the problem by looking at the D_2O scissoring frequency (out of plane) by RAIRS (Reflection–absorption infrared spectroscopy) [Cla04]. This was clearly present in D_2O, is by no means connected to O–O distance like OD stretch frequency and is a definitive proof of intact D_2O layer on Ru(0001). Maybe even more impressive was the second finding – that H_2O adsorbs intact as well, but dissociates upon desorption. This is a very clear consequence of the *Ubelohde effect*, stating that the zero point energy (and also the shape of the potential energy curve in the Figure 1.2) is different for H_2O and D_2O, and hence the barrier to dissociation can be surmounted in the case of the lighter isotope, but the D_2O molecule desorbs intact, since larger energy is needed for its dissociation.

Further, they employed helium atom scattering technique (instead of water damaging LEED) to evaluate the adsorption geometry (similar results have been achieved also by [Kon06, Tra07]) and connected the data with further DFT calculations. The resulting undissociated structure is nowadays widely accepted [Hod09] and in their case consists of chains of D–down networks and flat–lying molecules on atop sites [Gal09]. In agreement with the former statement, the latest 'clean' XPS data show evidence for the structure outlined in the Figure 1.14 as well: the core–level shift of Ru $3d$ photoemission peak indicates Ru atom coordination that can be only reached in the D–down case and is nearly identical to Pt(111) surface [Sch10].

Much easier to understand is the growth of thicker films on the D_2O wetting layer. Although Ru(0001) and Pt(111) surfaces are obviously very similar, crystalline ice layers adsorb with a preferential orientation imposed by the metal on platinum [Su98], but no such orientation can be observed in the ice multilayers on Ru(001) [Den03b]. This could be a consequence of a slightly different structure of the first bilayer [Haq06, Hod09] or simply of the stronger water and Ru(0001) interaction which flattens the first ice layer more, making it less supportive of ordering than Pt(111)[13]. Nevertheless, on both surfaces the first layer is 'hydrophobic' as mentioned above and ice forms (after fully wetting the metal) clusters on top of the first bilayer (Stranski–Krastanov growth mechanism) [Haq07, Wal08]. The sticking coefficient is nearly equal to 1.0 for metal as well as for ice surface, reflecting the fact that it is energetically equivalent to chemisorb directly at the metal or to form a hydrogen bond with other water molecules [Bro96].

There are slight differences between the growth of amorphous and crystalline ice: in the latter case the water clusters grow on the adlayer and gain thickness up to a nominal coverage of 10 BL, but still leaving more than 60 % of the first bilayer exposed, as can be shown by chloroform adsorption [Haq07, Kon07]. After that, those formations preferentially gain height, but even at a nominal coverage of 60 BL there are still almost 30 % of the wetting layer unveiled – it becomes inaccessible only after 90 BL are adsorbed. In contrast, amorphous ice clusters completely block the first layer water from view as the first 2 to 3 BL are adsorbed, creating a continuous film [Haq07].

Amorphous layers on Ru(0001) crystallize by random nucleation in the bulk water, thus independent on the substrate [Smi96, Kon07]. This is not entirely surprising, even not for very thin

---

[13]The LEED spectrum from ice adlayer on Pt(111) shows also a different pattern – $(\sqrt{39} \times \sqrt{39})R16.1°$ [Haq02], whereas on Ru(0001) water forms a $(\sqrt{3} \times \sqrt{3})R30°$ overlayer. Interestingly, the pattern on Pt(111) indicates a metastable film that restructures upon electron impact to form a similar adlayer as on Ru(0001) [Har03].

layers [Yam09], if one takes into account the rather weak interaction between the wetting layer and the remaining ice structure [Wit99].

Although studies of H_2O on Ru(0001) have started much earlier (e.g. in [Thi81]) than those of D_2O, due to the more stable structure and large IR absorption in air, our studies are mainly focused on the structure and dynamics in D_2O. The heavier isotope is enabling us to strictly control the purity of employed water (e.g. by the absence of high–temperature peak in the TDS spectra indicating oxygen contamination) and due to its stronger adherence to ice rules it is believed to represent the ice structure much better.

1.1.4. Spectral assignment of D_2O molecular vibrations in ice

In most of the experiments presented in this thesis, water is identified with its vibrational spectrum. Changes in its local environment or in its structure are observed through the resonance shifts or amplitude modulations and hence a reliable assignment of modes is of great importance for the correct interpretation of our results. This Section should provide a brief and rather compact overview over the data obtained in different types of vibrational spectroscopy for ice and D_2O adsorbed on a metal surface. As in the investigated region between 2200 to $2800\,\mathrm{cm}^{-1}$ mainly the stretching OD vibrations are present, this overview will focus mainly on those resonances.

OD stretch vibrations and their interactions

In a graphical summary, the possible vibrational transitions in ice and in D_2O on a metal surface is displayed in the Figure 1.15. In the top two parts not only the stretch resonances (ν_1 and ν_3) are listed, but also the lower frequency modes are shown, because they may interfere with each other and form combination modes in the spectral region of interest, as will be clear from the tables below.

On the surface of ice several modes may become visible. As a general rule, one can state that the vibrational frequency of a water stretch mode is strongly dependent on the local conditions of the hydrogen bonded network. A deuterium atom will experience a very different potential if it is vibrating between two hydrogen bonded oxygens than if it is vibrating freely (shown also in Figure 1.2). Simultaneously, the closer the corresponding oxygens are, the softer is the created atomic potential and thus a lower OD vibrational frequency results. Another very important factor is the actual coordination of the water molecule in vibrational motion – generally, the frequencies of coordinated D_2O molecules are lower (potentials softer) than of partially or uncoordinated molecules [Wal06]. The obviously less regular O–O distances and lower water coordination in amorphous ice leads to the expected broader peaks in a vibrational spectrum. The spectra of crystalline ices I_h and I_c offer sharper resonances, but due to the identical O–O distances in hydrogen bonding are indistinguishable within the present experimental error [Wha77].

In a water molecule, the intramolecular coupling is rather weak. This can be understood either mechanically as the consequence of a large mass difference between the deuterium and oxygen, or on quantum mechanical grounds as a result of very small intramolecular coupling constant especially in the condensed water phase [Sad99]. The intermolecular coupling is, however, very strong, leading to collective in–phase vibrations of high intensity. To evaluate their role in the spectra and to distinguish them from the molecular modes, isotopic mixtures have been investigated. Since the vibrational frequencies of the OH bond are very different from the OD resonances, there is no coupling between them. A spectrum of e.g. $4\,\%$ of D_2O (or HDO) in
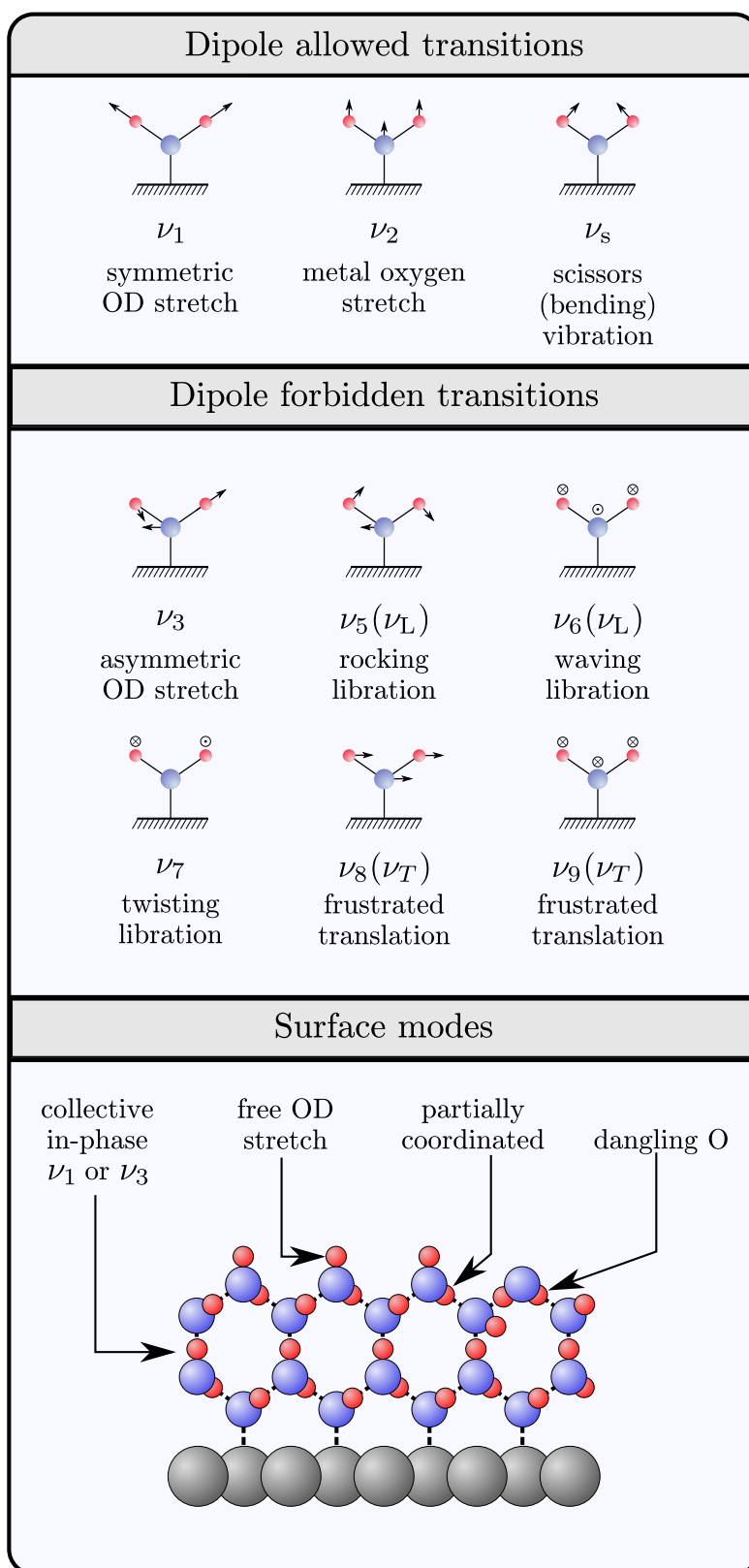
Figure 1.15.: Illustration of the possible vibrational resonances (not only) in the OD stretch region.

pure H_2O therefore reveals only the uncoupled vibrations as for example in [Sch77, Rit77, Rit78, Dev90b, Woj93].

Another form of coupling one has to be aware of is the *Fermi resonance*, first discovered and explained for the CO_2 molecule [Ras29, Fer31]. Here two modes of the same symmetry and nearly equal energy split apart, whereas the weaker mode gains (and the stronger looses) intensity. The reason for this behavior lies in the fact that such two modes will interfere (due to their proximity and symmetry) and the result of their interaction will be represented as a linear combination of the unperturbed eigenfunctions. This leads to a situation, where also a mode that would be forbidden by the selection rules (and is thus weak or vanishing) contains a large part of the eigenfunction of the allowed mode and its intensity increases and vice versa. Very illustrative is this behavior in the case of a simple CO_2 molecule – in its IR spectrum a transition (bending mode) at $673 \, \text{cm}^{-1}$ exists with an overtone at $1346 \, \text{cm}^{-1}$, which should be not visible in the Raman spectrum, where only a transition around $1330 \, \text{cm}^{-1}$, corresponding to symmetric stretch (invisible in IR) is expected. However, a pair of lines at $1284 \, \text{cm}^{-1}$ and $1392 \, \text{cm}^{-1}$ is found instead [Ras29].

Relevant OD stretch resonances between 2200–2800 cm^{-1}

The lower part of the Figure 1.15 shows the vibrations expected on the ice surface. They include collective symmetric in–phase stretch (ν_1) of fully coordinated molecules as well as the collective asymmetric in–phase stretch (ν_3) with a slightly higher frequency. Further present on surfaces or defects are the vibrational transitions of partially coordinated D_2O molecules, that should produce a broad peak due to the rather smooth distribution of different coordinations at the interfaces or irregularities in ice structure. A molecule with oxygen not engaged in any hydrogen bond (dangling O) is expected to produce a rather hard potential for the oscillating deuterium atom and due to the higher frequency of this oscillator as compared to other partially coordinated species this might be seen as a separate peak. Finally, the resonance with the highest energy will be the free OD (dangling D) vibration where one deuterium points towards vacuum. A very similar distinction of possible vibrational modes on the ice surface can be found in the literature [Gro07, Buc07].

The assignment of particular frequencies to those motions is based on the literature overview summarized in the following tables. Data measured close to $100 \, \text{K}$ were preferentially collected.

Phase	Assignment	Vibrational frequency [cm^{-1}]	Reference(s)
Crystalline	$\nu_1 - \nu_T$	2205	[Sch77]
	ν_1	2294	[Sch77]
	ν_1	2295	[Wha77, Won75]
	not assigned	2304	[Ock58]
	ν_3 (TM)‡	2427	[Wha77, Won75]
	ν_3	2427	[Sch77]
	not assigned	2477	[Ock58]
	$\nu_3, \nu_1 + \nu_T, \nu_3 + \nu_T$	2488	[Sch77]
	ν_3 (LM)‡	2502	[Wha77, Won75]
	ν_1 (out–of–phase)†	2547	[Wha77, Won75]
	$\nu_3, \nu_3 + \nu_T$	2550	[Sch77]
	possibly $\nu_1 + \nu_T$	2640	[Sch77]
	not assigned	2730	[Ock58]
Amorphous	ν_1	2318	[Wha77]
	ν_3 (TM)‡	2381	[Wha77]
	ν_3 (LM)‡	2483	[Wha77]
	ν_1 (out–of–phase)†	2530	[Wha77]

† Out of phase with the immediate neighbors.
‡ TM and LO denote the transversal and longitudinal mode, respectively [Mat03].

Table 1.1.: Overview over the vibrational frequencies observed in the Raman spectrum of ice.

Phase	Assignment	Vibrational frequency [cm^{-1}]	Reference(s)
Crystalline	fully coordinated	2300–2500[c]	[Row95]
	ν_1	2332	[Wha77, Ber64]
	not assigned	2353[b]	[Sch94]
	ν_1	2366	[Dev90b]
	not assigned	2395	[Ber64]
	ν_3 (TM)[‡]	2425	[Wha77]
	$2\nu_2$ Fermi resonance	2425	[Ber64]
	not assigned	2430[b]	[Sch94]
	ν_3	2443	[Dev90b]
	$2\nu_2$ Fermi resonance	2432	[Dev90b]
	fully coordinated[a]	2440–2533[*]	[Thi84, Thi87]
	ν_3 (LM)[‡], ν_1 out–of–phase[†]	2485	[Wha77, Ber64]
	ν_1[a]	2481[*]	[Thi81, Thi87]
	not assigned	2484[b]	[Sch94]
	fully coordinated (out–of–phase)	2580	[Dev95]
	distorted four–coordinated	2580[c]	[Row95]
	partially coordinated	2590–2640[*]	[Thi84, Thi87]
	dangling O (out–of–phase)	2640	[Dev95]
	dangling O (triply coordinated)	2645[c]	[Row95]
	free OD	2725	[Dev95]
	free OD (triply coordinated)	2725[c]	[Row95]
	$\nu_1 + \nu_T$[a]	2730[*]	[Thi84, Thi87]
Amorphous	ν_1	2385	[Dev90a]
	ν_3 (TM)[‡]	2436	[Wha77]
	ν_3	2470	[Dev90a]
	ν_3 (LM)[‡], ν_1 out–of–phase[†]	2499	[Wha77]
	distorted four–coordinated	2580[c]	[Row95]
	dangling O (triply coordinated)	2650[c]	[Row95]
	free OD	2727[b]	[Sch94]
	free OD (triply coordinated)	2728	[Dev95]
	free OD (triply coordinated)	2728[c]	[Row95]
	free OD (doubly coordinated)	2749	[Dev95]

[*] D_2O frequencies calculated from H_2O spectra assuming isotope ratio of 1.35 [Mik86].

[†] Out of phase with the immediate neighbors.

[‡] TM and LO denote the transversal and longitudinal optic mode, respectively [Mat03].

[a] Wrong assignment due to electron induced dissociation. Measured on Ru(0001) surface.

[b] Data taken from mesoscopic ($\approx$ 50 bilayers) ice film on Pt(111) surface.

[c] Assignment after a computational simulation of the spectrum.

Table 1.2.: Overview over the vibrational frequencies observed in the IR spectrum of ice.

Phase	Assignment	Vibrational frequency [cm^{-1}]	Reference(s)
Crystalline	ν_1	2295[*†]	[Su98]
	ν_1	2295[*]	[Gro07]
	ν_1	2300[‡]	[Kub02]
	not assigned	2370[*]	[Gro07]
	bonded OD	2360[*]	[Wei02]
	ν_3	2430[*†]	[Su98]
	ν_3	2470[‡]	[Kub02]
	$\nu_1 + \nu_T$	2530[*†]	[Su98]
	combination mode	2540[‡]	[Kub02]
	not assigned	2520[*]	[Su98]
	free OD	2725[‡]	[Kub02]
	free OD	2730[*]	[Su98]
	free OD	2740[*]	[Gro07, Wei02]

[*] D_2O frequencies calculated from H_2O spectra assuming isotope ratio of 1.35 [Mik86].
[†] Partially ferroelectric phase on Pt(111).
[‡] Thick film ($\sim$70 BL) on the Pt(111) surface.

Table 1.3.: Overview over the vibrational frequencies observed in the SFG spectrum of ice.

Phase	Assignment (model)	Vibrational frequency $[\text{cm}^{-1}]$	Reference(s)
Crystalline	ν_1, fully coordinated (D–up)	2260^*, 2200	[Men04][a] [Men05][a]
	partially coordinated (D–up)	2530^*, 2460	[Men04][a] [Men05][a]
	free OD (D–up)	2760^*, 2710	[Men04][a] [Men05][a]
	free OD (D–up)	2706	[Fei03]
	ν_1, fully coordinated (D–down)	2070^*, 2032	[Men04][a] [Men05][a]
	partially coordinated (D–down)	2630^*, 2470	[Men04][a] [Men05][a]
	free OD (D–down)	2630^*, 2710	[Men04][a] [Men05][a]
	ν_1, fully coordinated (half–dissoc.)	1800–2270^*, 2015	[Men04][a] [Men05][a]
	partially coordinated (half–dissoc.)	2560^*, 2530	[Men04][a] [Men05][a]
	partially coordinated (half–dissoc.)	2540	[Fei03]
	ν_1 (ice)	2296	[McG78]
	probably ν_3 (ice)	2434	[McG78]

[*] Data for D_2O have been calculated from H_2O spectra assuming the isotope ratio of 1.35 [Mik86].
[a] Calculated for 1 BL on Ru(0001) surface.

Table 1.4.: Overview over the calculated vibrational frequencies of ice.

1.2. Electron transfer and confinement – experiments and models

Ever since solvated electrons have been discovered in ammonia [Wey64] and water [Har62], confined excess electrons and their dynamics have drawn much attention in many diverse fields of physics, chemistry and biology [Lon90, Leh99, Kev81]. The fascination by this species is understandable – in chemistry and physics the electron is the simplest anion and its transfer between different species one of the most fundamental processes. In biology, electron transfer is a primary step in photosynthesis [Was92] and a voltage difference across membranes created by confined charges is a key aspect for ion permeation [Dzu05]. Excess electrons in ice structures are of general interest also in astrophysics and atmospheric science, mainly because of their high reactivity [Ber09, Lu10, Jen94].

The aim of the following Section is to share this fascination by reviewing some of the important aspects regarding electron trapping or confinement in water, with emphasis on the interaction with well defined structures like ice or small water clusters. The study of the latter can namely provide a level of detail that is difficult to achieve in the bulk [Jor04]. The aspects mentioned here can help to understand the electron localization on ice surface investigated in Chapter 5 in a broader, more general context.

1.2.1. Solvated electron: just add water?

When an extra electron is added to water, a hydrated electron is formed. One can think of several ways to add an electron: radiation, ionization of H_2O molecules, charge transfer to solvent (e.g. from iodine anions: $I^- + \hbar\omega \rightarrow I\cdot + e_{solv}^-$), homogeneous or heterogeneous charge transfer – all processes of vast importance for technology ranging from solar cells to nuclear reactors.

In bulk water, the hydrated electron is believed to be confined in a roughly spherical cavity with a radius of 0.22 to 0.24 nm and to occupy an s–type ground electronic state[14] [Jor04]. The transition to the excited p–state gives rise to a broad (0.84 eV) absorption spectrum near 1.7 eV [Du07]. The electron spin resonance experiments and theoretical models agree that in the electron confinement the first solvation shell plays a major role and mostly influences e.g. its spectral response [Kev81, Lud04]. In agreement with this observation, the widely accepted *Kevan model* of solvated electron was proposed as it is depicted in Figure 1.16. The cavity (solvation shell) bearing the excess charge is formed by approximately six octahedrally distributed H_2O molecules and is about 4 Å large [Zha06]. Radial distribution functions obtained from quantum simulations of the hydrated electron system yield the distance to the nearest hydrogen and oxygen of 2.3 and 3.3 Å, respectively [Sch87]. The water molecules stabilize the electron not by reorienting their *dipoles* as could be expected, but rather by rearranging the single O—H bonds towards its center. If a hydrogen is not involved in the hydrogen bonding, it becomes the most electropositive acceptor site and can form a 'pseudo–hydrogen bond' with the electron [Kim97]. Alternative models discuss the possibility of even lower amount of water molecules being involved in the stabilization: the formation of an solvent–anion complex [Mar99] or hydrated hydronium radical $(H_3O)_{aq}$ [Sob07].

In general, electron in its s–ground state can be excited either to a p–like state, or to the delocalized conduction band of the solvent (shown in Figure 1.16 left). The measurements of the transient absorption dynamics reveal three distinct time scales for its decay process – 50

---

[14]Recently, studies emerged showing that an electron can be stabilized on the *surface* of liquid water, although its binding energy there is lower than in the bulk. The lifetime of this species was found to exceed 100 ps [Sie10b].
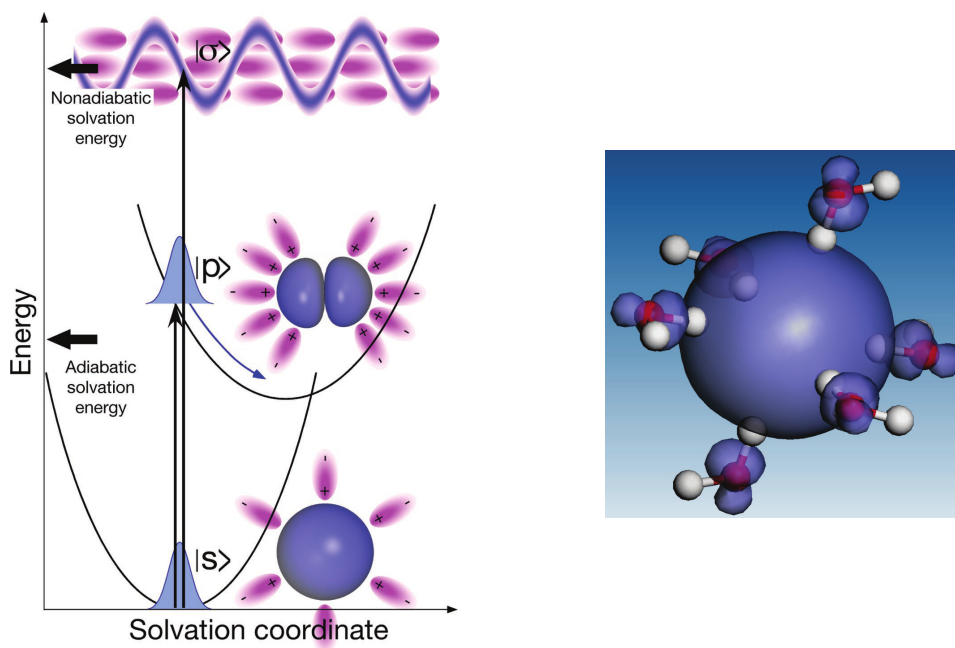
Figure 1.16.: Left: electron excitation to a p–like state and to a delocalized conduction band of the solvent. Right: Kevan model of the solvated electron. Adopted from [Zha06].

femtoseconds, 200 to 300 fs and 1 picosecond [Bar89, Jor04]. In the model of adiabatic solvation [Yok98], the fastest time constant is attributed to librational motion (hindered rotation) of the electron surrounding molecules, because it exhibits a strong dependence on hydrogen isotope present in the water $(\tau(D_2O)/\tau(H_2O) \sim 1.4)$. The 200–300 fs process is assigned to nonradiative decay (nonadiabatic internal conversion) of the p to the s state. In the 1 ps event, the long–time relaxation of the s state takes place.

The excitation to the conduction band of the solvent proceeds according to the adiabatic solvation model from the $p^{\dagger}$ state reached after the initial 50 fs and is responsible for the delocalization of the excess charge resulting in its transfer to different solvent sites [Yok98]. Unfortunately, the exact mechanism of the motion through the water is still not known.

If the absorption spectrum of the solvated electron is measured at various temperatures, one can observe a pronounced shift of the absorption maximum towards lower energies with increasing T. Close to the boiling point of water the absorption peaks at 1.531 eV, a general trend shows a slope of the temperature induced spectral shift of $-2.4 \, \mathrm{meV \, K^{-1}}$ [Jou79]. Using deuterated water yields a minor change in the peak position of about 0.025 eV that almost does not change in the whole temperature range.

A possible explanation for this phenomena lies in the reduction of hydrogen bonding – the interaction energy with water molecules is lowered due to the increased thermal motion of the molecules. It was estimated from computer simulations estimated that the number of hydrogen bonds is smaller by about 15 % at 373 K in comparison with their number at room temperature [Mar99].

Different from ammonia, where the blue color of a solvated electron can be observed for days, in water its spectral signatures vanish after a time in the order of several µs [Har62, Tho99]. It is the large amount of possible decay channels and the unknown nature of electron transport in aqueous media that accounts for the fact that most of the studies of electron confinement were

performed on small charged water clusters.

1.2.2. Sticky big electrons: confinement in ice clusters

Starting from the smallest size, a single water molecule does not bind (and will not attach) an electron[15]. It is the collective interaction between the water molecules that is essential to confine the excess charge in a cluster, but also in the liquid water as can be inferred from the enormous reduction in the photon energy required (6.4–6.5 eV) to produce the hydrated electron in bulk water, e^-(aq), versus the photon energy required (12.6 eV) to produce an electron from an isolated water molecule, i.e. to ionize it [Coe06]. Collective interactions enable the electron to exist in states that are less localized than, for instance, the valence orbitals of water molecules. Every neutral atom (with no charge) or molecule possess either a multipole electric moment or polarizability. Thus, all such species could, in principle, be able to bind an electron based on the classical electromagnetic theory. However, such a electrostatic interaction must be large enough to generate a bound state, which was theoretically predicted for particles or clusters with a dipole moment exceeding 1.625 D, but owing to the electronic exchange repulsion no molecular species with a dipole moment smaller than 2.5 D was found to form an energetically stable electron complex (the stability is expressed in terms of energy needed to remove an electron from the complex – the *vertical detachment energy*, VDE). A single water molecule ($\mu = 1.85$ D) is hence not capable of binding the excess charge. Water dimer ($\mu = 2.6$ D) is the smallest water cluster that accepts an electron attachment (the binding energy is 50 meV) [Lee91]. When the cluster size increases, it starts to resemble the solvated electron state. For a cluster of 4 molecules the dipole–bound state decays rapidly (within 200 fs) by vibrational autodetachment, but already in a cluster $(D_2O)_5$ the 'solvent' rearrangement takes place stabilizing the excess charge [Leh99]. The energy the electron gains corresponds to several hundreds meV and the confinement attributed to cluster isomerisation takes less than 3 ps. Enhanced stability of the cluster–electron system, yielding an electron lifetime of several tens of picoseconds might be the consequence of large dipole in the cluster caused by the iodine ion used as a source for the solvated electron.

The optimized geometry and excess electron orbital for a pure water cluster is shown in Figure 1.17. To prepare such clusters and measure their vibrational spectrum is experimentally
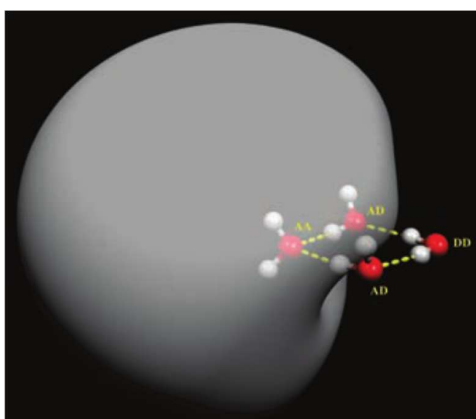
Figure 1.17.: Electron interaction with a small water cluster. Adopted from [Ham04].

challenging, but can be achieved by nanomatrix spectroscopy [Ham04]. From such measure-

---

[15]It is possible to create a water radical anion $H_2O^-\cdot$ in the reaction between $O^-\cdot$ and methylamine [De 84].

ments, supported by the theory, already some flavors of electron solvation can be tasted: the excess charge is closely associated with a single water molecule attached to the supporting network through a double H–bond acceptor motif [Ros06]. The dipole moment and both hydrogen bonds point towards the space with a large electron probability density.

Moving to larger sizes soon becomes computationally not tractable, especially due to the large number of independent degrees of freedom in the system and a very exact level of theory needed to treat the very diffuse electronic state precisely[16]. Larger clusters also offer a rapidly growing number of conformations and of possible solvation sites and can offer the possibility to confine an electron *inside* of the cluster (internaly bound states) or in a way that significant electronic amplitude appears *outside* of the molecular framework (surface bound states), the first very much resembling the solvation in the water.

This is where the controversy starts: many different theoretical approaches predict a stabilization on the cluster surface for molecular assemblies consisting of 32 H_2O molecules or less and admit the possibility of internally bound state to exist only in an aggregate of more than 64 molecules [Bar87, Bar88]. Additionally, also in clusters like $(H_2O)_{500}$ a surface bound electronic state might exist, at least as a metastable species and can be internalized if the cluster temperature is large enough [Tur06, Mar10]. The existence of this metastable state has been confirmed experimentally as well [Ver05b], although with the aim to show the many possible bound states in the electron/cluster system. Where the theory and experiment do not converge is the existence of internally bound electron in small clusters [down to $(H_2O)_{11}$] [Pai04].

The problem has many facets. The first study of electron confined in a small water cluster $(H_2O)n$ with $n = 2$–69 revealed a perfectly linear correlation between the vertical detachment energy and the cluster size approximated by $n^{-1/3}$ (see Figure 1.18). Moreover, if the correlation
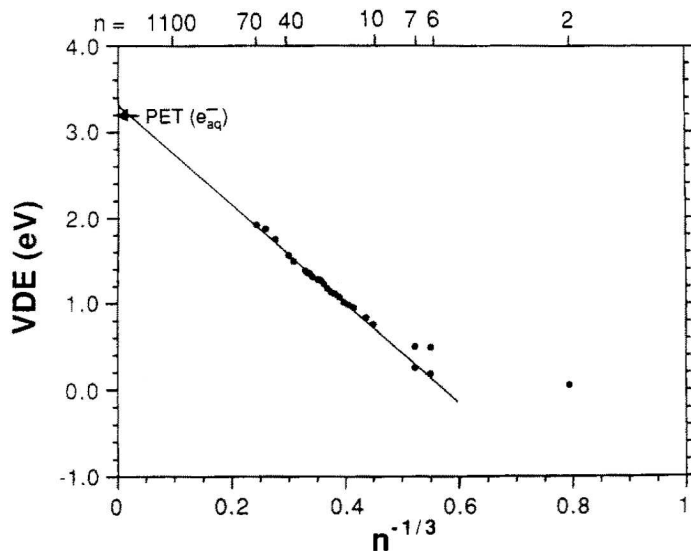
Figure 1.18.: Vertical detachment energy as a function of cluster size. The extrapolated value for an infinite cluster corresponds almost exactly to the photoelectric threshold for hydrated electrons [PET(e_{aq}) = 3.2 eV]. Adopted from [Lee91].

is extrapolated to an infinite cluster size the energy is obtained that is needed to create a free

---

[16]In many works, CCSD(T) (coupled–cluster single and double with non–iterative triple excitations inclusion) using a large basis set with diffuse orbital functions is used. The comparison of computing cost of this method to identical DFT calculation was made in reference [Her06].

charge carrier in ice plus the width of its conduction band [Lee91]. The authors concluded that this result is in agreement with the classical electrostatic description and has to be interpreted as a proof of a internally hydrated electron in nearly all cluster sizes.

This very intuitive statement was, however, proved wrong later [Mak94]. In their theoretical work, Makov and Nitzan showed that both interior *and* surface states manifest the linear scaling of the VDE with $n^{-1/3}$. More than that – in the developed continuum dielectric model the free energy of transfer between the surface and the cluster interior is essentially zero. Vanishing is hence the energy difference between the VDE for an internally and surface bound electron and measuring the detachment energies becomes not appropriate to resolve either solvation site.

In contrast to this prediction, a photodetachment study showed several the existence of three different cluster isomers exhibiting various VDE and assign one of those to the internalized electron state, based on the highest binding energy and its preferential formation at higher cluster temperatures [Ver05b]. Following debate, best characterized by the quotation: 'in our opinion' [Tur05b] did not resolve the problem [Tur05a, Ver05a, Tur05b, Tur06, Coe06]. Newer experimental studies have even found an electron bound to the cluster even stronger than the one previously discussed and showing an unusual size–selectivity, as it becomes prominent only if the number of molecules equals to certain magic numbers [Ma09]. From this selectivity the authors again infer the internal confinement of the excess charge.

Regardless of the real bonding site in this intermediate range, both theory and experiment agree on the possibility of electron localization at the surface or in the interior of a very large (more than 200 molecules) water cluster [Mad09]. This is of particular importance for the present work, as the ice structure on Ru(0001) very much resembles clusters grown on a metal substrate (see also Section 1.1.3). An electron can be thus stabilized either on the ice surface [Bal05] or in the interior [And05]. Although the data and models presented in Chapter 5 do not present a general answer to this problem, they offer a possible way how to look on the electron stabilization and understand its dynamics in a particular system. More research would be required to confirm, how this small piece fits to the general mosaic of the electron confinement problem.

1.2.3. Frozen hot electron: a two–photon photoemission study

Solvated, confined electrons can be utilized as a chemical species and drive technologically important processes. The simple idea, to just add electrons to an unsaturated aromatic molecule A and obtain more saturated compound B, is known in organic chemistry as the Birch reduction [Bir58]. Reaction conditions are, however, very demanding – dissolving alkali metals in ammonia can lead to an explosion, if traces of water are present. On the other hand, the large lifetime of ammoniated electrons enhances the reaction yield in this harsh environment.

To increase the stability of water–electron complex would be an ultimate goal, if one thinks about reaction taking place in biological environments, or simply about less demanding alternative to the Birch reduction. Water radiolysis studies have shown, that an electron is spectroscopically detectable up to several μs after its creation. The longest lifetime reported for an solvated electron, however, is several minutes and was found in a time–resolved two–photon photoemission (2PPE) study [Gah04, Bov05a, Stä07a, Bov09]. One of the main goals of this thesis is to explain this extraordinary stability of the excess charge and to offer a better microscopic picture of the processes involved. This is done in Chapter 5 (page 147). However, it may be useful before to summarize and discuss the 2PPE experimental data before, which is the aim of the following Section.

Two–photon photoemission spectroscopy

Photoemission (or one–photon photoemission) spectroscopy is a well established method to probe the electronic structure of occupied states at diverse surfaces from core–levels up to the valence band [Cah03]. If two photons instead of one are used – first with variable energy below the substrate's work function and another one with the energy sufficient to overcome the vacuum level in the consequent step, it is possible to examine the unoccupied states as well. Basic scheme of the 2PPE process is shown in Fig. 1.19. After the first photon (*pump*) is
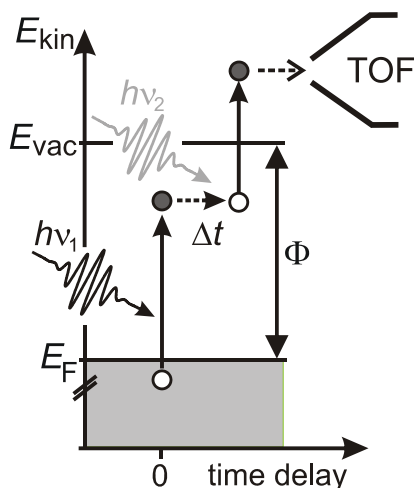
Figure 1.19.: Principle of a time–resolved two–photon photoemission experiment. Two pulses, $h\nu_1$ and $h\nu_2$ overlap on the surface and excite electrons. The amount of energy carried by each of the two photons may differ, but in sum is grater than the system's work function, so that doubly–excited photoelectrons can be detected, while their kinetic energy is measured by a time–of–flight spectrometer.
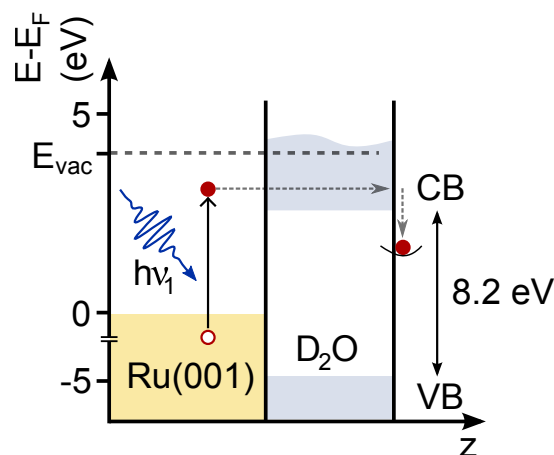
Figure 1.20.: Schematic energy diagram of electron trapping mechanism in ice. Electrons are excited from metal to a state overlapping with the conduction band (CB) of ice. From this state they can relax and stabilize, altering local ice structure so that their binding energy increases.

absorbed, the substrate electrons are excited into an intermediate state, from where the second photon (*probe*) can provide them with enough energy to leave the system in a determined direction, with a certain amount of kinetic energy, that is measured by a detector (time–of–flight analyzer). If pump and probe are a part of different ultrashort laser pulses, electron dynamics, i.e. the temporal evolution of electron binding energies in unoccupied states can be explored by adjusting the delay between them. As an example, experiments complementary to those introduced in Section 1.3.3 and examined in Chapter 6 have been performed and are able to resolve the ultrafast thermalization of hot electrons after fs–laser excitation [Lis06]. In this case, energy from hot electrons is almost completely transferred to the phonon heat bath on a timescale of approximately 500 fs, but some unoccupied states, whose wavefunction overlap with the substrate's surface states is small, can hold an electron for much longer time. Molecules adsorbed on the surface can effectively push–out or screen charges [Mar02, Ber04] and lead to their localization [Ge98], what usually results in longer lifetimes, too. Unoccupied states under investigation (between E_F and E_{vac}) can belong to adsorbate layers as well [Gah00]. In

such case, the electron is effectively transferred from one medium (metal) into another. Similar charge transfer is of key importance for various processes ranging from electronic devices to photosynthesis. More about applications and a deeper theoretical insight into 2PPE experiment can be found in numerous reviews [Pet98, Ech04].

Detecting frozen electrons

If 2PPE spectra of thin, crystalline ice layer ($\sim 4\,\mathrm{BL}$) supported on Ru(0001) single crystal surface are collected with the first photon energy larger than $3.4\,\mathrm{eV}$, a state at $2.3\,\mathrm{eV}$ above Fermi level (E_F) is revealed (see Fig. 1.21 left). This spectral feature (denoted as e_T) has an
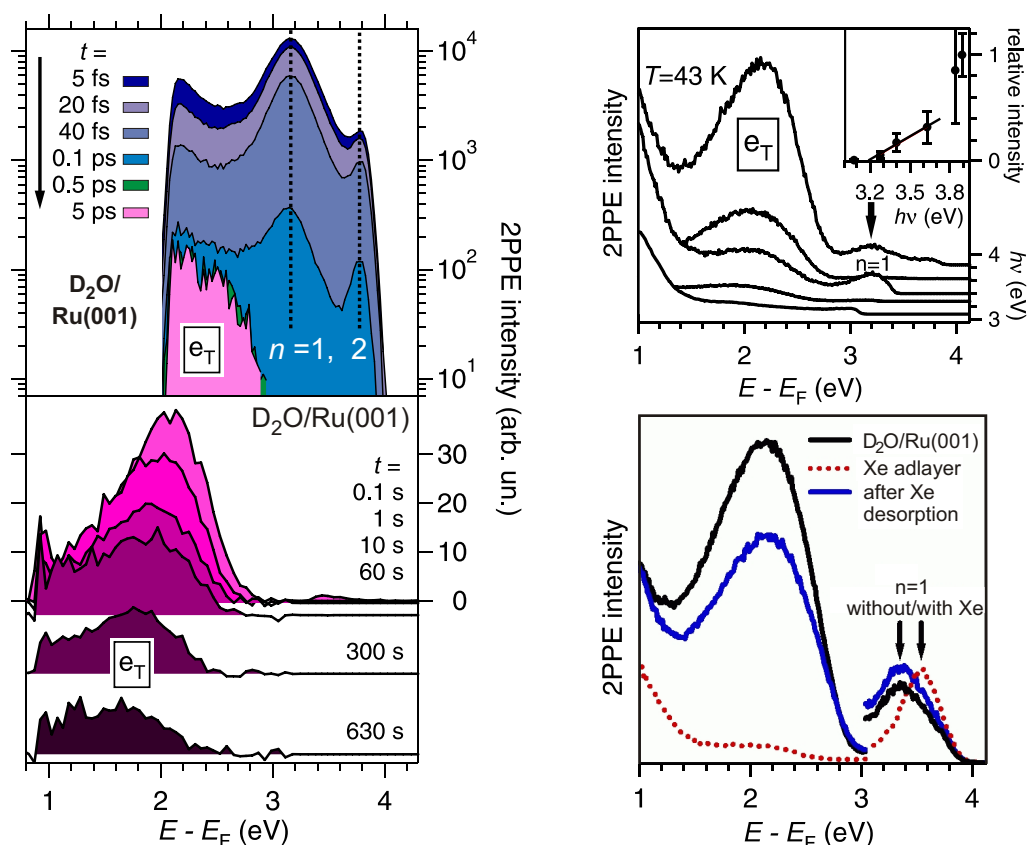
Figure 1.21.: A brief summary of 2PPE results. Left: Temporal evolution of the e_T state attributed to trapped electrons. States with $n = 1, 2$ are the first and the second image potential state (IPS), respectively. On a logarithmic intensity scale, considerable, though not full, depopulation of e_T state within the first $5\,\mathrm{ps}$ is recorded. The e_T level occupation does not significantly change over next $600\,\mathrm{s}$, but its energy shows a large shift towards Fermi level. Top right: Intensity of the e_T state as a function of the photon energy in pump pulse. Clear is the threshold at $3.2\,\mathrm{eV}$, when trapped electron signature starts to appear. Bottom right: Xe–titration experiment. The population of the e_T state can be reduced dramatically, if trapping sites are blocked by a rare–gas atom. Reproduced from [Bov09].

extraordinary long lifetime of several minutes and exhibits behavior significantly different from other electronic states present in the 2PPE spectrum.

First, its temporal evolution shows a large stabilization (increase in binding energy – although still negative in absolute number) of about $\sim$1 eV on a timescale of several *seconds*. For comparison, in other states no temporal shift in energy can be observed and a lifetime of at most several tens of fs is measured. The new feature has a considerable width as well: more than 1 eV, compared to $\sim$0.5 eV of other spectral resonances.

Further, this unoccupied energy level is not populated completely by the first UV pulse, its intensity rather increases with the number of incident photons coming from consequent pulses and reaches a photostationary state (where population and depopulation are in equilibrium) with a time constant of 0.17 s at a laser repetition rate of 400 kHz and a fluence of 0.02 mJ/cm^2. Having such a long lifetime, it is not surprising, that the e_T spectral signature is independent on pulse length varied between 100 and 300 fs, whereas the intensities of other states decrease considerably with increasing pulse length.

Interesting is the structural effect as well – in amorphous ice, that should change the electronic structure of ruthenium almost in the same way as the crystalline D_2O, no long–lived state is detected [Gah02, Gah04]. A feature corresponding to the unoccupied electronic state confined in ice appears at 2.77 eV and within the first 300 fs stabilizes by about 0.85 eV towards the Fermi level [Gah04]. However, after 400 fs this new state is depopulated and no electrons with corresponding energy are detected. Similarly, for coverages below 1 BL the e_T feature does not appear.

Together with the deeper knowledge of the electronic structure in the band gap of ice (discussed in Section 1.1.2), a conclusion can be drawn, that the electrons detected as e_T peak are species trapped and confined by the crystalline ice structure. This seems reasonable, because a perfect crystalline solid does not provide states between the conduction and valence band, which hinders the energy decay of stabilized excited carriers back into metal, as a scattering event between the electrons from below the Fermi level and from a higher lying confined state is improbable for this reason (there are no states to scatter into). Moreover, the wave function overlap of the newly created state with the states in the metal can be low (due to a screening effect of water molecules), which imposes a further restriction for the electron decay. The experiments also allow to resolve some additional aspects of the trapping mechanism:

The clear threshold energy of 3.2 eV coincides with the onset of the first image potential state (IPS[17]). This leads to the assumption, that this IPS is directly involved in population of the e_T state. On the other hand, its lifetime is about 5 fs [Bov05c] after deconvolution. This time is not sufficient for water molecules to reorient and screen or stabilize the charge. It is therefore inferred, that preexisting traps are populated after excitation – sites, where electron can reside longer and stabilize.

The dependence of electron trapping on ice structure and other findings can be explained easily in this framework as well. Figure 1.20 schematically introduces the energetics of trapping mechanism. Bandgap between conduction band (CB) and valence band (VB) of crystalline ice is way too large for 3.5 eV photons to overcome. The E_F of Ru(0001) lies above the Fermi level of ice and approximately 3.2 eV below the CB of ice. To excite electrons and inject them into the unoccupied ice states this energy is required. This is, however, true only for crystalline ice, where the bandgap is really state–free. As shown in Figure 1.7 on page 17, the projected density

---

[17]Image potential states are horizontally delocalized, unoccupied electronic states above Fermi level, that arise due to the charge screening, if an electron is localized in close vicinity to a metal surface (an image charge density of opposite sign in surface layers is created, which mirrors the excited charge). If the substrate exhibits a bandgap in its bandstructure, it may be not possible for an electron to tunnel directly into the metal. This repulsive surface potential together with attractive force having origin in the image charge create a potential well, more precisely a Rydberg series of bound surface states [Ech78, Ech86].

of states in amorphous solid exhibits significant amount of states in the bandgap attributed to structural defects [Zal98]. Usually, such structural deformation has a closer overlap with the metal wavefunction as well, what explains the different electron stabilization in amorphous ice compared to its crystalline counterpart. If namely preexisting trapping sites in ice are predominantly populated by excited charges, those states should posses lower energy and due to higher tunneling probability (given by the larger wavefunction overlap) decay faster into the metal in amorphous case, which is indeed observed. Similarly, low water coverages (below 1 BL) do not support electron stabilization probably due to the spatial proximity and hence better wavefunction overlap between such state and metal, which has the same consequences as in case above.

Further important aspect of electron confinement concerns the distribution of electron density along the surface normal – as discussed in previous Section, confined charges generally reside on top of an ice cluster and not inside of such structure, where hypothetically better coordination could be achieved. For thin, bulk ice layer the same question can be posed: is the electron located at D_2O–vacuum interface, or rather stabilized inside?

To address this problem, Xe–adlayer has been dosed on top of crystalline ice. Measurements show, that ∼4 layers of Xe are needed to cover the water clusters completely, what is a particularly obvious demonstration of the cluster morphology of crystalline D_2O (discussed in Section 1.1.3). After Xe coadsorption, the majority of available preformed sites on the surface is spatially blocked by a rare gas atom. A 2PPE measurement comparing the e_T intensity before and after codeposition is presented in Figure 1.21 (bottom right panel). Evident is that the e_T state is almost completely unoccupied, if surface electron traps are closed. Together with the dramatic drop of population of trapped electrons, the first IPS shifts to larger energies. Even though its binding energy plays a major role in populating e_T state (see Fig. 1.21 top right panel), it can be shown, that this shift is clearly not the most important reason for 2PPE signal decrease between 1.6 and 3.0 eV. It is therefore concluded, that a (delocalized) surface site preferentially offers a confinement place for the excess electron. A very similar experiment has been reported for ice/Cu(111), where surprisingly electrons tend to be preferentially confined in the bulk under the same conditions and exhibit shorter lifetimes [Mey08]. Results presented in Chapter 5 offer a very intuitive explanation for this phenomenon, which confirms the validity of the model presented there.

Theoretical model of electron trapping

Despite of numerous difficulties connected with the nature of hydrogen bonding and uncertainty in form and distribution of trapping sites, theoretical model for electron trapping has been developed using *ab initio* calculations based on first–principles density functional theory (DFT) [Bov09].

The basic assumption in the theoretical treatment of electron stabilization is that the sites responsible for trapping do exist on the surface before the electrons are photoejected into the water overlayer (as stated before, the short lifetime of the 1 IPS is not sufficient for a dynamic formation of any electron trap[18]). Assuming different generic structural defects on the surface of a D_2O–network, their formation energy was calculated in order to elucidate the possibility of charge stabilization in any of the expected preexisting arrangements. The binding energy of an electron to a trapping site is calculated as a difference between the energies of a charged and

---

[18]In this consideration the possibility is not included that the electrons might alter the local structure of ice considerably during their stabilization and form states that are available also for the charge carriers excited in the next steps.

the neutral trap. Employed theoretical approach includes the interaction of an excess electron with the valence electrons of individual D_2O molecules and therefore allows the decay from an excess electron state at a surface trap into the ice layer as well.

Regardless of the actual layer stacking in the bulk, structure of hexagonal ice (I_h) with (0001)–surface termination was taken as a substrate. The computed surface cell, that allows to localize the electron laterally at the traps is rather large. It consist of 3 BL of ice and 10 BL of vacuum, confinement sites are represented in a 4×4 surface unit cell of ice I_h(0001). Investigated defects include surface vacancies (an entirely missing D_2O molecule), divacancies, orientational defects in the outermost bilayer and admolecules at the surface layer. Examples for some of the considered defects (Bjerrum D and L defects that are compensated at the ice vacuum interface rather than by diffusion into the bulk, as the former requires less energy; see also Section 1.1.2) are depicted in Figure 1.22(a). The notation follows the behavior of water
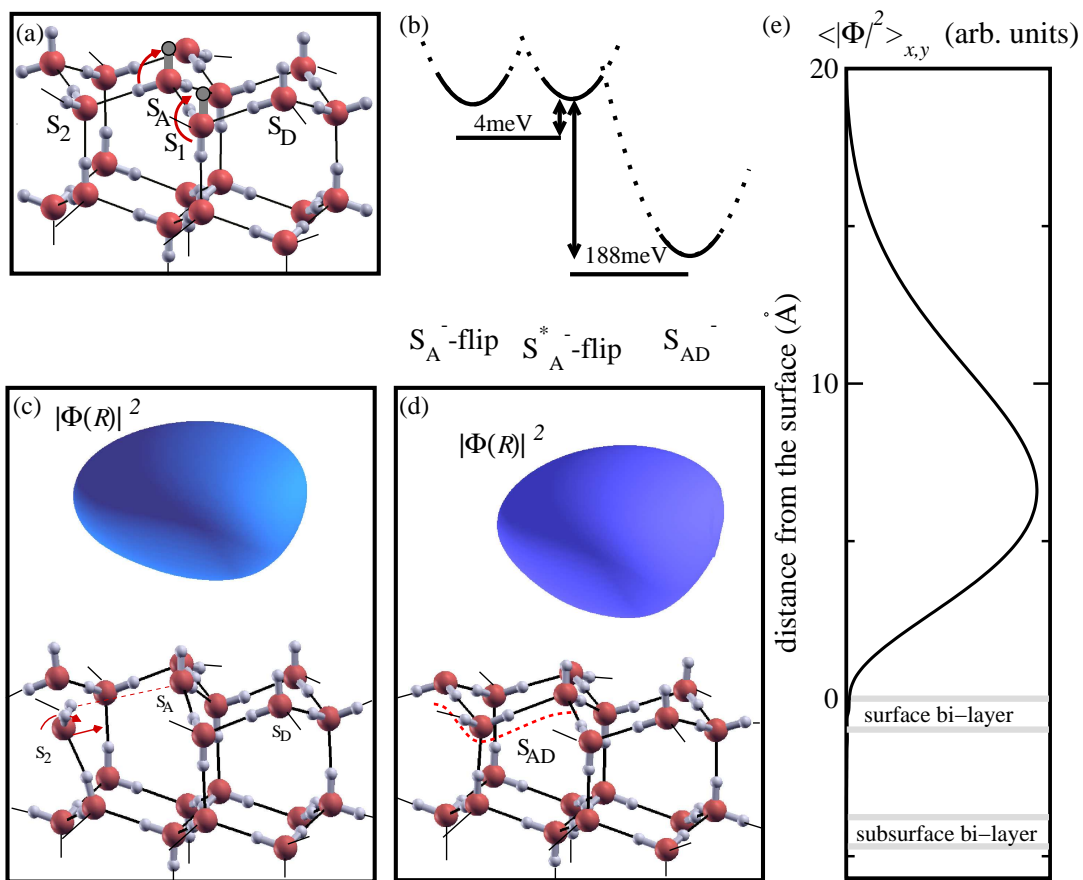
Figure 1.22.: Illustration of defect sites investigated in the theoretical model for electron trapping. (a,c,d) Defects created by flipping of different OD bonds and the reorganization of their neighboring molecules, (b) energy diagram for the S_1 flip and its stabilization (with excess charge), (e) distribution of the projected probability density of an electron localized above the ice layer. Reproduced from [Bov09].

molecules involved in hydrogen bonding. A fully coordinated D_2O molecule contributes to the H–bonded network with two bonds donating electrons to its neighbors ($O...D–O$) and two bonds accepting electrons ($O–D...O$) from water molecules in the vicinity. If one of those bonds is broken at an interface, the affected molecules become either lone pair donor (S_D, S_1)

or acceptor (S_A, S_2).

If formation energy for every expected configuration is calculated, it can be considered as a very good measure for the relevance (abundance) of the corresponding defect site. As for vacancies and divacancies this energy is very large, they are rejected from further examination. Moreover, it can be shown, that they do not offer any strong trap. From energetic point of view, the most favorable orientational defect is the acceptor molecule S_A, that reorients such, that one of the OD–bonds points towards the vacuum (S_A–flip). Apparently, it changes its S_A configuration and resembles S_D type of coordination. Additionally a Bjerrum L–defect is created, forcing undercoordinated neighboring water molecules to reconstruct as shown in Figure 1.22(d). Alternatively, the molecule S_1 can reorient (S_1–flip). Nevertheless, this motion is connected with a larger formation energy. In both cases the reorientation of surrounding molecules leads to the restoring of the natural surface coordination as depicted in Figure 1.22(c). The formation with both D atoms pointing towards the excess electron, similar to the bonding site in small clusters [Ham04] turned out to be unstable.

After electron is bound to one of the two stable defects discussed above, its probability density resides essentially outside the ice layer. Figure 1.22(e) shows this situation as the in–plane average of the excess electron wave function $\langle \Psi^2 \rangle$) along the surface normal for the electron located at a S_A–flip. Figure 1.22(c,d) also shows that the state occupied by the excess electron is laterally well localized. The most important result of the simulation is that the formation energy of a structure arising from the S_1–flip might have a negative formation energy in the presence of an electron (see Figure 1.22(b)), which could stabilize the electron–ice complex at the surface. The presence of a stable charge could lead to its further stabilization, unfortunately not treated here in a more detail.

1.3. Dynamics at surfaces: energy transfer between substrate and adsorbate

One of the most fundamental questions that arises, if one studies the surface/adsorbate systems and particularly the reactions taking place at interfaces, is certainly the one about the energy transfer. For many years, thermal desorption spectroscopy (TDS) in its many flavors has been the main tool for investigation of such processes and it was able to provide one at least with the kinetic parameters like the adsorption energy value – i.e. with the minimum energy that needs to flow from a substrate to the adsorbate to induce its desorption [Mil87, Kin75]. However, no information about the transfer *mechanism* could be extracted as this method studies systems in thermal equilibrium, where the energy contents of all subsystems does not really change.

To investigate the energy *transfer*, it would be very convenient to study the system that is brought out of the equilibrium state in some way. Different energy channels would then be activated depending on the actual imbalance between the individual subsystems and the energy flow could be traced.

The first step in the following Section will therefore be an attempt to address the question, which relevant subsystems can play a role particularly in a process like desorption from a metallic substrate and how do they interact with the adsorbed molecules. After several coupling models are reviewed, the modeling of desorption yield parameters is introduced. They do not only offer an insight into the final amount and energy distribution of the desorbing species, but also considerably enhance our knowledge about microscopic processes that are responsible for the desorption from a surface.

1.3.1. Adiabatic and non–adiabatic energy transfer

Many theories in solid–state physics (e.g. the jellium model) aimed to describe the quantum mechanical features of real metals make use of the separation between the electron gas and the lattice. This distinction is quite natural, as it separates very different entities with similar properties present in one system they share. This concept in not unknown to theoretical physics as well – the Born–Oppenheimer approximation (BOA) [Bor27], a starting point for almost all theoretical studies regarding chemical reaction dynamics, separates nuclear and electronic degrees of freedom for a couple of good reasons, too. It is therefore justified to approximate a solid substrate in this way and consider the interaction of the electronic and phononic subsystems with an adsorbate in the following.

Adsorbate–phonon coupling: adiabatic desorption

The conventional image of the desorption process one could take from the thermal desorption spectroscopy is that heating the substrate enhances the energy of lattice vibrations (phonons) and an adsorbate encounters stronger and stronger 'kicks' from the substrate atoms that may drive it from its equilibrium position over the desorption barrier. Such a process is schematically depicted in the Figure 1.23. The whole process takes place on a single potential energy surface curve and is easy to understand as nuclear degrees of freedom of the adsorbate couple to the nuclear degrees of freedom of the substrate. In Born–Oppenheimer approximation, the electronic and phononic subsystems are in thermal equilibrium, because the nuclei are much heavier than electrons and their comparably slow oscillation can be hence followed immediately by them resulting in the equal temperature of both 'heat baths'.
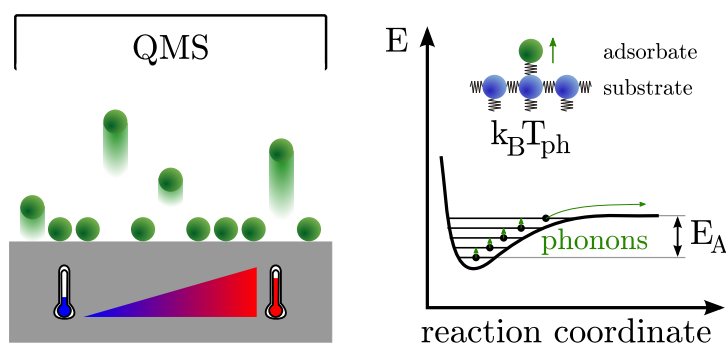
Figure 1.23.: Example scheme of a phonon mediated desorption.

Adsorbate–electron coupling: non–adiabatic desorption

If the electronic subsystem has to contribute to the desorption process, it is evident, that the BOA has to break down. A wording has been adopted in experiments and theory of ultrafast photoinduced phenomena to name those phenomena as non–adiabatic or diabatic.

In the classical thermodynamics, where this name is borrowed from, processes are called adiabatic, if no heat is exchanged between the system of interest and the surrounding space. A typical adiabatic process, fast gas expansion from a volume V_0 to V_1 under, say, atmospheric pressure (p_{atm}), leads to the cooling of the gas. Energy is transferred to the surrounding in form of work ($W = \int_{V_0}^{V_1} p_{atm} \, dV$), but given a short time, the energy transfer from the surrounding (in form of heat) is negligible. In other words, an adiabatic process can be considered as a result of negligible thermal coupling between the surrounding space and the system itself.

Similarly, in a solid the electrons are often treated as an 'uniform electron gas' (e.g. in the mentioned jellium model) that is in contact with the lattice. If electrons gain energy on an ultrashort timescale, their temperature increases rapidly, but due to the Born–Oppenheimer approximation (adiabatic) they can have no influence on the 'heat' – energy contained in lattice vibrations – of phonons. Only inelastic processes like electron–phonon scattering, or phenomena like diffusion can lead to a cooling of the electron gas. A typical sign of such a coupling is the typical time delay of ∼1 ps until both subsystems equilibrate.

However, in some cases the BOA is not valid. In the non–adiabatic processes the heat contained in electronic subsystem can be transferred directly into the phonon oscillations of the adsorbate. In such a case the energy is redistributed with almost no delay yielding a comparably high transient adsorbate temperatures. From a theoretical point of view, such a situation may occur, if two adiabatic potential energy surfaces (PES), e.g. of the ground and excited state with the same symmetry, cross (avoided crossing[19]; see Figure 1.24) [Wor04], or if for any molecular motion – such as vibration, rotation or translation – there exist a resonant electronic excitation in the metal [HG95]. Typically, the PES refers to a potential energy curve created by electrons, along which the movement of the nuclei takes place. It is therefore reasonable to assume that two different electronic states create two distinct potential wells. They are very unlikely to cross at a certain nuclear configuration, which most often leads to the adiabatic potential wells that have a shape as if composed of a part of each of the potentials and that are not degenerate at any point. If a particle occupying the energetically lower state in Figure 1.24 desorbs from the surface in an adiabatic way, it always follows the lowest curve, fulfilling the thermodynamic

---

[19]Vibronic (vibrational and electronic) coupling, or conical intersection between two electronic states denote the same phenomena.
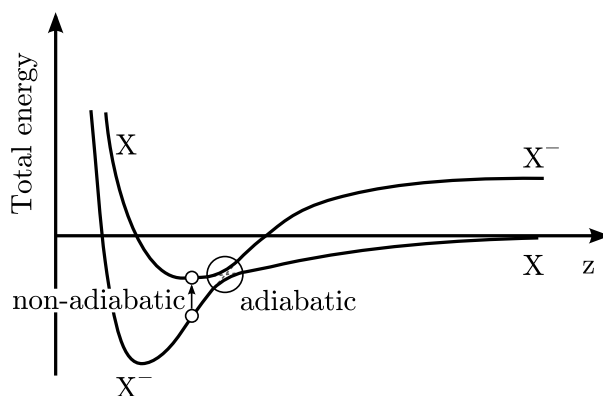
Figure 1.24.: A potential energy surface with an avoided crossing. The two PES curves with the same symmetry approach each other, but at the nuclear configuration that leads to their crossing this is always avoided in diatomics and usually avoided in polyatomic systems.

requirement that the Gibbs free energy should be minimized. The situation is different, if the electronic subsystem is brought out of equilibrium and heated rapidly. According to the adiabatic theorem[20] [Bor20] it will not follow the lower PES, as the time to reorganize the electronic structure close to the crossing point (in the Figure 1.24 required by the charge transfer to the metal) may not be sufficient and the system undergoes a non–adiabatic jump into the upper curve [Gre97, Wod04]. It is obvious that this non–adiabatic jump has severe consequences for the desorption behavior. Even if the system decays to the lower lying state after some time, it can return to a vibrationally excited state (due to its better overlap with the state on the upper PES) which will enhance the desorption probability. The origin of the non–adiabatic coupling can be found by looking into the form of the Hamiltonian, where especially in the vicinity of a conical intersection, the terms describing nuclear motion do not only depend on nuclear mass, but almost exclusively on the derivative coupling $\boldsymbol{F}_{ij} = \langle \Phi_i | \nabla \Phi_j \rangle$ [Wor04].

Up to now, the treatment of the electron–nuclear coupling has been quite general. In the subject of the presented study – on a metal surface – a whole manifold of PES exists, which are formed due to the electron–hole pair excitations in the substrate and their excitation energy starts practically from zero. It is therefore possible that even a nuclear motion may cause an electron excitation, which is probably the simplest nonadiabatic process [Lun05, HG95]. This also makes obvious that non–adiabatic energy transfer should never be simply neglected in the surface/adsorbate systems.

Desorption induced by electronic transition (DIET) and the friction model

So far, a mechanism has been discussed that allows electrons to non–adiabatically jump from one PES to another. But how is this possibility related to the energy transfer into the adsorbate and how can this phenomenon cause a desorption?

A general working picture of such a process is offered in Figure 1.25. Electrons that are allowed to leave the ground state PES can be excited into an anti–bonding lowest unoccupied orbital and this may lead directly to a desorption (DIET). This is probably the case e.g. for oxygen

---

[20]The exact formulation of this theorem states: "A physical system remains in its instantaneous eigenstate if a given perturbation is acting on it slowly enough and if there is a gap between the eigenvalue and the rest of the Hamiltonian's spectrum." This also means, that in case of rapidly varying conditions the probability density of a quantum mechanical system remains unchanged ($|\Psi(\boldsymbol{r}, t_1)|^2 = |\Psi(\boldsymbol{r}, t_0)|^2$).
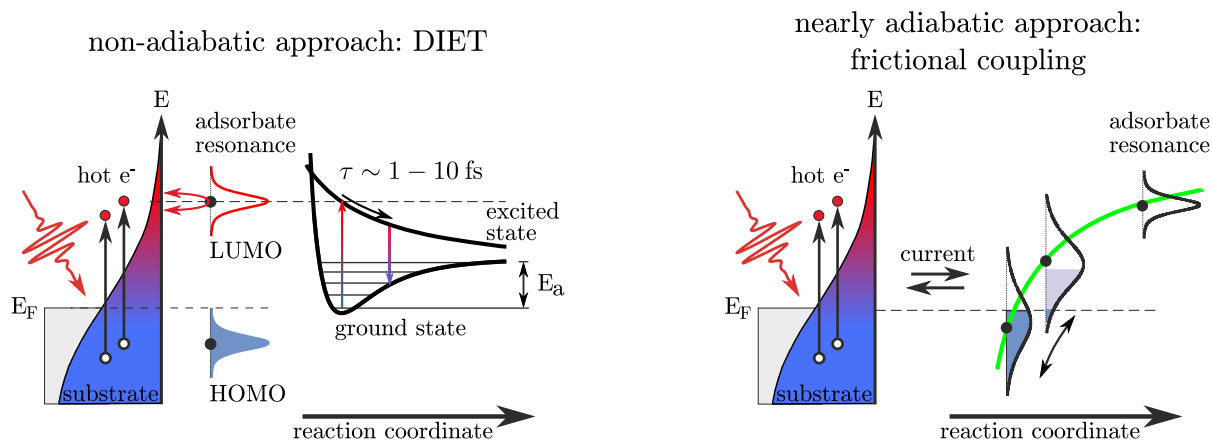
Figure 1.25.: Illustration of the desorption mechanism induced by electron transitions. Right: electrons excited from the substrate to the bonding or antibonding molecular orbital of the adsorbate may cause its desorption either in one (DIET) or several excitation–deexcitation (DIMET) cycles. Left: on an unexcited substrate, the highest lying adsorbate state changes its position with respect to Fermi level during its vibration. The emptying and refilling of this state by substrate electrons effectively acts as a friction that damps this vibration. In a reverse process, if electron density above the Fermi level is sufficient, the electrons being transferred to the adsorbate state may cause its desorption.

desorption from Ru(0001). Figure 1.26 depicts the theoretically calculated density of states (bonding and anti–bonding), overlapped with the Fermi function $\langle n(E) \rangle$ (see Equation 1.1) that shows the states reachable for electrons of given energy distribution, characterized by the temperature of the electronic subsystem (see Section 1.3.2). However, the excited PES does not need to be antibonding [Ant80]. In many cases, more than one excitation is necessary to overcome the activation barrier of the desorption. Desorption induced by multiple electronic transition (DIMET) [Mis92] proceeds via repeated excitation and deexcitation cycles, where the system gains energy due to the difference in the actual position of the system on the higher lying PES: excited electrons exhibit certain lifetime until they decay, which gives them a possibility to relax. The small change of the system's state during this time may lead to a better overlap between the excited state and a vibrationally excited level of the electronic ground state. The deexcitation therefore occurs with the largest probability into an energetically richer configuration then the initial one. If the vibrational excitation rates are larger than the corresponding damping constants, then repeating this cycle may lead to a desorption.

There are several signs characteristic for DIMET, the most obvious one is the strongly nonlinear dependence of the desorption probability on the number of incident photons (fluence). In most cases, the required photon flux is enormously high (~ 4 photons/Å [Bon99]) and achievable only with an ultrashort laser pulse. Many experiments can be described qualitatively very well within the framework of this model, although the unknown nature of the excited PES limits the theoretical modeling only to a macroscopic description of the energy flow between the substrate and the adsorbate [Mis92].

The breakdown of the BOA in an ultrafast surface reaction must be solved in another way to obtain a quantitative agreement between the theory and experiment. An especially successful possibility is to reject the unknown excited PES from the calculation and to leave the adsor-
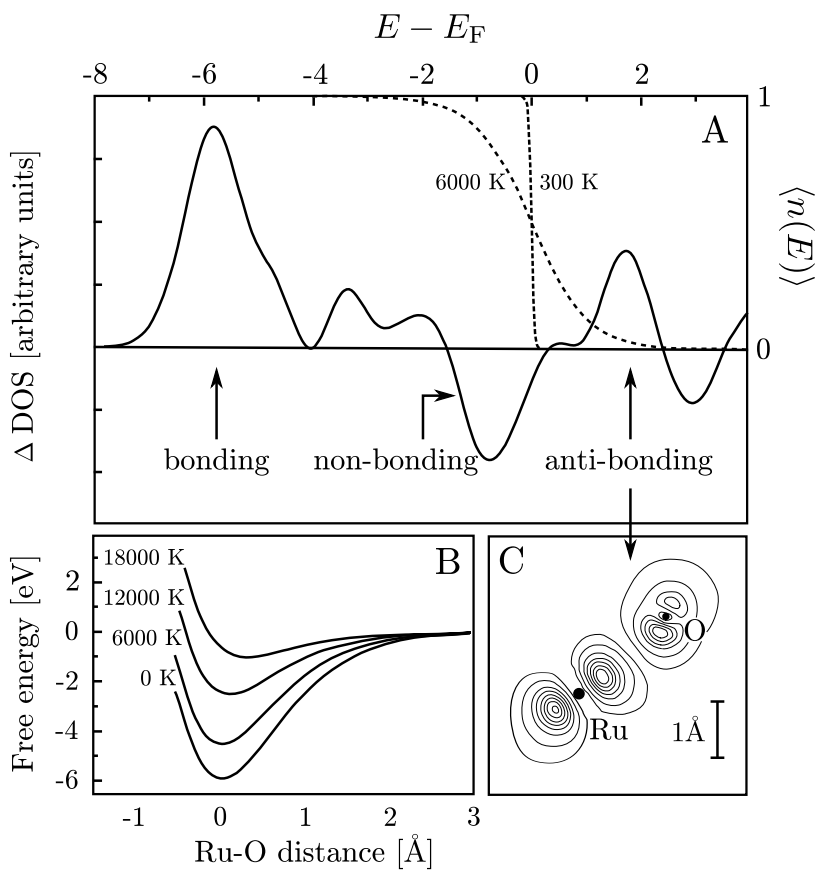
Figure 1.26.: After oxygen is adsorbed on Ru(0001), the density of states of the metal changes as it is indicated by **A**. The bonding states arise that are well below the Fermi level together with non–bonding states extending up to E_F. Additionally, anti–bonding states are formed, but are not occupied normally due to their position in the energy spectrum (1.7 eV above E_F). However, if the electronic temperature is high, the hot tail of the electron energy distribution $\langle n(E) \rangle$ (cf. Eq. 1.1) contains population of particles capable of filling this state and weaken the Ru–O bond. The electron density distribution along the bond axis, corresponding to the anti–bonding peak, is shown in form of Ψ^2 in **C**. The weakening of the Ru–O bond is also obvious from free energy curves (**B**) that are analogous to the potential energy surfaces shown before. Adopted from [Bon99].

bate on the ground potential energy surface during the whole reaction path instead[21]. The non–adiabaticity is brought into play via the *electronic friction*, which simply quantifies the coupling of the adsorbate degrees of freedom and the hot electron energy distribution. The process is schematically depicted in Figure 1.25 left. The coupling between the electrons and adsorbate allows the hot electrons to exert fluctuating forces on the nuclear coordinates and induce desorption [Lun06]. This can be simply illustrated in the following way: consider a broad adsorbate resonance (say the π^* orbital in case of a diatomic molecule; broad due to its short lifetime, since an electron can tunnel into the metal and back easily) being partly

---

[21]Alternatively, the ground potential energy surface can represent the "effective" PES created by the superposition of a continuum of nearly parallel surfaces arising due to the mentioned manifold of excited states originating from the resonant electron–hole pair excitations.

filled. If it vibrates parallel to the surface normal, its position with respect to the Fermi level changes, which leads to a current (electron flow) between the adsorbate and the substrate. In this mechanism, electron–hole pair excitations are involved as electrons are indeed transferred back and forth, which causes damping of the resonance. In the reverse process, a resonance vibration can be invoked by forces exerted by hot electron distribution acting on the nuclear coordinates. The strength of this vibrational dumping, or coupling between the substrate and the adsorbate, is expressed as the electronic friction coefficient, η_{el}, and is inversely proportional to the vibrational lifetime. Its value can be calculated directly from the first principles DFT theory or from the molecular dynamics simulations [Lun06, Tul93].

Although both discussed mechanisms offer a valid approach to solve the breakdown of the Born–Oppenheimer approximation for metal–adsorbate and similar systems, both offer advantages in different cases of interest. Due to its purely non–adiabatic approach, DIET/DIMET is successful in describing high–lying adsorbate states or negative–ion type resonances (as shown in Figure 1.24). Because of the significantly different PES in such a case and a large electron redistribution along the desorption process, the reaction pathway can not follow an adiabatic potential. On the other hand, in many cases (an in the one presented here) the adsorbates do not form any narrow, long–lived states when approaching the metal surface and their interaction with the metal does not lead to a dissociation. Here, the frictional approach is clearly more appropriate.

At the end it should be noted that despite our attempt to make a clear distinction between those two mechanisms, which is justifiable from the experimental point of view, theoretical studies exist that combine both viewpoints in one formalism [Bra95, Mis95]. Its detailed description would, however, go beyond the scope of this thesis.

Resolving energy transfer mechanism between substrate and adsorbate

In the preceding paragraphs, the most important subsystems in the solid – the phononic and electronic – have been discussed. The distinction between electrons and lattice that was intuitively made allows one to independently increase the energy content in the electronic subsystem (e.g. by applying an ultrashort laser pulse) without simultaneously heating the lattice. Performing such an experiment enables us to evaluate the effectivity of the energy transfer between electrons and the adsorbate *before* the electronic subsystem reaches the thermal equilibrium with the lattice, and after this time one can investigate how the desorption proceeds when the energy is dissipated into the substrate phonons and through other channels. In this way, many surface processes and their coupling to different subsystems have already been characterized. However, to make use of this established method, last building block is necessary: up to now, our main concern was the energy transfer between the individual subsystem and the adsorbate. Of course, electrons and lattice interact with each other as well [Kag57] and therefore to fully understand the energy transfer mechanisms, this coupling has to be taken into account, too. A two–temperature model, describing their interaction is therefore introduced as next. A graphical summary of the topics discussed so far, which will try to guide the reader also in the next parts is presented in the Figure 1.27.

1.3.2. Two–temperature model

In the focus of the following section is the interaction between electrons and phonons in general, with emphasis on their equilibration after the electronic subsystem is excited with an ultrashort
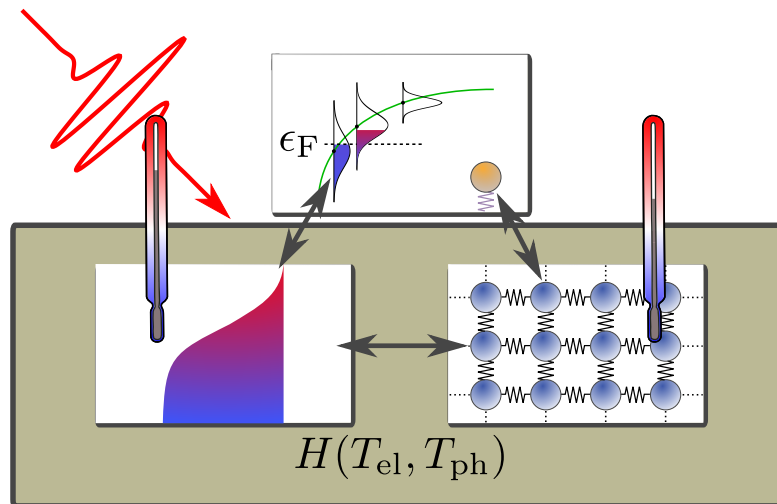
Figure 1.27.: A general outline of energy transfer mechanisms in a substrate/adsorbate system. The total energy stored in the metal is separated to a phononic and an electronic part. They are brought out of equilibrium e.g. by an ultrashort laser pulse that interacts only with electrons. Before their energy is dissipated into bulk and lattice vibrations, the response of the system to transiently hot electron distribution can be followed.

laser pulse. Probably the first question that arises in this context is the fundamental one – how can the energy contained in each subsystem be realistically described and how to account for the fact that this energy is not distributed equally. Again, inspired by thermodynamics, where the total energy of a system (gas) can be described by its *temperature*, which is a value expressing the energy in all degrees of freedom of the system, one can assign a temperature to the electronic and phononic subsystem in the substrate. Similar to the thermodynamical pendant, where the temperature is related to the energy *distribution* of energy states via Boltzman statistics, the energy distribution in the electronic subsystem can be described by Fermi–Dirac statistics[22]:

$$\langle n(E_i)\rangle = \frac{1}{e^{(E_i - E_{\mathrm{F}})/k_{\mathrm{B}}T_{\mathrm{el}}} + 1} \tag{1.1}$$

and in the phononic subsystem by the Bose–Einstein statistics:

$$\langle n(E_i)\rangle = \frac{1}{e^{\hbar\omega_i/k_{\mathrm{B}}T_{\mathrm{ph}}} - 1} \tag{1.2}$$

where $\langle n(E_i)\rangle$ is the average occupation probability of a state with the energy E_i (or $\hbar\omega_i$) – a function that determines the distribution for any given phononic or electronic temperature. One assumption needs to be made and will be discussed in detail later – that those functions are always a good description of electron energies, even after ultrashort pulse irradiation. This may be true, if the electron energy distribution attains the given shape fast enough after the excitation. In such a case namely, the whole energy transfer can be simply expressed by two coupled differential equations [Ani74, New91, Gro95, Fri06]:

$$C_{\mathrm{el}}(T_{\mathrm{el}})\frac{\partial}{\partial t}T_{\mathrm{el}} = \frac{\partial}{\partial z}\left(\kappa_{\mathrm{el}}\frac{\partial}{\partial z}T_{\mathrm{el}}\right) - H(T_{\mathrm{el}}, T_{\mathrm{ph}}) + S(z,t) \tag{1.3a}$$

$$C_{\mathrm{ph}}(T_{\mathrm{ph}})\frac{\partial}{\partial t}T_{\mathrm{ph}} = \qquad\qquad + H(T_{\mathrm{el}}, T_{\mathrm{ph}}) \tag{1.3b}$$

---

[22]Valid for non–degenerate distribution of identical, indistinguishable fermions.

   This formulation is extremely elegant and one can 'read' it in the following way: the total energy deposited in the electronic subsystem ($dU/dt = C_{\mathrm{el}}(T_{\mathrm{el}})\frac{\partial}{\partial t}T_{\mathrm{el}}$) equals to the energy absorbed from the optical excitation ($S(z, t)$) and is reduced in time via the electron–phonon coupling ($H(T_{\mathrm{el}}, T_{\mathrm{ph}})$). Further it is distributed into the metal by thermal diffusion, which is expressed as the first term in the Equation 1.3a in a form identical to Fick's second law. Only the diffusion along the surface normal is considered, because the size of the laser spot is large compared to the lateral diffusion length. In the second line a fact is expressed that phonons gain energy exclusively via non–elastic scattering with electrons, which is reasonable in cases when the sample interacts with an optical field and was the purpose of the experiment.

   The system of differential equations 1.3 can be solved numerically [Den99] which generates the temporal evolution of the surface electron and phonon temperatures as depicted in the Figure 1.28. Following further assumptions are present in the modelling:
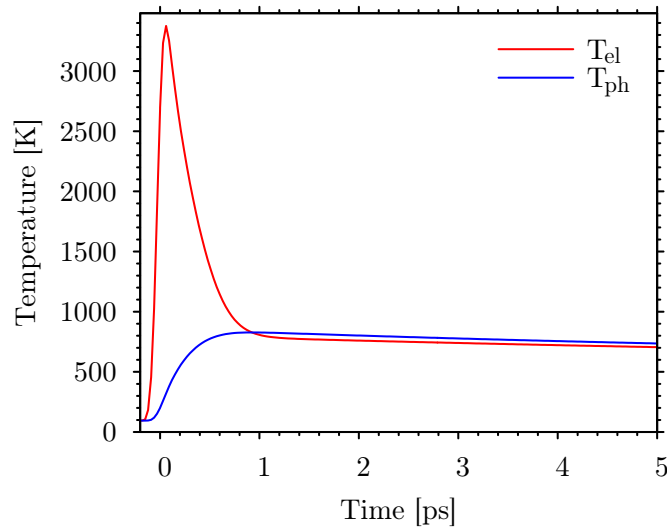
Figure 1.28.: Temporal evolution of electron and phonon temperature at the sample surface ($z = 0$) after an optical excitation with a 100 fs pulse with a fluence of $80\,\mathrm{J/m^2}$.

Electron heat capacity   The electron heat capacity $C_{\mathrm{el}}(T_{\mathrm{el}})$ can be expressed as a product of the temperature independent coefficient γ_{el} and the electronic temperature [Kit96]

$$C_{\mathrm{el}} = \gamma_{\mathrm{el}}T_{\mathrm{el}} \tag{1.4}$$

with

$$\gamma_{\mathrm{el}} = \frac{\pi^2}{3}\mathcal{N}(\epsilon)k_{\mathrm{B}}^2 \tag{1.5}$$

where $\mathcal{N}(\epsilon)$ is the density of states in the relevant energy interval, which is usually taken to be close to the Fermi energy ($\epsilon = E_{\mathrm{F}}$). In case of Ru(0001), the value of γ_{el} amounts to $\sim 3.3\,\mathrm{mJ\,mol^{-1}\,K^{-2}}$ [Ree70, Kit96]. As in the calculation the volume specific heat capacity coefficient is used, this value is converted to $400\,\mathrm{J\,m^{-3}\,K^{-2}}$ using the molar mass and density of the metal. Together with other relevant material parameters it is listed in Table 1.5.

The attentive reader may have noticed that the heat capacity coefficient calculated using Equation 1.5 and the tabulated value of $\mathcal{N}(E_{\mathrm{F}})$ differs from the experimentally measured γ_{el}. And indeed, if the density of states is calculated for zero temperature, it describes a state, where

Electron gas heat capacity coefficient	γ_{el}	400	$\mathrm{J\,m^{-3}\,K^{-2}}$
Electron gas thermal conductivity[*]	κ_0	117	$\mathrm{W\,m^{-1}\,K^{-1}}$
Debye temperature	θ_{D}	415	K
Fermi energy	E_{F}	0.827	Ry[†]
Density of states at Fermi level[‡]	$\mathcal{N}(E_{\mathrm{F}})$	11.8	states/atom/Ry[†]
Molar mass	M_{mol}	101.07	$10^{-3}\,\mathrm{kg\,mol^{-1}}$
Density	ρ	12100	$\mathrm{kg\,m^{-3}}$
Electron–phonon coupling constant	g_∞	185	$10^{16}\,\mathrm{W\,m^{-3}\,K^{-1}}$
Refractive index (800 nm)	$n_r + \mathrm{i}\,n_i$	$5.04 + \mathrm{i}\,3.94$	
Refractive index (266 nm)	$n_r + \mathrm{i}\,n_i$	$1.11 + \mathrm{i}\,2.93$	

[*] Equals to thermal conductivity of Ru at 300 K.
[†] The energy unit 1 Ry corresponds to $2.179\,783 \times 10^{-18}$ J ($13.605\,692$ eV).
[‡] Value calculated by the linear muffin–tin orbital method.

Table 1.5.: List of the relevant material parameters of ruthenium. Compiled from [Den03c, Fri08, McM68, Ree70, Jep75, But77, Ded81, Kit96, Pal98, Bon00a, Lid07, Bos09, Hoh00].

Ru is superconducting. In this phase, the electron–phonon coupling is strong and the value of γ_{el} does not depend solely on the electronic density of states. In a simplest approach, the coupling can be expressed by a constant factor $(1+\lambda)$[23] obtained from the quantum mechanical calculations and is approximately 1.38 for ruthenium metal [McM68]. After this correction, the calculated γ_{el} fits the experimental value very well.

Another point that needs to be verified when applying the assumption expressed by the Equation 1.5 is the expectation of a constant density of states close to the Fermi level. As can be seen from the Figure 1.29, the actual density of states may change rapidly with the energy in some cases and the parameter γ_{el} is no longer energy (ergo temperature) independent. This expresses the fact, that the interaction between the electrons depends on the available phase–space for electron–electron scattering processes. Nevertheless, for ruthenium, we can safely neglect this dependence, as the density of states is almost flat around the Fermi level.

Electron thermal conductivity The thermal diffusion into the metal is described by the electron thermal conductivity, a coefficient analogous to the diffusion constant. Within the Sommerfeld theory of metals, for the thermal conductivity of electron gas the following relation can be derived [Ash76]:

$$\kappa_{\mathrm{el}} = \frac{1}{3} C_{\mathrm{el}}(T_{\mathrm{el}}) v_{\mathrm{F}}^2 \tau = \frac{1}{3} \gamma_{\mathrm{el}} T_{\mathrm{el}} v_{\mathrm{F}}^2 \tau \tag{1.6}$$

Here v_{F} is the Fermi velocity (usually of the order $10^6\,\mathrm{m\,s^{-1}}$) and τ the average time the electron can travel without a collision. As the possible collision partners are only other electrons or the lattice, this time can be further expanded as

$$\frac{1}{\tau} = \frac{1}{\tau_{\mathrm{el-ph}}} + \frac{1}{\tau_{\mathrm{el-el}}} \tag{1.7}$$

It can be shown [Kan98] that if the electron temperature remains below

$$T_* \approx \sqrt{E_{\mathrm{F}} T_{\mathrm{ph}}/k_{\mathrm{B}}} \tag{1.8}$$

---

[23]With electron–phonon coupling constant λ that is described later on page 53; see also Equation 1.15
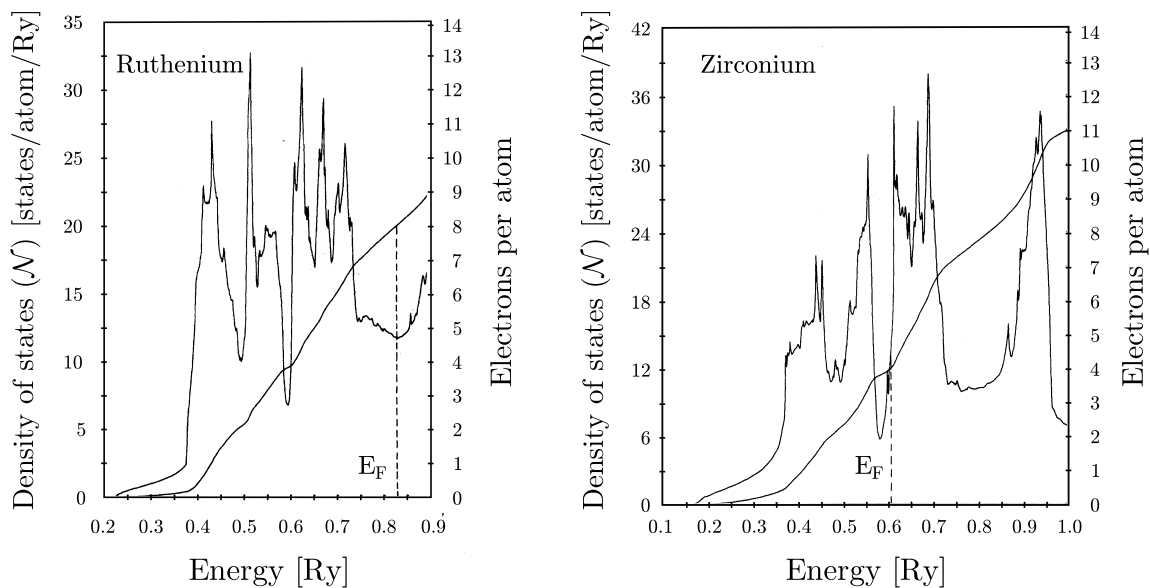
Figure 1.29.: Density of states of two hcp transition metals zirconium and ruthenium. The figure illustrates, how the assumption of constant density of states around Fermi level made in Equation 1.5 may fail in certain cases. Graphs adopted from Ref. [Jep75].

which is for Ru approximately $5700\,\mathrm{K}$, the electron–phonon collisions determine the heat transport. As their scattering rate is in a good approximation proportional to $\tau_{\mathrm{el-ph}} \propto \hbar/(k_{\mathrm{B}}T_{\mathrm{ph}})$, in combination with Equation 1.6 one obtains

$$\kappa_{\mathrm{el}} = \kappa_0 \frac{T_{\mathrm{el}}}{T_{\mathrm{ph}}} \tag{1.9}$$

where all proportionality factors were put into the material constant κ_0.

In the two temperature model, only the thermal diffusion in the electronic subsystem is considered, because on the ultrashort timescale the heat transferred with the sound velocity in the metal (through lattice vibrations) can be in best case transported over a distance comparable to the optical penetration depth (see page 54). This inefficiency can be also estimated by evaluating the Equation 1.6 that has a more general validity and postulates a dependence of thermal conductivity on the square of the particle velocity ($\kappa \propto \langle v \rangle^2$). Considering the Fermi velocity for electrons ($\sim 10^6$) as the effective quantum mechanical analog to the sound velocity ($\sim 10^3$) of lattice vibrations, one can estimate the ratio $\kappa_{\mathrm{el}}/\kappa_{\mathrm{ph}} \propto \langle v_{\mathrm{ph}} \rangle^2/v_{\mathrm{F}}^2 \leq 10^{-5}$. Based on this consideration, it is clear that the thermal conductivity in metals is essentially of electronic nature and the coefficient κ_0 is equal to the thermal conductivity of the pure metal under normal conditions, when the electronic and the phononic subsystem are in equilibrium ($T_{\mathrm{el}} = T_{\mathrm{ph}}$). For metals with large variation in density of states, where the linear dependence between the electronic temperature and the heat capacity does not hold (Eq. 1.4 and thus also 1.6), κ_{el} is often estimated from the fit function to the available thermal conductivity data for the corresponding metal [Mis95].

Electron–phonon coupling The interaction between electrons and phonons can be intuitively understood from a picture of a metal consisting of fixed positive ions with the free electron gas around. If the position of ionic cores is disturbed by a phonon, the potential in the lattice

changes and the electrons are affected, thus liable to scatter to another state. The corresponding term in the Hamilton operator describing the electron–phonon coupling can be evaluated in the perturbation theory framework to[24]:

$$H = \frac{1}{(2\pi)^3} \int \frac{dN_{\boldsymbol{q}}}{dt} \hbar\omega_{\boldsymbol{q}} d^3 q \qquad (1.10)$$

This integral (energy transfer due to the electron–phonon coupling per volume per second) represents a sum over all elementary phonon absorption and emission processes ($dN_{\boldsymbol{q}}/dt$ is the change in the occupation of the corresponding phonon state) weighted with the energy transfer per collision ($\hbar\omega_{\boldsymbol{q}}$). Assuming the phonon and electron distribution follows Equations 1.2 and 1.1, respectively, the Equation 1.10 gives [Gro95, Kag57]:

$$H(T_{\mathrm{el}}, T_{\mathrm{ph}}) = f(T_{\mathrm{el}}) - f(T_{\mathrm{ph}}) \qquad (1.11)$$

with

$$f(T) = 4g_\infty\theta_{\mathrm{D}} \left(\frac{T}{\theta_{\mathrm{D}}}\right)^5 \int_0^{\theta_{\mathrm{D}}/T} \frac{x^4}{e^x - 1} dx \qquad (1.12)$$

This result is one of the fundamental parts of the two temperature model: knowing the Debye temperature θ_{D} [Ree70, Rao77, Ded81][25] and the material specific electron–phonon coupling constant g_∞ for Ru [Bon00a], the energy transfer between the two main subsystems in a solid can be described as a function of their temperature.

The Equation 1.12 can be reduced further, which greatly facilitates the numerical evaluation of the electron–phonon coupling rates. The function

$$g(T) = \frac{f(T)}{g_\infty T} = 4 \left(\frac{T}{\theta_{\mathrm{D}}}\right)^4 \int_0^{\theta_{\mathrm{D}}/T} \frac{x^4}{e^x - 1} dx \qquad (1.13)$$

does not vary greatly at temperatures larger than θ_{D} as can be seen from Figure 1.30 and is often approximated to unity. Under conditions relevant for energy transfer in the surface area of solid, irradiated by an ultrashort laser pulse, this is usually in a very good agreement with the experiments and enables one to write [All87, Bro90, Bon00a]:

$$H(T_{\mathrm{el}}, T_{\mathrm{ph}}) = g_\infty(T_{\mathrm{el}} - T_{\mathrm{ph}}) \qquad (1.14)$$

with g_∞ being the same factor as introduced above.

Due to its importance not only for the surface science, but also for the theory of strong–coupled superconductors, the electron phonon coupling constant is an highly interesting material parameter. It allows one to calculate the critical temperature below which the solid becomes superconducting [McM68, But77]. To avoid confusion while connecting the two different fields of physics, please note that the constant g_∞ is not directly the electron–phonon coupling constant

---

[24]At this place, the quotation »Now fills thy sleep with perturbations« (W. Shakespeare, The Tragedy of King Richard the Third (1597)), taken from an excellent textbook dealing with electron–phonon coupling [Zim60] should show exactly the way that the author will *not* go. The derivation of the Equations 1.10 – 1.12 is hardly illustrative and would probably not be helpful at this point. Nevertheless, it can be found in [Zim60, Wag06, Den99].

[25]The data in the references show that the Debye temperature changes at low temperatures. This is already clear from its definition ($\theta_{\mathrm{D}} = \hbar\omega_{\mathrm{D}}/k_{\mathrm{B}}$ [Ash76]) that connects it with the energy of the highest lying phonon mode. The erroneously often taken value of $600\,\mathrm{K}$ is valid for zero temperature, the experimental value under normal conditions is given in Table 1.5. It should be however noted, that the literature values vary in the wide range between 400–$550\,\mathrm{K}$.
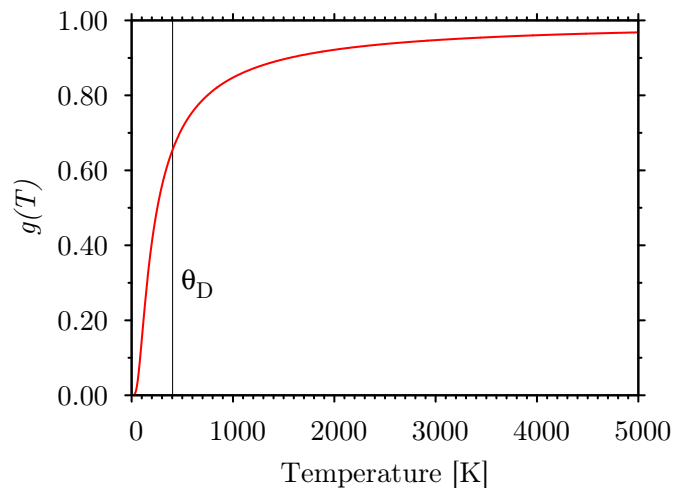
Figure 1.30.: Graphical evaluation of the high temperature electron–phonon coupling approximation. The value of the variable θ_D is set to 404, which corresponds to the theoretical value calculated from maximum phonon frequency in [Ded81]. In materials with higher θ_D the investigated curve $g(T)$ is less steep and the approximation in Equation 1.14 becomes problematic.

usually denoted as λ in the superconductivity theory. Their relation can be, however, expressed simply as [All87, Bro90]

$$g_\infty = \frac{3\hbar\gamma_{\mathrm{el}}\langle\omega^2\rangle}{\pi k_{\mathrm{B}}}\lambda \tag{1.15}$$

where $\langle\omega^2\rangle$ is the square of the average phonon frequency that is accessible e.g. from He or neutron scattering data [Bra97, Hei00, Smi81] as the frequency of the phonon longitudinal mode along the K–point in the phonon dispersion curve. The experimental value of $680\,\mathrm{meV}^2$ corresponding to a phonon frequency of $6.3\,\mathrm{THz}$ is in excellent agreement with the theoretically calculated dispersion curves [Bos09, Hei99, Hei00].

The experimental approach discussed here offers an unique possibility to directly measure the electron–phonon coupling constant g_∞ and hence λ and to the best of our knowledge this has been the only method capable of obtaining this value without any free parameters experimentally[26] [Bon00a, Hoh00, Bro90]. The determined $\lambda = 0.4$ for Ru (cf. Ref. [Bon00a]) is in a good agreement with the theoretical predictions [McM68, But77, San89], which additionally justifies the assumptions made up to now.

Optical excitation   The last term in the Equation 1.3a deals with the energy transfer between the optical field and the metal. Generally, the electric field of a photon can be expressed as

$$\boldsymbol{E}(\boldsymbol{r}) = \boldsymbol{E}_0 e^{\mathrm{i}(\boldsymbol{k}\boldsymbol{r}-\omega t)} \tag{1.16}$$

which is the classical solution of the wave equation with $\boldsymbol{r}$ being the propagation vector and $\boldsymbol{k} = 2\pi\boldsymbol{n}/\lambda_0 = 2\pi(\boldsymbol{n}_r + \mathrm{i}\boldsymbol{n}_i)/\lambda$ the complex wave vector. The imaginary part of the latter is responsible for the damping and therefore for the absorption of light in the medium. This can be shown from a simple consideration, where the light propagation is restrained into one

---

[26]Calculating λ from the critical superconducting temperature requires additionally a theoretical input in form of the calculated Morel–Anderson Coulomb pseudopotential [McM68].

dimension and the material is isotropic, so that the expression for light intensity in the medium can be written as

$$I \propto |E|^2 \propto |e^{2\mathrm{i}(kz-\omega t)}| = |e^{(-z/\delta)}e^{2\mathrm{i}(2\pi n_r z/\lambda_0 - \omega t)}| \tag{1.17}$$

This formulation is known as the Lambert–Beer law with optical penetration depth

$$\delta = \frac{\lambda_0}{4\pi n_i} \tag{1.18}$$

where λ_0 is the wavelength of the wave in vacuum. For Ru, one can easily calculate from 1.18 that the intensity of an optical wave at 800 nm decreases to $1/e$ of its initial value after passing 16.2 nm in the metal.

Although the penetration depth is rather low, not all incident light is absorbed in this thin outer layer of the crystal, but a considerable part is reflected. Knowing the complex index of refraction for Ru, the amount of reflected light can be calculated from the Fresnel formulas[27] [Dem08]:

$$R_\perp = \left(\frac{\cos\alpha - n\cos\beta}{\cos\alpha + n\cos\beta}\right)^2 = \left(\frac{\cos\alpha - \sqrt{n^2 - \sin^2\alpha}}{\cos\alpha + \sqrt{n^2 - \sin^2\alpha}}\right)^2 \tag{1.19}$$

$$R_\parallel = \left(\frac{n\cos\alpha - \cos\beta}{n\cos\alpha + \cos\beta}\right)^2 = \left(\frac{\sqrt{1 - (\sin\alpha/n)^2} - n\cos\alpha}{\sqrt{1 - (\sin\alpha/n)^2} + n\cos\alpha}\right)^2 \tag{1.20}$$

for light polarized parallel to the reflection plane and perpendicular to it, respectively. The result of their evaluation for two wavelengths relevant in this thesis is offered in a graphical form in Figure 1.31.
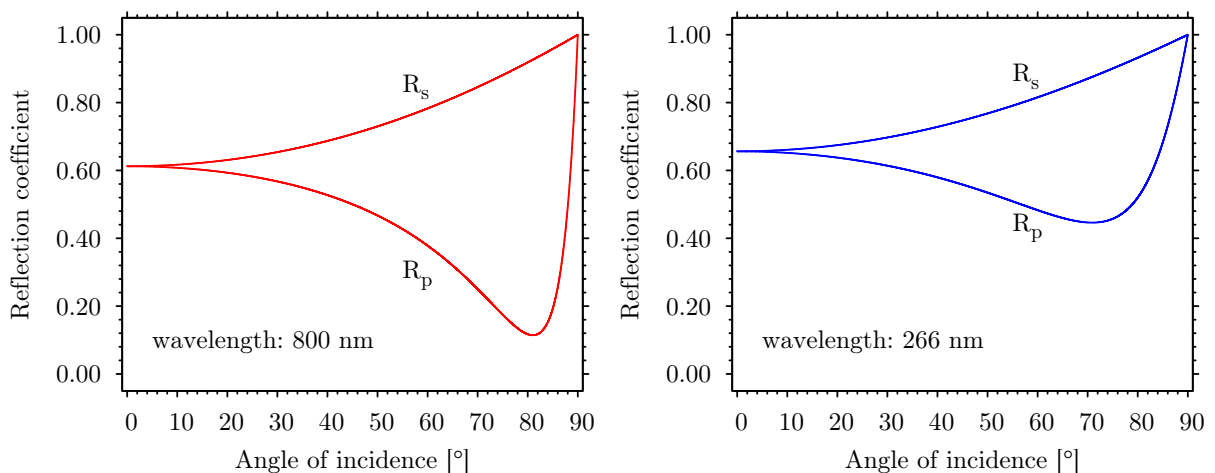
Figure 1.31.: Reflectivity curves for Ru calculated from equations 1.20 and 1.19 for two relevant wavelengths. The angle of incidence is the angle between the surface normal and the light propagation vector.

Now the optical field intensity decay in the medium has been discussed and the reflected part estimated, so how can the excitation term $S(z,t)$ be formulated? If the energy conservation requirement should be valid, then the definite integral $\int_{-\infty}^{\infty}[\int_0^{\infty} S(z,t)dz]dt$ must yield the total

---

[27]The Fresnel equations are a bit more complex in reality, in Equations 1.19 and 1.20 our situation is taken into account and the refractive index of the medium in contact with the crystal (vacuum) is set to 1.

energy contained in the absorbed part of the laser pulse. This problem is not difficult to solve, as the intensity decay term is a simple exponential function, so that a plausible possibility is:

$$S(z,t) = \frac{(1-R) \cdot I(t)}{\delta} \cdot e^{-z/\delta} \tag{1.21}$$

where $I(t)$ represents a pulse with a Gaussian time profile in the model.

Phonon heat capacity   In the Debye approximation the capacity of lattice vibrations to store thermal energy is described by [Ash76]

$$C_{\mathrm{ph}}(T_{\mathrm{ph}}) = 9 n_{\mathrm{a}} k_{\mathrm{B}} \left(\frac{T_{\mathrm{ph}}}{\theta_{\mathrm{D}}} \right)^3 \int_0^{\theta_{\mathrm{D}}/T_{\mathrm{ph}}} \frac{x^4 e^x}{(e^x - 1)^2} dx \tag{1.22}$$

with atomic density $n_{\mathrm{a}} = 7.21 \times 10^{28}\,\mathrm{m}^{-3}$ for Ru to maintain consistency in energy units used until now. This equation can not be further simplified and the integral is evaluated in the program, which is one of the most time consuming steps in the calculation.

Empirical proof of the two–temperature model: on the short life of the hot electron

At the end of this Section, the crucial assumption of the two temperature model is discussed again, namely the approximation of thermalized electron distribution (following Fermi–Dirac statistics; see Equation 1.1) immediately after the optical excitation. There is obviously no reason in a metal with an almost flat density of states distribution around the Fermi level to favor the excitation of lower lying electron states over those being closer to the E_{F}. Therefore the true picture immediately after the ultrashort laser pulse reaches the sample, corresponds rather to the left part of the Figure 1.32, than to its thermalized counterpart on the right. This
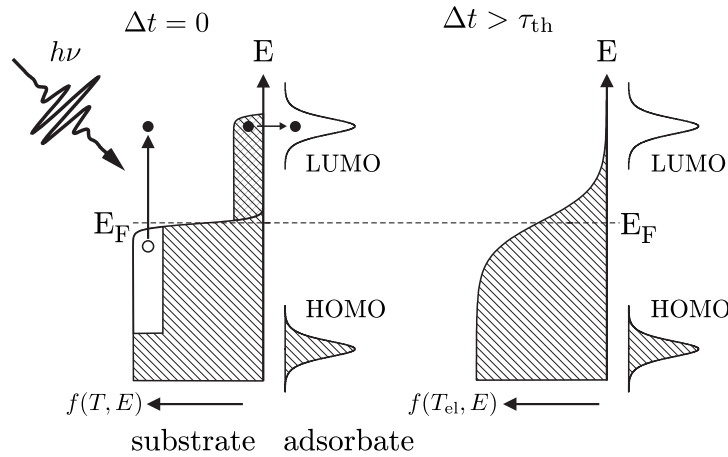
Figure 1.32.: Thermalization of electron energy distribution after ultrashort laser pulse. Adopted from [Lis04].

may have severe consequences for the two temperature model as presented here and in some cases our model simply fails for this reason [Fan92, Gro92, Del95, Lis04].
It is not only the temperature of the electronic subsystem that is no longer a valid description of the energy distribution stored there, or several assumptions mentioned before that are violated if the electronic temperature is too high. The usability of our model is intrinsically limited also

by other channels for energy transport that become relevant (e.g. ballistic transport[28]) [Hoh00, Lis04], by the electron–phonon scattering with non–thermal electrons and most importantly, by the possible different nature of interaction with the adsorbate, as it is demonstrated in Figure 1.32, but clearly visible also from Figure 1.26.

Despite of all the reasons named, the two temperature model is capable of describing most of the experimental data very well. It is therefore highly interesting to proof, in which cases the two–temperature model can work and which improvements can be implemented to enhance its application area.

Hot electron relaxation time   First, it is intuitively clear that the time the electrons need to thermalize will be the main factor determining whether the set of equations 1.3 will appropriately describe the studied system or not. Experiments in thick gold films [Fan92] show that the thermalization of hot electrons can take up to 1300 fs which would definitely lead to a failure of our model, since this time is comparable to the electron–phonon thermalization time and a single electronic temperature is thus at almost any instant only a number without a physical meaning. Nevertheless, it could be also found that this long time applies only if the Au sample is irradiated by a fairly low fluence of $120\,\mu\mathrm{J\,cm^{-2}}$. At $300\,\mu\mathrm{J\,cm^{-2}}$ the electronic subsystem has reached its thermal equilibrium already within $\sim$670 fs.

This interesting result naturally leads one to ask, what determines the temporal evolution of a given electron distribution after optical excitation? Considering the electron–electron scattering as the process leading to the thermalization, this question becomes quite subtle, especially for highly excited particles. To answer it, one needs to leave the electron gas approximation where electrons are fully independent like atoms of the ideal gas[29] and make use of the Fermi–liquid theory that describes this process more appropriately [Ash76]. For the lifetime ($\tau_{\mathrm{e-e}}$) of a quasiparticle with energy $\epsilon = E - E_{\mathrm{F}}$ that interacts with electrons having a Fermi distribution of temperature T, this theory predicts a value of [Pin66, Gro95]:

$$\frac{1}{\tau_{\mathrm{e-e}}} = \frac{m_{\mathrm{eff}}^3}{16\pi^4\hbar^6} \langle W \rangle \frac{(\pi k_{\mathrm{B}}T)^2 + \epsilon^2}{1 + e^{-\epsilon/(k_{\mathrm{B}}T)}} \tag{1.23}$$

Here, m_{eff} is the electron's effective mass, the constant $\langle W \rangle$ is the angle–averaged scattering probability. It is also obvious that if ϵ is large – as in the situation we consider ($\sim$1.5 eV) – the term $\pi k_{\mathrm{B}}T$ and the exponent in the denominator can be safely neglected. In this way the temperature T does not need to describe a thermalized subsystem and the expression is valid also for non–thermal distribution. The rigorous expression 1.23 is often further reduced within the random phase approximation, so that one obtains [Pin66, Fan92]:

$$\frac{1}{\tau_{\mathrm{e-e}}} = \frac{\pi^2\sqrt{3}\,\omega_p}{128} \left(\frac{E - E_{\mathrm{F}}}{E_{\mathrm{F}}} \right)^2 \tag{1.24}$$

with the plasma frequency

$$\omega_p = \sqrt{\frac{ne^2}{\epsilon_0 m_{\mathrm{eff}}}} \tag{1.25}$$

---

[28]Ballistic transport is an energy channel that is always opened. However, ballistic electrons in many d–metals posses a penetration depth comparable to that of the light and thus this sort of energy transfer can be neglected. Although, in metals like gold the ballistic depth is much larger, it is still limited, which leaves the thermal diffusion to be the preferred heat transport channel into the bulk *after* the electron subsystem has thermalized [Hoh00]. The higher energy is deposited in single electrons, the more effective in terms of energy amount transferred can this channel therefore be, especially in the first phase after optical excitation.

[29]In such a case, the scattering probability per unit time would be $1/\tau = \rho ne^2/m_{\mathrm{eff}}$ with τ being the Drude relaxation time, n electron density, m_{eff} electron's effective mass and ρ electric conductivity [Kit96].

which is the same as in the Drude model, where n denotes the electron density, e is the elementary charge and ϵ_0 the permittivity of the free space. To emphasize the key message the Equations 1.23 – 1.25 attempt to convey even more, they can be simplified to the following form:

$$\tau_{\text{e}-\text{e}} \propto \frac{1}{\sqrt{n}} \left(\frac{E_{\text{F}}}{E - E_{\text{F}}} \right)^2 \tag{1.26}$$

Now, one is obvious: the scattering probability grows rapidly with increasing electron energy. This phenomenon is connected to the Pauli exclusion principle and also to the fact, that there are usually more states available for scattering into, if the electron energy is high and conversely, the electrons at the Fermi level are extremely unlikely to scatter, as all possible final states are already occupied. For the two temperature model this law is a rescue: the hotter the electrons are, the shorter lifetime they can expect. Due to their short lives (even as short as 10 fs [Gro92]) their interaction with phonons and the adsorbate is strongly limited. Additionally, there is a quantity argument: assuming the interaction of a hot electron with its colder counterpart creates two species with half of its initial energy, the probability of one of those to interact with either phonons or the adsorbate is twice as high as the probability of the original non–thermalized one. Thus in many cases, especially if the metal is irradiated by high fluences, the thermalization takes a negligible amount of time and does not need to be taken into account[30]. The second factor, the free electron density is also considerably larger for ruthenium than for gold crystal mentioned in the experimental example above.

Although normally the arguments above are satisfactory and the two temperature model performs well, under some experimental conditions it appears to be necessary to include the not thermalized electrons into the model though. This is achieved by adding another electronic subsystem to the solid, which will represent the non–thermal electrons, but can be surprisingly described by the Fermi–Dirac statistics (with higher temperature) as well. Such a procedure is reported to enhance the functionality of the model to very low fluences, where probably no desorption could take place [Lis06, Fan92].

Ballistic transport In general, the list of energy transfer channels mentioned so far is not complete. Energy transport via ballistic electrons [Bro87] is the second often considered extension to the two temperature model. It applies especially if the energy from the optical pulse deposited in the metal – and hence the highest electron temperature – is low. In such a case, the thermal diffusion can not immediately compete with the electrons moving at Fermi velocity ($\sim 10^6\,\text{m}\,\text{s}^{-1}$) and ballistic transport may transfer considerable amounts of energy away from the surface. Of special importance is this fact for thin films. One way to implement the larger energy deposition depth into the two temperature model is to rewrite the Equation 1.21 describing optical excitation as the source term in the following way:

$$S(z,t) = \frac{(1 - R) \cdot I(t)}{(\delta + \delta_{\text{bal}})} \cdot e^{-z/(\delta + \delta_{\text{bal}})} \tag{1.27}$$

Here δ_{bal} is the ballistic penetration depth, which is usually of the order of 100 nm for gold, but comparable to optical penetration depth for d–metals like Ru [Hoh00]. This extension resolves primarily the initial ballistic heat transport and does not account for later times, where the

---

[30]There is another (correct) interpretation of the Equation 1.26 consistent with the preceding explanation: the lifetime of the non–thermal electrons depends on the density of states of the excited metal around the Fermi level. As this is much larger in Ru than in gold, it will contribute to a faster thermalization as well.

heat diffusion is more effective.

The existing 2PPE[31] experiments on Ru [Lis04, Lis06] are very helpful to estimate the relevance of the abovementioned corrections for our experiments that will be discussed later in Chapter 6 as well. The photoemission is the ideal method to study the actual electronic distribution after an ultrashort pulse: after the sample is excited, the electron distribution can be probed by a second ultrashort pulse with energy lower or approximately equal to the work function of the metal. The energy distribution of the photoemitted particles provides a direct information about the occupation of the hot electron states and thus an instantaneous 'snapshot' of electron energy distribution. The only drawback of this method is the limited laser intensity that can be used for the excitation: the more intense pulses emit large amount of electrons and the interactions within the charge cloud (space charge) would distort the image of the true energy distribution in the substrate.

If the Ru(0001) crystal is excited by $0.6\,\mathrm{mJ\,cm^{-2}}$, up to $20\,\%$ of electrons are non–thermal at the time delay of $100\,\mathrm{fs}$ after the excitation, which represents the largest fraction compared to any other time instant. It could be also shown, that this fraction decreases with increasing fluence and that the thermalization time follows the same trend (due to the overall higher energy of excited electrons, as explained above). Extrapolated to the excitation density used in experiments discussed in this thesis, the upper limit for the thermalization time should not exceed a few tens of femtosecond. Together with the high ultrashort pulse induced temperatures in the electronic subsystem (favoring diffusion over the ballistic transport) this justifies the assumption of instant thermalization made in our model. The preceding experiments on Ru performed in the same laboratory and aimed to test the liability of the described model further justify the simplifications made in the modeling [Bon00a, Fun99].

1.3.3. Metal–adsorbate coupling

The concept of temperature introduced to both substrate subsystems is very elegant and so far quite intuitive. If one wants to discuss the coupling between the substrate and the adsorbate, the probably most straightforward idea is to assign it its own temperature (T_{ads}) as well. It is immediately clear from chemical kinetics that any thermally activated process (e.g. desorption) with an activation energy E_{a} will proceed with a rate similar to that expressed in the Arrhenius–like form

$$R = \nu_0 e^{-E_{\mathrm{a}}/k_{\mathrm{B}}T_{\mathrm{ads}}} \tag{1.28}$$

and the question will arise, how can a single effective temperature of the adsorbate species be derived from the knowledge of the temperatures in the substrate heat baths and how to express the prefactor ν_0. In the following, the frictional approach introduced earlier (Section 1.3.1) is applied, mainly due to the more natural inclusion of desorption induced by the phononic subsystem into the model and also due to the expected lower vibrational excitation of surface–leaving molecules, which keeps the adiabatic PES to be a good description for the actual state of the system during the desorption.

Harmonic oscillator master equation

A good starting point for determining the effective adsorbate temperature based on the modeled temperatures of subsystems in the substrate, is to consider them as coupled harmonic oscilla-

---

[31]A brief and general introduction in two–photon photoemission spectroscopy can be found in Section 1.2.3 on page 36.

tors [Mis95]. A formulation of the Fokker–Planck equation in the Markovian limit predicts the temporal evolution of the probability P_n of an oscillator being in state n as

$$\frac{dP_n}{dt} = \frac{\eta_s}{e^{\hbar\omega/k_B T_s} - 1} \left[(n+1)e^{\hbar\omega/k_B T_s} P_{n+1} + n P_{n-1} - (n+1+ne^{\hbar\omega/k_B T_s}) P_n \right] \qquad (1.29)$$

In this relation, $\hbar\omega$ is the oscillator level spacing and η_s the strength of the coupling between the oscillator and the surrounding heat bath with an instantaneous temperature T_s (may be non–adiabatic as well). In the limit $n = 0$ and $T_s \to 0$ the equation is reduced to[32]

$$\frac{dP_0}{dt} = \eta_s P_1 \qquad (1.30)$$

which shows that the coupling strength η_s can be related to the oscillator population lifetime τ_1 by $\tau_1 = 1/\eta_s$ or alternatively to the homogeneous spectral line width (FWHM) of the oscillator by $\hbar\eta_s = \Delta E$ [Mis95].

The average vibrational energy U_v of the oscillator with respect to the zero point energy is given by the weighted sum of level populations as [Mis95, Bud93]

$$U_v = \hbar\omega \sum_{n=0}^{\infty} n P_n \qquad (1.31)$$

and therefore multiplying the Equation 1.29 by $n\hbar\omega$ and summing over all n yields for the temporal evolution of U_v (in the limit $\hbar\omega \gg k_B T$)[33]

$$\frac{dU_v}{dt} = -\eta_s(U_v - U_s) \qquad (1.32)$$

with U_s being the vibrational energy of the oscillator in equilibrium with its environment. The vibrational energy distribution of either oscillator and its surroundings can be described with Bose–Einstein statistics:

$$U_x = \hbar\omega \left(e^{\hbar\omega/k_B T_x} - 1 \right)^{-1} \qquad (1.33)$$

The expression 1.32 is very similar to the rate equation of the first order chemical reaction. The coupling strength, or *friction coefficient* η also has the dimension of s^{-1} and a similar meaning in the theory: it represents the rate constant of the process, in which the oscillator v attempts to equilibrate with its neighbors but can do so only with a time constant of $\tau = \eta^{-1}$ [Mis95]. If we now leave the general notation, the oscillator v can represent the adsorbed molecule and surrounding s will be a subsystem of a solid. The expression 1.32 therefore presents the energy transfer between the adsorbate and the substrate, taking into account the quantum mechanical nature of the adsorbate vibrations. If the level spacing $\hbar\omega$ in the system is small compared to the temperature $k_B T$, one can make use of the identity

$$\lim_{\hbar\omega \to 0} \frac{\hbar\omega}{e^{\hbar\omega/k_B T} - 1} = k_B T \qquad (1.34)$$

and replace the vibrational energies with temperatures in 1.32. The two subsystems in the substrate can be treated independently and obviously modify the adsorbate temperature in the same way. The final expression for adsorbate temperature will thus read

$$\frac{dT_{ads}}{dt} = \eta_{el}(T_{el} - T_{ads}) + \eta_{ph}(T_{ph} - T_{ads}) \qquad (1.35)$$

---

[32]We make use of the identity $\lim_{x \to +\infty} e^x/(e^x - 1) = 1$ and $\lim_{x \to +\infty} 1/(e^x - 1) = 0$. The limit could be introduced also as $\hbar\omega \gg k_B T$, which is true for many real systems.

[33]Here, the rule $\sum_{n=0}^{\infty}(n^2 + n)P_{n+1} - \sum_{n=0}^{\infty} n^2 P_n = -\sum_{n=0}^{\infty} n P_n$ is applied.

Finally, a brief comment to the approach above – to treat the quantum mechanical oscillators classically – is necessary. One has to be aware of the fact that some intramolecular vibrations posses a significant level spacing $\hbar\omega$ that is even comparable to the $k_B T$ term at high temperatures. In such a case the Equation 1.32 has to be integrated and the expression for the adsorbate temperature becomes more complicated. The reason for Equation 1.35 to be the standard for evaluation of energy transfer is illustrated in the Figure 1.33, where the quantum mechanically and classically calculated adsorbate temperature coupled to the heat bath evolving thermally along the solid line is shown. The difference between those curves is quite modest and arises
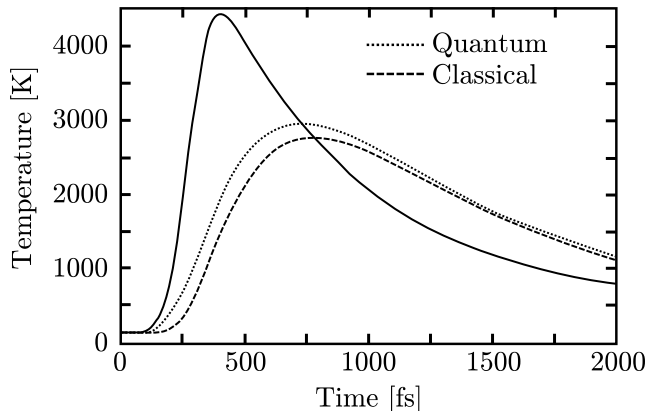
Figure 1.33.: A comparison between the quantum mechanical solution of the master equation 1.29 and its classical limit $(k_B T_v \gg \hbar\omega)$ for a inverse coupling strength of $\eta^{-1} = 355\,\text{fs}$. The solid line shows the input bath temperature profile used in the calculation which interacts with the oscillator v for $0.5\,\text{ps}$ to reach either of the classical (dashed) or the quantum mechanical (dotted) temperature evolution. Adopted from [Mis95].

due to a lower heat capacity of a quantum mechanical system (limited amount of levels) as compared to its classical analog.

Nevertheless, neither this last correction to the substrate–adsorbate coupling offers the perfect solution. The harmonic potential we assumed, is a satisfactory approximation only if the first few vibrational states of the system are relevant, as it is the case in the desorption. A parabolic well would namely never allow the molecule to leave the surface. Alternative approaches therefore include e.g. the solution to the Langevin equation [Lun06], or temperature–dependent friction [Bra95], but their rigorous apparatus is aimed more to calculate the friction coefficients from first–principles methods, than to explain the experimental data, whereas the treatment presented here offers a very convenient way in a reasonable agreement with our observations.

Rate of the desorption process

Obtaining the adsorbate temperature, the first step was made, enabling us to use the rate equation 1.28 which has been the goal of this Section. To find the definitive expression for the desorption probability (or rate), it is equally important to know, how the prefactor ν_0 ("successful–attempt frequency") can be determined from the available system parameters.

In its derivation, the Fokker–Planck equation is solved again in its classical limit, now formulated in a way that allows to calculate the energy distribution function $W(\epsilon, t)$ as [New91, Bra95]

$$\frac{\partial W}{\partial t} = \eta_s \frac{\partial}{\partial \epsilon} \left[\epsilon \left(1 + T_s(t) \frac{\partial}{\partial \epsilon} \right) W \right] \tag{1.36}$$

The solution is found within the boundary conditions: first, it is physically reasonable to assume that in a harmonic oscillator picture the initial vibrational distribution is concentrated at the bottom of the potential well, second, as the friction is normally small, Kramers low–friction limit applies [d'A75, Bra95]. The detailed description of the steps leading to the mathematical derivation of the rate formula can be found elsewhere [New91], the physically important result is, that the prefactor in Equation 1.28 is friction dependent

$$R = \nu(\eta)e^{-E_\mathrm{a}/k_\mathrm{B}T} \tag{1.37}$$

which is in agreement with our interpretation of friction coefficient as being proportional to the fluctuating and frictional forces acting between the substrate and the adsorbate that govern the energy transfer within those two heat baths. The full rate equation obtained from 1.36 reads

$$P_\mathrm{des} = R(t) = \frac{\eta_\mathrm{s}E_\mathrm{a}}{k_\mathrm{B}} \int \frac{e^{-E_\mathrm{a}/k_\mathrm{B}T_\mathrm{ads}(t)}}{T_\mathrm{ads}(t)}dt \tag{1.38}$$

if the friction coefficient η_s is assumed to be time–independent. The measurable quantity, desorption yield, can be consequently expressed as

$$Y = \int R(t)dt \tag{1.39}$$

The friction coefficient η_s is supposed to express the coupling between an oscillator (adsorbate) and the heat bath (either phonons or electrons). If the adsorbate would interact only with the electronic subsystem, one could easily replace η_s by η_el. To include also the phonon–adsorbate coupling, one can make a similar assumption as in 1.35 and treat both heat reservoirs as independent. As their interaction is well described by the two temperature model, this approximation is justified and one can make use of the Mathiessen's rule and write [Ash76, Wag06]:

$$\frac{1}{\tau_\mathrm{eff}} = \frac{1}{\tau_\mathrm{el}} + \frac{1}{\tau_\mathrm{ph}} \tag{1.40}$$

or

$$\eta_\mathrm{s} = \eta_\mathrm{eff} = \eta_\mathrm{el} + \eta_\mathrm{ph} \tag{1.41}$$

The last equation is used in the present work to describe the coupling strength between each of the two subsystems of the metal and the adsorbate. Both values η_el and η_ph can be obtained from a fit to the experimental data and belong to the important results discussed in Chapter 6.

Two–pulse correlation: measuring the adsorbate–substrate coupling strengths

Ultrashort laser pulses offer the possibility to *transiently* increase the temperature of the electronic subsystem in a metal that can couple, as discussed above, to the adsorbate degrees of freedom and *transiently* increase its temperature, which leads to a higher desorption rate. However, the electronic subsystem is only hotter than the lattice vibrations for usually ∼1 ps. Obviously, the possible higher desorption rate in this short time interval cannot be measured directly, as the molecule will hardly move more than a few nanometers during this time, so even though it is on the way to desorb, it will still feel the attractive potential from the surface. The usual measurable quantity is the desorption yield as defined by Equation 1.39. In this value all temporal information is seemingly lost (summed up in the integral).

One way to extract it from the yield though is to employ the two pulse correlation experimental scheme [Bud91]. Here, the pulse is divided into two (unequal) parts that reach the sample with a defined delay. The temperature evolution of either subsystem during a pulse sequence is shown in Figure 1.34 (left). Due to much higher heat capacity and less effective heat transport in the
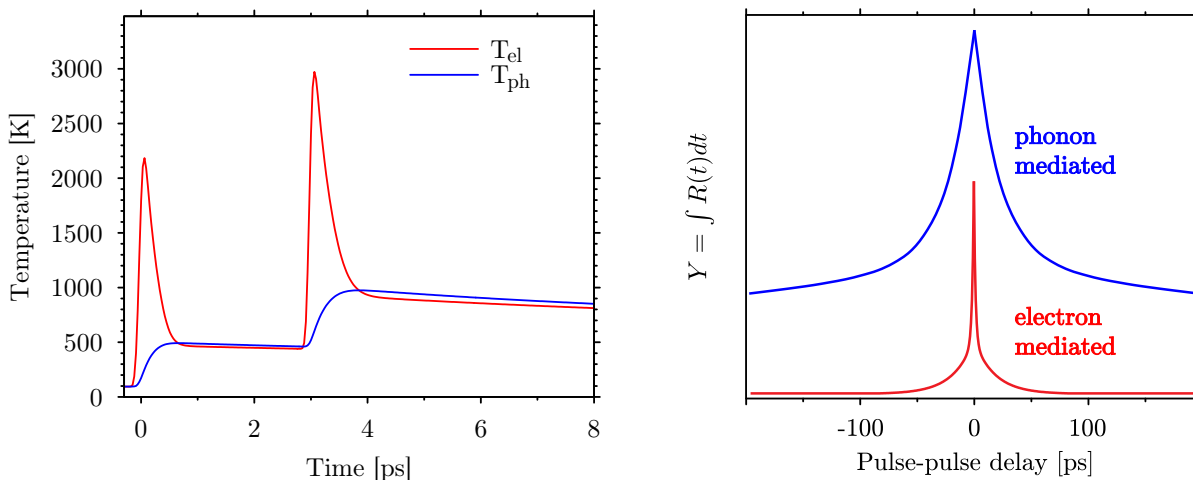
Figure 1.34.: Two–pulse correlation principle. Two unequal pulses (41 and $56\,\mathrm{J\,m^{-2}}$) reach the sample and create a transient thermal imbalance between the electrons and the lattice at the sample surface (left). Due to the slower cooling of the phononic heat bath the temporal delay of the pulses within several picoseconds does not influence its maximal temperature, which leads to a broad response of the yield measured as a function of the pulse–pulse delay (right).

lattice, its cooling is slow, so that delays of several picoseconds do not influence the maximal temperature of this bath considerably. The maximal temperatures of electronic subsystem are, in contrast, very sensitive to delays of several hundreds femtoseconds, as can be guessed from the total width of the first peak showing the surface temperature of the electronic bath after the first pulse has arrived. Thus, if an adsorbate would be coupled entirely to the lattice heat bath, its desorption rate, proportional to its temperature, would not change considerably either in a wide range of delays. The measured desorption yield, plotted as a function of the temporal pulse–pulse separation would show a shape displayed in the right part of the Figure 1.34 with a FWHM of typically several tens of ps. A fully electron driven desorption would show a different yield–delay correlation: the maximal adsorbate temperature (and hence desorption rate) would be reached only if the two pulses are almost overlapping, which implicates a very narrow curve with FWHM of $\sim 1\,$ps as indicated in the Figure 1.34.

In reality, the adsorbate may also interact with both subsystems so that neither of them can be fully neglected. Two–pulse correlations with FWHM of a few tens of fs are usually a typical example of such a coupling. From the fit to the obtained data, following the procedure described above, one can extract the friction coefficients η_{el} and η_{ph} that are of similar size and the coupling times that are larger than the electron–phonon equilibration time. In such a situation, additional information is necessary to decide on electron or phonon mediation [Fri06]. Additionally, experiments on CO/Cu(100) show, combining a two–pulse correlation measurement and REMPI (Resonance enhanced multi–photon ionization), that even within one adsorbate system different desorption pathways can be followed [Str96]. Depending on the frictional coupling estimated empirically, the leaving molecules exhibit different energy partitioning into various degrees of freedom.

It is important to stress here that even if a reaction is mediated by hot electrons and shows a significant rate enhancement only during a short time, this is not only a result of transiently elevated temperature in this subsystem, which would have nothing to do with a desorption under normal conditions. At lower temperatures namely, the hot electron levels are populated as well, only with a much lower probability. If one compares the Fermi–Dirac distributions for 300 and 3000 K at approximately 0.8 eV – which would correspond to the hot electron tail in the latter situation – it can be seen that the probability of finding an electron in this level for the colder sample is approximately 1×10^{12} times lower. Multiplying this probability by the available time for desorption (1×10^{-12} s in the hot–electron scenario) shows that the reaction probability on the realistic time scale (1 s) remains the same and although the electronic energy transfer channel is much 'narrower' under real conditions, it can be active as well.

Finally, in a two–pulse correlation, several special cases might occur that should be only briefly mentioned in this context. In the preceding sections, it has been assumed that the light is first absorbed by the metal and transferred into adsorbate via the frictional coupling. However, theoretically the adsorbate can absorb photons as well and desorb *without* an interaction with the substrate heat baths. In such a case, the two–pulse correlation should have a width comparable to the pulse duration, which is typically ∼100 fs. Another option recognizable in this setup appears, if the low–energy vibrational modes of the adsorbate are excited and decay with a time constant comparable to the lattice cooling. This is visible in the two pulse correlation as wings on the corresponding time scale [Fri06].
From all mentioned cases, it is clear, how powerful this experimental scheme is in evaluating the nature of the desorption process. After giving its main idea in the present Section, its experimental implementation will be described in Section 3.2.2 in a more detail.

2. Experimental setup

After the first Chapter tried to convey the experimental *ideas*, the following Chapter makes the consequent attempt: it invites the reader to understand the way we look at them. First, the vacuum system used to reduce the complexity of the investigated phenomena is introduced. Further on, the femtosecond laser system is presented as the main tool and its main characteristic, that are of crucial importance for the experiments discussed later are presented. These two separate devices create the 'backbone' of the experiment and all experimental innovations and experimental methods introduced in the next Chapter can be to some extent seen as the extensions of their functionality. To provide the essential information about the optical and vacuum part of the setup is therefore the main goal of this Chapter.

2.1. Ultra high vacuum system

All experiments presented in this thesis are performed in the ultra–high vacuum (UHV). Although this is not necessary for the SFG–spectroscopy, it is probably the only way to keep the investigated surfaces clean and well defined [Ert94]. Moreover, valuable information can be obtained by employing the retarding field analyzer introduced later in the Section 3.4, which is based on the direct electron detection possible only in the UHV. The resolution in the desorption yield measurement is also greatly enhanced in vacuum, as will be clear from the Section 3.2.2.

Base pressure below 10^{-10} in the chamber allows to neglect coadsorption of any contaminants from the surrounding environment[1]. Such high vacuum is achieved by pumping a stainless–steel UHV chamber with a serially connected membrane pump (creates vacuum of about 1 mbar) and two turbomolecular pumps. To accelerate the pumping process, the chamber is heated to 130 °C for at least 24 h (bake–out) after each venting, in order to promote desorption of (mostly) water from the chamber walls. The pressure evolution is recorded by a Bayard–Alpert ionization pressure gauge, working in the pressure range between 10^{-4} and 10^{-11} mbar. Typical residual gas spectrum before an experiment is shown in Figure 2.1.

The residual gas spectrum is a kind of finger print of a specific chamber with its own equipment and used for a certain experiment. The typical vacuum gases like H_2, H_2O, CO and CO_2 are present in every UHV chamber either due to their continuous gas desorption from metal filaments (usually contaminated with traces of carbon) used in the experiment, or due to the large surface area of the chamber walls, where water vapor with a high adsorption energy can adsorb while the chamber is opened. Some of the peaks in Figure 2.1, however, do not belong to those easily distinguishable species. As an example, mass 19 is fluorine, which arises due to the electron induced desorption from the rod system that is cleaned by the hydrofluoric acid in the manufacturing process. Similarly, the traces of mass 20 are a result of the long–term chamber exposure to the D_2O vapor, as the water dosing system is extensively passivated by D_2O every day to assure isotopic purity of the adsorbate. The unusually high signal of atomic oxygen (mass 16) can be attributed to the fact, that the Ru crystal is prepared in the oxygen

---

[1]At this pressure, a monolayer of molecules would adsorb on the surface after a time longer than 2.5 h, even if the sticking probability is 1.
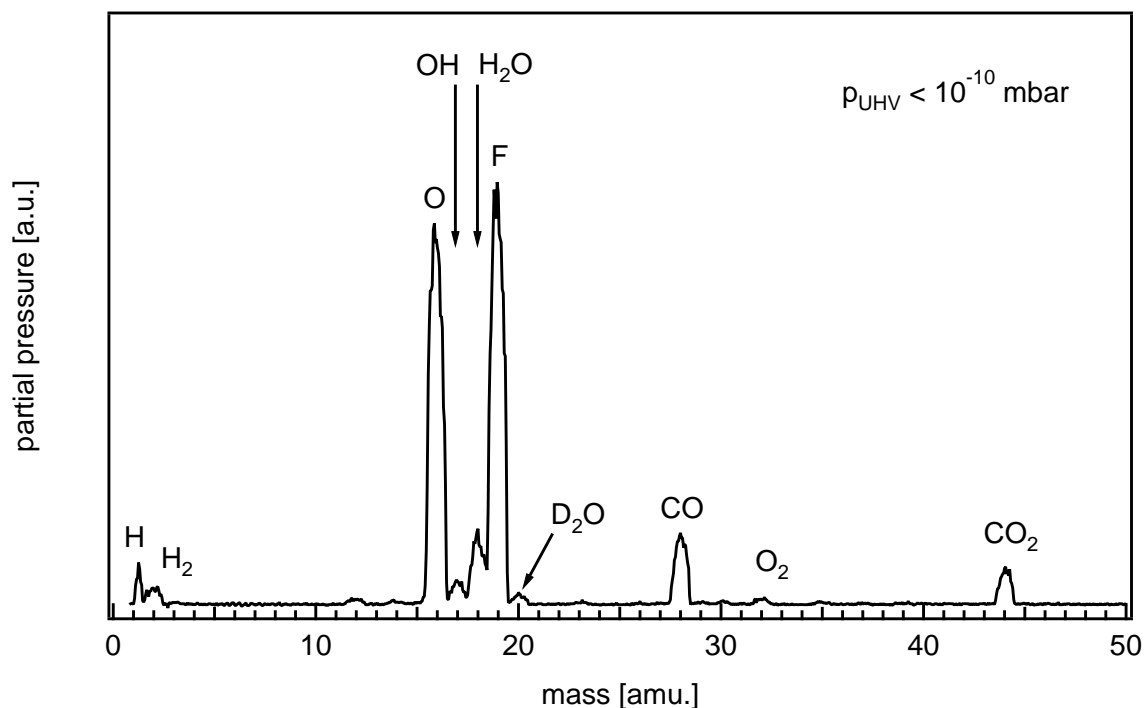
Figure 2.1.: Typical residual gas composition in the SFG chamber.

atmosphere every day, therefore electron induced desorption of O from chamber walls can be expected as well.

The chamber is equipped with a standard set of surface–science tools. To increase the partial pressure of selected gases inside, commercial leak valves are used. Two customized pinhole dosers, that can be moved close to the sample face, support controlled adsorbate dosing by increasing the pressure locally through a 5 μm diameter pinhole and allowing to dose the UHV poisoning gases like D_2O or CO without affecting the quality of the vacuum. They have been developed by the previous coworkers and are described in detail in several publications [Fun99]. For coverage estimations and femtochemistry measurements, a Balzers (Inficon) QMG–421 quadrupole mass spectrometer has been employed, however the partially customized electronic circuits used to readout the data differ substantially for both kinds of measurements (for details see Section 3.2). Another mass spectrometer with the ionization volume embedded in a Feulner cup [Feu80] allows to measure partial pressures of selected gases with a very high sensitivity, however, it has been not employed for water measurements due to the risk of isotopic water contamination in the closed volume of a cup. Its detailed description can be found in previous thesis work [Den03a].
Retarding field analyzer developed within the framework of this thesis and described more thoroughly in the Section 3.4 is used to detect kinetic energy of electrons leaving the sample after photoionization.
Another device connected directly to the chamber is a sputter gun, providing high kinetic energy Ar^+ ions, that can be employed to clean the sample surface. A general overview over the geometrical arrangement of the above–mentioned components offers Figure 2.2. It partially illustrates the possible optical paths of employed laser beams (discussed in Section 2.2) as well.
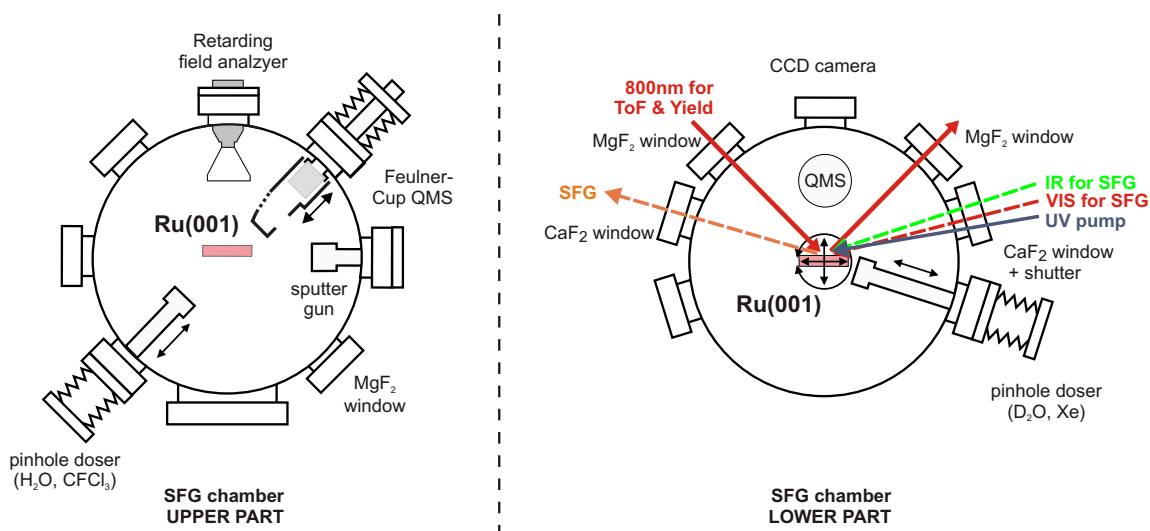
Figure 2.2.: A top view on the two optical levels of the SFG chamber. It has a cylindrical shape with two concentrical optical stages. On the left side the preparation part is depicted, the right side is an illustration of the chamber part, where all measurements explained below take place. Instruments are attached to ISO–CF flanges in the same geometry as shown here.

2.1.1. Sample mounting and manipulation

The most critical component in the vacuum is the sample holder. It not only allows the moving and rotating of the Ru(0001) single crystal under UHV conditions, but also makes possible the heating of the sample to more than $1650\,\mathrm{K}$ and simultaneously can act as a cold part of a liquid He cryostat, achieving temperatures as low as $40\,\mathrm{K}$, all in a well controlled fashion. The lower part of the sample holder designed on the very beginning of this thesis is shown in Figure 2.3. The mounting point of the sample holder is a commercial continuous flow cryostat (Janis research Supertran system, model ST 400) equipped with electrical feedthroughs for high voltage, DC line voltage and thermocouples. It is mounted to an XYZ manipulator operated by a computer controlled step motor device. A differentially pumped rotational stage makes further possible to rotate the sample to any required direction in space. The cryostat is terminated by a copper head, where the cooled components are attached. A specially shaped Cu block is highly polished and connected to the cryostat head with the largest possible contact area. Its bottom part can be seen as the middle post of the sample holder in the Figure 2.3. Since the cryostat is always connected to the ground, in order to keep the possibility to set the sample to a defined potential two additional symmetrical copper blocks are attached to this middle part, both electrically isolated by a sapphire plate that is a poor electric but good heat conductor at low temperatures[2]. The only electrical contact between these blocks is established through the Ru sample, which is held by two Ta wires clamped to each side of the sample holder. The folded wire shape aims to buffer the strain imposed on the crystal during the heating [Yat97]. Allowing the current to flow through the wire via thick copper feeds connected to external power

---

[2]The volume resistance of a sapphire crystal exceeds $10^{14}\,\Omega\,\mathrm{cm}$ and thermal conductivity is $42\,\mathrm{W\,m^{-1}\,K^{-1}}$ at $20\,^{\circ}\mathrm{C}$. This corresponds to a material with the thermal conductivity comparable to steel or lead, but with the electrical resistivity of rubber or glass.
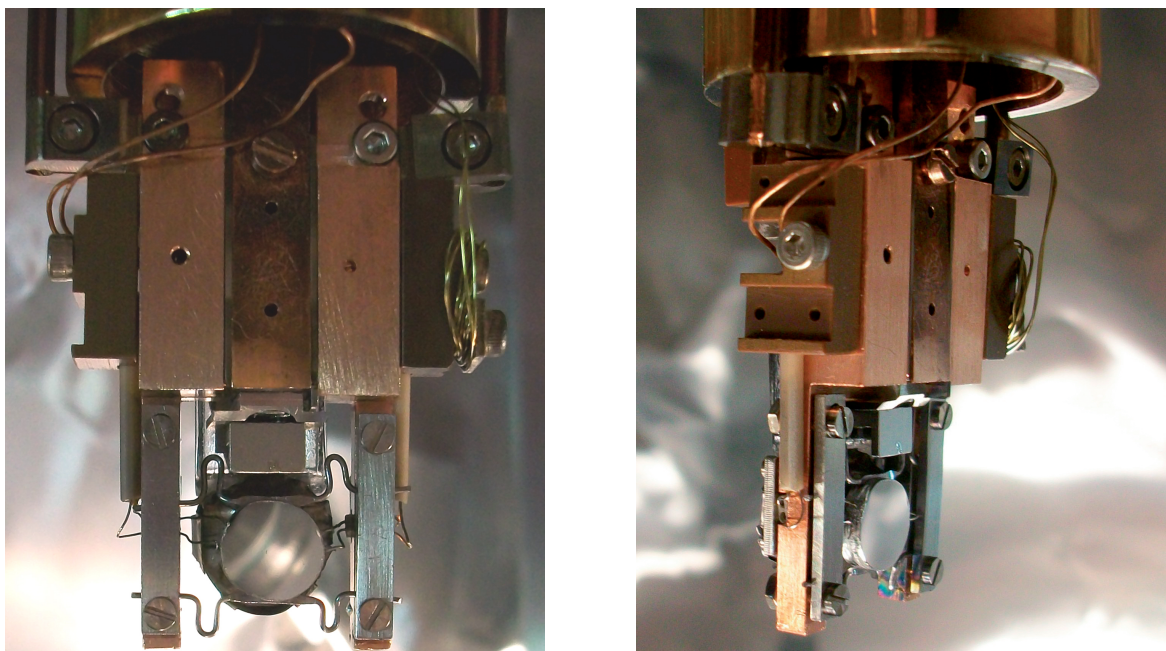
Figure 2.3.: The Ru(0001)–sample holder: front and side view. The middle copper finger is an extension of the cryostat, two symmetrical copper blocks are electrically isolated from the middle part by sapphire plates. The Ru(0001) crystal is held by two Ta wires, which are used to heat the crystal as well. Two thin thermocouple wire pairs are spot–welded to the crystal as well. Behind the crystal thin filament for electron beam heating is placed and shielded.

supply , the sample can be heated up to 1000 K in a well controlled way. Behind the sample a shielded filament is placed and is used for the fast sample heating ("flash") to much higher temperatures[3]. This is achieved by the electron impact on the sample that is grounded and in close vicinity of the filament heated by a current of 3.14 A and set to a negative potential of typically −1000 V. Due to the large electric fields in the chamber during the filament operation this type of heating is used only for sample preparation purposes.

The actual sample temperature is measured by two pairs of type K thermocouples that are spot–welded to the side of the Ru crystal. As the Kapton insulation of the thermocouple pair is not stable at temperatures above 700 K, large part of unprotected wire is kept apart from metallic parts of the sample holder in the ceramic tubes.

2.1.2. Ru(0001) surface cleaning and preparation

Only a clean and well defined surface is a suitable support for the crystalline adsorbates and allows to understand the investigated processes without introducing too much complexity into the system of interest. For the crystal preparation established procedures have been followed [Mad75, Mus82, Den03a, Wag06], whereas the initial preparation of a freshly cut Ru single crystal differs from the everyday cleaning procedure.

---

[3]Although very high sample temperatures are achievable, the upper limit in the presented setup is 1530 K, which corresponds to the melting point of the type K thermocouple considering its typical tolerance as well.

Initial preparation

The Ru sample (2 mm thick, 8 mm diameter) is cut from a single crystal rod and consequently polished to an orientation accuracy of ≤0.5° with the diamond grains of the size down to 0.25 µm to the mirror quality. According to Auger electron spectra (AES), the usual impurities found in ruthenium single crystals are carbon, sulphur and oxygen [Mus82], the freshly cut crystal can be additionally covered by the remains from the polishing procedure. All contaminants can be removed in a cycle consisting of three steps:

(i) The sample is sputtered by a beam of Ar^+ ions accelerated to the grounded sample by a potential difference of up to 3000 V. The sputtering current i.e. the ion flux reaching the sample amounts to several tens of µA. The beam diameter is larger than that of the sample and the crystal is moved during this process to assure the best possible homogeneity in the surface ablation degree. One cycle lasts for approximately 20 min, the argon background pressure is 2×10^{-5} mbar.

(ii) Heating the sample to 1250 K in the oxygen atmosphere (O_2 pressure in the chamber background amounts to 2×10^{-7} mbar) for circa 20 min leads to the oxidation of impurities that are consequently desorbed, as the desorption temperature (T_{des}) of corresponding oxides is much lower than the T_{des} of carbon or oxygen and well below 1000 K. The temperature is chosen such that it is slightly below the maximum oxygen desorption temperature as well to support the sticking and diffusion of the O–atoms on the surface.

(iii) Annealing the sample to 1700 K leads to surface healing and to oxygen removal [Böt99]. The RuO_2 that covers ruthenium after exposing it to the O_2 atmosphere decomposes at this high temperature. The sample temperature is followed by an external pyrometer, whose accuracy has been tested in the lower temperature range by comparing the indicated temperature to the value measured by a thermocouple pair or to a known settings of the electron beam heating.

These steps are repeated until no traces of contaminants are present in the AES or until a desired characteristics (mostly its unique shape) of a CO thermal desorption spectrum (TDS) is achieved, since this is the most sensitive measure of surface cleanness and quality [Kos92, Pfn83].

Routine crystal cleaning and preparation

One of the usual problems one meets in the surface science is to keep the surface clean under experimental conditions. To remove traces of oxygen that is present in traces in residual gas from the surface, a frequent heating of the sample is required. However, one drawback of this procedure is the constant migration of the contaminating carbon from the Ru bulk to the surface at elevated temperature [Shi08]. The carbon Auger peak at 274 eV further overlaps with the ruthenium signature at 272 eV, therefore it is hard to determine the exact amount of C present on Ru surface by this method every day. As a consequence, the daily preparation routine differs from the initial preparation only in the intensity of performed steps:

(i) The Ar^+ sputtering is performed with lower ion currents, typically 5 µA. For 20 min the sample is sputtered by ions accelerated by the 0.5 kV voltage difference at least at 7 different positions. Ionized is the Ar gas from chamber background, where its pressure is set to the value of 1×10^{-5} mbar. Both, pressure and acceleration voltage are chosen such that the ion beam diameter is larger than the whole sample in order to avoid beam focusing that could destroy the homogeneity of the crystal face.

(ii) The heating time of the sample in the oxygen atmosphere is reduced to 10 min. The background pressure of 2×10^{-7} mbar is maintained during that time, as it provides sufficient sticking and hence reaction (impurity oxidation) probability. The temperature used in initial preparation is kept as well.

(iii) Due to the lower melting point of the type K thermocouple the sample temperature must not exceed 1530 K. Although other thermocouple pairs are capable of measuring higher temperatures as well, their accuracy in the temperature range below 100 K is often poor. However, at this temperature complete oxygen desorption from Ru can be observed and the heating to even higher temperatures is normally not necessary. A short flash heating is regularly followed by means of TDS to control the oxygen desorption. Such a step presents the last point in the Ru sample preparation.

2.1.3. Ice layer preparation

Water molecules adsorb on a clean ruthenium surface below 185 K, at temperatures lower than ~170 K they are already able to form multilayers. As the phase diagram of ice is rather complicated and its mobility is due to the strong hydrogen bonding considerably limited (diffusion is frozen below 120 K), very well defined conditions are required to prepare a selected ice structure reproducibly. Moreover, water on a metal surface is extremely sensitive to the traces of the usual UHV contaminants such as hydrogen or oxygen [Doe82], in the case of D_2O, traces of H_2O can affect its intact growth as well. In the following, the adopted standard 'recipes' for D_2O ice layer preparation are therefore introduced and are strictly followed in the everyday routine. This introduction is, however, not intended to be exhaustive and for a deeper explanation of the water–metal interaction the reader is referred to the Section 1.1.3.

Water dosing system   To ensure the highest purity of dosed gases, a gas system has been developed with a separate dosing line for D_2O, H_2O and other gases. To minimize the possibility of adsorbate contamination from the chamber background, experiments with both water isotopes have even been carried out on different days if possible.

The water ($\geq 99.999\,\%$ isotopic purity of either isotope) is purchased in a sealed glass bottle of 1 ml volume. This bottle is cleaned, put into a glass tube with an ISO–CF DN16 flange adapter, connected to the gas system and pumped, until a stable pressure well below 1×10^{-3} mbar is reached. After that, the evacuated tube can be closed and disconnected from the system. Under vacuum the small bottle is crack–opened and connected again to the gas system.

As the glass tube is not constantly evacuated, but frequently in use for several months, even a small leak well below our leak–check detection limit could contaminate the water inside. Therefore, on an everyday basis the D_2O glass is immersed in liquid nitrogen, frozen and consequently pumped until the vapors have reached the pressure of 1 mbar. This process is similar to distillation: until the water in the glass is in its solid state, the possible traces of other atmospheric gases (O_2, N_2) can be removed. Their solubility in solid water is – compared to the liquid state – also greatly reduced. If the contaminating gases are present in the glass tube, the recorded pressure in the gas system with frozen water first increases, but after reaching ca. 0.6 mbar it decreases again and rises once more only when the water starts to sublimate. Normally, this freeze–thaw–pump process was repeated three times, or until the mentioned initial increase could be observed.

In the next step, the stainless steel walls of the dosing system were passivated. For this purpose, the D_2O was injected into the chamber on the same way as during the dosing, but at a lower

total pressure and for a limited time. The isotope ratio between the detected H_2O and D_2O was checked by the QMS and usually after an hour it has converged to the value related to the cracking pattern of a pure mass 20[4], which was a signal that the water in the system is highly pure and can be dosed.

Crystalline ice layers preparation   The Ru(0001) single–crystal, continuously cooled by liquid helium, is first flashed to 1530 K to desorb any impurity. While the sample is cooling down, its temperature is set to stay at 155 K using resistive heating and a PID controller (Lakeshore 340). At this constant temperature the crystalline ice layers are grown by dosing D_2O at rates lower than 2 BL/min via the passivated pinhole doser[5]. Usual dosing time under these conditions does not exceed 6 min. Immediately after this time has elapsed, the sample heating is switched off and the manipulator transfers it to the SFG position, with the face turned towards the QMS. In the next step, the ice layer is annealed by heating the crystal to 160 K for ∼5 s, which yields a compact, crystalline ice layer [Gah04]. A TDS is used to follow the water desorption during this process, as the vapor pressure of crystalline and amorphous water differ significantly at this temperature. The amorphous domains, possibly still present in the ice layer, will either crystallize or desorb, which leads to an initial spike in the isothermal TDS. After that a signal at a constant level is only recorded, which is attributed to the desorption of a perfect crystalline structure [Haq07]. As will be discussed later in Chapter 4, the SFG spectra are very sensitive to the actual ice structure and the quality of the crystalline phase can be hence recognized immediately. Together with a TDS, these are two independent *ex post* checks of our preparation procedure.

The preparation of a **single ice bilayer** is derived from the procedure above. All the steps are exactly followed, the only change in the procedure consists of a longer annealing time. At 160 K, the crystalline ice multilayers desorb with a low rate and the desorbed amount can be followed simultaneously by the QMS. If its signal converges to zero, all molecules from the ice multilayer are desorbed, but since the binding energy of the D_2O molecules in the first bilayer is higher, this layer remains intact. Again, a reliable check of a perfect monolayer provide the TDS and SFG, the latter method being especially sensitive due to the intense free OD stretch appearing immediately at coverages larger than 1 BL (see Chapter 4 for more details).

Amorphous ice layers preparation   Normally, the amorphous ice was prepared by dosing the water onto the Ru(0001) crystal below 50 K and at higher deposition rates [Haq06]. This procedure yields a porous solid [Ste99]. In the measurements discussed in the Chapter 4, a compact amorphous ice is also investigated. This was prepared by dosing D_2O in the same way, but at 120 K.

Despite the large effort put into the preparation, the actual water coverage in the experiment can vary slightly ($\pm5\,\%$). Therefore, it is always determined from an integrated TDS taken after every single measurement.

---

[4]Due to the arrangement of the instruments in the chamber, this ratio is not exactly 0.25 as expected for the cracking pattern of D_2O, but usually higher, as the dosed molecules do not reach the QMS directly, but may first interact with the chamber walls. A TDS from the water adsorbed on the clean Ru(0001) sample from the doser passivated in the procedure above shows no peak at the mass 17, corresponding to the OH fragment characteristic for a possible isotope contamination.

[5]Dosing at higher temperatures is preferred over dosing an amorphous film and consequent annealing, as the resulting layer in the latter case could still contain fractions of amorphous phase [Doh00, Dev95].

2.2. Femtosecond laser system

It would hardly be legitimate to begin the title of this thesis with the word "Ultrafast", if the described investigations would concern mainly effects lasting more than several picoseconds. An established way – widely developed in the last 20 years – to follow such a fast dynamics is based on the interaction of matter and the light provided by a sub–picosecond laser system. And indeed, the investigation of the ultrafast energy transfer between the substrate and an adsorbate (Chapter 6) as well as the highly nonlinear effects enabling us to follow the interface structure of ice (Chapters 4 and 5), both require very short pulses with a high peak intensity to be at least realizable.

In the first case, such a pulse triggers the desorption and its limited temporal width allows to resolve the coupling of the adsorbate to surface electrons, which equilibrates with the system's phonons on a timescale lower than $\sim$1 ps. High intensity is needed to deposit enough energy in the metal layer that reflects most of the light. A closer explanation of those phenomena was discussed in the Section 1.3.3.

In the second situation, only ultrashort UV and IR–pulses provide the possibility to map the vibrational dynamics of ice, which is extraordinarily fast due to the exceptionally efficient coupling of single water molecules within a hydrogen–bonded network. As the Fourier transform indicates, short pulses are spectrally broad and can be conveniently used in the spectroscopy covering a larger wavelength region of interest. The large number of nonlinear effects exploited in the generation of those pulses, together with the nonlinearity of the SFG process itself demands high intensities achievable only in a ultrafast pulse.

For those reasons, this Section will serve as a guide through the employed laser system and accent several points important for the experiments described later. A general scheme showing the most important parts of the laser setup is shown in the Figure 2.4[6]. To describe its parts in detail and explain it is the aim of the next paragraphs.
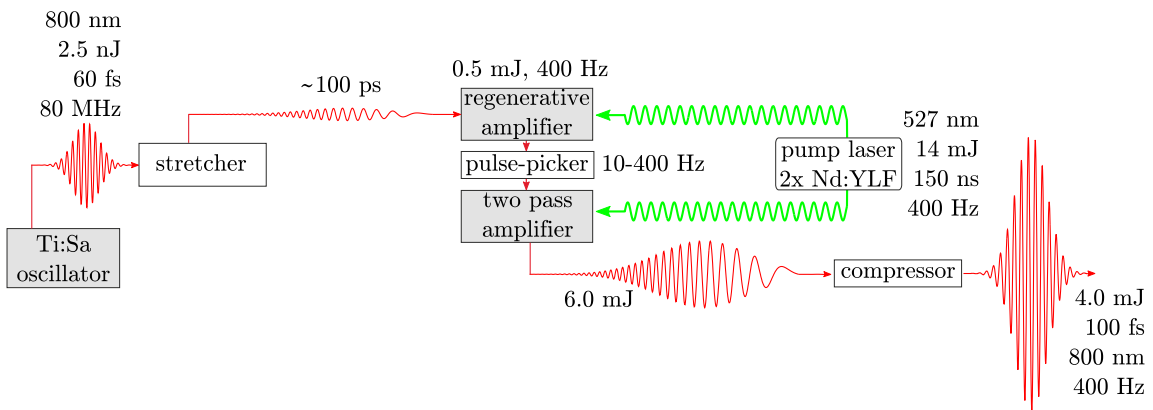
Figure 2.4.: Overview of the most important components in the laser system employed. The chirped pulse amplification technique is illustrated and pulse parameters at its every stage are listed.

---

[6]The way it is embedded in the SFG setup is discussed later in the Section 3.2.3 and shown as Figure 3.9. Other exploited beam paths can be derived from it, therefore it can be regarded as a representative one.

2.2.1. Generation and amplification of ultrashort 800 nm laser pulses

As can be seen from the Figure 2.4, the generation of intense, ultrashort 800 nm pulses is based on the commercial Ti:sapphire oscillator (Vitesse; Coherent, Inc.) that seeds the amplifier chain (Quantronix–Titan II–amplifier; Quantronix, now Excel Technology Europe, GmbH.) consisting of a regenerative and a multipass amplifier, both being pumped by a synchronized, pulsed Nd:YLF laser. The setup is a slightly modified version of the arrangement developed by the Quantronix corporation, described in the reference [Fu97].

Ti:sapphire laser is the most widely used solid–state laser, which is mainly due to its remarkable and unique properties – simple electron structure ($3d^1$ configuration of the Ti^{3+} ion), very broad fluorescence (670–1070 nm) and absorption band that peaks around 490 nm [Koe03, Mou86]. The first fact eliminates the possibility of excited–state absorption, which reduces the efficiency of other transition–metal doped lasers. The light emitted from a Ti:sapphire crystal will also not be reabsorbed there because of the large spectral separation of the two bands. The broadband fluorescence spectrum allows the generation of extremely short pulses, as will be shown later and absorption maximum around 500 nm opens the possibility to pump such a laser with an argon gas or a frequency–doubled Nd:YLF laser. The host material sapphire itself possess many advantageous properties – very high thermal conductivity, chemical inertness, mechanical stability and high damage threshold.
In this system, Ti:sapphire is not only the lasing medium but is used in the amplification stages as well. Here, the pulsed and synchronized Nd:YLF is the laser of choice due to its very long fluorescent lifetime (480 µs). Pulsed pumping is preferred because of the comparably short fluorescence lifetime of Ti:sapphire (3.2 µs), which results in a small product of stimulated emission cross section times fluorescence lifetime ($\sigma\tau_f$). Usually, the output of the Ti:sapphire laser is centered at 800 nm, where the amplification gain reaches its maximum.

Generation of fs–pulses

Having introduced the Ti:sapphire laser, its ability to produce ultrashort pulses should be discussed in a more detail. In fact, this type of laser is able to produce the shortest pulses that have ever been achieved in a solid state laser or from a laser oscillator at all [Mor99, Bra00]. However, to generate pulses of 4.8 fs length [Mor99, Sut99], i.e. less than two periods of light and approaching the limit of 3.7 fs, where the pulse duration converges to the light oscillation period, a lot of effort is required and it already is a separate research field. Interestingly, all those achievements have been accomplished by a more sophisticated design of the laser cavity, but the principle of the ultrashort pulse generation remains the same – the passive or self mode–locking in the Ti:sapphire crystal, which is also used in our system as well.

Mode–locking   In a laser resonator of length L, many frequencies can oscillate independently. The spectral width of such a laser beam is limited only by the gain bandwidth of the corresponding lasing medium, which can be – as in case of Ti:sapphire– very large. To satisfy the condition for a standing wave inside of the laser cavity, the separation of those frequencies (modes) has to be $\Delta\nu = c/2L$. In practice, the L is typically 1 m, so the frequency spacing amounts to approximately 0.15 GHz. Now, considering the typical 100 fs laser pulse with a corresponding bandwidth of 4.4 THz (a wavelength range of 10 nm around the central frequency of 800 nm), one can easily calculate, that almost 30 000 modes oscillate independently in the cavity. The output signal consists of their mutual interference pattern, that has no regular temporal structure, the intensity is averaged over the time and the laser is said to be in a *cw* (continuous

wave) mode.

This situation would change dramatically, if one could force the modes to oscillate in a fixed phase, so that their interference concentrates all the power to a single coherence spike repeating with a period corresponding to the cavity round–trip time $t = c/2L$ [Fre95]. This situation is illustrated in the bottom part of the Figure 2.5.

Several techniques have been developed to achieve a fixed phase between the cavity frequen-
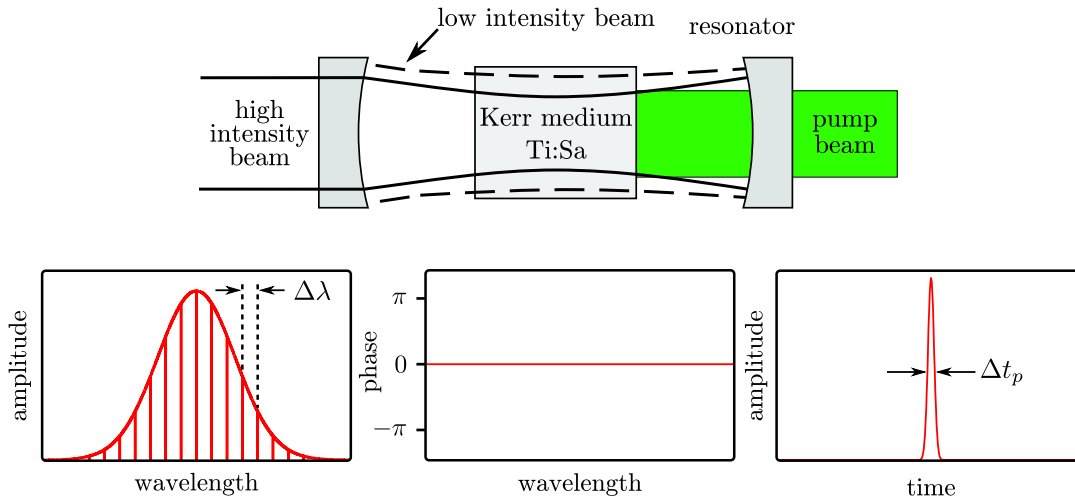
Figure 2.5.: Bottom: The idea behind the mode locking technique is to fix the phase of the individual cavity modes oscillating at frequencies separated by $\Delta\nu = c/\Delta\lambda$ so that their constructive interference results in a single, temporally short intensity burst. Top: The scheme of the soft aperture Kerr–lens mode–locking, the employed method to achieve the phase–matching.

cies, the shortest pulses are, however, achieved by the technique called Kerr–lens mode–locking (KLM). Its special type, the soft–aperture KLM, employed in our Ti:sapphire oscillator shall be explained in the next paragraph.

Kerr–lens mode–locking Although several sophisticated methods of altering the properties of laser cavity to obtain ultrashort pulses have been developed, paradoxically, the most reliable way to achieve the mode–locking is to 'let it happen' – the only thing that is required is a right medium inside the cavity. This is the reason, why this type of mode–locking is often called passive or self–starting. In the resonator, small laser field strength fluctuations are always present either as a consequence of the quasi–stochastic cavity mode interference process, or they can be induced, e.g. by a short mechanical impulse given to the end mirror of the resonator. If the pumped cavity medium can absorb (attenuate) more the less intense parts of the laser field, then only the transmitted stronger components will be amplified. The situation in the resonator is a simple one: the absorbed weak intensities can not participate in inducing the stimulated emission from the population–inverted laser medium, whereas the transmitted strong intensities will be coherently enhanced due to this process. This allows their intensity to increase further until only the initial strong field fluctuation (mode) oscillates in the cavity and the resonator will mode–lock itself.

In the soft aperture mode–locking this is achieved by exploiting the nonlinear optical Kerr effect in the Ti:sapphire crystal. The phenomenon causes the material's refractive index to be

dependent on the intensity of the light passing:

$$n(\omega, I) = n_0(\omega) + n_2 I(\omega, t) \tag{2.1}$$

Similar to some other nonlinear effects discussed in Section 3.1 this situation arises from the anharmonic motion of bound electrons in a medium under the influence of an intense propagating field [Fre95]. Given a Gaussian beam profile inside the resonator, the intensity–dependent refractive index effectively acts as an intensity–dependent lens. As this electronic response is virtually instantaneous, it only affects the beam that has induced it, so that the strong pulses tend to be focused more than the weak ones. If additionally the diameter of the pumping beam is smaller than the beam spontaneously emitted by the Ti:sapphire crystal (or possess a Gaussian intensity distribution), as shown in Figure 2.5, the stronger focused, more intense laser pulse will encounter a better overlap with the pumping beam as the rest of the modes. Repeating this process will consequently mode–lock the beam in the resonator. In this way, the Verdi diode laser pumped Vitesse oscillator system can achieve 60 fs long pulses with a repetition rate of 80 MHz and a spectral width of 35 nm. One general problem in creating even shorter pulses lies intrinsically in the Kerr–effect: in a simple picture, if the refractive index is changed in time as a function of the passing laser field intensity, the speed of light in the medium changes as well and alters the phase delay in the beam in a similar nonlinear way as the optical intensity changes (this phenomenon, so–called self–phase modulation is, however, too special to be treated in this context). To compensate for this effect resulting in a temporal chirp of the laser pulse, special chirped mirrors and other elements are used in the resonator.

It should be also noted that not all modes have to be phase–locked in a resonator, in fact, such a situation can hardly be achieved. However, the pulse length depends on the number of modes N locked in the laser cavity via the expression

$$\Delta t = \frac{\alpha}{N\Delta\nu} \tag{2.2}$$

where the constant $\alpha = 2\ln(2)/\pi = 0.441$ for a Gaussian pulse. For a sech^2 pulse[7] frequently used to describe the ultrashort pulses, the constant $\alpha = 0.315$. This relation, the time–bandwidth product, shows the lower limit for the duration of a mode–locked pulse in a situation, when a single frequency is phase–locked in the resonator [New83]. In the literature, such pulses are denoted as bandwidth–limited. Put in other words, this limit is reached, when the pulse duration approaches the oscillation period of light from a given source. For a general overview where the frontiers of ultrafast pulse generation currently are, please refer to the recent review [Kra09].

Amplification of ultrashort laser pulses

Unfortunately, the ultrashort laser pulses are difficult to amplify mainly due to their high peak intensity that imposes severe restrictions on the choice of the optical components (mainly amplifier crystals) and greatly limits their lifetime. Moreover, nonlinear effects, such as the optical Kerr effect, but also other intensity–dependent phenomena like self–phase modulation, gain saturation or supercontinuum generation, could seriously distort the beam profile and the pulse structure. A way to circumvent this problem is to temporally stretch the pulses in a controlled way and to compress them again after their amplification. This method, the chirped pulse amplification [Bac98], is widely used and its particular application to our setup can be seen in Figure 2.4.

---

[7]Fitting the data to the hyperbolic sechant, the temporal intensity distribution in the form $I(t) = \frac{1}{2\tau}\text{sech}^2\left(\frac{t}{\tau}\right)$ is assumed, with $\text{sech}(x) = \frac{2}{e^x + e^{-x}}$.

Stretcher   The output of the Ti:sapphire oscillator is first sent to the grating stretcher, where a linear temporal chirp is imposed on the pulse by a strongly dispersive element – the grating pair. To avoid all the problems mentioned above, pulse lengths of almost 1 ns are usually created in this first step.

Oscillator pulses, stretched to 100 ps in our case, are amplified in the amplifier chain in two steps. Firstly, in a regenerative amplifier (Quantronix 4810 Ti:Sa RGA) that produces a very high gain, but as will be shown later, due to its construction it produces a lot of parasitic reflections and an additional linear chirp. Secondly in the two–pass amplifier that provides optimal pulses, but becomes hard to align if the number of passes through the gain medium is high. The first stage of the pulse amplification is illustrated in the Figure 2.6.
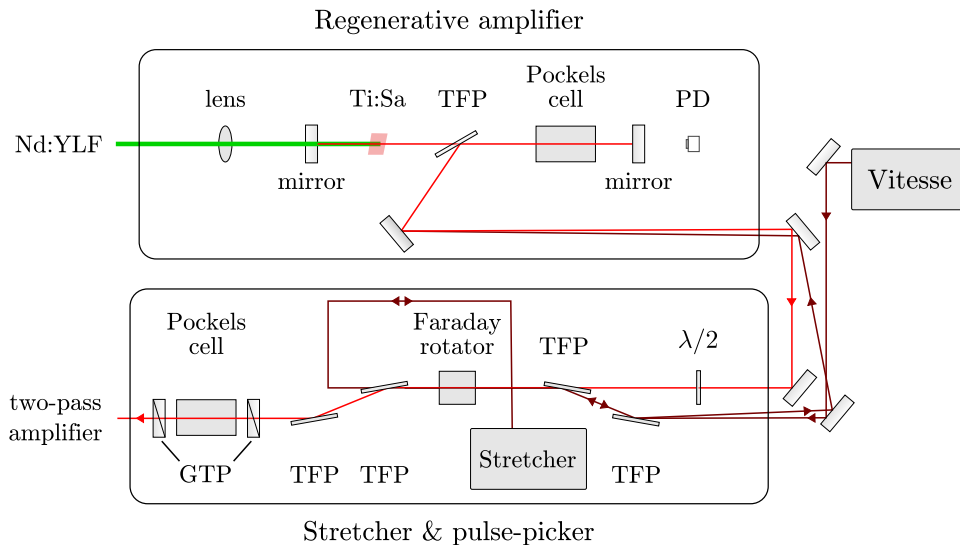
Figure 2.6.: The first amplification stage of the employed laser system is shown. The dark–red pulses mark the path of the oscillator pulse to the stretcher and continue on the almost same way to the regenerative amplifier. Here, the red pulses depict the amplified beam that continues further to the pulse–picker: a Pockels cell placed between two crossed Glan–Thompson polarizers.

Regenerative amplifier   If the output intensity from an oscillator is not sufficient for an experimental purpose, the probably most straightforward idea how to amplify it is to let it pass through a similar cavity as the one used for its generation – to re–generate the pulse – although in this step a higher total intensity can be achieved due to its longer duration. However, all amplified light should become accessible and no light should remain in the resonator as it is necessary in an oscillator to maintain the mode–locking. Such a regenerative amplifier [Bad85, Vai90, Wyn94], frequently used for amplification of laser pulses with a low repetition rate is schematically depicted in the Figure 2.6.

An optical resonator containing the Ti:sapphire crystal is pumped by a part ($\sim 35\,\%$; $5\,$mJ) of the frequency–doubled output of the Nd:YLF laser. From the other side, the horizontally polarized light[8] from the oscillator will enter the cavity and be reflected on the thin film polarizer.

---

[8]Polarized parallel to the propagation plane constituted by the beam and its reflection and is often denoted as p– or π–polarization. A beam with a polarization perpendicular (German: senkrecht) to this plane is conventionally named as s– or σ–polarized.

The next element it passes is the Pockels cell. This device consists of a nonlinear crystal, KD*P, that changes the phase delay between the perpendicular electric field components of the transmitted light wave, depending on the applied voltage, and a set of electrodes. By applying a suitable voltage, the Pockels cell can act as a voltage controlled waveplate. If no voltage is applied on the crystal, the light is transmitted unchanged and is finally reflected out of the resonator by the polarizer without reaching the Ti:sapphire crystal. As our goal is to achieve pulses with high intensity in every single pulse, the repetition rate of the seed oscillator (80 MHz) is too high, since the total gain achieved in an amplifier system would be distributed among many individual pulses. Therefore the majority of the oscillator output is blocked in the regenerative amplifier in this way and only pulses with a frequency of 400 Hz are intensified. This is achieved by synchronizing the voltage of the Pockels cell with the oscillator trigger signal downscaled in a divider. A similar synchronization adjusts the timing of the Nd:YLF laser, so that with a frequency of 400 Hz the Ti:sapphire crystal in the cavity of the regenerative amplifier is pumped and simultaneously the polarization of a pulse from the seed is changed in the Pockels cell by two times $\lambda/4$ and it is therefore not immediately rejected from the resonator. These pulses travel through the population–inverted crystal and gain intensity. On the other hand, by reflections on the Pockels cell or via its imperfect switching a part of this gain is continuously lost. The population inversion of the Ti:sapphire is also depleted after several round–trips. As a consequence, after approximately 18 cycles the pulse intensity reaches its saturation, as can be seen on the signal from a photodiode placed behind the highly reflective cavity end mirror in the amplifier. At this time, high voltage is put again on the Pockels cell and the amplified light is coupled out from the regenerative amplifier. To suppress the large number of pre– and post–pulses, the beam must pass a pulse picker, consisting of a further Pockels cell placed between two crossed Glan–Thompson polarizers. This Pockels cell is synchronized to switch the polarization of light immediately after the beam was released from the regenerative amplifier and hence allows only the desired part of the light to pass. Its perfect timing can be found by checking the residual output rejected by the Glan–Thompson polarizer that should in the optimal case only consist of the rejected pre– and post–pulse. The resulting pulses possess an energy of the order of several hundreds µJ, which is an increase of five orders of magnitude compared to the individual pulses emitted from the oscillator.

Two–pass amplifier and compressor The low frequency, preamplified seed pulse is in the next step led to a two–pass amplifier optimized for high pulse energies and efficient energy extraction from the Ti:sapphire crystal. Here, the lasing medium is pumped very intensively by the rest of the energy from the Nd:YLF laser pumping the regenerative amplifier and by an additional laser of the same type (527 nm light, together with an energy of $\sim$22.5 mJ/pulse). The perfect overlap of the pumping and the laser beams in the crystal is necessary to obtain the optimal, Gaussian–shaped pulse profile as it is needed in the measurement, especially to correctly quantify the desorption yield (see Section 3.2.2). After the already intense input beam has passed the Ti:sapphire two times, its energy is additionally increased by a factor of 10. Due to the strong pumping, the stimulated emission occurs from a saturated level responsible for the population inversion, therefore the possible fluctuations in the output beam are less than 3 %.

In the last step, the pulses are compressed in a grating compressor, which removes the linear chirp imposed by the stretcher and other components in the amplifier system. As the peak power becomes very high at the compressor, the beam diameter on the compressor grating has to be rather large. The reflections on the grating reduce the energy of the pulse by approximately

35 %, but it can be compressed to a length below 80 fs and a final energy exceeding 3.8 mJ. A more detailed description of the presented laser setup can be also found in reference [Fun99].

2.2.2. Generation of ultrashort IR–pulses

For years, the supercontinuum generation in strongly nonlinear media like optical fibers in combination with an optical parametric amplifier (OPA, introduced in Section 3.1.1) was the only source of a tunable, coherent and ultrashort IR radiation. Although optical parametrical oscillators[9] (OPO), capable of creating tunable light in relatively narrow infrared wavelength range have been known since early sixties [Gio65b], it was only the advent of powerful ultrafast lasers together with synthesis of novel highly nonlinear media that allowed to create femtosecond infrared laser pulses with a duration comparable to that of the pump pulse. The advanced nonlinear media have solved one of the major problems of the OPO setup, which has been the required large number of passes through the crystal and hence a temporal broadening of the pulses generated and the lost of the OPA gain due to the different group velocities of the signal (idler) and the pump pulse in the medium. Similar to the Kerr–lens mode–locking case mentioned above, the evolution of devices able to generate ultrashort IR pulses led paradoxically to more and more simple setups with improved optical components and better specifications. One such commercial device, TOPAS (Traveling–wave optical parametric amplifier of superfluorescence) [Dan93], has been used as the IR source for experiments discussed in this thesis. A scheme, showing the main light conversion steps in this instrument, is depicted in Figure 2.7.
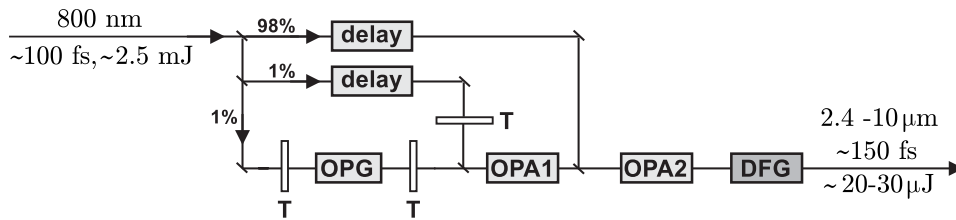
Figure 2.7.: The working principle of TOPAS. The processes OPG, OPA1 and OPA2 are depicted in the order they take place, however, all of them occur in the same BBO crystal. The DFG process is an optional step in TOPAS and takes place in an $AgGaS_2$ crystal suitable for light generation in the wavelength range between 2.4–10 µm.

In a 'black–box' approach, a part ($\sim$60 %) of the 800 nm light from our Ti:sapphire laser system described earlier enters the device, 'travels' through four nonlinear processes (no resonator is required due to their high nonlinearity) and by tuning their parameters, ultrashort IR pulses of desired frequency are obtained. However, the processes in between are rather complex and involve many nonlinear optical phenomena not connected to this thesis. Therefore, while explaining the inner life of TOPAS in the next couple of lines, the reader will be rather referred to the corresponding literature than bothered with too much details.

The capability of an OPO to convert the visible pump beam into the tunable pulses in the near infrared region has been already mentioned and it is a good starting point for explaining the working principle of TOPAS. Its basic idea is to drive a similar process – first to convert

---

[9]An optical parametrical oscillator consists of a resonator cavity similar to the laser oscillator, however, a χ^2–nonlinear optical crystal is placed inside. Pumped with a high intensity laser output, the input light frequency is converted to two components of lower frequency that fulfill the phase–matching condition in the crystal. In the resonator cavity, where those beams are permitted to bounce between the end mirrors, every pass through the nonlinear medium additionally enhances their intensity via an OPA process.

the frequency of the input light into two appropriate, tunable components like OPO and then to combine them or rather their harmonic frequencies. This approach is surprisingly successful when using 800 nm light – all frequencies in the range between 239 nm to 11 µm are achievable in a reasonable power. This is an additional factor that strongly motivates one to understand this device.

OPG stage   After entering TOPAS, the input light is split and about 1 % is focused into the nonlinear BBO crystal. Different from an OPO, the pulses of lower frequency are generated in a much more effective way by using the superfluorescence of the nonlinear media inside. From the theory of parametric transitions in a single–atom system it is known, that quantum fluctuations of the electric field can be amplified to a macroscopic power level in an OPA, which gives rise to the processes like optical parametric fluorescence [Har67] and optical parametric emission [Bye68][10]. Those phenomena do not require signal or idler field to be present in the crystal during the OPA process, both are created from the pump beam, if the corresponding phase–matching condition in the nonlinear crystal is fulfilled.

If a parametric transition in a many–atom system is considered, a correlation between single atoms regarding their spontaneous emission can be found [Dic54, Reh71, Bon75]. A system can be either excited by a coherent pulse into a "correlated state" which has a macroscopic electric dipole that radiates, or the system can spontaneously create such correlations. The first case is commonly denoted as superradiance, the second one as superfluorescence. An exciting property of superfluorescence is that such an assembly of N dipoles radiates with a peak intensity proportional to N^2. Moreover, it possess large bandwidth and is highly directional. One can distinguish it from the superradiance based on the small temporal delay between the pump and superfluorescent pulse, which represents the time required for the individual atomic dipoles to come into phase lock due to the coupling between them [Mal87]. It is also the phenomena that can convert the 1 % of the input light to two optic waves with lower frequency very efficiently in only one pass. Depending on the phase–matching in the BBO crystal (can be adjusted by changing its angle), the signal and idler pulses can be created with frequencies between 1180 nm – 1620 nm and 1620 nm – 2484 nm, respectively.

OPA and DFG stage   In the further step, both pulses are considerably amplified in two consequent OPA processes. The design of the instrument allows them to take place in the same BBO crystal. The last OPA process is strongly saturated which minimizes the pulse–to–pulse fluctuations inherited from the OPG process. After the final amplification the pulses are nearly bandwidth–limited and the overall efficiency of the conversion process is estimated to 35 %.

The obtained tunable frequencies can now be used, frequency–doubled and mixed depending on the intended application. To obtain the infrared frequencies in the D_2O stretch region, the pulses have to undergo another nonlinear process – in an $AgGaS_2$ crystal wavelengths from 2.4 to 10 µm can be produced via DFG. To separate the signal and idler beam from the desired output, a 1 mm Ge filter has been put into the beam path under the Brewster angle. Finally, the tunable IR pulses with the energy of up to 20 µJ[11] are ready for the experiment.

---

[10]Both processes are often commonly denoted as optical parametric generation (OPG). The OPA has to be driven at fairly high gains to amplify the quantum fluctuations to such a scale, but this way of frequency conversion is much more effective than the generation of supercontinuum, as in the OPG the phase–matching conditions have to be fulfilled and therefore light with a narrower range of frequencies is produced as the spatial angle for beam propagation is limited.

[11]The actual energy depends on the IR wavelength as well.

Several additional remarks have to be made for the sake of completeness:

(i) First, during all works, TOPAS has been pumped with 400 Hz repetition rate only. The superfluorescence in the BBO and the last OPA step are driven close to the damage threshold of the crystal: if the pulse energy is increased, the instrument must be readjusted or the energy compensated.

(ii) The effect of different group velocities of signal, idler and pump can not be fully suppressed even if only one beam pass through the nonlinear crystal is granted. For ultrashort pulses the dispersive optical components like the lenses in the telescope, the crystal itself and alike may play a role. This effect can be partially neutralized, if the compressor in the amplifier system is slightly overcompensated. The pulse duration is then longer on the output side of the Ti:sapphire laser system, but optimal after passing TOPAS. This compensation has been made whenever only SFG spectroscopy has been performed and no other devices or processes requiring the ultrashort 800 nm beam (especially the tripler, see Section 3.3) have been involved.

(iii) The remaining 800 nm light not converted in TOPAS is further used as the VIS pulse in the SFG measurement. To make this pulse spectrally narrow, a simple pulse shaper, shown in Figure 2.8, is used to cut out a small wavelength region from the Fourier plane. To avoid spatial chirp, the beam is guided on the same way from as to the grating, differing only in height, which allows us to separate the output. An extremely usefull guide to pulse shaping addressing more complex arrangements as well is given in reference [Mon10].
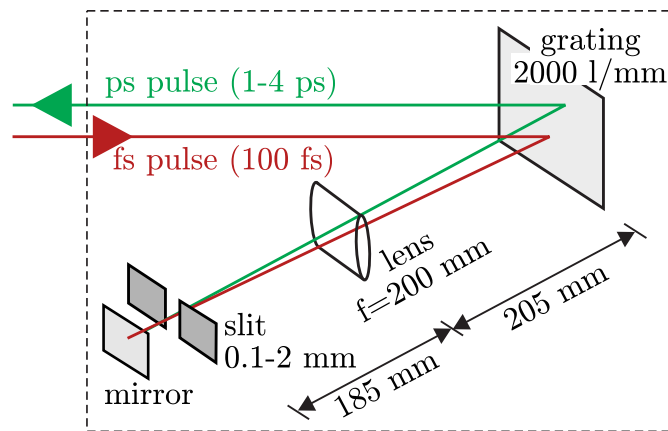
Figure 2.8.: A scheme of the employed pulse shaper.

In the following Chapter (Section 3.3), the further path of the large part ($\sim$40 %) of the light available from the amplifier system will be discussed. In the pump–probe SFG setup, these photons are converted to ultrashort 266 nm pulses in a noncollinear optical frequency tripler developed and build in the framework of the presented thesis. Therefore a separate Section 3.3 on the page 109 is devoted to this device.

2.2.3. Characterization of laser pulses

The reliability of all data obtained in this thesis is strongly correlated to the quality of the employed beams. Therefore their main signatures have been checked on an everyday basis,

some important characteristics even before every single measurement. In the following, the brief overview over the optimal pulse characteristics is given.

Ultrashort 800 nm pulses

The spectrum and the temporal profile of the Ti:sapphire amplifier output is plotted in Figure 2.9. To obtain the spectral information, a commercial grating spectrometer has been used. Compared to the output from the oscillator (not shown), the peak is slightly red–shifted towards 800 nm, which is expected as the maximum gain in the Ti:sapphire crystal is reached at this wavelength.

Even more important information is contained in the temporal envelope of the pulse. As
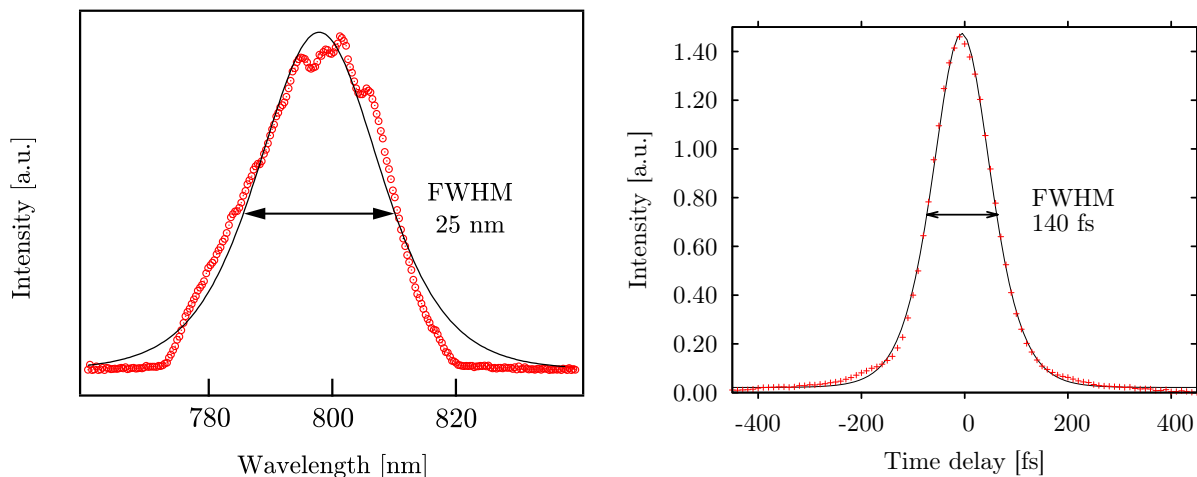
Figure 2.9.: The spectrum and the autocorrelation of the Ti:sapphire amplifier output. From the right graph the pulse duration can be calculated and amounts to ≈90 fs

the pulses are not very complex (unshaped, with no chirp, longer than several light oscillation periods) and their temporal evolution copies the sech^2 shape almost exactly, an autocorrelation is the best choice to follow it. In the autocorrelation, the characterized pulse is usually split into two equal parts and overlapped again in an appropriate nonlinear medium, so that the generation of second harmonic is possible. The intensity of the generated SHG light can be then expressed as

$$I_{\mathrm{SHG}}(\tau) \propto \int_{-\infty}^{\infty} I(t) \cdot I(t - \tau) \mathrm{d}t \tag{2.3}$$

where τ is the delay between the two pulses. If the investigated autocorrelation trace has a sech^2 shape, the deconvolution of Equation 2.3 assuming two identical pulses gives the ratio between the full width at half maximum (FWHM) of the autocorrelation and of the original pulse to be 1.543 [Fre95, Dem08]. A typical pulse duration of our amplified pulses is hence ≈90 fs.

A very critical issue in the desorption yield measurement (see Section 3.2.2) is the actual beam profile. Figure 2.10 shows a typical spatial intensity distribution in the beam taken with a CCD camera. To achieve the required high fluences, the beam is focused on the sample with a telescope. It can be also diverted from the direct path to the sample and enter a reference beam path, where it is first attenuated by reflection on two wedge windows and consequently imaged in the distance from the last lens identical to that of the Ru(0001) crystal. A pass through
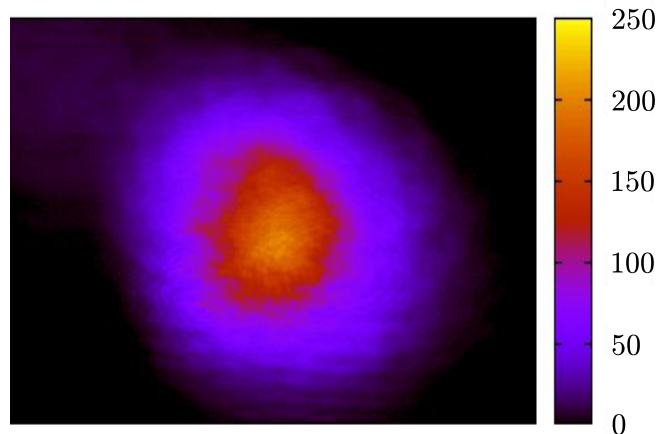
Figure 2.10.: A spatial profile of the 800 nm beam. Its almost perfect Gaussian shape can be fitted to obtain its real dimensions that vary in the experiment due to the necessary beam focusing with a telescope to an appropriate size. Such a beam shape is expected from a laser oscillating in the fundamental transverse mode (TEM_{00}).

a filter is to be avoided due to the possible self–focusing of a small–size, intense beam, which distorts the measurement.

UV pulse characterization

The spectrum of the UV beam (Figure 2.11 right), which represents the output from the non-colinear optical frequency tripler described later (Section 3.3), has been recorded with a fiber grating spectrometer (Ocean Optics HR 4000+). It is obviously much narrower than the spec-
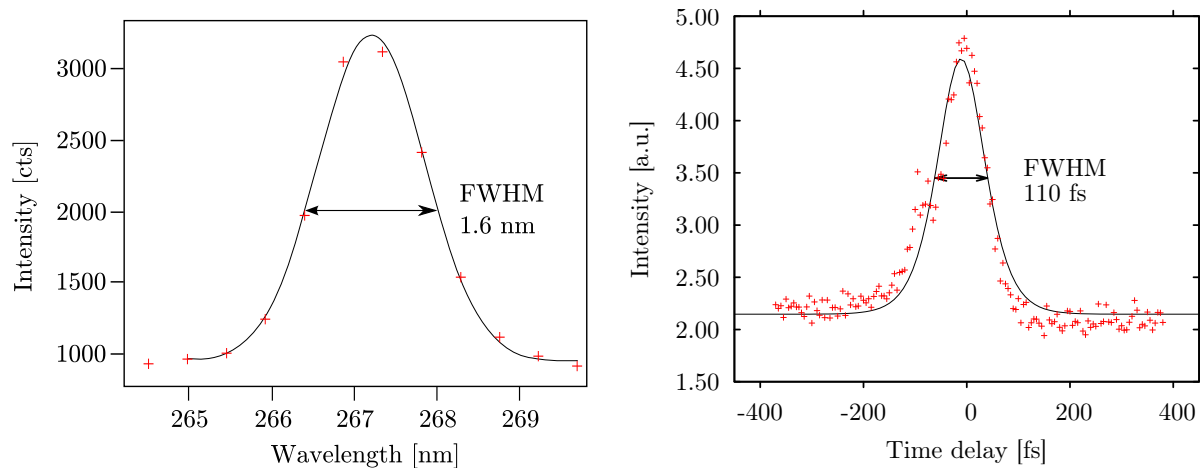
Figure 2.11.: The spectrum and the autocorrelation of the tripler output. The left graph depicts a cross–correlation between the 90 fs long 800 nm pulse and the 266 nm beam, which after deconvolution yields a pulse duration of $\approx$65 fs.

trum of the input 800 nm beam, which can be explained by the larger light oscillation frequency: assuming the same pulse duration, the time–bandwidth product yields the same bandwidth ($\Delta\nu$) for both pulses. Therefore the larger frequency ν of the 266 nm beam is broadened less in the wavelength due to the smaller $\Delta\nu/\nu$ ratio. Its width of ≈ 2 nm is indeed compatible with the time–bandwidth product.

A more difficult task is to measure the pulse duration of the UV light. Instead of using a nonlinear effect (like DFG in BBO) which is often connected with an enhanced light dispersion, as most of the compounds do absorb in the UV, we decided to make use of the retarding–field analyzer (RFA, introduced in the Section 3.4) and the photoemission phenomena (discussed in the Section 1.2.3 and 3.4). In a simple view, an electron is emitted from the Ru(0001) crystal if the photon energy in the incident light is sufficient to overcome its work function. This is the case for the 266 nm UV pulses, if the ruthenium is covered by at least ~ 0.3 BL of ice. If another pulse spatially and temporally overlaps with the UV, electrons from lower energy levels can be emitted as well. This is detected by the RFA as an considerable increase of signal intensity and allows to find the perfect temporal and spatial overlap even of the ultrashort and invisible (IR) beams. Such a cross–correlation measurement between the UV pulse and the 90 fs long amplifier output is shown on the left side in the Figure 2.11. It is difficult to deconvolute such a spectrum if the initial shapes of both pulses are unknown. However, the error in the obtained pulse duration is negligible, if a Gaussian shape for both initial pulses is assumed[12]. The advantage of this approach lies in the properties of the Gaussian function: its convolution with itself yields another Gaussian, whose FWHM (Δ_{CC}) follows the relation

$$(\Delta_{\mathrm{CC}})^2 = (\Delta_1)^2 + (\Delta_2)^2 \tag{2.4}$$

where Δ_1 and Δ_2 are the FWHM of the initial pulses. Within this picture, the length of our UV pulses is ≈ 65 fs. One can understand this result from a consideration discussed more thoroughly later in the Section 3.1: the intensity of a frequency doubled (or sum frequency) pulse is proportional to the square of the intensity (or to the product of intensities) of the original beam. Put in other words, even within a single pulse the efficiency of frequency doubling is much larger in the most intense part than in the rest. This leads quite naturally to a narrowing of the pulse duration which is, however, often compensated by the dispersion in the medium. In the tripler, two independent SFG processes take place and the corresponding nonlinear crystals are very thin. Thus, a decrease in the pulse length is expected. An excellent demonstration of this behavior offers the Figure 3.15 in the Section 3.3.4 with corresponding discussion.

TOPAS output characterization

Both beams exiting TOPAS are used in the SFG experiment. The spectrum of the IR beam is shown in Figure 2.12. The central wavelength of the IR pulse can be varied over a wide range, however in the measurements in this thesis only the interval between 3250 and 5000 nm (2000 and 3100 cm^{-1}) was exploited. The radiation at ~ 2340 cm^{-1} is absorbed completely in air after passing only several centimeters due to the intense, asymmetric CO_2 vibrational transition. This can be avoided by purging the beam path with the dry nitrogen (see Section 3.2.3). The example pulse spectrum in the Figure 2.12 covering a region of ~ 150 cm^{-1} in the SFG spectroscopy was recorded with a commercial (Jobin–Yvon) grating spectrometer. The light

---

[12]In fact, if the autocorrelation of the amplifier output pulse in Figure 2.9 is fitted to a Gaussian function, the FWHM value is identical to the sech^2 fit, although the latter obviously describes its shape much better.
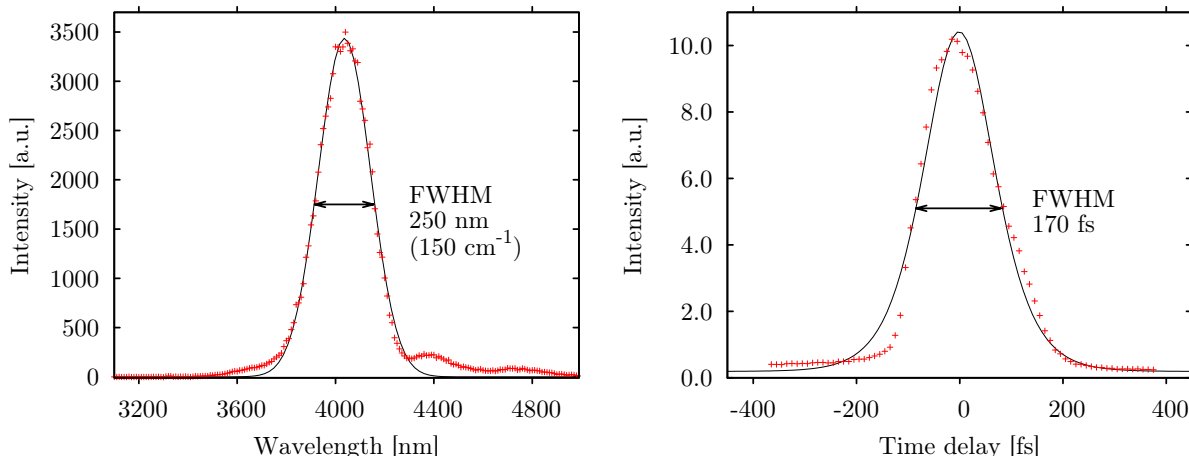
Figure 2.12.: The spectrum and the cross–correlation of the TOPAS IR output in the frequency range corresponding to the OD stretch resonance (partially coordinated, see Section 1.1.4). In the cross–correlation, the IR pulses are convoluted with the UV light to achieve a better temporal resolution. The estimated pulse duration is ≈160 fs.

was first dispersed by a grating (120 lines/mm, blaze–wavelength 5 μm[13]) and by controlled change of its angle, the corresponding IR intensity was measured by a liquid–nitrogen cooled MCT detector (mercury cadmium telluride detector, based on an alloy of CdTe and HgTe that may possess an extremely small band gap which is suitable for large wavelengths; cooling is required to suppress the thermal noise).

The temporal envelope of the pulse is obtained from the cross–correlation between the UV and the IR pulse. The pulse duration is found to be ≈160 fs at FWHM. Note, that the temporal pulse width may be longer, if the system is not purged. Due to the proximity to the CO_2 vibrational transition the dispersion of air can namely become large for some wavelengths. This, however, does not apply to our case.

The spectrum of the VIS light remaining after IR generation in TOPAS is plotted in Figure 2.13. It has been usually taken with a fiber spectrometer, whose resolution is lower than the actual pulse width, mainly due to the dispersion in the fiber itself. However, this type of spectra was frequently taken to check the real wavelength of the VIS beam required for the correct estimate of the SFG wavelength. From the former measurements, the time–bandwidth product and also from the SFG data it is clear that its spectral width amounts to ∼0.5 nm at 792 nm central wavelength.

Shaping the pulse shrinks it to a narrower spectral FWHM, but on the other side, the significant grating dispersion leads to a considerable temporal chirp, i.e. to longer pulses. The cross–correlation between the UV and shaped VIS reveals the pulse duration of 2.65 ps. This value is strongly dependent on the distance of the shaper slit blades, but usually does not exceed 4 ps. With this settings, high spectral resolution in the SFG can be achieved, therefore it has been mainly used to precisely characterize the D_2O/Ru(0001) system and to precisely determine the vibrational frequencies in Chapter 4.

---

[13]Gratings with grooves that have a sawtooth profile possess a high diffraction efficiency for selected wavelengths and orders, where most of the energy is concentrated.
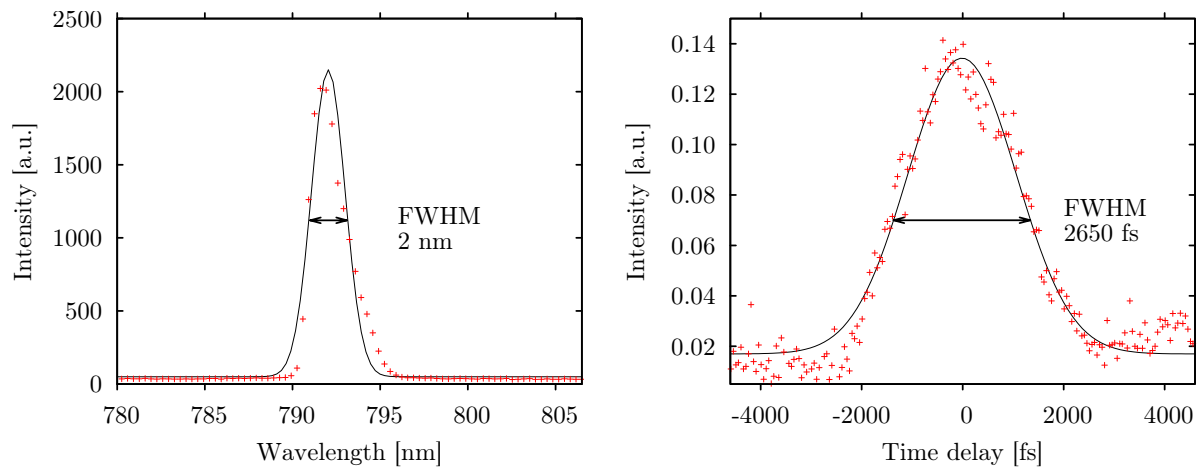
Figure 2.13.: The spectrum and the cross–correlation of the TOPAS VIS output after pulse shaper. The spectrum is artificially broadened in the fiber of the spectrometer, its actual width is ∼0.5 nm. Cross–correlation shows the convolution of the UV and shaped 792 nm pulse, the extracted pulse duration is identical to the FWHM of the cross–correlation peak.

3. Experimental methods and important innovations

3.1. SFG vibrational spectroscopy

In the underlying thesis the main tool for investigation of structural changes in ice is a nonlinear vibrational spectroscopy method based on the sum frequency generation at its interfaces. The optical nonlinearity is, however, not only exploited in this technique, but is essentiall property of the most important elements of the laser system used and crucial factor in the generation of IR light of tunable frequency.

In the following a brief introduction into the basics of nonlinear optics is given with emphasis on the theoretical background necessary for understanding the second–order nonlinear processes and the phenomena discussed later in the experimental part in Chapter 2 and for the correct interpretation of results in Chapter 5.

3.1.1. Nonlinear optics

Nonlinear optics (NLO) examines phenomena that can occur in matter as a consequence of the modification of its optical properties in the presence of light [Boy03, She84]. Those effects are nonlinear in the sense that they arise when the response of a medium depends in a nonlinear manner on the strength of the electric field contained typically only in a laser pulse in sufficient magnitude. More precisely, by optical nonlinearity usually the dependence of polarization $\mathbf{P}(\boldsymbol{r}, t)$ of a material (or dipole moment per unit volume) on the strength of the applied optical field $\mathbf{E}(\boldsymbol{r}, t)$ is considered. In the linear optics, the induced polarization is directly proportional to the field strength and can be described by the relationship[1]:

$$\mathbf{P}(\boldsymbol{r}, t) = \epsilon_0 \chi^{(1)} \mathbf{E}(\boldsymbol{r}, t) \tag{3.1}$$

with proportionality constant $\chi^{(1)}$ being the linear susceptibility[2], ϵ_0 is the permittivity of free space. However, if the external field becomes strong[3], as it is the case in a femtosecond laser pulse, the linear polarization of matter is no longer a sufficient approximation and higher order terms have to be taken into account. Then the total polarization of a medium can be described by a series expansion:

$$\mathbf{P}(\boldsymbol{r}, t) = \epsilon_0 \chi^{(1)} \mathbf{E}(\boldsymbol{r}, t) + \epsilon_0 \chi^{(2)} \mathbf{E}^2(\boldsymbol{r}, t) + \epsilon_0 \chi^{(3)} \mathbf{E}^3(\boldsymbol{r}, t) \dots \tag{3.2}$$

$$\mathbf{P} = \mathbf{P}^{(1)} + \mathbf{P}^{(2)} + \mathbf{P}^{(3)} \dots \tag{3.3}$$

where $\boldsymbol{\chi}^{(n)}$ are nonlinear susceptibilities of n–th order, having tensorial form in general and the $\mathbf{P}^{(n)}$ is the n–th term in the series. This is of course valid only under the assumption that

---

[1] SI units are used; in gaussian unit system, often used in the literature, the ϵ_0 prefactor is ommited.

[2] In a more general approach, due to the molecular symmetry and local–field effects, $\mathbf{P}(\boldsymbol{r}, t)$ is not necessarily parallel to the applied field $\mathbf{E}(\boldsymbol{r}, t)$ and $\chi^{(1)}$ becomes a first–rank tensor (i.e. vector).

[3] Although still weaker than the intramolecular field felt by an electron, otherwise strong photoionisation can occur and the series expansion 3.2 does not need to converge anymore [Boy03].

the response of the medium is instantaneous and the losses or dispersion in the matter can be neglected.

The close relationship between the external field and the medium polarization has an important consequence: the polarization associated with the (nonlinear) response of a material can itself act as a source of electromagnetic field. In a simple example, one can consider a second order nonlinear material experiencing a field composed of two distinct frequency components:

$$\mathbf{E}(t) = (\mathbf{E}_1 e^{-i\omega_1 t} + \mathbf{E}_1^* e^{i\omega_1 t}) + (\mathbf{E}_2 e^{-i\omega_2 t} + \mathbf{E}_2^* e^{i\omega_2 t}) \tag{3.4}$$

According to Eq. 3.2 and 3.3 the resulting induced second order polarization is

$$\begin{aligned}\mathbf{P}^{(2)} =& \epsilon_0 \boldsymbol{\chi}^{(2)} [\mathbf{E}_1^2 e^{-i2\omega_1 t} + 2\mathbf{E}_1\mathbf{E}_2 e^{-i(\omega_1+\omega_2)t} + 2\mathbf{E}_1\mathbf{E}_2^* e^{-i(\omega_1-\omega_2)t} \\ &+ \mathbf{E}_2^2 e^{-i2\omega_2 t} + \text{c.c.}] + 2\epsilon_0\boldsymbol{\chi}^{(2)}[\mathbf{E}_1\mathbf{E}_1^* + \mathbf{E}_2\mathbf{E}_2^*]\end{aligned} \tag{3.5}$$

The physical interpretation of this equation is that the incident optical fields with the frequencies ω_1 and ω_2 are able to generate a transient polarization of dipoles in the medium, which reacts in the nonlinear way by converting a part of the incident light to photons at frequencies $2\omega_1$, $2\omega_2$, $(\omega_1 + \omega_2)$ and $(\omega_1 - \omega_2)$. The process of obtaining the first two frequency components is commonly denoted as the second harmonic generation (SHG) [Fra61, Fra63], following two terms give names to sum and difference frequency generation (SFG and DFG) [Bas62a], respectively. The latter effect is known as optical rectification and generates a static electric field across the nonlinear crystal, as the term $\mathbf{E}_n\mathbf{E}_n^*$ with zero frequency can not be a source of electromagnetic radiation [Bas62b]. Both SFG and SHG can be intuitively understood as being a process of generating a sum of the two photons entering a nonlinear matrial. In fact, they are in many aspects similar, unlike the DFG as can be seen from Figure 3.1.
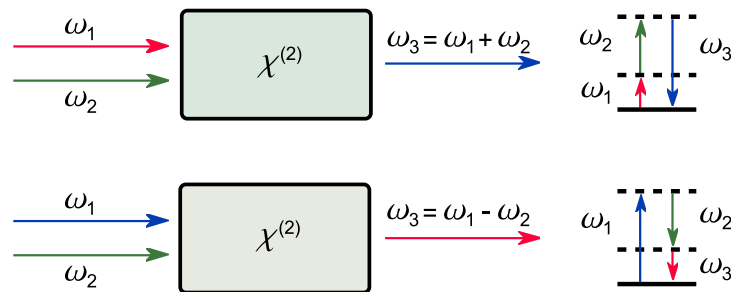
Figure 3.1.: A graphical scheme of the SFG (top) and the DFG (bottom) process. On the right side their energetics is outlined in a simple three level diagram.

In the DFG case, the energy conservation requires that for every photon at created frequency ω_3, one photon at frequency ω_1 has to be destroyed and another photon with frequency ω_2 is released by stimulated emission in the presence of another photon with the same frequency. This phenomena is known as the optical parametrical amplification OPA[4] and is widely used to amplify optical laser pulses at various wavelengths, where a corresponding coherent source is not available (see e.g. Section 2.2.2). For this purpose a nonlinear crystal is placed inside of a resonator cavity with two mirrors possessing a high reflectivity at frequency ω_2 or/and ω_3, so that an *optical parametrical resonator* is created. In such an arrangement, pump light (ω_1)

---

[4]The word parametric denotes a process in which the initial and final quantum mechanical state are identical. A nonparametric process usually involve a population transfer between the real energy levels and the energy transfer to the material medium becomes more likely.

enters the cavity and the selected[5] output frequencies are amplified. Conventionally, the output optical wave with higher frequency is called signal, the lower frequency part labeled idler. The desired frequency can be chosen and tuned by altering specific parameters of the system (e.g. crystal temperature, orientation, etc.).

Nonlinear optical susceptibility

The nonlinear optical susceptibility contained as prefactor in Equation 3.5 deserves a special treatment, as it is the main quantity that determines the amplitude of second–order processes, like SFG and imposes restrictions on the media where they can take place. In a simplified situation, where an atom is treated as a harmonic oscillator (Lorentz model) the nonlinearity of a medium can be simulated by a nonlinearity in the restoring force exerted on the electron [Boy03]. In contrast to a quantum–mechanical treatment [Bon05], this approach can not properly describe the complete nature of the nonlinear phenomena, but offers a good and illustrative starting point to explain some of its main characteristics.

One can divide the nonlinear media into two groups based on their internal symmetry – there are *centrosymmetric* materials that also possess an inversion (mirror) symmetry and materials, where this *inversion symmetry is broken*. In either of them the collective movement of electrons, giving rise to the induced polarization will encounter a different potential as is depicted in the Figure 3.2. In a centrosymmetric medium, the potential function must be symmetric under the operation $x \to -x$. If this condition is considered in the equation of motion for a harmonic oscillator, all even–order responses vanish. The easiest way to demonstrate this is to take the part of induced polarization responsible e.g. for the SFG process

$$\mathbf{P}^{(2)} = \epsilon_0 \boldsymbol{\chi}^{(2)} \mathbf{E}_1(t) \mathbf{E}_2(t) \tag{3.6}$$

and invert the sign of the incoming field [Arn10]. In such a case, the polarization must change its sign as well, however, due to identical (centrosymmetric) atomic structure, the $\boldsymbol{\chi}^{(2)}$ is insensitive to this transformation and does not change. One obtains

$$-\mathbf{P}^{(2)} = \epsilon_0 \boldsymbol{\chi}^{(2)} [-\mathbf{E}_1(t)][-\mathbf{E}_2(t)] \tag{3.7}$$

which is simultaneously fulfilled only if $\boldsymbol{\chi}^{(2)} = 0$.

If the inversion symmetry in the medium is broken, the potential energy function of the Lorentz oscillator becomes asymmetric and the even order nonlinear processes are allowed. It should be emphasized that this simple picture helps to understand a number of phenomena correctly. For example, it is often erroneously assumed that an isotropic material can not be used to generate second–order nonlinear processes (e.g. in [Arn10]). However, such a prominent example as GaAs crystallizes in a cubic lattice (is not birefringent), but represents a strongly nonlinear material with one of the largest second–order nonlinear susceptibilities. The reason is its zincblende unit cell with intrinsically broken inversion symmetry. In a similar way the weak second–order nonlinear response of chiral liquids [Gio65a, Bel00, Bel01, Ver98] can be understood based on the definition of a chiral compound as being different from its mirror image.

If the atoms in a nonlinear behave like oscillators, each developing an oscillating dipole moment with a component at the frequency $(\omega_1 + \omega_2)$, it is obvious that the interference between the emitted light waves can occur. The largest intensity in the SFG signal can be expected if the

---

[5]The wavelength is chosen mainly by the crystal orientation that must satisfy the phase matching condition (momentum conservation) for any selected wavelength (see below).
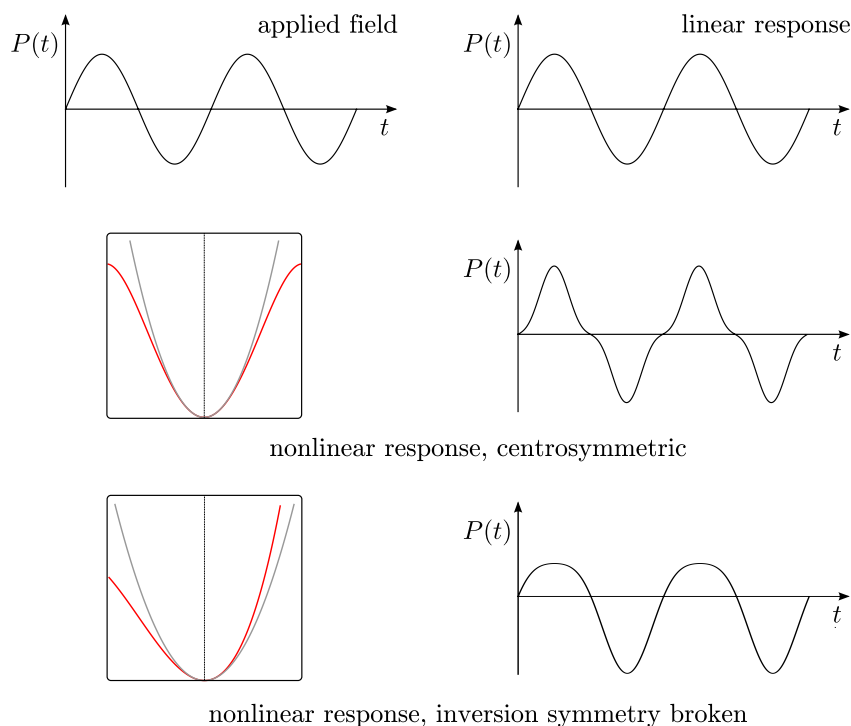
Figure 3.2.: Symmetry properties of the nonlinear optical susceptibility. In the top level the applied electric field is shown and if passing through a linear optical material, the induced polarization will copy its original shape. If the medium provides a nonlinear response and is centrosymmetric (middle), its electrons move in a potential shown by the red curve (gray represents an ideal parabolic potential). The polarization changes in a way that can be characterized by the waveform on the right side (here: $\sin(\omega t) - 0.25\sin(3\omega t)$). For a non–centrosymmetric medium the waveform is shown in the bottom level (the function plotted is: $-0.2 + \sin(\omega t) + 0.2\cos(2\omega t)$. Adopted from [Boy03].

periodic array of dipoles oscillates in phase and adds constructively, giving rise to a highly directional sum–frequency output and to the *phase–matching condition*. From this consideration also follows that e.g. amorphous compounds lacking long–range order will hardly contribute to a second–order nonlinear process, as there is no way to arrange the dipoles that are not correlated over a longer distance (more than with their closest neighbors; see Section 1.1.2) so that they do not interfere destructively.

   A further place, where an asymmetric potential is felt by electrons is at a surface of a solid or liquid, where the centrosymmetry is always broken. As many of the crystal classes do possess an inversion center, second–order nonlinear effect offer a way how to investigate the processes at the surface without an interference with the usually much larger bulk signal.

3.1.2. SFG vibrational spectroscopy

Nicknamed 'new light on hidden surfaces' [Rok04], the SFG spectroscopy, exploiting the second–order nonlinear process of the same name, has become an established and widely used method to explore surfaces and interfaces. Its advantages are intuitively clear – it is very convenient to use vibrational spectroscopy to trace processes on a molecular level, but it is usually easier to detect light at lower frequencies (higher energies) than in the infrared region. With SFG,

one can have both – if two pulses are overlapped on the sample, one with a defined infrared frequency and a second defined in the visible range, the sum–frequency (SF) signal containing vibrational information as visible light can be observed. But its main virtue is that if the underlying medium is centrosymmetric, this method is *intrinsically surface sensitive*[6].

For two beams, infrared and visible, the general scheme of an SFG process involving a resonant vibrational transition in a thin adsorbate layer is shown in Figure 3.3. Using the electric (optic)
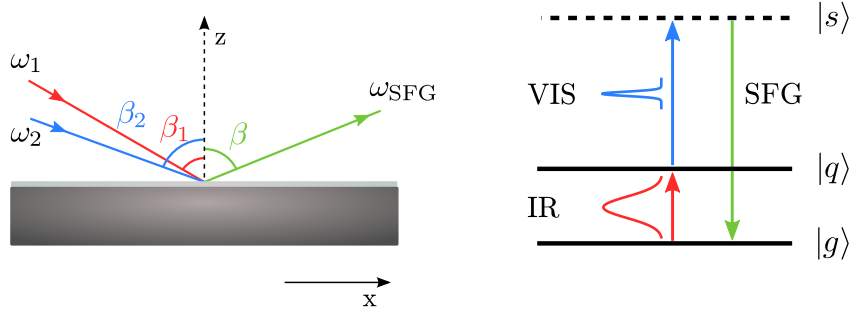
Figure 3.3.: SFG geometry and energy level scheme.

field induced polarization expressed in the Equation 3.6 as a source of the SF radiation, the SF intensity (I_{SFG}) can be calculated by solving Maxwell equations [Blo62, vdH98, She01, Unt02b], whereas the main problem is to express the nonlinear polarizations and electric field strengths *inside* of the adsorbate layer. For this purpose a Fresnel matrix (known also as optical transfer matrix) is used [Bor75]. In general, the I_{SFG} is proportional to the intensities of the incoming fields[7]:

$$I_{\mathrm{SFG}} \propto \left| \boldsymbol{P}_{\mathrm{SFG}}^{(2)} \right|^2 \propto \left| \boldsymbol{\chi}_{\mathrm{eff}}^{(2)} \right|^2 I_{\mathrm{IR}} I_{\mathrm{VIS}} \qquad (3.9)$$

where the effective second–order nonlinear susceptibility $\boldsymbol{\chi}_{\mathrm{eff}}^{(2)}$ is introduced that contains all geometrical and light polarization dependent factors that influence the actual electric field experienced by the adsorbate molecules. It is also affected by the interaction of the field with surrounding media that usually produces a constant, frequency independent response (see also discussion below) and can be thus split into a non–resonant and resonant contribution

$$\boldsymbol{\chi}_{\mathrm{eff}}^{(2)} = \boldsymbol{\chi}_{\mathrm{NR}}^{(2)} + \boldsymbol{\chi}_{\mathrm{R}}^{(2)} \qquad (3.10)$$

where the latter becomes important when the incoming IR field is in resonance with a vibrational transition in the adlayer. The resonant part is further dependent on the number of oscillators (i.e. on coverage θ): in a microscopic scale, it is namely closely related to the angular average of the molecular hyperpolarizability (second–order polarizability of a molecule) $\langle \boldsymbol{\beta} \rangle$[8] [Ric02, She89]:

$$\boldsymbol{\chi}_{\mathrm{R}}^{(2)} = \frac{N}{\epsilon_0} \langle \boldsymbol{\beta} \rangle \qquad (3.11)$$

---

[6]It should be noted that this statement is valid only within the quantum–mechanical electric dipole approximation, where the total Hamiltonian is expressed in the form

$$\hat{\boldsymbol{H}} = \hat{\boldsymbol{H}}_0 - \hat{\boldsymbol{\mu}} \boldsymbol{E}(t) \qquad (3.8)$$

with $\hat{\boldsymbol{\mu}} = -e\hat{\boldsymbol{r}}$ being electric dipole moment operator and all other contributions to the polarization of a medium [e.g. from electric quadrupoles ($\boldsymbol{E}(\nabla \boldsymbol{E})$) or magnetic dipoles ($\boldsymbol{E} \times \boldsymbol{B}$)] are neglected.

[7]For a more general formula allowing to extract the molecular orientation from the SFG spectra see Appendix A.

[8]This expression is generally valid if *one* resonant transition is considered.

In a system, where more than one resonant transition (vibrational mode) is present in the given frequency range covered by the IR pulse, the contribution to the total hyperpolarizability from the q–the mode becomes [Buc01, Ric02]

$$\beta_{lmn,q} = \frac{\langle g|\boldsymbol{\alpha}_{lm}|q\rangle\langle q|\boldsymbol{\mu}_n|g\rangle}{\omega_{\mathrm{IR}} - \omega_q + i\Gamma_q} \tag{3.12}$$

within a molecular coordinate system (lmn) and with $\boldsymbol{\alpha}_{lm}$ and $\boldsymbol{\mu}_n$ representing the Raman and dipole vibrational transition elements, g and q the ground and vibrationally excited state as shown in Figure 3.3, respectively. The expression 3.12 contains directly formulated selection rules for the resonant SFG process: to be allowed, a vibrational mode must be both IR *and* Raman active. Here, again the broken inversion symmetry requirement can be seen from a different angle – all molecules possessing an inversion center are either Raman or infrared active, but can never be both at the same time, as this is only possible in the non–centrosymmetric media.

To analyze the SFG data, the usually unknown transition moments are merged into fitting constants. A very often used resonant shape (already indicated by Eq. 3.12) is the homogeneous Lorentzian profile [Zhu87, She96, Zhu99, Vid05, Arn10, She06] described by

$$\boldsymbol{\chi}^{(2)}_{\mathrm{eff}} = \boldsymbol{\chi}^{(2)}_{\mathrm{NR}} + \sum_q \boldsymbol{\chi}^{(2)}_{\mathrm{R}} = |A_{\mathrm{NR}}|\, e^{\mathrm{i}\phi_{\mathrm{NR}}} + \sum_q \frac{|A_q|\, e^{\mathrm{i}\phi_q}}{\omega_{\mathrm{IR}} - \omega_q + \mathrm{i}\Gamma_q} \tag{3.13}$$

Here, A_q, Φ_q, ω_q and Γ_q are the amplitude[9], phase, resonant frequency and damping constant (half width at half maximum) of the q–th mode, the non–resonant contribution is characterized only by its amplitude and phase. As the latter usually stems from surface electrons [Tad00], its phase can be set to zero so that the constant ϕ_q expresses the relative phase between the resonant and the non–resonant part (please refer to Section 3.2.3 for more details). Inserting the obtained expression into the Equation 3.9, the SFG intensity (signal) can be written as

$$\mathrm{I}_{\mathrm{SFG}} \propto \left| |A_{\mathrm{NR}}| + \sum_q \frac{A_q e^{\mathrm{i}\phi_q}}{\omega_{\mathrm{IR}} - \omega_q + \mathrm{i}\Gamma_q} \right|^2 I_{\mathrm{VIS}} I_{\mathrm{IR}} \tag{3.14}$$

The details of its evaluation and of the spectral deconvolution of the measured data are discussed in Section 3.2.3.

3.1.3. SFG spectroscopy with broadband IR pulses

Having discussed the resonant nature of the SFG process and its connection to the Raman and infrared vibrational spectroscopy and thus directly to the vibrational spectra of the single molecular layer on a surface, a more practical point of view should be addressed next. If the valuable information contained in the SFG signal should not get lost due to a poor resolution, at least one of the employed pulses has to be spectrally narrow. The *femtosecond* laser pulses used in our setup provide the necessary intensity to drive a second–order nonlinear process, but also automatically possess a large bandwidth – this becomes obvious when they are converted from the time into the frequency domain by a Fourier transform. As a compromise between the resolution and the intensity, the visible pulse is spectrally narrowed in a way that is described

---

[9]The amplitude A_q is also proportional to the number of oscillators contributing to the q-th mode, as it is obvious from Eq. 3.11.

later in the Section 2.2.2. This solution offers many advantages:
First is the larger spectral width of the IR pulse that can cover a wide frequency range without the need to be tuned over a resonance. Using one pulse, one can conveniently cover a frequency range of about $150\,\mathrm{cm}^{-1}$ as it is shown in Figure 3.4. If the frequency of the infrared pulse
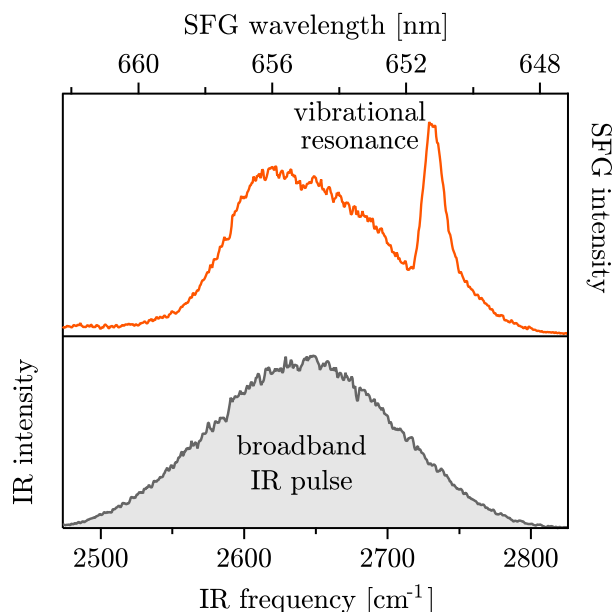
Figure 3.4.: SFG spectroscopy employing broadband IR pulses. In the bottom panel the spectrum of the infrared pulse is shown. It is measured as the SFG signal from bare Ru(0001) surface, as in the absence of a resonance this is directly proportional to I_{IR}. At the resonance wavelength the signal is enhanced (shown in the top panel) and in the case shown it appears together with the contribution from the metal surface.

matches a vibrational transition, the SFG signal is resonantly enhanced (cf. Equation 3.14) and this can be clearly resolved since the convolution of the very narrow visible pulse and the IR pulse essentially copies the shape of the latter.
A second important advantage is the possibility to resolve the ultrafast dynamics of surface processes. Keeping the IR pulse short allows to collect vibrational spectra of molecules several tens of femtoseconds after e.g. an optical excitation. In this way, the laser induced desorption of CO from Ru(0001) could be followed and its microscopic mechanism revealed [Bon00b].

SFG on metal surfaces

On a metal surface, the presence of free electrons may significantly influence the measured vibrational spectrum by its interaction with the electric field in the IR frequency range. In fact, it imposes a new 'selection rule' for vibrational modes that can be observed: If a dipole (or its component) is oscillating parallel to the metal surface, it will not be visible (it will not contribute) in the vibrational spectrum. The reason is the image dipole created in the metal that will effectively cancel the dipole moment change accompanying the molecular vibrational motion (see Figure 3.5). On the other hand, dipoles oscillating perpendicular to the surface will exhibit a larger dipole moment change for the same reason.

A very similar effect is responsible for vanishing of the IR field polarized in the direction perpendicular to the plane of incidence (*s*–polarized or *p* polarized with the angle of incidence
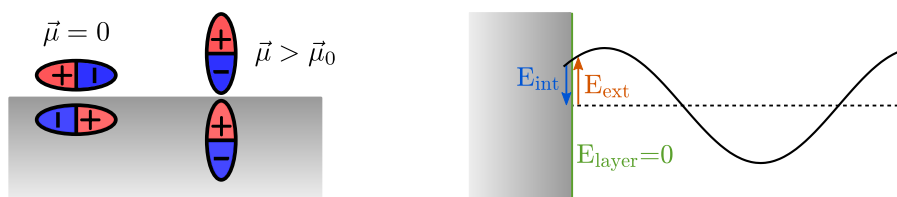
Figure 3.5.: Illustration of the dipole and the image dipole at a metal surface leading to a vanishing or an amplification of the corresponding vibrational mode in the IR spectrum (left). The effective filed experienced by a molecular adlayer is vanishing for infrared frequencies with electric field oscillating perpendicular to the surface normal (right).

close to zero): In the proximity of a metal surface its slowly varying amplitude is always compensated by the free electron gas and the electromagnetic field experienced by the adsorbed molecule is essentially zero [Gre66]. This applies not only to the first monolayer, influenced are also thicker films (e.g. in case of copper oxalate films on Cu, layers up to 25 nm thick [Yat87]). In the experiments presented here, only SFG with a p–polarized IR beam is therefore feasible and performed with the largest possible angle to the surface normal.

A further complication is the nonlinear response of the surface electrons. The broken inversion symmetry at the interface leads to a comparably large background that is independent on ω_{IR} only if the frequencies of the incident fields are much smaller than the frequency of plasma oscillations in the metal [Pet95] and do not coincide with the metal's interband transitions [Tad00]. The interaction between this non–resonant background and resonant amplitudes gives rise to the characteristic line shapes discussed in the Section 3.2.3.

In the experiments presented here, both input frequencies are well below the plasma frequency of Ru(0001) surface electrons (for d–metals typically ∼10 eV). The wavelength of the visible light is kept constant at a value, where the shape of the non–resonant response does not exhibit any phase (ϕ, introduced above) modulation and essentially copies the spectrum of the IR pulse. Its amplitude varies only under the influence of different adsorbate species and coverages, which is also considered in the Equation 3.14 above.

3.2. Performed experiments and experimental methods

In a typical experiment, usually many of the ideas and instruments described in the previous Chapters and Sections are exploited simultaneously. Due to the considerable complexity of the system, the aim of the following Section is mainly to provide the information necessary to understand the interplay between the different parts of the experiment and to introduce the way, how it leads to the final result. Not only is the experimental setup for each type of investigation discussed thoroughly, but the evaluation and the modeling of the measured data is also introduced, as in some of the cases (particularly in the SFG spectroscopy) it is the only way to extract the information from the experimental results.

3.2.1. Thermal desorption spectroscopy

Maybe a good starting point for the discussion of employed experimental methods is to briefly introduce the thermal desorption spectroscopy (TDS), as it is the method used in all experiments mainly to confirm the quality of the sample and to estimate the total amount of adsorbate on the surface, but the data obtained here bear much more valuable information which is used e.g. for the rough estimate of the binding energy of an adsorbate to the substrate.

The general idea of a TDS experiment is rather simple: if the adsorption is not a thermally activated process and the desorption is seen as its reverse, than the adsorbate binding energy can be estimated in a convenient way from the desorption activation energy. This can be easily calculated from the temperature at which the adsorbed species leaves the surface, whereas the desorbing amount (rate) can monitored sensitively by a mass spectrometer.

In a classical setup therefore one heats a surface (or a filament), covered with a coverage of θ, with a constant heating ramp $\beta = dT/dt$. Using the Arrhenius expression for the rate of the desorption process, the adsorbate starts to desorb when the surface temperature T approaches the desorption activation energy E_{des} and the change in the coverage can be expressed by [Kin75]

$$- \frac{d\theta}{dt} = \nu \theta^n e^{-E_{\text{des}}/k_{\text{B}}T} \tag{3.15}$$

which is known as the Polanyi–Wigner equation. The constant ν denotes the attempt frequency and is usually set to $10^{13}\,\text{s}^{-1}$ [Thi87, Sch94], the exponent n is the reaction order. For a first order desorption (a process that is independent on the concentration of other species on the substrate), the expression 3.15 can be simplified assuming reasonable heating rates to [Red62]

$$E_{\text{des}} = k_{\text{B}} T_{\text{max}} \left(\ln \frac{\nu T_{\text{max}}}{\beta} - 3.64 \right) \tag{3.16}$$

which is known as the Redhead formula and relates the peak desorption temperature T_{max} directly to the activation energy of desorption. Although a detailed analysis could yield further kinetic parameters of the desorption [Tom96], for the purposes of the present work the Equation 3.16 presents a sufficient description. Further evaluation is not made also due to the strong lateral interaction between the adsorbed water molecules that influences our desorption spectra and additionally complicates the evaluation. Nonetheless, a phenomenological analysis of the TDS spectra of Ru(0001)–supported thick ice layers was already successfully applied to reveal the D_2O crystallization dynamics [Smi96].

3.2.2. Measurements of the desorption dynamics

Measurement of the laser induced desorption yield

More in the focus of this thesis is the desorption process from Ru(0001) crystal not induced by a heating of the sample, but as a consequence of irradiation with ultrashort laser pulses, as it offers a genuine way to look on the dynamics of the energy transfer between the substrate and the adsorbate as discussed in the Section 1.3.

The experimental setup for the measurement of laser induced desorption yield is sketched in Figure 3.6. A laser beam from the amplifier system is focused on the sample, whereas its intensity
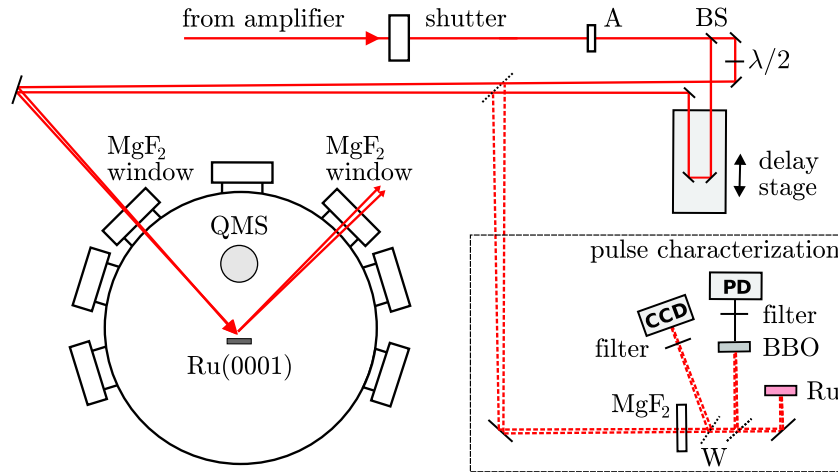
Figure 3.6.: Experimental scheme of the laser induced desorption yield measurement. The beam from the amplifier can be either guided directly to the sample or split into two parts with a variable time delay. Desorption from Ru(0001) is followed by the QMS, pulse shape is recorded with a CCD camera prior to each measurement, pulse length is determined from an autocorrelation. To avoid the sample damage the laser pulse with the desired intensity is sent to a reference Ru(0001) crystal first. (A = attenuator; BS = beam splitter; $\lambda/2$ = wave plate; PD = photodetector; W = glass wedge).

can be varied by an attenuator consisting of a $\lambda/2$ wave plate and a thin–film polarizer. This solution is preferred over an arrangement involving optic filters, because it allows a continuous power modulation without a need to change the optic path and the homogeneity of the beam profile is affected less. Depending on the experiment, the beam can either travel directly to the sample, or can be split into two nearly equal parts by a beam splitter. As they travel along different paths, their relative delay is set by moving a delay stage. The two beams overlap on the sample. A flip mirror marked by a dashed line in the Figure 3.6 is used to divert the beam(s) into the reference path. Its distance from the sample in the chamber is exactly equal to the distance to the reference crystal, CCD camera and nonlinear BBO crystal used to find the temporal pulse overlap on the sample. In this part of the experiment all essential laser parameters are determined prior to each single measurement.

Yield–weighted fluence   The autocorrelation measurement used for the pulse length characterization was examined in detail in Section 2.2.3. In the same Section also the spatial intensity distribution of the employed pulses was shown, exhibiting a Gaussian beam profile. It is evident that the simple use of overall laser intensity (that varies across the beam) as a measure

of deposited energy would not correspond to the actual situation on the sample surface, where different parts of surface experience an irradiation with different energies, which will lead to a different desorption yield depending on the relative position of a (infinitesimally small) sample part within the beam. One way to express the real amount of energy deposited across the Ru(0001) surface with a physically meaningful quantity, taking into account that the desorption yield is a function of absorbed laser energy is to introduce the *yield–weighted fluence*, $\langle F \rangle$. The measured beam profile image can be evaluated pixel by pixel and an intensity can be assigned to each of them depending on their relative contribution to the total beam power. Further, the contribution of the pixel i to the total yield w_i is calculated as

$$w_i = Y_i \propto F_i^n \tag{3.17}$$

where the exponent n expresses the (possible) nonlinear dependence of the reaction yield on the absorbed fluence F_i. Weighting the assigned intensity (fluence) with its relative contribution to the total desorption yield leads to

$$\langle F \rangle = \frac{\sum_i w_i F_i}{\sum_i w_i} = \frac{\sum_i F_i^{n+1}}{\sum_i F_i^n} \tag{3.18}$$

Usually, the constant n is not known and must be estimated experimentally from a series of measurements where the fluence of the arriving beam is varied and the induced yield (first–shot yield) estimated (see Section 6.1.1). If the obtained data (yield vs. non–weighted fluence) are plotted and fitted by a power law, a first guess (iteration) for the n is obtained. The fluence is than in next steps weighted with the obtained factor (and plotted as yield vs. yield–weighted fluence), until self–consistency is reached in this iteration process, i.e. the power of the fitted power law equals to the exponent used to calculate the value of the yield–weighted fluence.

Estimating the desorption yield The laser induced desorption yield can be recorded by a quadrupole mass spectrometer (QMS) as a total current caused by the desorbed species, ionized and detected in the secondary electron multiplier (SEM). However, a lot of information gets lost in this process as only a number of arriving ions integrated over the whole desorption time can be extracted from the data. A scheme of a more sophisticated setup, allowing to measure a time–of–flight (TOF) spectrum of the desorbed species and thus their kinetic energy is shown in Figure 3.7. As the repetition rate of our laser system is with 400 Hz still too high to distinguish between desorption induced by single pulses, its frequency is decreased by a factor of 20 in the pulse–picker[10] (see Section 2.2.1 on page 77). Integrating a fast shutter into the beam path allows to reduce the frequency even further and to block all pulses except of the desired one. The opening signal for the shutter is sent from the computer synchronized with the laser trigger so that only one whole pulse can pass. The trigger also starts the data acquisition on the multichannel scaler (Stanford research systems SR430). After the pulse arrives at the sample, desorption is induced and desorbed molecules fly towards the ionization volume. The flight time depends on their mass and velocity, but usually does not exceed several hundreds of µs. Molecules ionized in the QMS spectrometer are detected by the SEM in an identical form as in the retarding–field analyzer (discussed in Section 3.4.3): the pulses representing high voltage breakdown on the highly resistive layer are obtained, with a width of approximately

---

[10]The advantage of this step is obvious: the alignment in the regenerative amplifier optimized for 400 Hz is preserved and rejecting the pulses just before they enter the multipass amplifier has the advantage of not loosing a substantial amount of available power. The energy of the single pulses is correspondingly high, so that this frequency is never employed to pump the TOPAS.
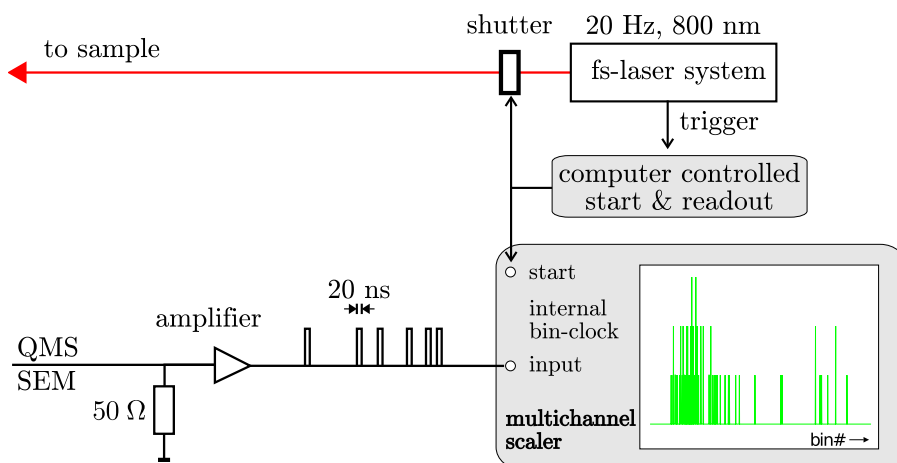
Figure 3.7.: Experimental scheme of the time–of–flight measurement.

20 ns. Those signals are amplified and recorded as 'events' in the multichannel scaler. This device has started the acquisition with the trigger that arrived before and counts the number of 'events' emerging on its input within a narrow time window of 0.16 µs determined by an internal clock. This represents the smallest time step (and hence the best molecular translational energy resolution) achievable in our setup. A curve as in Figure 3.7 is read out from the multichannel scaler by the computer, containing the information about the *amount* of desorbed molecules as well as about the *time–of–flight* (i.e. kinetic or translational energy) of the arriving species.

First shot yield   Let us first examine the desorption yield in a more detail. How to express the desorbed amount of molecules induced by a single pulse of a given fluence in a reasonable quantity like e.g. coverage? If the fraction of desorbed species would be known, this number would also have the meaning of the desorption probability upon single pulse irradiation. To obtain it, one can simply repeat the procedure introduced above and measure the time–of–flight spectra for several (usually 20–50) laser shots. The curve constructed by integrating the data and plotting them against the laser shot number is then similar to that shown in Figure 3.8. Obviously, from the plot one can not only estimate the total signal that would be produced if all molecules would desorb after a single pulse (area of the blue bars), but also the pulse–to–pulse laser intensity variations can be compensated if a model curve is fitted to the data. The model is based on an Arrhenius–like expression for the desorption process and in case of a first–order desorption this corresponds to an exponential decay (shown as a black curve in Figure 3.8). It is introduced in a more detail in Section 6.1.1 together with the discussion of the experimental data, as it contains more information that can be extracted to characterize the particular system, which is out of the focus of the current Section.

Translational (kinetic) energy distribution   If now the additional information contained in the time–of–flight spectrum should be evaluated and converted e.g. to the kinetic energy distribution, several aspects have to be considered.

   The kinetic energy of a particle can be calculated from its mass and velocity. As the mean free path of a particle under UHV conditions amounts to several hundreds of kilometers, collisions with the particles present in the background and along the path to the QMS ionization volume can be safely neglected. The velocity of a desorbed molecule can be hence calculated from the
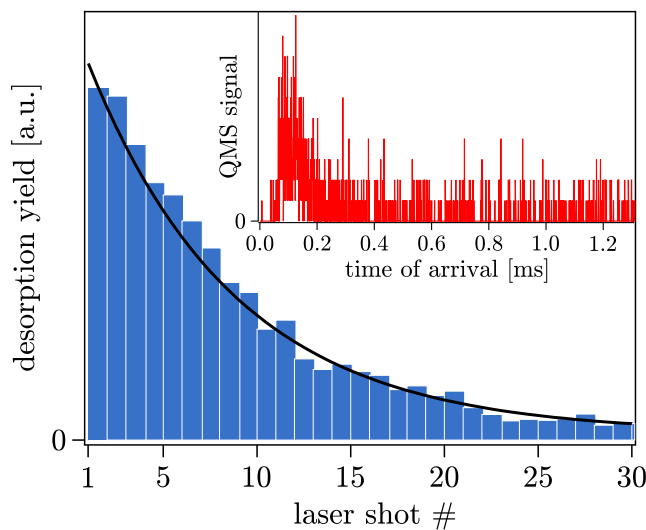
Figure 3.8.: Desorption yield as a function of the laser shot number. Blue bars show the time integral of the corresponding TOF spectrum (inset). The decay shows the depletion of the amount of adsorbed species on the surface and is fitted by a curve corresponding to the first order process (see text).

direct sample–ionization volume distance (QMS ionizer is usually spatially very localized) and the time needed to reach it. The latter quantity is not directly known – the TOF spectrum (yield vs. arrival time) always contains an offset, arising from the additional time needed to detect the ionized molecule. This is different for every particle mass and depends on many factors that are hard to quantify exactly. Nevertheless, it is possible to estimate it experimentally in a reliable way. For this purpose a low pressure of desired gas is created in the chamber background and the laser beam focused exactly into the ionization volume. If the ionizing current is switched off, the recorded signal arises only from molecules ionized by the laser with a nominal flight time equal to zero. The observed detection time can be hence considered as the offset caused by flight time in the quadrupole system and the response time of the whole electronic setup. In this way the time axis of a TOF spectrum can be corrected.

It is a bit misleading that the time–of–flight spectrum is not the same as the time–of–flight distribution [Zim94, Zim95]. To obtain the latter, one has to consider the different residence time of molecules with different velocities in the QMS ionization volume, which results in a lower detection probability of the fast species. If the measured spectrum is represented by $S(t)$, the TOF distribution $I(t)$ will be proportional to $I(t) \propto t^{-1}S(t)$. The function $I(t)$ physically represents the detected flux of molecules versus time. In an infinitesimal time interval dt the number of molecules passing the ionization volume is $I(t)dt$, which is equal to the number of molecules with the corresponding velocity ($v = r/t$) described by the velocity distribution $P(v)$, so that one can write

$$I(t)dt = P(v)dv \tag{3.19}$$

Using the identity[11] $|dv/dt| = r/t^2$ gives

$$P(v) = \frac{t^2}{r}I(t) \propto \frac{t}{r}S(t) \tag{3.20}$$

---

[11]The use of the absolute value (Jacobi–determinant) is justified, as the flight direction does not play a role in this consideration. Moreover, a negative velocity distribution is not a physically meaningful concept.

where r is the flight distance. Usually, the velocity distribution of the desorbing molecules is Maxwell–Boltzmann like (desorption from one site, or a single reaction channel), and can be described by the flux–weighted v^3 Maxwell distribution that has the form

$$P(v)dv = \frac{1}{2}\left(\frac{m}{k_B T}\right)^2 v^3 \exp\left(-\frac{mv^2}{2k_B T}\right)dv \tag{3.21}$$

where T is the translational temperature related to the mean translational energy via the expression $\langle E \rangle = 2k_B T$ and m is the molecular mass.

For the routine data evaluation the equations 3.20 and 3.21 are combined. As mentioned above, the time–of–flight spectrum is measured for 20–50 laser shots, each containing the same information. Their sum is thus fitted to the function

$$S(t) = A\frac{d^3}{t^4}\exp\left(\frac{-mr^2}{2k_B T(t - t_0)^2}\right) \tag{3.22}$$

where A is a setup specific proportionality factor. It contains most notably the detection probability and is dependent on the solid angle of the detection.

Fluence dependence and the two–pulse correlation The experimental setup for the measurement of laser induced desorption yield is rather versatile and can be employed for two types of measurements. First is the fluence dependence, where a TOF spectrum is measured for various fluences up to the damage threshold of the Ru(0001) crystal. All desorption experiments are performed on 1 BL of water that is prepared as described earlier (Section 2.1.3, page 70). To gather as many data points as possible, the beam is focused on the sample so that up to 7 independent measurements in only one preparation can be performed in different separated regions of the crystal. Positions on the Ru(0001) surface are changed by moving it in the plane perpendicular to the surface normal (and thus surface–QMS ionizer direction). The same focused beam enters also the reference beam path where its properties (i.e. intensity and profile) are measured prior to every TOF sequence (up to the spot depletion).

Measurement of the two–pulse correlation (see Section 1.3.3) resembles the fluence dependence measurement. Here the original pulse of a given fluence that is fixed throughout the measurement is divided into two parts that reach the sample with a variable time delay. To avoid their interference close to their temporal overlap, the polarization of the delayed pulse is changed by a $\lambda/2$ wave plate. Additional effort is required to ensure the optimal spatial and temporal overlap at the sample surface, this is however facilitated by a very narrow angle between the two pulses, so that they effectively overlap on a rather large distance. Both beams are characterized separately before every measurement. In the data evaluation the difference in the absorbed energy for both polarization is considered. The intensity loss caused by reflections on the MgF$_2$ window of the UHV chamber is estimated to 10 %. The described measurements applied to the D$_2$O/Ru(0001) system together with a detailed interpretation can be found in Chapter 6.

3.2.3. SFG spectroscopy

The substantial part of phenomena investigated during this thesis are connected to molecular vibrations at interfaces, therefore the SFG spectroscopy (introduced in the Section 3.1) is the most appropriate method to study them. Many details of such an experiment have already been introduced – the sample preparation is treated in the Section 2.1.3, the generation of

ultrashort IR and UV pulses is discussed in Sections 2.2.2 and 3.3, respectively. The actions in between, especially the light path from the laser to the detector, is schematically depicted in the Figure 3.9.
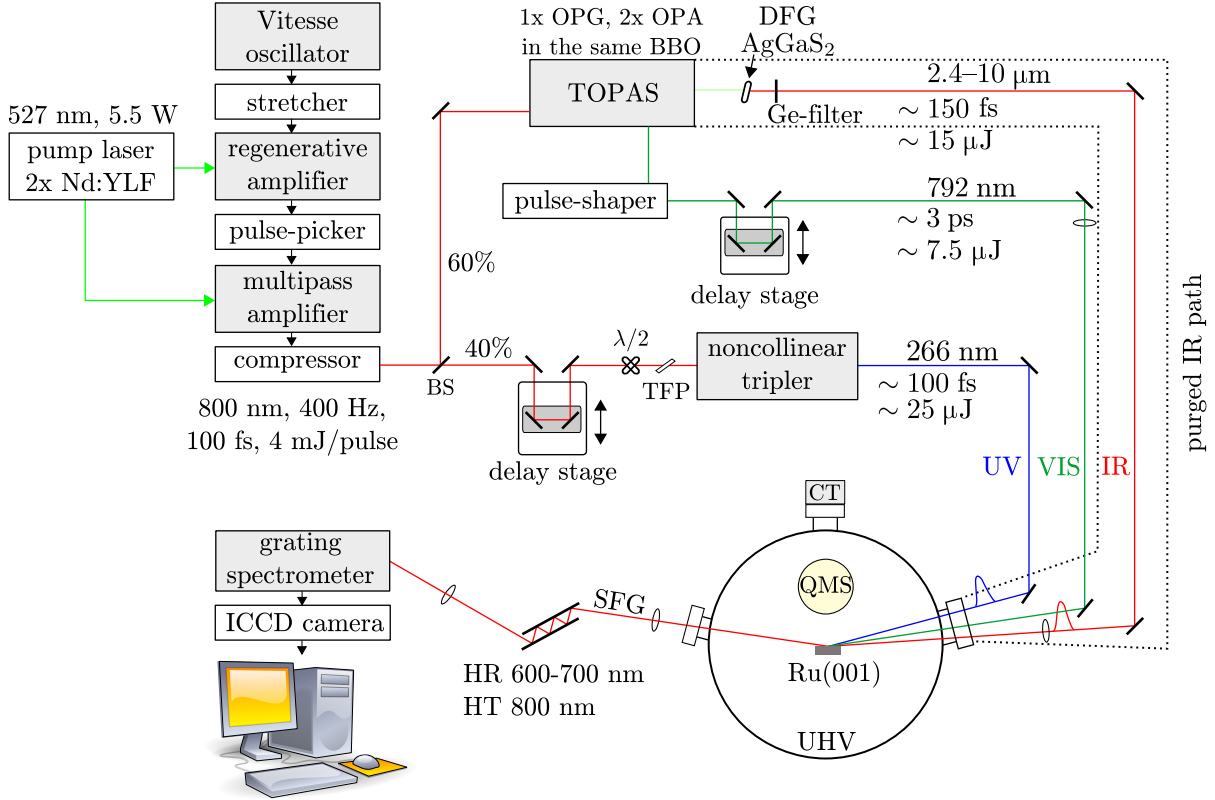
Figure 3.9.: A scheme of the employed laser system with the SFG beam path.

The SFG beam path

The IR and VIS light do not leave TOPAS with the same delay, as the last OPA process has a larger efficiency when pumping light arrives earlier than the signal and idler photons. This temporal difference has to be compensated, which is achieved by a different path lengths for both beams. The fine tuning of the overlap can be accomplished via a delay stage that has been implemented for most of the time in the VIS beam path.

To achieve the highest possible SFG yield, the beams are focused on the sample, which locally increases their intensity. The investigated ice layer on Ru(0001) surface is much thinner than the wavelength of the employed light, therefore the efficiency of the SFG process can not be optimized by increasing their Rayleigh length, as it is common in a macroscopic nonlinear or laser media. It is rather desired to design the beam path in a way that the maximum intensity is focused into smallest possible area, i.e. to use short focal lengths. Therefore, the CaF_2 lens for the IR beam is placed very close to the CaF_2 window that serves as the optical input into the UHV chamber. As in the Gaussian beam propagation theory the beam radius in the focus (ω_f) is proportional to the product of the beam wavelength (λ) and the focal length of the lens (f)[Dem08]:

$$\omega_f = \frac{\lambda f}{\pi \omega_o}, \tag{3.23}$$

putting the lens for the VIS beam to the same distance would result in a much smaller (approximately 5×) spot size[12] on the sample, if the initial beam radii ω_0 are identical. For this reason, the lens focusing the visible up–conversion light has a correspondingly larger focal length and is placed further away from the sample.

The light output from the TOPAS keeps the horizontal polarization given by the input beam unchanged. To create the maximal field intensity at the surface it is therefore reasonable to choose a possibly flat angle of incidence. Both beams, overlapped temporally and spatially reach the Ru(0001) crystal under an angle of $\sim$75° to the surface normal. Due to the momentum conservation (or phase matching condition), under a similar angle the SFG light will leave the chamber. The energy conservation determines its wavelength $\lambda_{\mathrm{SFG}} = (1/\lambda_{\mathrm{IR}} + 1/\lambda_{\mathrm{VIS}})^{-1}$ to be in the range between 645 and 685 nm for 2000 to 2800 cm^{-1} infrared and 792 nm up–conversion wavelength.

The intensity of the generated SFG light is many orders of magnitude lower than the intensity of the input beams. As the wave vector of the up–conversion pulse is also much larger than the wave vector of IR pulses, the SFG beam of minute intensity will travel over a long path with the intense VIS beam. Nevertheless, neither a long distance is sufficient to separate them, as even the visible stray light will still overwhelm the sensitive detection device. The use of edge or notch filters is inconvenient, because they rarely transmit more than 90 % of light at frequencies that should be transmitted and one pass is not enough to get rid of the up–conversion light. A very successful idea was to use reflective optics – mirrors with an optical coating transmitting the beam at 800 nm but reflecting the SFG wavelength almost completely. A pair of them can be arranged as shown in the Figure 3.9, providing several reflections at once, which is very convenient for the spatially restricted detection beam path.

Finally, the SFG light is dispersed in a classical grating spectrometer (Triax 320, Horiba Jobin Yvon)[13] and imaged on the chip of the intensified charge–coupled device (ICCD) camera (Princeton Instruments, 576 G/PE–E). This instrument consists of a low–noise CCD circuitry placed behind an image intensifier. Photons entering the camera first generate electrons via the photoemission from a photocathode. A micro–channel plate is attached behind it to amplify the photocurrent while preserving the spatial information about the photon impact. Due to the secondary emission intensified electron beams impinge on a fluorescent screen that is imaged and digitalized via the CCD. To reduce the noise level, the whole device is cooled with a Peltier element. However, the design of the ICCD allows a much better noise suppression: the image intensifier works very much as the channel electron multiplier (CEM) introduced earlier and for the signal amplification in electron cascades it requires high voltages as well (900 V in this case). Such a voltage can be applied for a very short time ($\approx$5 ns), limiting the whole detection to this narrow time window. As the repetition rate of our laser system is 400 Hz and the SFG pulse duration is lower than 200 fs, most of the time only noise would be detected by a continuously working detector. It is hence very convenient in our situation to apply the high voltage only for 20 ns synchronously with the laser trigger arriving to the camera. This setting also allows to measure the low intensity SFG signal and helps to suppress the remaining part of the VIS stray light, as it usually travels over a different distance and hence possess a longer delay with respect to the trigger.

It would not be possible to align the invisible beam paths without a reliable reference path that

---

[12]Note, that the area of such a beam – which is obviously the more important quantity – would be then 25× smaller.

[13]It should be mentioned, that the SFG light always exhibits a spatial chirp due to a different phase matching condition for different up–converted IR wavelengths. In some cases, if the designed detection beam path is long, this dispersion can be even used instead of a spectrometer [vdH98].

has been created similar to the previous case by a mirror that can be flipped and diverts the light right before it enters the chamber to a $LiIO_3$ crystal at the position analogous to that of the Ru(0001) single crystal. The whole SFG beam path has been rebuilt and realigned many times during this thesis. Only a minute optimization of the laser system output, e.g. by tuning the overlap of the pumping beams in the multipass amplifier, causes severe deviations from the optimal path of the beam due to the several tens of meters distance that the light has to travel until it reaches the sample. Nevertheless, with a good reference path it was always possible to restore the optimal setup after only several hours.

Apart from maintaining and small improvements made in the existing SFG setup, some completely new features have been added.
The non–collinear optical frequency tripler introduced in the Section 3.3 considerably enhances the ability of the existing setup to investigate processes which are triggered by larger photon energies. Apart from the used 4.66 eV, photons with energies 3.1 eV and 1.55 eV (the input wavelength) can easily be coupled out and are even available simultaneously. The tripler exploits as its input a part of the amplifier output that is not used in TOPAS. The pulses have to be delayed considerably to arrive at the sample at the same time with the IR pulses as the distance the light passes in TOPAS is large. The final temporal overlap is adjusted precisely via a motorized delay stage (Physik Instrumente, PI M-535) and found by maximizing the photoemission signal on the sample as it is described in Section 2.2.3 for their cross–correlation measurement. For fluence dependent measurements the beam intensity has to be changed smoothly and neither the optical path of the beam nor its shape should be affected. A similar arrangement of the $\lambda/2$–waveplate and the thin–film polarizer as in the desorption yield measurements has been used to attenuate the light before it enters the tripler.

A further major improvement was the design and construction of a transparent cover that allows to purge the IR beam path with dry nitrogen. Apart from structural differences discussed in the Section 1.1.3, one reason to investigate D_2O ice layers rather than H_2O is the presence of water vapor in air, which absorbs in almost the same wavelength region as water adsorbed on a surface. If the beam path is not under vacuum or enclosed and continuously purged, such a measurement is not possible. However, unfortunately even in the D_2O region, the asymmetric CO_2 stretch complicates the reliable detection of all resonances. As this problem hindered us to unambiguously confirm a key conclusion derived from the data presented in Chapter 5, the SFG beam path has been shortened considerably, enclosed in a transparent housing and purged with the dry nitrogen. The possibility to control selected optical components remotely has been added as well. Considerable effort has been put into the designing of possible beam inputs, as many beams have to cross or enter the same optical path. Also the TOPAS is not proposed to be a part of such a setup. Figure 3.10 is intended to graphically present the capabilities of the final version of the purged beam path. In the CO_2 absorption region the measurements could be performed as if no trace of this gas would be present and even our best resolved data averaged over large number of scans did not exhibit its signature. This is of particular interest, because the opened frequency window bears a substantial part of the fully coordinated OD stretch resonance of amorphous and the very important fully coordinated asymmetric OD stretch of crystalline ice.
Measurements in the H_2O absorption region (around $3100\,cm^{-1}$) were possible as well, although the intensity of the IR radiation in this case was rather small. Water exhibits a very broad and intense absorption band between 2800 and $3800\,cm^{-1}$ and its extinction coefficient in this region is larger than that of CO_2 in its maximum absorption range. Together with the fact, that the H_2O content in air is much higher the CO_2 abundance, this shows the limits of a method based
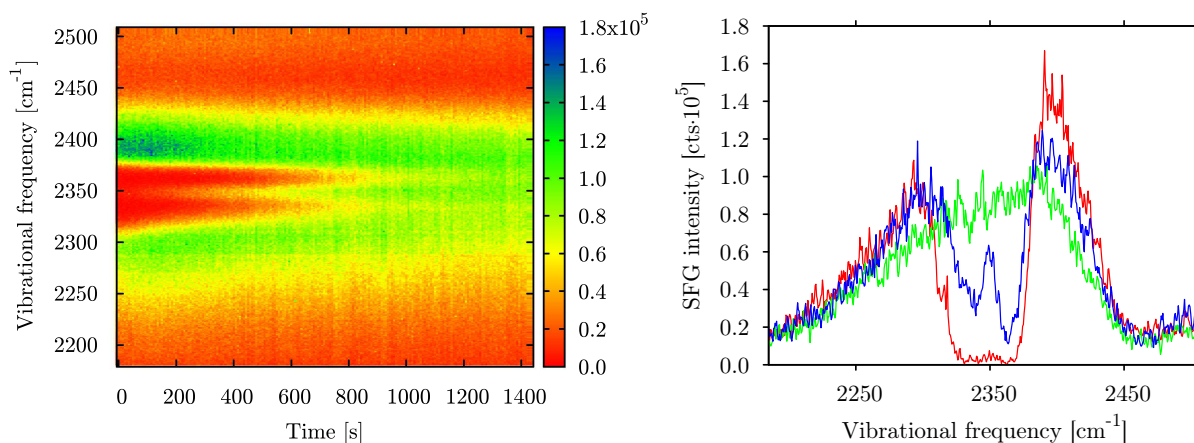
Figure 3.10.: Evolution of the IR spectrum during the nitrogen purging. In the left part the spectra are collected in the real time and compiled into 2–D plot, the right part displays a vertical cut through this data and shows the shape of the IR intensity distribution without purging (red), an intermediate state during the purging (blue) and the final state (green), which provides an evidence that the CO_2 signature could be completely removed.

on a dilution of contaminating gas by another gaseous substitute.

In any case, the described beam path offers an excellent infrastructure for SFG measurements and the presented modifications enhance its capabilities greatly, so that all intended measurements could be performed and data of high quality was obtained.

Performing an SFG measuement

While the sample is prepared (as described in Section 2.1.2) and the dosing system is cleaned (Section 2.1.3), the laser beam quality is checked and the TOPAS settings are changed to produce the desired wavelength (Section 2.2.2). The spatial and temporal overlap can be first checked in the reference beam path.

After the sample is clean and in thermal equilibrium with the cooled cryostat head, ice layers can be dosed (Section 2.1.3). On the ice covered Ru(0001) surface the final check of the detection path and temporal/spatial overlap is performed. During the measurement, the sample is located in front of the ionization volume of the QMS. This position can not be fixed exactly, therefore deviations of the order of several tens of µm can arise. Their compensation by small adjustments of the beam overlap is straightforward. The check of the perfect spatial and temporal match of the IR and UV pulse is performed at this stage as well.

Following the characterization phase, the sample is shortly heated to 1530 K and a well defined D_2O layer is prepared on the surface. The total coverage is controlled via the dosing time that has been calibrated before and checked after each measurement by a TDS. This method is preferred even in measurements, where the ice coverage is continuously varied and an SFG spectrum could be taken simply along with the TDS, obtaining all data in a single run. The drawback of the latter method lies in the thermal properties of the sample holder – the Ta wires providing the resistive heating during the temperature ramp do not fix the sample tightly and their thermal expansion leads to a small change in the sample angle. Due to the natural spatial chirp of the SFG beam mentioned above, this could have severe consequences for the quality of the data. Along with the evolution of the sample holder, as the twofold bended wires have been

introduced (see Figure 2.3), this problem disappeared, nevertheless, such a measurement was performed only if the angular stability has been proven several times prior to every experiment. After each measurement completed by a TDS, the sample was exposed to the IR and VIS beam once again and a spectrum from the bare surface was measured as a reference (non–resonant background). The obtained data have been evaluated after the spectrometer system calibration following the procedure described later on page 105.

Calibration of the ICCD spectrometer

The infrared spectrum of the adsorbate/vacuum interface can be in principle obtained from an SFG spectrum easily, if the SFG and the up–conversion wavelength are exactly known. However, often the required precision is hard to achieve, as already small errors ($0.2\,$nm) in the VIS or SFG wavelength estimation decrease our resolution dramatically ($5\,$cm^{-1} at $640\,$nm). An optimal way to circumvent this problem would be a suitable reference in the IR wavelength range that could be used in the measurement as a marker. In the frequency region of the coordinated OD stretches it is reasonable to exploit the asymmetric stretch resonance of CO_2 in air before it is completely removed by purging. Although the broad band covers several tens of wavenumbers, it exhibits a narrow dip at $2349\,$cm^{-1}, where SFG light can be detected [Nie45] (see also Figure 3.10). To obtain a fixed frequency point in the free OD region, a gas cell was inserted into the beam path and filled with diluted CH_4 that possess known absorption bands around $2740\,$cm^{-1} and a difference SFG spectrum has been recorded with and without the gas inside. Based on the overlap with a reference data set from the literature, an exact vibrational frequency of $2730.5\,$cm^{-1} could be assigned to the narrow free OD resonance that emerges if several amorphous ice multilayers cover the Ru(0001) substrate [Den03a].

Knowing the actual frequency of those two markers, all other frequencies in the region of interest can be determined. Their position relative to the calibrated points can be calculated from the characteristics of the ICCD camera/spectrograph system. In the SFG wavelength range, Ne gas discharge lamps (Pen–Ray, LOT Oriel) have been used to characterize the spatial distribution of wavelengths on the ICCD chip. The obtained calibration curve is plotted in the Figure 3.11. Every time the TOPAS settings have changed and the spectrometer grating has been moved, this calibration has been rechecked to eliminate the possible error in pixel–wavelength assignment, which may appear due to the small changes in the angle of the mechanically moved grating[14]. After that, the pixel position is converted to wavelength with high accuracy and from the infrared marker, which is appears at a known SFG wavelength, the true up–conversion frequency is calculated. Its value is used for the calculation of all other frequencies. The error in the obtained frequency is estimated to be lower than $1\,$cm^{-1} in the vicinity of the marking points and does not exceed $5\,$cm^{-1} in the whole frequency range.

Evaluation of the SFG spectra

In the Section 3.1, a purely theoretical approach yielded the following expression for the SFG intensity (cf. Equation 3.14):

$$I_{SFG} \propto \left| A_{NR}(\theta)e^{i\phi_{NR}} + \sum_q \frac{A_q e^{i\phi_q}}{\omega_{IR} - \omega_q + i\Gamma_q} \right|^2 I_{VIS} I_{IR} \tag{3.24}$$

---

[14]In fact, a small shift from the perfect position was only observed if the spectrometer gratings have been changed (three gratings are mounted inside, automatically interchangeable with each other) and the instrument readjusted their positions. The mechanical latch, used as a reference position for the maximal angle, unfortunately allows such a deviation.
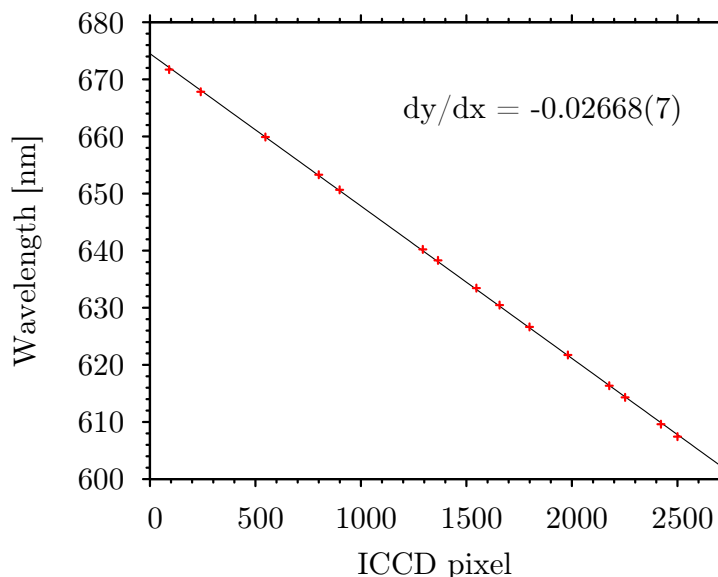
Figure 3.11.: The calibration curve of the ICCD camera/grating spectrograph system. The pixels of the ICCD camera are arranged in such a way that they reflect the energy axis. Wavelength range of $1\,\mathrm{nm}$ (corresponds in the OD stretch region to $\approx 23\,\mathrm{cm}^{-1}$) is imaged on 37 pixels.

The real constants A, ϕ, ω and Γ denote the amplitude, phase, frequency and damping factor (half width at half maximum) of the corresponding resonance, respectively. Despite of numerous approximations accepted during the derivation of this relation, it describes the measured SFG spectra very well [Arn10, Bai95, Bon00b, Bon01, Bon05, Che02].

Line shape of a SFG resonance The vibrational resonances are assumed to possess a Lorentzian line shape, as this is the most common solution of the equation of motion with a simple damping inclusion (for details see Section 3.1). This 'line profile consistency' allows to extract the vibrational transition from this model in a similar form as in the more conventional absorption or emission spectroscopy. However, the introduced idea of the $\chi^{(2)}$ tensor as being the sum of the non–resonant (NR) and resonant part allows their combination in this non–linear case. In many situations the resonant contribution is the dominant one and the non–resonant part can be neglected. However, when a vibrational mode has a very low amplitude or is damped strongly (as it is found in our data), its contribution may become comparable to the NR term, which causes interference between those two parts and results in a Fano–shaped intensity profile [Fan61]. The best way to visualize this interference is to use an alternate form of Equation 3.24 and for simplicity first assume only one resonance being present in the underlying system. We obtain:

$$
\mathrm{I_{SFG}} \propto \left[\left(A_{\mathrm{NR}} + \frac{A_1 \Gamma_1 \sin(\phi)}{(\omega_{\mathrm{IR}} - \omega_1)^2 + \Gamma_1^2} + \frac{A_1(\omega_{\mathrm{IR}} - \omega_1)\cos(\phi)}{(\omega_{\mathrm{IR}} - \omega_1)^2 + \Gamma_1^2} \right)^2 \right.
$$
$$
\left. + \left(\frac{A_1(\omega_{\mathrm{IR}} - \omega_1)\sin(\phi)}{(\omega_{\mathrm{IR}} - \omega_1)^2 + \Gamma_1^2} - \frac{A_1 \Gamma_1 \cos(\phi)}{(\omega_{\mathrm{IR}} - \omega_1)^2 + \Gamma_1^2} \right)^2 \right] I_{\mathrm{VIS}} I_{\mathrm{IR}} \qquad (3.25)
$$

Now, inspecting the expression in the square brackets reveals important facts about the possible SFG line shape. If the phase ϕ equals to $\pm\pi/2$, the cosine terms vanish identically. The resonant

and the non–resonant part on the first line is either added or subtracted, but the Lorentzian shape is preserved, even though the peak will appear as a *decrease* in the total SFG intensity in the latter case. The term on the second line can be neglected in this consideration as it vanishes close to the resonance due to the damping factor. In a non–realistic scenario it could cause a small, symmetric peak broadening if the Γ was very small.

Setting the ϕ to 0 (π) leads to slightly more complicated behavior: the SFG intensity decreases (increases) as the light frequency (ω_{IR}) approaches the resonance frequency (ω_1), remains unchanged if those frequencies match and increases (decreases) for larger photon energies. Due to the second term, which always increases the total intensity, the point symmetrical curve could theoretically loose this symmetry. As the key factor determining the final shape of the spectrum is mainly the amplitude of the NR part, under the conditions of interest ($A_{NR} \approx A_1$) the influence of the second term can be neglected as well.

The possible line shapes, representing each of the discussed situations, are depicted in the Figure 3.12. The probably most striking difference to the conventional linear spectroscopy is the

$$\phi = \pi/2 \qquad\qquad \phi = 0 \qquad\qquad \phi = -\pi/2$$
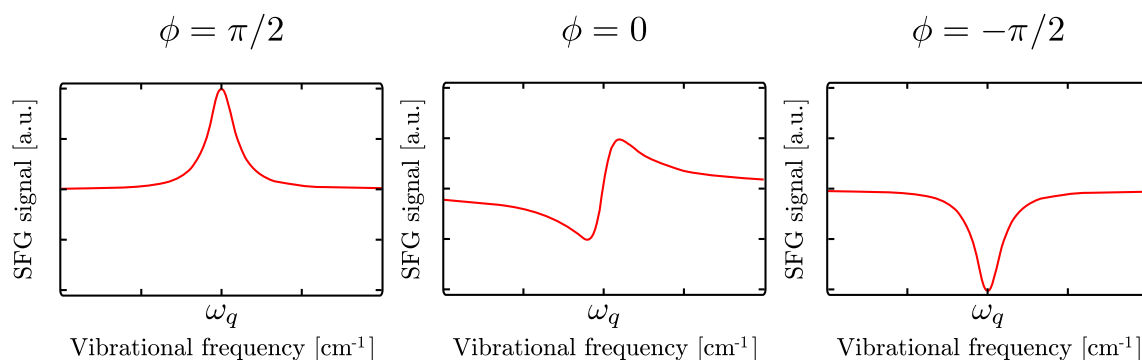
Figure 3.12.: Possible SFG line shapes for different values of the resonant phase (ϕ).

actual spectral position of a resonance in the SFG spectrum: it may appear at a frequency, where no resonant signal change can be observed (see the situation for $\phi = 0$). It is also obvious, that the spectral information is very hard to extract intuitively during the measurement and often only the consequent fitting procedure can provide one with the spectral parameters of interest. Moreover, as can be seen from Equation 3.24, the spectrum consists of convolution of the VIS and IR intensities as well, which presents a further complication.

Fitting the SFG data The obtained SFG data was fitted using commercial software (Igor Pro 6), employing self–developed procedures and using the built–in Levenberg–Marquardt algorithm for solving non–linear curve fitting problem via the least–squares method. The non–resonant background signal could be substituted in place of the convolution $I_{VIS}I_{IR}$ as it is proportional to the same. The unknown fitting parameters constitute the effective $\chi^{(2)}$ value as discussed above. The fitting Equation 3.24 has been modified slightly in order to assign a more defined physical meaning to the obtained values:

As the NR component of the SFG signal often stems solely from the metal surface electrons, its phase ϕ_{NR} can be set to zero [Tad00]. In such a case, the resonant phases express the relative phase $\Delta\phi$ between the vibrational mode and the NR part.

For a more convenient definition of the resonant amplitude, the Lorentzian line can be normalized. It can be found, that $\int_0^\infty I(\omega)\,d\omega = 1$ if $I(\omega) = \Gamma/\pi \cdot 1/((\omega - \omega_0)^2 + \Gamma^2)$. Substituting the expression $A'_q\sqrt{\Gamma_q/\pi}$ for A_q in the fit equation therefore yields a set of parameters, where the

individual peak area (the SFG signal intensity) is simply $(A'_q)^2$. The modified relation reads

$$I_{SFG} \propto \left| |A_{NR}(\theta)| + \sum_q \frac{A'_q \sqrt{\frac{\Gamma_q}{\pi}} e^{i\phi_q}}{\omega_{IR} - \omega_q + i\Gamma_q} \right|^2 I_{VIS} I_{IR} \qquad (3.26)$$

The choice of A'_q has been made in this way, as it is now proportional to the number of oscillators in resonance with the exciting frequency (see Section 3.1) and can serve for a direct comparison to linear optical spectroscopies. Particular examples of the fits will be given later, along with results in Chapters 4 and 5.

3.3. Non–collinear optical frequency tripler

The posibility to exploit nonlinear optical phenomena to generate laser light with frequencies for which no suitable source is available was mentioned earlier in the Section 3.1. One such commercial device, TOPAS, was introduced in the previous chapter as a source of IR radiation. To obtain the light at the pump frequency of 266 nm, a non–collinear optical tripler has been designed, built and characterized in the framework of this thesis. Its simplified scheme is shown in Figure 3.13:
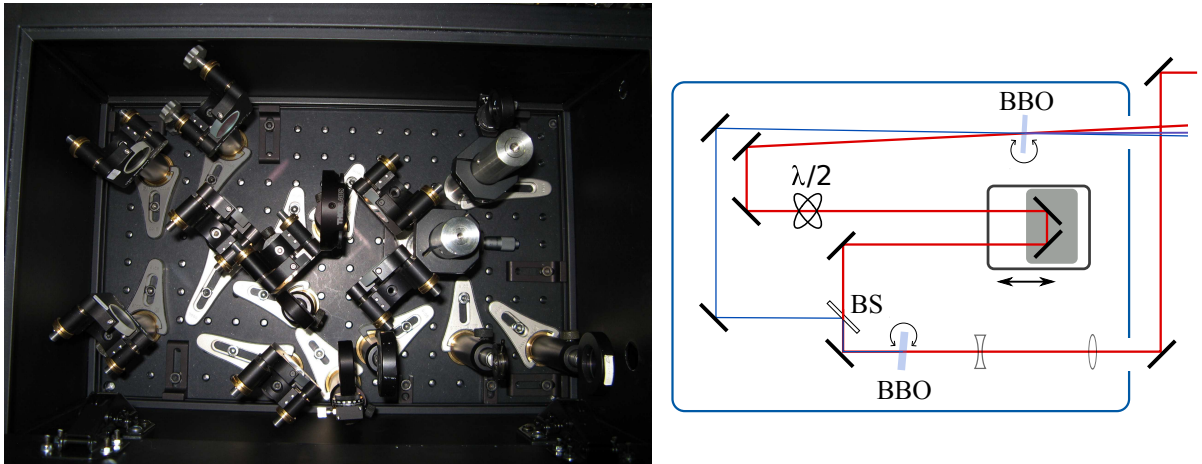
Figure 3.13.: Optical frequency tripler.

3.3.1. Design of the tripler

The input light is diverted from the amplified output of the laser system described in the previous Section. Approximately 1/3 of its power, corresponding to 0.45 W (1.12 mJ/pulse) have been exploited. The p–polarized, 800 nm light enters the tripler, where the beam diameter is first reduced in a simple telescope to approximately 50 % of its original size. At this size the beam intensity is close to the damage threshold of the employed anti–reflection coated mirrors. In the second step the input wavelength is converted in a BBO crystal with a conversion efficiency of approximately 20 % to 400 nm photons. The type I phase matching that necessarily applies in the SHG process if one linearly polarized beam is used, results in the s–polarized output wave (perpendicular to the incident electric field; see below). The two frequencies are further separated from each other by a dichroic beam splitter that is highly reflective for 800 nm and highly transmitting in the 400 nm region. The remaining part of the original beam is then guided through a delay stage and a $\lambda/2$–wave plate, where its polarization is turned by 90°. Both, now s–polarized beams are spatially and temporally overlapped in the second BBO crystal, where they create the desired p–polarized 266 nm beam. The conversion efficiency of the whole device after this last step is approximately 4.5 % which is up to 50 µJ/pulse of energy available for the experiment.

3.3.2. Phase–matching considerations

In designing any nonlinear optical device, special care has to be taken especially to choose the right nonlinear medium for all relevant processes. The choice of the BBO crystal is eligi-

ble for its high nonlinearity, birefringence and hence ability to obtain perfect phase–matching and particularly because of its transmission in the whole desired wavelength range down to 200 nm [Nik91, Rin93].

Apart from the proper choice of the crystal, there are several other important parameters that influence the conversion efficiency. All are in some way connected to the possibility to achieve a perfect phase matching in the BBO. It has been mentioned before (in Section 3.1) that the intensity of SFG or SHG radiation depends strongly on the wavevector (momentum) mismatch. In the microscopic picture, large mismatch corresponds to a geometrical arrangement of oscillating dipoles that leads to a destructive interference of photons of the sum–wavelength in the forward direction. In terms of physically meaningful quantities the dependence of sum–frequency intensity (I_{SF}) on the wavevector mismatch ($\Delta k = k_{SF} - k_1 - k_2$) can be expressed as [Boy03]:

$$I_{\mathrm{SF}} = \frac{8d_{\mathrm{eff}}^2 \omega_{\mathrm{SF}}^2 I_1 I_2}{\epsilon_0 n_1 n_2 n_3 c^2} L^2 \mathrm{sinc}^2(\Delta k L/2) \tag{3.27}$$

where d_{eff} is a constant, that for a fixed geometry and beam polarization corresponds to the effective part of the $\boldsymbol{\chi}^{(2)}$ tensor, L is the interaction length and n_x are the refractive indices of the medium at the wavelength of all participating beams. This formula predicts a strong decrease of the sum–frequency intensity if the phase matching is not optimally adjusted and $\Delta k = 0$ is not valid (see Figure 3.14(b)). However, under realistic conditions (normal dispersion) the equation

$$k_3 = k_1 + k_2 \Rightarrow n_3 \omega_3 = n_1 \omega_1 + n_2 \omega_2 \tag{3.28}$$

does not possess a solution for any ω–set as the refractive index increases with increasing frequency. Therefore while working with a negative uniaxial crystal[15] like BBO its birefringence is used to compensate the dispersion and to achieve the perfect phase matching.

If one considers the first frequency–doubling process in the tripler, the phase matching condition for the SHG process ($\omega_1 = \omega_2 = 800$ nm; $\omega_3 = \omega_1 + \omega_2 = 400$ nm) would necessarily require that $n_3 = n_1 = n_2$. This is clearly not achievable in an optically isotropic crystal where the dispersion must be taken into account. In BBO, assuming the same polarization of both beams propagating as ordinary rays, the indices are $n(800) = 1.66$ and $n(400) = 1.69$. An uniaxial anisotropic medium, however, offers two non–equivalent axes and hence two refractive indices for every wavelength, as can be seen from a set of empiric Sellmeier equations for BBO valid in the spectral range of interest [Eim87]:

$$n_{\mathrm{o}}^2 = 2.7405 + \frac{0.0184}{\lambda^2 - 0.0179} - 0.0155\lambda^2 \tag{3.29}$$

$$n_{\mathrm{e}}^2 = 2.3730 + \frac{0.0128}{\lambda^2 - 0.0156} - 0.0044\lambda^2 \tag{3.30}$$

Here λ denotes the wavelength in μm, n_{o} and n_{e} represent the refractive indices for the ordinary and the extraordinary ray[16], respectively. Assuming a beam that enters the crystal is linearly polarized, it propagates as an ordinary beam if its electric field vector oscillates perpendicular to the plane containing the wavevector k and the optic axis, i.e. it possesses no component parallel to the optic axis (see Figure 3.14(a)). The refractive index of such a beam is a constant (n_{o})

---

[15]An uniaxial crystal is a birefringent (optically anisotropic) crystal with one *extraordinary* optic axis along which the light propagation speed is different from the other two axes in the crystal coordinate system. A negative uniaxial crystal denotes a medium having refraction index in the ordinary axis larger than the refraction index along extraordinary axis ($n_{\mathrm{e}} < n_{\mathrm{o}}$).

[16]Extraordinary in this context describes a beam, that violates Snell's law of refraction. Even if it enters a birefringent medium parallel to the surface normal, it does not continue in a parallel direction, but is diverted.
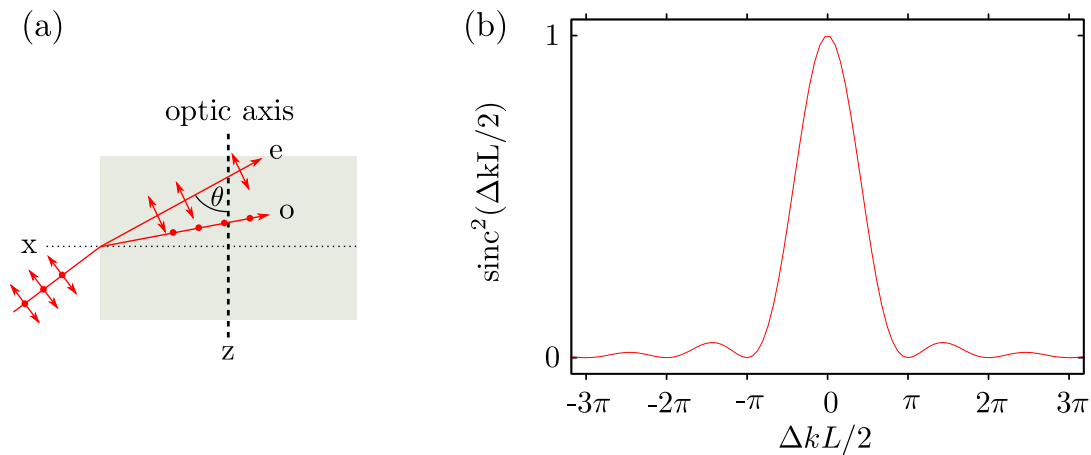
Figure 3.14.: (a) Directions in a birefringent crystal. Light entering a birefringent crystal always splits in two components: one perpendicular to the plane containing the wave propagation vector and optic axis (ordinary ray) and another oscillating in this plane (extraordinary ray). (b) The change in the output SF intensity as a function of the wavevector mismatch shows the extraordinary sensitivity of the desired output on the phase matching condition.

independent on the beam direction. In all other cases, the beam propagates as the extraordinary ray and has an index of refraction that depends on the angle θ beween the optic axis and the wavevector of the linearly polarized incident beam $(n_e(\theta))$. Changing this angle can therefore be used to "mix" the refractive index to a desired value required for the perfect phase matching. It can be found that the dependence of the refractive index on θ follows the equation [Bor75]:

$$\frac{1}{n^2(\theta)} = \frac{\sin^2\theta}{n_e^2} + \frac{\cos^2\theta}{n_o^2} \tag{3.31}$$

After its evaluation one can find, that if the condition $n(400) = n_o(800) = 1.66$ has to be fulfilled, the angle between the incident beam and the ordinary optical axis of BBO must be set to 29.2°. A very similar calculation has to be performed for the second nonlinear process in the tripler as well. Here we require that $n(266) = 1.68$, which is the case at an angle of 44.3°. These angles are not adjusted manually, but crystals with corresponding orientation are cut and used in the tripler.

In the previous case study, type I (or (*ooe*)) phase matching has been considered, as both input beams propagating in the ordinary direction possess the same polarization. However, in BBO type II (although only *eoe*) phase matching is equally possible due to the symmetry of the $\boldsymbol{\chi}^{(2)}$ tensor. Here the input beams possess a polarization perpendicular to each other and the crystal angle is adjusted to achieve a suitable refractive index for one input *and* the output ray in the extraordinary direction. Evaluating the equations above results in 60.6° as an optimal angle for such a process[17]. One drawback of such a scheme is the higher absorption cut–off of output frequency along the ordinary axis, however, at 266 nm this should not play a decisive role. In general, an advance of such a setup is, that less birefringence is needed.

---

[17]To calculate the value of θ for practical use, the walk–off angle of the input extraordinary beam has to be taken into account and the crystal has to be cut and oriented according to that slightly different angle.

3.3.3. Effective nonlinearity of the BBO crystal

An even more important quantity for estimating of the sum–frequency yield and choosing the right type of phase matching for experimental purposes is the effective nonlinearity constant d_{eff}. For BBO, belonging to the trigonal $3m$ crystal class, it can be calculated from the equations [Mid65, Kle03]:

$$d_{\text{eff}}^{\text{I}} = d_{31} \sin\theta - d_{22} \cos\theta \sin(3\phi) \tag{3.32a}$$

$$d_{\text{eff}}^{\text{II}} = d_{22} \cos^2\theta \cos(3\phi) \tag{3.32b}$$

for type I and type II phase matching respectively[18]. The angle θ has been introduced before as the angle between the optic axis and the wave propagation vector k. The ϕ is the azimuthal angle between the propagation vector and the xz crystalline plane, i.e. the angle between the projection of the wavevector into the xy plane and the x–axis. As a matter of terminology, usually the z–axis represents the optic axis. The nonlinear crystal can be cut either in the yz–plane or the xz–plane, leaving the xz or yz plane for beam propagation, respectively. In the first case, $\phi = 0°$ and therefore this orientation is optimal for type II phase–matching, as d_{eff} reaches its maximal value here, the second case provides then $\phi = 90°$ and is best suited for type I phase–matching. Substituting the known experimental parameters into the equations 3.32 and assuming optimal conditions for phase–matching of either type reveals a much higher SF yield obtained in the first case. The experimental values for the effective nonlinearity agree with the result suggested by this estimation and under given experimental conditions (wavelengths: output and second harmonic from a Nd:YAG laser; crystal thickness: 4.5 mm) amount to $1.75\,\text{pm V}^{-1}$ and $1.45\,\text{pm V}^{-1}$ for type I and type II phase matching respectively [Kle03, Arm96]. This justifies the choice of the *non–collinear* tripler setup, as such an arrangement allows one to exploit the BBO nonlinearity in desired wavelength range with far greater efficiency.

On the account of non–collinearity it should be added, that for a crystal oriented to match the proper value of θ, changing this angle has much less effect on resulting SF intensity than the change in azimuthal angle ϕ. Therefore a properly cut nonlinear crystal has to be rotated along only one axis, which greatly reduces the effort to maximize the output intensity. Consequently, if two beams are to be overlapped in the non–collinear tripler, the most convenient way is to let them propagate close in the plane defined by this rotation axis and the surface normal, since under these conditions the angle walk–off is negligible.

3.3.4. Employing ultrashort pulses

Equation 3.27 also suggests the independence of the strength of the output signal on the interaction length, but it is derived under the assumption, that the intensity of the SF light grows constantly within the whole interaction length and is not depleted by a reversed process ($\omega_3 \rightarrow \omega_1 + \omega_2$, see DFG in Section 3.1.1). Unconsidered is also the possibility, that the output wave can get out of phase with the driving polarization. Unfortunately, both is the case in thick BBO crystals and the efficiency of the three wave mixing is in fact lower, if L is greater than approximately $1/\Delta k$.

A further complication arises, when ultrashort pulses are used. Pulse duration is greatly influenced by the length of the path traversed through the nonlinear medium as can be seen from Figure 3.15. Although the pulses employed here are longer than those in the referred exper-

---

[18]The corresponding constants are $d_{31} = (0.16 \pm 0.08)\,\text{pm V}^{-1}$ and $d_{22} = (2.22 \pm 0.09)\,\text{pm V}^{-1}$ [Lid07]. Although available scientific papers all agree on form of Equations 3.32a and 3.32b, the data sheets of many crystal producers often offer confusing constant sets, nonexisting $\boldsymbol{\chi}^{(2)}$ elements and original, rather magic formulae for calculation of the actual d_{eff}.
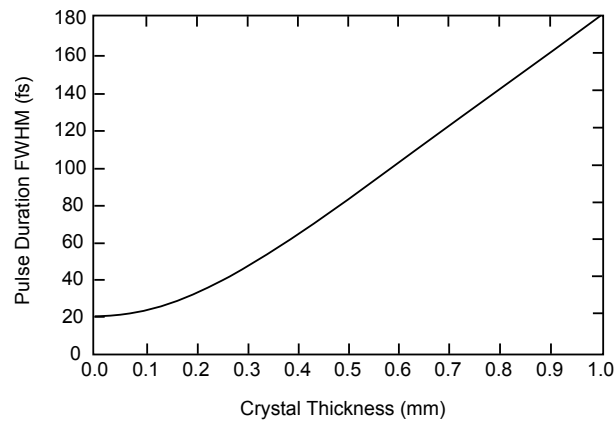
Figure 3.15.: A 30 fs short pulse is frequency doubled in a nonlinear BBO crystal. Plotted is the output pulse duration versus crystal thickness. Reproduced from Ref. [Liu94].

iment [Liu94], both the dephasing probability and the dispersion[19](causing the pulse length stretching) rapidly increase with decreasing wavelength. Therefore the nonlinear crystals used in the tripler possess a different thickness – 0.4 mm for the first, SHG process and 0.2 mm for the second, SFG process.

The pulse length characteristics of the tripler output beam is discussed in the more appropriate context in Section 2.2.3 on page 82, as the corresponding measurement requires exact knowledge of the temporal shape of the IR–sampling pulse as explained there.

With pulse duration below that of the input beam and the power sufficient to excite enough electrons from Ru into the ice overlayer, the tripler was successfully implemented into the working setup of the SFG experiment and played the crucial role in obtaining all the data presented in the Chapter 5.

---

[19]For the output extraordinary ray, the dispersion $dn/d\lambda$ amounts to $-0.0193\,\mu m^{-1}$, $-0.158\,\mu m^{-1}$ and $-0.694\,\mu m^{-1}$ for 800 nm, 400 nm and 266 nm, respectively.

3.4. Retarding–field analyzer

Water adsorbed on a metal surface may interact strongly with its electrons, as has been thoroughly discussed in Sections 1.1.3 and 1.3.3. This interaction is usually accompanied by a change in the work function (Φ) of the first metal layers, which indirectly reflects its strength. A crystalline ice monolayer on Ru(0001) surface lowers its Φ by 1.26 eV, which is a change of 25 %. Section 1.1.3 already stated that the binding of water to this surface is very strong compared to other metals, leading to the surface wetting and to a desorption temperature of 180 K. Even in the next layers, a difference of 0.2 eV in the work function is observed between the crystalline and amorphous structure of ice multilayers.

This high sensitivity of the work function to the type and structure of the adsorbate in general has served for example in many theoretical studies as a reference value, that each plausible adsorbate structure must agree with [Gal09, Men05]. But the work function change has a similar significance in experimental studies as well, since it provides a very sensitive measure of structural changes, that would in the water case peak for the perfect ice XI – a ferroelectric structure – in a massive $\Delta\Phi$ of approximately 2.1 eV/BL [Ied98] (see also Section 1.1.2).

In the time the presented measurements were performed and electronic origin of the structural changes in water has gained more and more experimental evidence, for the same reason the need of a device emerged that is capable of measuring the work function change without a contact to the sample and highly locally, preferentially only within the UV pump spot. Additionally, the possibility to follow the temporal evolution of Φ in the real time during the measurement and as a function of photon dose was required, as well as a design suitable for the integration into the rather limited space and angle boundaries available within the SFG setup. On the other hand, as the work function change was expected to be large, the resolution of such a device could be a matter of compromise if the other conditions were fulfilled.

As a result, a small retarding–field analyzer (RFA) mounted on a customized ISO–CF DN40 flange has been designed, implemented, tested and calibrated and later successfully employed in the experiment. The whole electronics capable to run and read the data from the analyzer, as well as the computer programs to process them in the real time have been developed. A set of photographs showing different views on the RFA without the shield is shown in the Figure 3.16 and is intended to provide the reader with a picture worth keeping in mind while reading the remaining lines of this Section. Before a detailed information about the RFA design and capabilities can be given, a brief introduction into its working principle is offered.

3.4.1. Principle of the electron kinetic energy measurement using retarding field analyzer

The usual way to measure the surface work function is to employ the photoemission spectroscopy as described in the Section 1.2.3. In its conventional fashion, the energy of photons that interact with a metal surface is varied and the possible emission of electron is followed by a sensitive detector. The value of Φ is easily found as the threshold photon energy at which the electrons are ejected from the metal with zero kinetic energy.

In our experimental setup, however, an external tunable source of radiation is not available and for many reasons (especially the guarantee of a perfect overlap with the probing beam) the better approach appears to be the use of the UV pump beam. Its energy is larger than the work
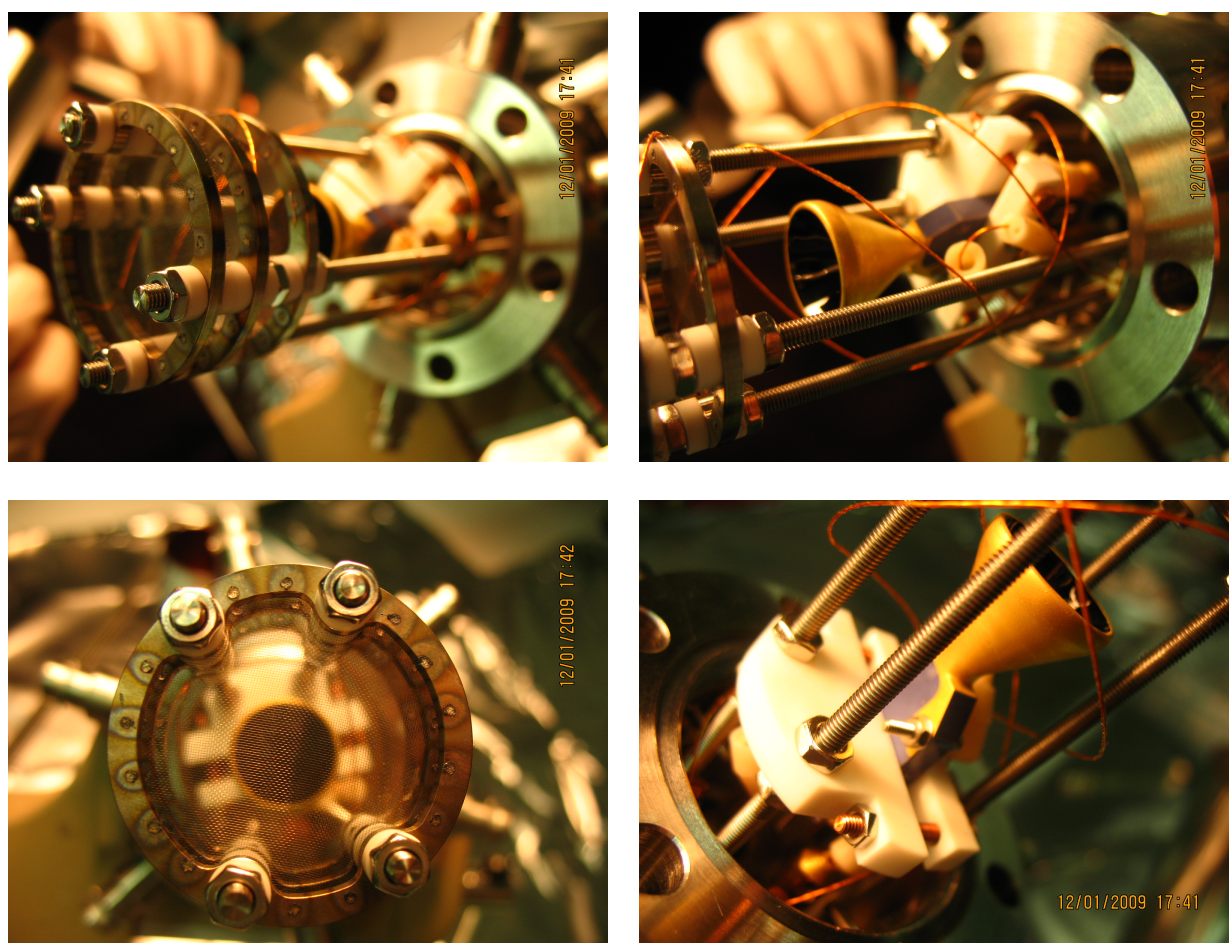
Figure 3.16.: A photograph of the retarding field analyzer

function of the ice covered metal[20] and hence it causes electron excitations not only from the Fermi level as the light in the conventional photoemission, but also from the underlying states. As a result, electrons with a broad range of kinetic energies are emitted, whereas the energy of every single electron depends on its initial state. The idea of the retarding field analyzer is to map this energy distribution, since it bears the information about the work function as will be explained later. This goal can ideally be achieved with an electron detector placed behind a grid with an adjustable potential. Increasing the voltage U_G set on the grid increases the energy barrier for the particles emitted towards the detector to a value of $-qU_\mathrm{G}$, if their flight direction matches the direction of the field created by the grids. Electrons with lower kinetic energy will not pass the barrier, which enables to map the emitted electron energy distribution simply by sweeping the voltage. In reality, the setup is somewhat more complicated, but the idea is the same. Figure 3.17 shows the optimal experimental arrangement of grids and detector in the employed RFA.

A detector – channel electron multiplier – is placed in a shielded tube behind three grids,

---

[20]The Ru(0001) single crystal covered by a multilayer of crystalline ice exhibits a work function of $(3.80 \pm 0.05)\,\mathrm{eV}$. If the multilayer is amorphous, the Φ value amounts to $(3.98 \pm 0.04)\,\mathrm{eV}$ [Gah04]. The employed UV pulse is still short and intense enough to induce the photoelectric effect from the bare Ru(0001) in a two–photon process ($\Phi_\mathrm{Ru} = 5.44\,\mathrm{eV}$ [Ber00]), although with a orders of magnitude lower efficiency.
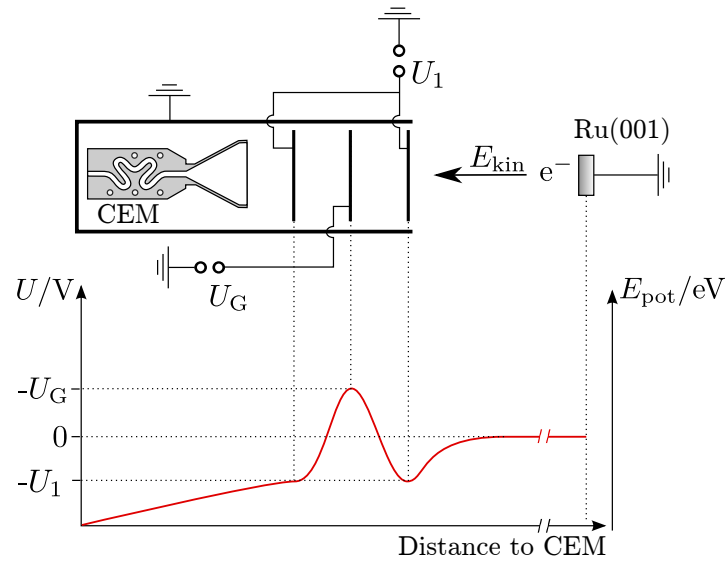
Figure 3.17.: Schematic arrangement of the most important elements in the RFA. For simplicity, the first and the last grid are shortcut in the illustration, but can be set independetly to any voltage in reality. On the bottom, the two–dimensional potential felt by an electron travelling parallel to the electric field created by the grids is depicted.

whose potentials can be controlled separately. To achieve the high sensitivity to the incoming electrons, this type of detector requires quite large voltage difference to be set across the highly resistive coating layer that provides the electron cascades. In the presented work, $0.1\,\mathrm{kV}$ were set on the front and $3\,\mathrm{kV}$ on the back side of the layer. The innermost grid therefore mainly shields the other two grids and the space in the chamber from this extraordinary high potential that resides on the wires, connectors and the channeltron device itself. The middle grid is the retarding grid. Its potential is proportional to the kinetic energy of a passing electron, if its trajectory is parallel to the grid normal. The first grid allows to focus the electron beam into the RFA or to switch off the electron flow into the analyzer. Without this first focusing step, setting a negative voltage on the retarding grid would create a repulsive potential and the electrons approaching the device would tend to diverge from their original path and collide with the shielding or the chamber walls rather than pass directly through the grid. Moreover, this would have a stronger influence on the electrons with low energies, as they can be diverted from their flight direction easily by any small potential eventually present in the chamber, despite of our effort to suppress this[21]. Note that the low energy electrons are of great importance for the calculation of a correct work function value, as will be explained later in this Section on page 120.

3.4.2. Measuring work function changes

Simulation of electron trajectories under experimental conditions

The optimal design analogous to the scheme in the Figure 3.17 can not be realized in the SFG chamber. Its geometry, the sample position in the optical level of the chamber and the positions

---

[21]It is not possible to account for the contact potential of every metal piece in our chamber. It is also not possible to shorten the electron path, since this is not compliant with the spatial restrictions in the SFG chamber.

of other instruments greatly restrict the available space for an RFA.

The short description of the setup above could already make obvious, how important the reliable knowledge about the ion trajectories – before and in the device – can be in such a more complicated case. The number of corrections that can be made 'on the fly' is also greatly reduced by its operation under UHV conditions. For a similar arrangement, as shown in the Figure 3.17, however with a geometry closer to that of the employed experimental setup, a profound simulation has therefore been realized [Zac09]. The modeling has been performed with a commercial PC program SIMION in the version 8.0.4 [Dah00]. The control of the program flow and the readout of relevant results from the simulation was achieved through a programming interface in the scripting language *Lua*.

In principle, the problem solved by the program SIMION can be generalized as finding a numerical solution to the Poisson equation

$$\Delta\phi(\boldsymbol{r}) = -\frac{\rho(\boldsymbol{r})}{\epsilon_0} \tag{3.33}$$

for a given arrangement of electrodes, i.e. the sample and the RFA parts. Here, the symbol ϕ is used for the potential of the electric field, ρ denotes the free charge density, Δ is the Laplace operator. In the vacuum and in the absence of the free charges, the right side of 3.33 equals to 0 and a homogeneous partial differential Laplace equation is derived. Its analytical solution is possible only for a limited set of simple cases, therefore one often has to find its numerical solution. This is offered in many computational–science textbooks as the prototypical example for an elliptic partial differential equation [Pre97]. Solving it leads to a potential map in the UHV chamber and through

$$\boldsymbol{E} = -\nabla\phi(\boldsymbol{r}) \tag{3.34}$$

the force $\boldsymbol{F}(\boldsymbol{r}) = q\boldsymbol{E}$ acting on any charge at any location in the chamber can be also calculated numerically. A possible magnetic field influence on the electron trajectories is neglected. For details concerning the implementation of the solution path in the SIMION program, please refer to [Zac09]. An example simulation result – a potential map in the simplified UHV chamber geometry showing also the modeling arrangement is presented in the Figure 3.18.
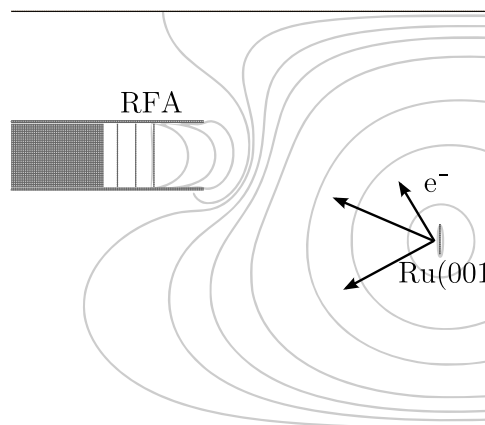
Figure 3.18.: Simulated potential map in the simplified UHV chamber geometry. In the depicted case, the sample voltage is set to $-2\,\text{V}$, the first grid to $15\,\text{V}$. The grey equipotential lines connect points with the same electric potential.

The actual goal of the simulation can be expressed in another way as the task to evaluate the RFA transmission probability, which gives us a more defined observable to compute. Here,

the transmission probability is defined as the probability of an photoemitted electron to reach the detector after passing all grids. Only if a sufficient amount of electrons can be detected, the setup is feasible and the number of degrees of freedom is greatly reduced. For this purpose, 25 000 electrons with a random velocity vector $\boldsymbol{v}_0$ and a selected energy $E_0 = m_e \boldsymbol{v}_0^2/2$ were simulated to leave the sample.

Simulation results: Implications for the design of the RFA

The modeling has revealed that the distances between the grids are much less important than expected and the desired electron trajectories can be controlled more precisely by tuning the voltage on the grids. The electrons are detected with an almost 100 % probability after they have passed the last grid, as the potential on the detector area that almost fills the entire rear part of the analyzer is very high. Therefore, only the adjustment of the front RFA part is reasonable. Due to the risk of repelling the electrons in the analyzer towards its walls before they can reach the retarding grid, the grids are stacked as close to each other as possible. This also increases the aperture for a hypothetical electron beam that passes the RFA. Clearly, the optimal position for the grids is flush with the shielding end.

The length of the RFA tube is not important. Different to its optical analogue, where a longer tube would enhance the spatial angle under which the electrons can pass the grids, here all charges can be attracted by a voltage (U_1) on the first grid[22]. As will be discussed later, this is not always appropriate and a shorter tube accepting a narrower spatial angle could even improve the energy resolution. However, due to the constraints in the UHV chamber, the RFA must end 15 cm away from the sample and a further shortening of this distance does not show any notable effect.

An RFA constructed with all the attributes mentioned above offers a model transmission curve depicted in the Figure 3.19. The data represent, considering the given spatial restrictions in the UHV chamber, the best achievable characteristics of our analyzer.

Simulation results: Implications for the RFA data processing

Evaluating the RFA properties based on the data from the Figure 3.19, several drawbacks of our method can be identified. Its main limitation is the very low detection probability even in the best possible design. For electrons with kinetic energy larger than 4 eV, the detection probability lies below 1 %. Not considered is the transmission of the grids, which reduces this number further by at least 50 %. However, it is not the insufficient number of detectable electrons which would be problematic in this context. The intensity of the UV laser pulse is very high and can produce an amount of electrons orders of magnitude larger than a CEM could detect in the current setting. On the other hand, to excite a large initial number of electrons, which is required to register them with a sufficient statistics, especially if the repetition rate of the laser is low, can lead to a space charge in front of the sample and considerably distort the kinetic energy distribution. Every measurement has therefore been performed with a signal intensity close to the detection limit and the channeltron settings were deliberately tuned to the maximum sensitivity even taking into account the risk of destroying the device by an electron source, such as a filament in the chamber, inadvertently switched on during its operation.

A further factor greatly influencing the measured kinetic energy of the electrons is their angular distribution. As it is obvious from Figure 3.18, none of the electrons is released from the sample in the direction parallel to the RFA grid normal. However, the part of the energy

---

[22]First (outermost) grid is the first from the viewpoint of a charge that passes the analyzer.
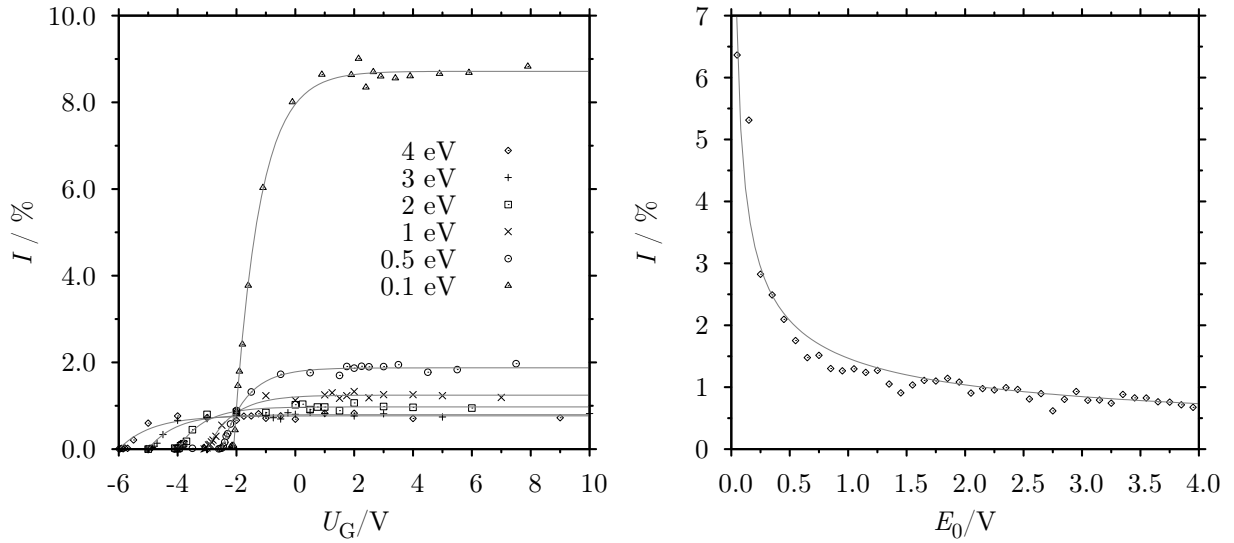
Figure 3.19.: Left: A simulated RFA curve. The electrons start from the sample at $-2\,\text{V}$ and at various energies (see the legend). The fraction of electrons that finally reach the detector is plotted as a function of the retarding grid voltage. Right: The transmission probability as a function of the initial electron energy immediately after leaving the sample (E_0). In both cases the first and the last grid are set to a constant voltage of $5\,\text{V}$.

contained in their momentum only in this direction can be mapped. The influence of the electron incident angle depends on the voltage set on the first grid:

If the actual potential difference between the sample and the first grid is zero, the key role plays the angle γ between the direct sample–detector path and the grid normal. It amounts to approximately $10°$ and therefore the measured energy is $E_x = m_e v_x^2/2 = \frac{1}{2}m_e v^2 \cos^2 \gamma = E_{\text{kin}} \cos^2 \gamma \approx 0.97\,E_{\text{kin}}$. This deviation is clearly visible in the simulation. By the inspection of the onset of every RFA curve in the Figure 3.19(left), a shift to a little lower negative energy than the energy conservation would require can be observed. Similar shift should apply to all electrons that reach the detector and therefore the final kinetic energy distribution measurement is not disturbed by this fact, although it requires a correction.

If the potential of the first grid is set to a value different from the sample, the angular distribution of the electron momenta becomes much wider. The grid acts as a lens and a part of the trajectories of electrons that would not be detected in the previous case ($\phi_1 = \phi_{\text{sample}}$) is bend towards the detector. Although a grid can change the electron path, it can not add energy to a particle as the same field which accelerated it towards the detector will slow down the electron after it has passed the grid. Overall, there is no energy gain and only the initial momentum component parallel to the grid normal counts. As electrons in this case have been collected over a wider spatial angle than in the case above, the final kinetic energy distribution will be artificially wider. This fact can be seen in the simulation as the deviation from a step change in the Figure 3.19(left). Electrons that start from the sample ($-2\,\text{V}$) with an energy of exactly $0.5\,\text{eV}$ should in an optimal case all reach the detector after the retarding voltage is increased above $-2.5\,\text{V}$. However, a saturation of the modeled signal is clearly visible at much later values. This complicates the measurement significantly and requires additional calibration and characterization of the device to correctly describe the low energy part of the electron kinetic energy distribution. Due to this difficulty, the measurements are preferentially performed with

a potential on the first grid similar to that of the sample.

Another important information can be drawn from the right curve in the Figure 3.19. The experiment simulated there is proposed to estimate the total probability of detecting an electron photoemitted with the kinetic energy E_0, if no retarding potential is applied. For this purpose, a relatively high positive voltage of 15 V is set to the retarding grid. The result is quite intuitive: the trajectories of slow electrons are much more influenced by a given constant field (force), exhibited by the first grid, than the trajectories of the faster species. As a consequence, the detected low energy electrons have a much broader angular distribution of their momentum vectors. The field they experience accelerates them to a velocity that is too large compared to their original velocity vector and regardless on its initial angle their resulting path will be governed mainly by the potential gradient in the chamber, which in this case will almost always lead towards the analyzer. The still low detection probability under these conditions is caused by the suboptimal position of the RFA in the chamber, which gives only a small effective aperture for the electrons that can be detected, leaving the rest to collide with the RFA wall. This, again, stresses the importance of the proper choice of the potential set on the first grid. The smaller its value with respect to the sample potential is, the lower fraction of electron trajectories it will distort significantly.

There is another way to circumvent the problem with the low energy electrons and their enhanced detection probability. If the sample is set to a negative voltage (e.g. to -2 V), the kinetic energy of the slowest electron will be larger than zero (at least 2 eV, assuming $\phi_1 = \phi_{\text{sample}}^{U=0}$), because all emitted particles do have a kinetic energy of at least 0 eV. Particles with a higher kinetic energy are less prone to follow a path completely influenced by the first grids attractive field. Moreover, if the voltages on the sample and on the first grid are adjusted properly, the electron detection probability is almost equal for all electron energies, as can be seen from the left graph in the Figure 3.19, comparing the detection probability for any energy at a voltage of approximately -2 V. This is in this case the lowest real barrier and all electrons arriving to the detector at an expected angle should be detected up to here. Thus, all other detected species, if detected, could obviously be neglected. To find the proper value of this potential as well as the adjustment of the sample/grid voltage is a matter of calibration. Also in this case, keeping a low voltage on the first grid is preferred.

Estimating the work function change from the electron kinetic energy distribution

After the true RFA intensity–voltage curve is obtained in the way described above, it indeed reflects the electron kinetic energy distribution, but its interpretation is not straightforward. A schematic view on this problem is offered by Figure 3.20(a). It shows the *total* energy of the excited electrons and introduces the important energy levels of the metal and the electron detector system, which is in the RFA represented by the retarding grid. It is namely its potential alone that decides whether an electron with a given kinetic energy will be detected or not. Other parts either only focus, or detect *all* electrons.

If the sample and the detector grid are shortcut (or both of them are set to an identical voltage), their Fermi levels are aligned as obviously no constant electric current flows between them. Their vacuum levels, however, may differ – the potential energy of an electron excited from any compound depends mainly on the compound–specific electron binding strength[23]. This does

---

[23]This statement is illustrative, but not fully correct. The electron charge density near to the surface usually has a different symmetry than the underlying lattice. This leads to a permanent dipole moment at the surface, which depends for instance on its orientation and requires a correction of the work function value derived from the Koopmans theorem [Koo34] as above. As an example, the polycrystalline tungsten exhibits a work function
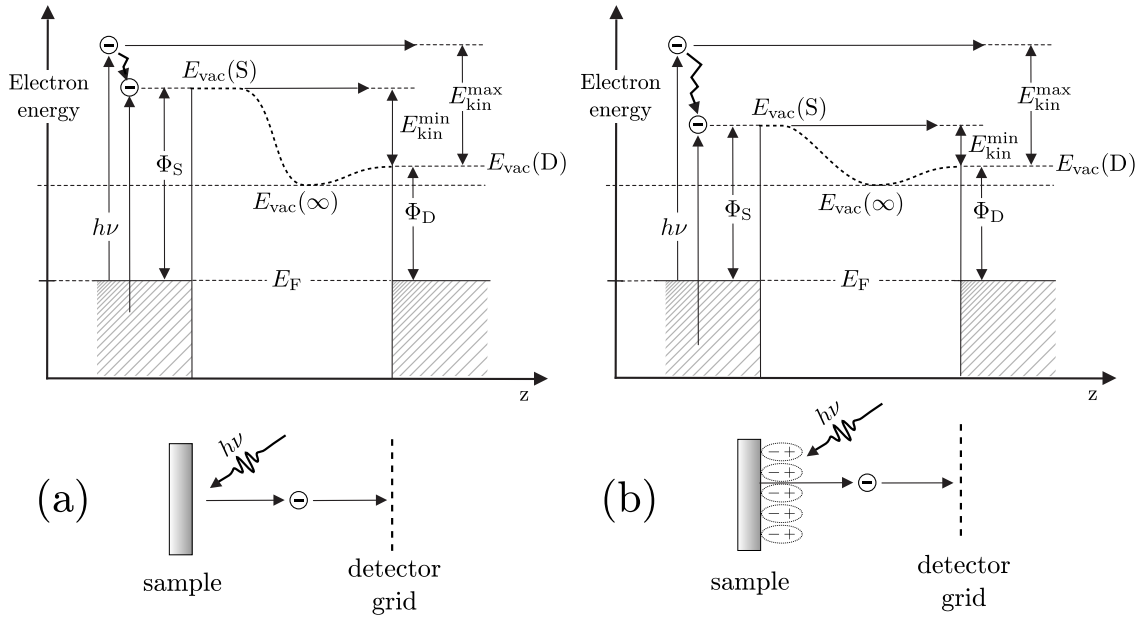
Figure 3.20.: An energy diagram showing the total energy of electrons excited by a pulse of energy $h\nu$ as well as the consequent processes – scattering and transport towards the detector, again with its energy level diagram. Depicted is the case of a bare metal surface and of a surface covered by an adsorbate with a dipole moment pointing away from the surface. Adapted from [Cah03]. Detailed explanation in text.

not only manifest itself in a different value of the work function ($\Phi = E_F - E_{\text{vac}}$) of the grid and sample, but causes any pair of connected metals to posses a different electric potential. Such a potential difference is known as the contact potential ($\Delta\phi = \Phi - \Phi'$), and exerts a force on a charged particle in the space between the sample and the detector. The contact potential has two important consequences for our measurement. First, the lowest kinetic energy of the photoemmited electrons is almost always different from zero. Given a detector with a work function lower than that of the metal, the higher potential energy of electrons in front of the sample will be converted into the kinetic energy during the flight and add to the total kinetic energy so that one can write

$$E_{\text{min}}^{\text{kin}} = \Delta\phi = \Phi_{\text{sample}} - \Phi_{\text{detector}} \tag{3.35}$$

which is valid for electrons that start from the sample with zero kinetic energy and

$$E_{\text{kin}}^{\text{max}} = h\nu - \Phi_{\text{sample}} + E_{\text{min}}^{\text{kin}} = h\nu - \Phi_{\text{detector}} \tag{3.36}$$

for electrons excited from the Fermi level. The sample work function can be expressed accordingly as

$$\Phi_{\text{sample}} = h\nu - E_{\text{kin}}^{\text{max}} + E_{\text{min}}^{\text{kin}} \tag{3.37}$$

showing the great importance of both edges of electron kinetic energy distribution.
The second consequence is that to map this whole distribution, positive voltages may be required on the detector to assure the detection of all electrons. In the presented design, the grid is made

of 4.55 eV, the W(113) face 4.46 eV and W(110) 5.22 eV [Lid07]. For more details see [Ash76].

of tungsten mesh with a Φ_{detector} of $\sim$4.55 eV [Lid07], which is a higher value than the work function of ice–covered Ru(0001) sample. If the first grid and the sample were grounded (set to the same voltage), the low energy electrons would be not able to reach the detector (as the potential of the grid would be higher). It is therefore crucial to keep in mind the difference between the voltage and the potential in this case. The RFA operation with a negative voltage on the sample as mentioned above is thus convenient for this reason as well.

There is another aspect worth noting before the data can be discussed. The kinetic energy distribution of electrons is *not* to overinterpret as the image of the density of states in the metal. The electrons with the highest energy are indeed, as illustrated in the Figure 3.20, coming from the Fermi level (E_F) of the substrate. However, the lowest energy electrons are not only emitted from the low–lying states below the E_F, but can represent the outcome of an e–e scattering process during the excitation in the metal itself. Unlike the broad angular distribution of the photoemitted electrons, this distortion of the low–energy edge can not be avoided and represents a source of systematic error. Although the probability of such a scattering is not high, it complicates the absolute estimation of the work function value. Nevertheless, our actual goal – to measure the work function *change* can be reached under the assumption that this probability is low and does not vary greatly upon a change in the work function.

Working with ultrashort intense pulses adds to the complexity of a RFA measurement as well, as the number of excited electrons can be that large, that their electrostatic interaction within the charge cloud in front of the surface (space charge) is not negligible and artificially spreads the electron energy distribution. In such a case, the change in the work function becomes apparent in the width of the electron kinetic energy distribution. Illuminating the sample with an identical amount of photons leads to a larger number of electrons if the work function of the sample is lower. If the electron density in the space charge is larger, the electrostatic interaction can be stronger, accelerating the fast and slowing down the slow electrons. In any case, only the sign of the work function change can be determined in this way. To suppress the space charge, lower laser intensities are used and detection of electrons takes place close to the detection limit of the channeltron.

Meaning of the work function change upon adsorption

As a short note, reasons for the work function change, as they are depicted in the Figure 3.20(b), should be explained more precisely. Our interest in the $\Delta\Phi$ value was sparked mainly by the – at the time not understood – processes in the ice layer upon electron confinement (see Chapter 5). What implications has a change in Φ for this phenomena?
We consider a water layer adsorbed on a Ru(0001) surface – a situation that has been thoroughly treated in Section 1.1.3. Such an arrangement of D_2O molecules will have a dipole moment which will be imaged in the metal. If it points away from surface, as shown in Figure 3.20(b), it will be compensated by a decreased electron density at the metal surface as compared to the bare metal. Lower negative charge density at the interface means a reduced barrier (vacuum level) for an escaping electron leading to a lower work function. The situation is symmetric and hence opposite, if the dipole moment points towards the sample. The theoretical calculations confirm this argumentation, predicting a work function value of 5.04 eV, if D_2O molecules in the first ice layer on Ru(0001) were aligned in 'D–down' (dipole pointing towards the surface) fashion and 2.4 eV for the 'D–up' (dipole pointing away from the surface) structure [Men05] (see also Section 1.1.3).
If a reorientation of D_2O molecules in ice takes place as a consequence of the charge confinement, mainly the water dipole moments should align. Due the solvation site at the ice–vacuum

interface (see Section 1.2.3) and some other factors, this should change the final work function and allows some conclusions made in Section 5.1.1.

3.4.3. Important technical parameters

As the RFA is a non–commercial instrument, a brief description of its components might be useful for the reader considering to build a similar device. The final technical drawing of the assembled RFA is shown in the Figure 3.21. An ISO–CF DN40 flange has been manufactured
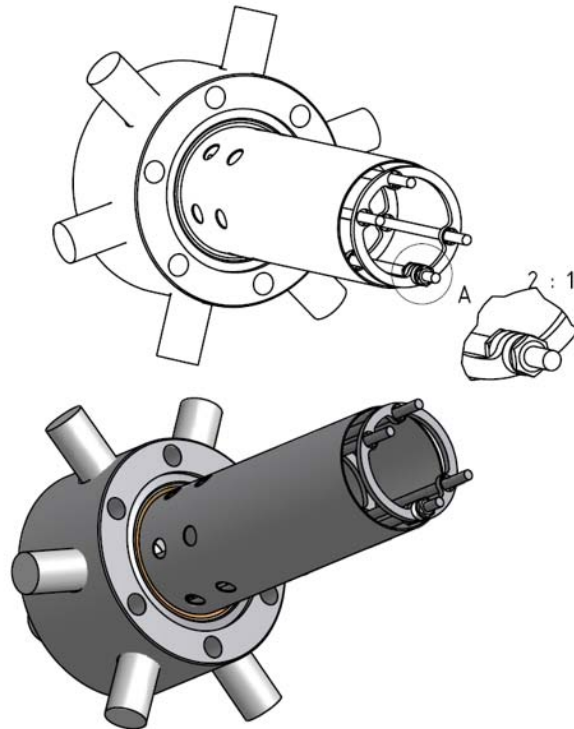
Figure 3.21.: A technical drawing of the assembled RFA–analyzer. Based on a customized ISO–CF DN40 flange with 6 BNC (side) and 2 SHV (front) connectors (placeholders in the drawing) a rod system is mounted providing a fixing point for a channel electron multiplier and three tungsten mesh grids. The whole device is shielded by a stainless steel tubular shield, mounted to the grounded flange by a special OHFC copper screw thread.

from a block of stainless steel, since extended thickness was required to place and mount all necessary connectors and no commercial alternative could be found. On the back side (not visible in the drawing), two SHV–feedthroughs are welded, providing a plug contact suitable for high voltages. Around the circumference, 6 BNC connectors offer the possibility to set a low voltage on the grids. In the back side of the hollow space bearing the connectors, four threads are placed, aimed to support the same number of threaded rods. A coarse screw thread is cut next to the cutting edge of the flange to provide a mounting point for the stainless steel shielding, which is attached to it with a copper orifice to avoid the damage of the device during bakeout, which exposes both components to a different elevated temperature. The shielding is manufactured from a thick foil with several holes in its bottom part to facilitate the gas pumping from the device.

A channel electron multiplier (CEM), KBL15RS from Dr. Sjuts Optotechnik GmbH is mounted

as the detector in the device. After particle or photon impact with sufficient energy it provides electron cascades with an amplification factor up to 1×10^8. This is accompanied with a source high voltage breakdown that can be read out via a capacitor and produces negative pulses of 8 ns length. The intensity of those pulses is to a good approximation proportional to the electric current induced by the given number of incident species. Such short pulses are amplified and then integrated in a boxcar integrator which is read–out using a newly developed computer program.

The CEM is mounted to the rod system behind the three grids made of a tungsten mesh with a transmittance (open area) of approximately 80 %. Such a dense network of very thin wires is necessary to assure the homogeneity of electric field in the proxmity of the grids and hence to increase the resolution of the device. All components are connected with their corresponding feedthrough plug by a polyimide isolated wire, the wires for the high voltage parts are additionally equipped with a ceramic isolation. To separate all components from each other a thin polyimide foil keeps apart the shielding from the grids. The rod system has no electric contact with the grids, which is achieved by a specially designed set of ceramic washers (see zoomed area in Figure 3.21). For connecting the grids and the wires, spot–welding appears to be a very convenient method.

The results achieved with the RFA are further discussed in the Section 5.1.1. Although they deliver the information this instrument was aimed to obtain, this device could perform much better in a setup, where less restrictions limit its function. We believe that the operation of an RFA is a genuine alternative to other methods that are intended to provide one with the value of the work function of any compound.

4. Interfacial structure of D_2O on Ru(0001)

The importance of ice surfaces for many areas of physics or atmospheric science cannot be overemphasized and some of the prominent examples demonstrating their relevance have been mentioned earlier in Section 1.1. Equally, for many research areas the interaction of the water with a metal surface is of key interest. As a model metal surface, Ru(0001) and Pt(111) have been studied most intensively, most probably due to the strong influence they exhibit on the chemisorbed water layer. Although SFG vibrational spectroscopy can provide an unique view at the water/metal interface and interactions, apparently the last results led to an interpretation of the obtained spectra not fully consistent with the other findings. In the following Chapter the interfacial structure of water on a Ru(0001) surface is reexamined using an improved experimental setup and benefiting from the knowledge obtained by other research groups in the meantime. At the end, a more consistent picture of the interaction between the model metal surface (Ru(0001)) and D_2O molecules can be drawn. Another aspect examined here is the surface structure of different phases of ice grown on the Ru(0001) substrate. Despite the interface–induced disorder in the layers, a clear difference between the amorphous and crystalline phase can be found. The oscillators contributing to the SFG vibrational signatures are located more precisely by coadsorption experiments and a model for the structure of the surface of both phases is discussed.

4.1. Introduction to the current research status

The initial motivation to perform the experiments presented in this Chapter comes from the investigations carried out by Denzler et al. that focus on the structure of the wetting water layer on the Ru(0001) surface [Den03a, Den03b, Den03c]. Before the more advanced topics are discussed, a brief summary of their results is therefore given with some of the conclusions reinterpreted in the light of the current understanding of the D_2O/Ru(0001) system.

4.1.1. Thermal desorption spectroscopy investigations

In the discussion regarding the theoretical calculations predicting a half–dissociated structure of the first water bilayer, the first convincing experimental argument confirming intact D_2O adsorption came from TDS measurements [Den03c][1]. As in the rest of the thesis the undissociated structure of the first water layer is assumed, it is worth spending some lines of text in a brief overview of the corresponding results.

There is a remarkable isotope effect accompanying the water desorption from a clean Ru(0001) surface: If the H_2O multilayers leave the surface, three distinct peaks can be observed in the corresponding TDS, whereas the part of the ice film without a contact to the metal exhibits a maximum around 150–160 K (depending on coverage) and the layer bonded directly to the Ru(0001) surface leaves it in two clearly separated peaks at 170 and 213 K (at the heating rate of $0.5\,\mathrm{K\,s^{-1}}$; see Figure 4.1). In contrast, pure D_2O was found to yield only one peak for

---

[1]More arguments were required by the opponents of this picture to exclude that the desorption peak of the wetting layer does not correspond to an *associative* desorption.
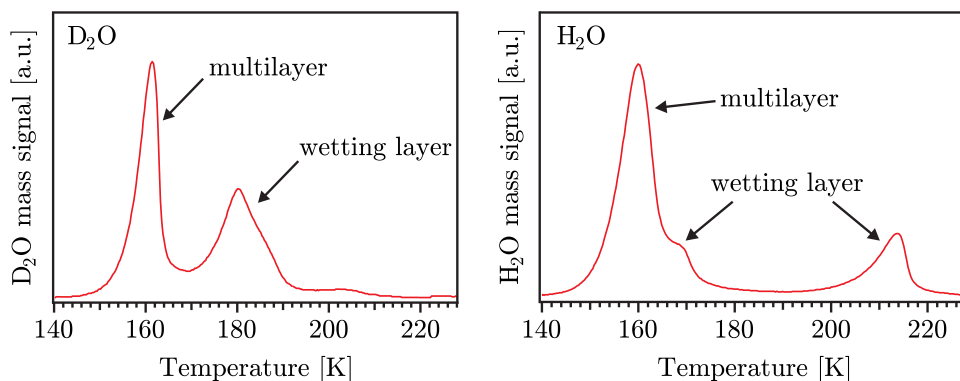
Figure 4.1.: TDS spectra of D_2O and H_2O desorbing from the Ru(0001) surface. Taken from [Den03c].

the multilayer and one peak (at ∼175 K) for the wetting layer. A the third, high temperature peak, appears only if oxygen or impurities contaminate the sample, which leads to a strain in the hydrogen–bonded structure of an otherwise nearly perfect, compressed bilayer. The structure of the wetting layer formed by either of the water isotope is indeed different: H_2O forms separated stripes with hexagonal internal structure and D_2O grows by covering the surface uniformly, since the Ubelohde effect (see page 23) most probably allows the latter type of water molecules to accept the structure enforced by the substrate [Hel95b]. The theoretical prediction [Fei02] concerned the most stable structure of both H_2O and D_2O and in both cases postulated a half–dissociated adlayer. It is therefore reasonable to expect that if the molecules break apart under the influence of forces arising from the interaction with the metal, their recombination upon desorption will not be perfect. Processes like diffusion may namely bring the dissociation products out of the distance range feasible for a reversed reaction and in such a case a measurable amount of fragments (hydrogen and hydroxyl) will remain on the surface. The hydrogen is particularly known to desorb associatively at temperatures exceeding the water desorption temperature, whereas the enhanced mobility of the hydrogen atom at higher temperatures also supports the diffusion of the reactants. The result of a hydrogen TDS measured after a water desorption with a specially designed mass spectrometer of extraordinary collecting efficiency (Feulner cup QMS [Feu80]) is depicted in the Figure 4.2. Obviously, both water isotopologues leave some fraction of hydrogen on the surface. Its amount grows up to the coverage of 1 BL nearly linearly and saturates there in both cases. This indicates that the picture of water dissociated only at steps or defects has to be discarded, as those sites should be saturated much earlier and remain blocked by the dissociation products. Similarly, dosing D_2O on a clean Ru(0001) surface at 230 K, which is above the D_2O desorption temperature, but still allows the water molecules to interact for a short time with the surface, does not lead to an accumulation of dissociation products. The consequent deuterium TDS resembles rather a desorption of impurities originating from the water dissociation at the large surface area of the gas handling system than the reaction products.

Much can be learned by comparing the intensities of the H_2 and D_2 desorption peaks in the Figure 4.2 right. After dissociation exclusively at steps or defect sites has been excluded, the total amount of measured hydrogen corresponds to the fraction of water molecules dissociated upon interaction with the surface. In the case of H_2O the area below the TDS peak corresponds to 14 % of the saturation coverage with H_2, which means that about 10 % of H_2O molecules
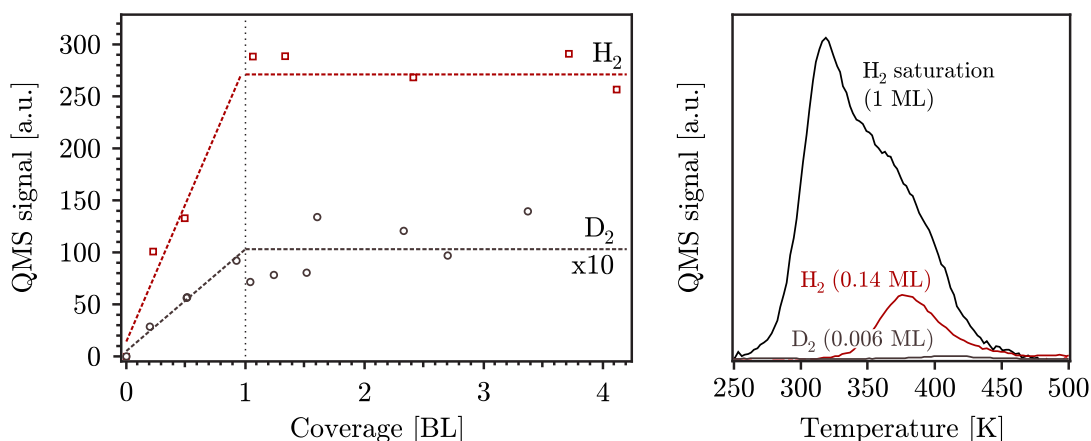
Figure 4.2.: Amount of H_2 and D_2 remaining on the Ru(0001) surface after a complete desorption of the corresponding water isotope. Left: the integrated QMS signal of the desorbing species as a function of the initial water coverage (dashed lines guide the eye). Right: Comparison between the TDS signal of hydrogen adsorbed on a clean surface and the signals for hydrogen remaining on the surface after water ($\sim$3.5 BL) desorption due to its (possible) dissociation. Data are corrected for the different QMS sensitivities to H_2 and D_2. Taken from [Den03a].

dissociate upon desorption[2]. In turn, D_2O molecules leave only a negligible (at least one order of magnitude lower) amount of D atoms on the surface.

Is it possible, though, that the D_2O bilayer is also (partially) dissociated, but due to the differences in the global structure of the adsorbed water its recombination is much more effective? Such a scenario is quite reasonable: the isolated H_2O stripes formed below 1 BL possess a larger amount of molecules neighboring to the free Ru(0001) surface and hence are more prone to diffusion of H atoms away from the corresponding OH fragments than the commensurate, epitaxial D_2O layer. To test this hypothesis, H_2 (D_2) was added to 0.6 BL of D_2O (H_2O) and a TDS measured. In either case, no desorption of water molecules containing both hydrogen isotopes was observed. Such a behavior casts doubts on the recombination scenario: neither H, nor D fragment are exchanged between the water structures and their neighborhood (which is expected if hydrogen can leave the structure) and the water desorbs as if no other adsorbate was present on the sample. Nevertheless, in the case of H_2O, clearly larger amount of HD is found to leave the sample as in the situation when only the pure H_2O is dosed.

These observations are fully consistent with the model of the water bilayer described in the Section 1.1.3. While the D_2O isotopologue adsorbs and desorbs molecularly intact from the Ru(0001) surface, the higher desorption temperature of a fraction of the H_2O bilayer (peak at 213 K) is responsible for its partial dissociation: The dissociated water molecule is in either case the thermodynamically more stable species on the Ru(0001) surface. Nevertheless, the energy barrier separating the intact water film from its most stable structure ($\sim$0.5 eV/molecule) makes this state kinetically inaccessible at temperatures well below 200 K. The dissociation rate, estimated from the Arrhenius equation and using the value for the energy barrier mentioned above, is, however, three orders of magnitude larger at 213 K than at 170 K. As the former is

---

[2]Considered is the different geometrical arrangement of hydrogen atoms on the surface, effectively yielding a saturation coverage occupying only 2/3 of the sites available for water adsorption. Note that hydrogen adsorbs dissociatively and thus the saturation coverage of H_2 (D_2) in fact represents a saturation of the surface with H (D) atoms.

the temperature where the desorption of the H$_2$O wetting layer starts, a dissociation process on a timescale of several seconds to minutes is feasible in this case, taking into account the calculated rate constant.

4.1.2. SFG spectroscopy on thin D$_2$O films

A deeper insight into the properties of adsorbed water was gained using the interface–sensitive SFG vibrational spectroscopy. Although the experimental setups employed in the previous works differ slightly from the setup employed in this thesis, the results can be well understood based on the description of our experiments that can be found in the Section 3.2.3. A typical SFG spectrum of 2 water bilayers is displayed in the top panel of the Figure 4.3 (black curve) and shows the whole OD stretch region of D$_2$O molecules adsorbed on a Ru(0001) surface. It
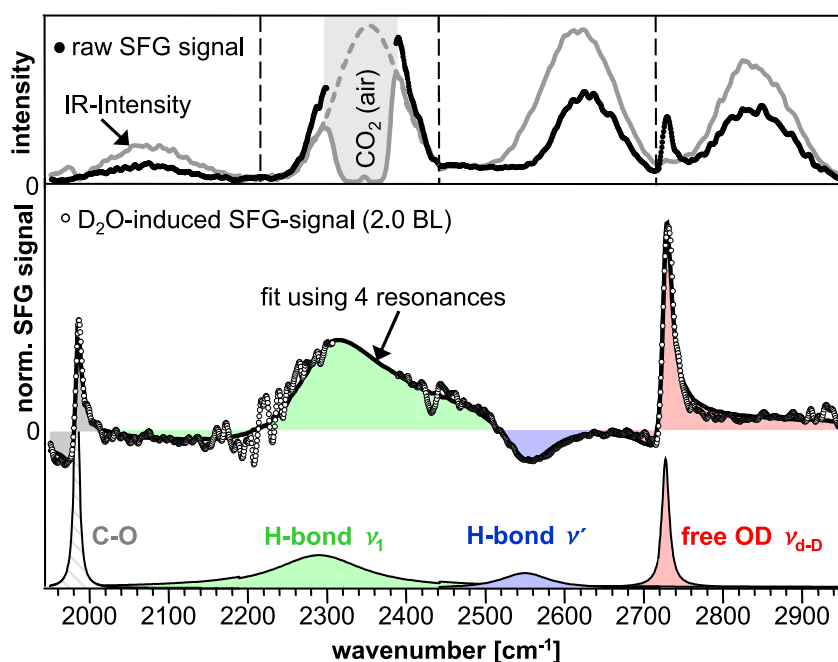
Figure 4.3.: SFG spectrum of D$_2$O (2 BL) as obtained by Denzler et al. [Den03b]. Top panel shows the raw data and the corresponding IR–intensity in the ultrashort laser beam employed in the measurement. Fitting the data to the Equation 3.26 yields three broad resonances shown in the bottom panel. In the middle part the data normalized to the incident IR intensity are shown after the non–resonant background amplitude (a fitting constant) has been subtracted.

was taken in four IR frequency windows (marked by the dashed vertical line), corresponding to different TOPAS settings, as the width of the generated IR pulse is not capable to cover the whole OD stretch region. The gray curve represents the signal of the non–resonant background measured from the bare surface and thus reflects the IR intensity at the given wavelength (see Section 3.1.3). It can be clearly seen that the data accumulation is impossible in the region between 2300 and 2400 cm^{-1} due to the strong light absorption by the CO$_2$ traces in air. Unfortunately, this coincides with one of the D$_2$O resonances and complicates the evaluation of its parameters, although it is theoretically possible to extract them from the wings of the main peak that are still visible.

The data can be fitted to the Equation 3.26, which yields a set of parameters for every resonance

(for each Lorentzian–shaped resonance q the amplitude A_q, the phase with respect to the non–resonant part ϕ_q, the resonant frequency ω_q, the half width at half maximum Γ_q and the amplitude of the non–resonant contribution A_{NR}; see Section 3.2.3). These fit results can be either plotted directly as in the bottom panel of the Figure 4.3, or the measured data can be displayed in the form normalized to the variable IR intensity as

$$I_{SFG|D_2O} \propto \frac{I_{SFG} - |A_{NR}|^2 I_{IR}}{I_{IR}} \tag{4.1}$$

which is shown in the middle panel of the Figure 4.3. This by no means represents the net signal from the D_2O layer, since the interaction with the non–resonant part of the spectrum is much more subtle and cannot be simply subtracted (see e.g. Eq. 3.25; obvious also from the apparently negative intensities). Therefore this form of data demonstration will be avoided in the following. Nevertheless, the results presented in this form illustrate the possible shapes of the SFG resonances in a very expressive way, starting from the raw data and (in principle) without a need to consider any fitting parameters[3]. Despite its complexity, the whole spectrum can be fitted assuming three Lorentzian–shaped OD stretch resonances at $2290\,\mathrm{cm}^{-1}$, $2550\,\mathrm{cm}^{-1}$ and $2729\,\mathrm{cm}^{-1}$ and the overlap of such a fitting function with the data is excellent (black line, middle panel of Figure 4.3).

The spectral assignment of the vibrational modes was based on a comparison with similar spectra in the literature [Wat01, Del97, Wha77, Buc99, Woj02, Mir98, Kub02, Men02a] and is in accord with Tables 1.1 to 1.4 compiled in the present work. The resonance at $2730\,\mathrm{cm}^{-1}$ was identified as the free OD (dangling D) vibration at the ice surface, the mode at $2550\,\mathrm{cm}^{-1}$ was attributed to the partially coordinated, hydrogen bonded OD oscillators and the vibration at $2290\,\mathrm{cm}^{-1}$ belongs to the fully coordinated OD stretch[4] (cf. Figure 1.15).

The SFG spectrum of two D_2O bilayers represents an important reference, as it shows the *intact* ice surface. The changes in the spectrum as the ice coverage decreases can be seen in the Figure 4.4. Dramatic is especially the decrease in the intensity of the free OD vibration that vanishes close to 1 BL. The amplitude of the other modes is reduced as well, although not as abruptly as of the first one, and this effect is accompanied with spectral broadening of the corresponding feature. The spectral positions and peak phases remain essentially unchanged. In comparison to the partially ferroelectric ice structure observed on Pt(111) (see Section 1.1.3), no considerable enhancement of the SFG signal is observed for coverages above 1 BL, which automatically allows to reject this multilayer structure from further considerations. Does the spectrum of the water adlayer, clearly different from the spectrum of an intact ice layer, indicate its (half–)dissociation?

The interpretation of the results is not straightforward. It cannot be expected that the structure of the water bilayer connected to the metal (and bound to it more strongly than to the other water layers as indicated by the TDS) will remain the same as in the ice. Moreover, the vibrational spectrum of water reflects mainly the distance between the two oxygens creating

---

[3]The coverage–dependent amplitude of the non–resonant background can be obtained from a measurement of SFG on a bare and covered surface off any resonance and the obtained value inserted into the Equation 4.1.

[4]It is important to emphasize that this vibration cannot belong to the fully coordinated species deeper in the ice volume as the corresponding sketch in the reference [Den03a] (or the more general picture in the Figure 1.15) might suggest. Due to the random directional distribution of the OD bonds connecting the individual sheets in ices I_c and I_h (consistent with the ice rules), an equal amount of fully coordinated OD resonators is pointing 'up' (towards the vacuum) and 'down' (towards the substrate). Such a layer will not contribute to the SFG signal as the change in the dipole moment in this structure after a vibrational excitation is zero. The origin of this vibration is more likely found in the fully coordinated oscillators connected to the D_2O molecules with a free OD bond (having a preferential orientation enforced by the vicinity of the surface) or alike.
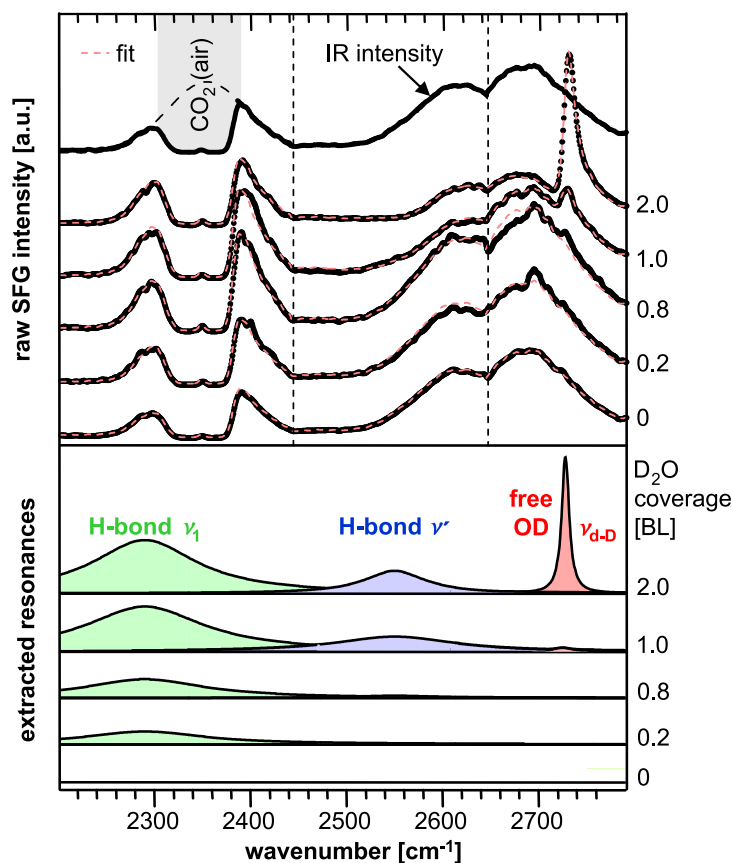
Figure 4.4.: Coverage dependence of the SFG signal from ice/Ru(0001). In the top panel the employed IR intensity is shown together with the raw data overlaid with the best fit function (dashed) to Eq. 3.26. The resonances are displayed in the bottom panel based on the obtained fit parameters. Taken from [Den03a].

the effective atomic potential of the hydrogen bond, which will definitely change under the substrate's influence and contributes to large spectral widths.

What can be said immediately after seeing the free OD signature vanishing is that the wetting layer cannot consist of a majority OD oscillators directed towards the vacuum as proposed by the standard bilayer model and illustrated e.g. in the Figure 1.10. However, the opposite case, with OD stretch pointing to the metal was also not identified in the spectrum. The possible explanations include the postulation of a weak and broad resonance covered by the partially coordinated peak [Den03b] (however, it should appear though at coverages below approx. 0.8 BL where the overlapping peak vanishes completely, but this is not the case) and a structure consisting of an equal amount of OD oscillators of either orientation [Men05], which is improbable for several reasons: First, it is difficult to accept the idea that the binding strength of water to the metal support does not depend on its orientation and neither of the structures ('D–up' or 'D–down') is thermodynamically preferred. Also difficult to understand is the equal frequency that the oscillation of a free OD and of an OD pointing towards the metal should (and indeed must in this case) exhibit. One of the objections against the 'D–down' model was the space consideration, derived from a LEED study, stating that if the water would point the OD bond to the surface along its normal, the covalent radii of the atoms would not fit into this

constrained space [Fei04]. It is therefore very improbable that a D_2O stretch vibration, highly sensitive to O–O distances lower than $0.1\,\text{Å}$ would not reflect this neither in its position, nor in its width[5]. Moreover, the same calculation that predicts the match of the discussed resonances within $1\,\text{meV}$ is more than $30\,\text{meV}$ $(250\,\text{cm}^{-1})$ off from the experimental value for the fully coordinated resonance (in the 'D–down' case). The most important argument highlighted by the authors is the sensitivity of the calculated work function to the correct water structure, but unfortunately this is reached only in a 'bilayer mixture' where the 'D–down' structure clearly prevails, which again lacks any experimental evidence.

The data shown here (Figure 4.4) were also (over)interpreted in the sense that the continuity (slowly varying amplitude and a constant spectral position and phase) seen in the evolution of the vibrational modes with the coverage is indicative of an intact water layer resembling the structure of ice. A closer look at the results, however, reveals severe discrepancies between the fit and the physical reality: the *fully* coordinated hydrogen bonded D_2O molecules are present in a considerable amount also at coverages, where no *partially* coordinated molecules can be seen[6]. This behavior was never explained and is most probably a fit artifact, arising partly due to the limited reliability of the fit in a spectral window with almost no signal at such low coverages. Additionally, a large fraction of the fitting curve is covering an IR frequency range strongly affected by the CO_2 absorption.

For the reasons discussed below, no difference in the SFG spectrum of amorphous ice layer and the layer prepared at $140\,\text{K}$ was observed in the previous work. Nevertheless, a valuable finding is that the mobility of D_2O molecules in a thin water film ($\sim 4\,\text{BL}$) significantly increases at $T_g = 110\,\text{K}$, which is lower than in the pure ice. This was found by coadsorbing H_2O on top of the D_2O layer, which suppressed especially the free OD signal. Upon sample heating, the free OD signature reappears in the SFG spectrum when the temperature of $110\,\text{K}$ is reached. This represents the temperature, where the two isotopes significantly intermix by diffusion in the multilayer. Nevertheless, no isotope exchange with the wetting layer was observed, confirming its high binding energy to the metal and indicative of a different character as compared to the ice multilayers.

---

[5]In fact, another work by the same authors predicts a clearly different vibrational frequency (and width) for a 'H–up' and a 'H–down' structure in the $H_2O/Ru(0001)$ system, the latter almost $150\,\text{cm}^{-1}$ red–shifted, if the isotope ratio of 1.35 is considered [Men04].

[6]Note that the intensity of the extracted peak is in either case normalized to yield the number of oscillators vibrating at the corresponding frequency (see Section 3.2.3).

4.2. Structure of D$_2$O multilayers on Ru(0001) surface

In the previous part, the form (phase) of the investigated ice multilayer was intentionally not mentioned. The authors assumed that the D$_2$O layer grown at slow rates and at 140 K was crystalline. Unfortunately, the indicator of the layer morphology they used was easy to misinterpret: due to the different coordination and hence binding strength of the individual molecules in the ice structure, the vapor pressure of the amorphous modification is significantly larger than that of the crystalline D$_2$O. This leads to a very pronounced shoulder ('amorphous bump') in the TDS spectrum around 160 K, when the layer crystallizes (see Figure 4.5). If the water
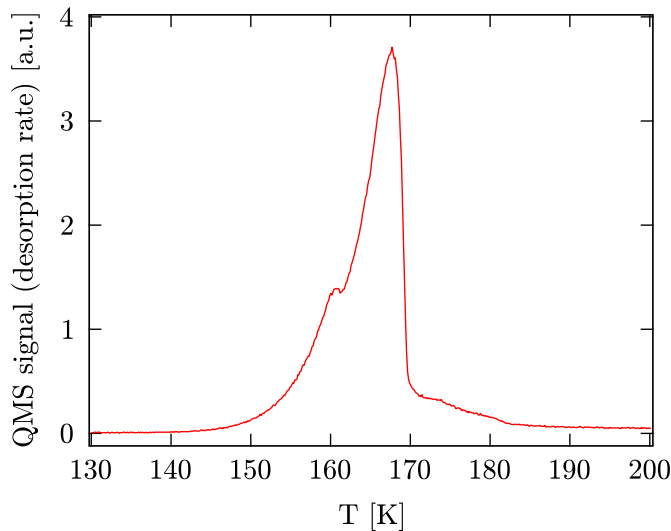
Figure 4.5.: A TDS spectrum of amorphous ice showing the pronounced change in its vapor pressure ('amorphous bump') upon the crystallization. Taken at a heating rate of $0.5\,\mathrm{K\,s^{-1}}$.

is dosed at 140 K, this shoulder is completely missing, which was interpreted as a proof of the adsorbate's crystallinity. Nonetheless, the hydrogen bonded system is far more complex and the purely amorphous form does not revert to the crystalline phase completely. There is a rather wide temperature window (including 140 K), where a liquid–like phase coexists with the growing crystallites [Doh00, Koh00, Jen97]. A TDS spectrum of this adsorbate does not exhibit the pronounced crystallization shoulder, but is far from crystalline – various estimates determine the amount of the amorphous fraction to be between 20 % to 50 %. Therefore, a slightly different preparation procedure for ice layers has been used in the present work, yielding a compact, crystalline ice structure: after dosing D$_2$O at 150 K, the layer is annealed for a short time to 164 K where the desorption rate is already significant (see Section 2.1.3, page 71 for more details). The isothermal desorption spectrum at this high temperature shows a narrow peak corresponding to the crystallization that proceeds with a very high rate [Doh00]. To make obvious the difference between the ice layer prepared in this way and by that obtained following the former recipe, Figure 4.6 compares a TDS of the predominantly amorphous structure (without a shoulder or 'amorphous' bump) and the crystalline structure after annealing to 164 K. The multilayer peak reveals a stronger bonding between the D$_2$O molecules arranged in a hydrogen–bonded network with the largest coordination, although the energy of the water–metal bond is still higher[7]. In

---

[7]It amounts to ∼0.5 eV if the evaluation is performed assuming zero–order desorption and using the Redhead formula with an attempt frequency factor of $10^{13}\,\mathrm{s^{-1}}$.
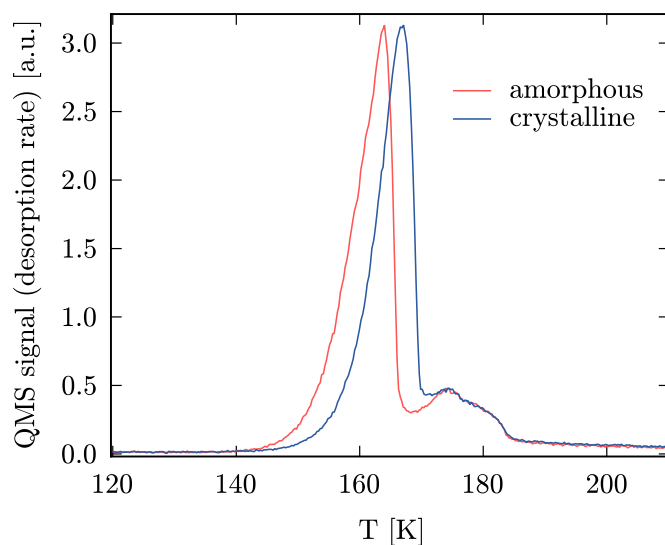
Figure 4.6.: A TDS spectrum comparing an amorphous and a crystalline ice layer. The data is acquired using a background QMS that is less sensitive than the Feulner cup technique, but also less dependent on the heating ramp and pumping speed of the enclosed volume. Taken at a heating rate of $0.5\,\mathrm{K\,s^{-1}}$.

contrast, the imperfect D$_2$O coordination in the (prevalently) amorphous ice modification leads to a much weaker H–bonded network, so that the D$_2$O molecules can desorb at slightly lower temperatures. Could this considerable difference in the D$_2$O layer preparation procedures actually explain the nearly identical shape of the amorphous SFG spectrum and that of the layer prepared at 140 K in the previous work [Den03a]? Was the latter spectrum one of amorphous ice as well?

On the one hand, one could argue that the *surface* of ice, which is only probed by SFG, is insensitive to the bulk structure and its spectrum would rather resemble that of the liquid water, especially due to the surface melting that occurs far below the melting point of water. This would mean that no change can be expected if the ice crystallizes – the uppermost layers can not achieve the full coordination and will be disordered in either case. The experimental evidence, however, does not fully support this idea. The surface of ice is pre–melted or liquid–like only above 200 K [Wei01b, Wei02]. To see whether the solid–like surface structure is influenced by the underlying layer order or disorder, the following Section presents our recent experimental results concerning this topic.

4.2.1. Morphology of crystalline and amorphous ice/Ru(0001) probed by SFG

In the previous, an attempt was made to show that the current understanding of the structure of D$_2$O ice supported on the Ru(0001) surface based on the SFG investigations is unsatisfying and to an large degree incompatible with other investigations on the same system. From a large part, the reason for those inconsistencies is the low data quality that is misleading to the fit such that the obtained spectrum is not reliable, especially at minute coverages when the total signal intensity is in any case very low. Nevertheless, to achieve data quality much higher than Denzler et al. [Den03b], a lot of experimental effort is required. As many of the consequences that were drawn from the SFG spectrum before are based on the properties of the (practically invisible) peak corresponding to a molecular vibration of fully coordinated species, a first step

was to build a purged beam path so that the traces of absorbing CO$_2$ could be removed and this vibration was observed whole in the SFG. Along with this, the beam path was shortened and optimized to a large degree. Another factor contributing to a better resolution was a choice of more overlapping spectral windows covered by the IR pulse width, leading to more independent measures of the peak intensity and providing a valuable cross–check between independent data sets which significantly restricts the fit to the data, operating with a relatively large number of free parameters. And finally, the employed preparation procedure allowed to probe the structure of truly crystalline ice. Figure 4.7 shows the results of those experiments for 8 BL of ice in a compact form. The raw data in the top panel are taken in three distinct spectral windows, each
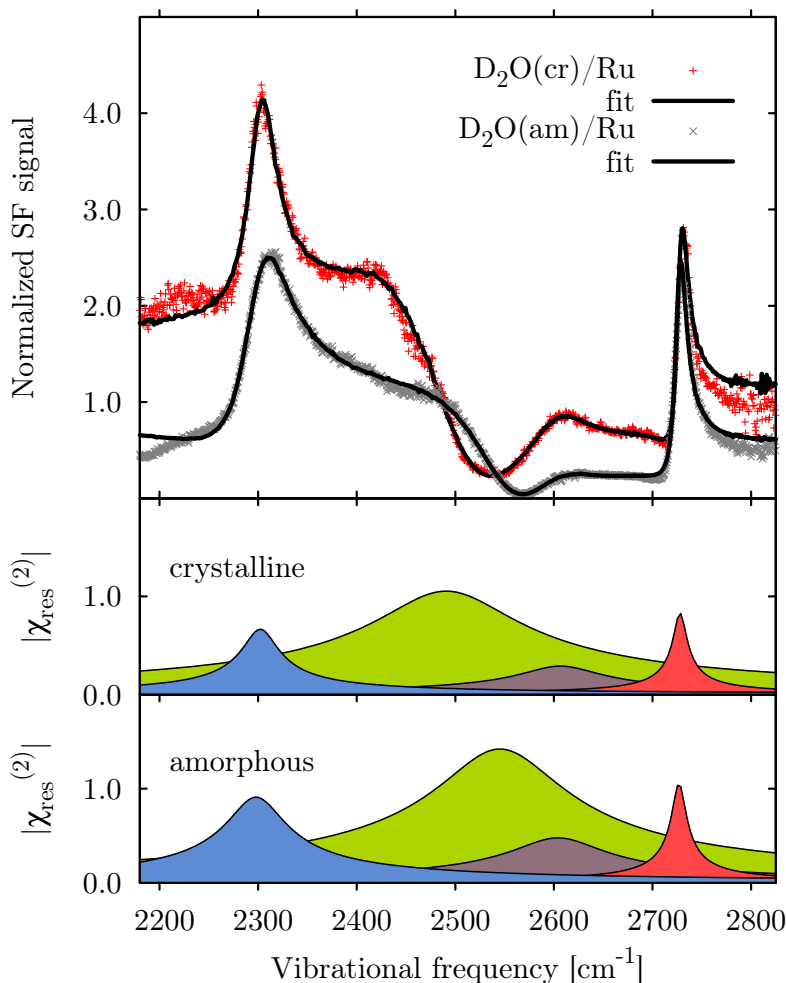
Figure 4.7.: SFG spectrum of 8 BL amorphous and crystalline ice. In the top panel the raw data normalized to the IR intensity is shown, together with the corresponding fitting curve. This consists in either case of Lorentzian–shaped resonances, proportional to $|\chi_{\mathrm{res}}^{(2)}|^2$ (see e.g. Equation 4.2 and 3.10). As the number of oscillators contributing to each resonance is again proportional to the square root of this value, this is plotted in the middle and bottom panel and more resembles a classical IR absorption spectrum.

covering approximately 200 cm^{-1} and upon tuning between those regions the IR wavelength has to be changed. To account for the non–constant intensity distribution in the wavelength domain, the spectra are normalized to the incident IR intensity. The result deserves a short

explanation, as it differs considerably from the classical infrared curves.

A good point to start its clarification is to begin with the gray markers representing the normalized SFG signal from the amorphous ice surface. It can be understood as consisting of a baseline (at the ratio of ~ 0.8), on which the resonances of the characteristic shape (explained in the Section 3.2.3) are superimposed. Since the IR intensity is measured as the SFG signal from the bare Ru(0001) surface, the factor of 0.8 is different from 1.0 only due to the metal–adsorbate interaction. It can be also seen that this value is independent on the photon energy.

The only way to extract the parameters of the vibrational resonances that alter this non–resonant line is to fit the experimental data to a model, like the one described earlier in the Section 3.2.3, which yields the Equation 3.26, now in the normalized form:

$$I_{\text{SFG}}^{\text{norm}} \propto \left| |A_{\text{NR}}(\theta)| + \sum_q \frac{A'_q \sqrt{\frac{\Gamma_q}{\pi}} \mathbf{e}^{i\phi_q}}{\omega_{\text{IR}} - \omega_q + i\Gamma_q} \right|^2 \tag{4.2}$$

This fit describes the data of Figure 4.7 very well, the small deviations at the red and blue end are a consequence of the small IR intensity in the corresponding off–resonant region. The obtained fit parameters are listed in the Table 4.1 and will be discussed later. Here only one additional point should be noted, namely that two of the peaks interact *destructively* with the non–resonant part which leads to a considerable decrease in the SFG signal intensity (see e.g. the right part of the peak at $2545\,\text{cm}^{-1}$). This emphasizes the importance of changes made to the previous setup, as the quality of the data recorded during a TDS measurement [Den03a] is by far not sufficient to measure this low signal reliably without being overwhelmed by the noise. The spectrum of the crystalline ice/Ru(0001) could be explained analogously, but apparently the signal levels at each side of the spectrum and away from any further resonance (as can be easily checked by just tuning the frequency further towards the red or blue side) do not match. This implies that the constant $|A_{\text{NR}}(\theta)|$ is in fact frequency dependent as well, if crystalline ice is adsorbed on the Ru(0001) surface. Moreover, on the red side (left) of the spectrum the non–resonant signal is *enhanced* upon crystalline D₂O adsorption, in contrast to the amorphous water structure adsorption that leads to a relative *decrease* of the observed signal (as compared to the bare surface). Obviously, this is connected to the adsorbate structure and indicates a very strong influence of crystalline water *multilayers* on the surface electrons in the metal, as the structure of the wetting layer is identical in both investigated cases (see Section 1.1.3). A more detailed explanation of this phenomenon is given below together with the discussion of structural differences between the amorphous and crystalline water layers deduced from the resonant part of the SFG spectra. Nevertheless, this fact complicates the fitting of the experimental data, since they patently cannot be described with only one $|A_{\text{NR}}(\theta)|$ for all resonances, as it would be possible in the amorphous case. Here, the existence of cross–terms in the expression 4.2 is extremely helpful and enables us to find the parameter $|A_{\text{NR}}(\theta)|$ as a fitting constant for every evaluated spectral part. Additionally, it can be shown that to a very good approximation this value is nearly constant on such a narrow range[8]. Although the fitting procedure becomes very demanding when performed in this way, it is possible to obtain fully consistent fit parameters

---

[8]Moreover, if our hypothesis concerning the origin of the varying intensity in the non–resonant contribution as a consequence of the coupling between the oscillations of the large adsorbate–induced dipole moment in the subsurface metal layer (large due to the ordered growth of the dipoles in the crystalline water layer) and the collective oscillations in the water layer is correct, the $|A_{\text{NR}}(\theta)|$ should vary slowly, similar to the further, off–resonant spectral regions. It should be also noted that the resonant enhancement of the SFG signal originating from the surface electrons (and leading to the metal–surface selection rule discussed in the Section 3.1.3) is already formally included in the resonant amplitudes A_q.

for identical resonances from the completely independent wavelength windows and still find a very good fit to the experimental data that is shown in the Figure 4.7 as the black line.

The fit to the measured spectrum of amorphous ice (8 BL) supported on the Ru(0001) surface reveals vibrational modes characterized by the set of parameters listed in the Table 4.1 and visualized in the bottom panel of the Figure 4.7. The free OD (at 2730 cm^{-1}), partially

OD resonance	ω [cm^{-1}]	A_q	ϕ_q [π]	Γ_q [cm^{-1}]
free OD	2730	5	0.11	7
dangling O (D–down)	2605	6	0.51	47
partially coordinated	2545	20	1.38	64
fully coordinated (symmetric, ν_1)	2298	9	0.22	30

Table 4.1.: Parameters of SF resonances in amorphous ice

(2545 cm^{-1}) and fully (2298 cm^{-1}) coordinated resonances have been observed and described earlier. Of particular interest is the new resonance discovered at 2605 cm^{-1} and assigned to the dangling O resonance (similar to [Row95, Men04]) that represents an oscillation opposite to the free OD vibration, pointing from the topmost ice layer down to the underlying (ice) substrate. Along with vibrational frequencies the resonant amplitudes are listed, however, those should be treated with care, as these values depend greatly on the molecular orientation and the polarization of the employed laser beams, although they are in principle directly proportional to the number of the contributing molecular oscillators. The resonant amplitudes and other parameters are best considered in context with the extracted resonant parameters of the crystalline ice, displayed in the middle panel of the Figure 4.7 and listed in the Table 4.2. Comparing

OD resonance	ω [cm^{-1}]	A_q	ϕ_q [π]	Γ_q [cm^{-1}]
free OD	2730	4	0.15	7
dangling O (D–down)	2610	3	0.56	42
partially coordinated	2490	16	1.23	73
fully coordinated (symmetric, ν_1)	2302	5	0.48	18

Table 4.2.: Parameters of SF resonances in crystalline ice

the two data sets we can clearly answer the question posed in the beginning and state that the surface of the amorphous and crystalline ice is indeed different. In the light of our findings we can also clearly see that the structure investigated previously by Denzler et al. spectroscopically resembled much more the amorphous modification. Characteristic is the position of the partially coordinated resonance that is shifted approximately 60 cm^{-1} towards lower energies in the crystalline case. One can readily understand this shift: in the Section 1.1.4 the influence of the molecular coordination on the vibrational frequency has been discussed, whereas it could be shown that the increasing D$_2$O coordination leads to a softer potential well for the hydrogen–bonded deuterium atom and thus to a lower OD vibrational frequency. A higher D$_2$O coordination, accompanied with the increased order in the hydrogen bonded system is expected for crystalline ice by definition.

The vibrational frequency is further closely connected to the distance between the two oxygen atoms creating the effective atomic potential for the hydrogen in a hydrogen bond, as demonstrated in the Figure 1.2. This is expected to be more defined, if the adsorbate is crystalline.

Comparing the widths of the fully coordinated resonances in either of the investigated cases, the amorphous modification really exhibits an almost two times broader symmetric stretch mode. The free OD vibration is a significant feature, but still relatively weak in both cases, considering its location in the interfacial layer and the orientation allowing to project the dipole moment change to a direction parallel to the surface normal in nearly all cases. This observation is consistent with the theoretical findings that for such an uncoordinated molecular species it will be energetically more favorable to reorient and saturate its hydrogen bonds to a maximum possible degree than to keep the order enforced by the underlying layers [Wit99]. The surface D$_2$O layer is thus *influenced* by the order in the hexagonal ice sheets below, but also possess a structure *different* from the bulk.

4.2.2. SFG spectra of D$_2$O on Ru(0001) in the low–coverage limit

Up to now, a rather thick ice layer was examined. Due to the hydrophobicity of the wetting D$_2$O layer on Ru(0001)[9], it is possible that the substrate influence does not play a significant role in determining the structure of the ice/vacuum interface beyond a coverage of ~8 BL. How do the vibrational resonances evolve with decreasing coverage and growing interaction with the substrate?

Coverage dependence of the fully coordinated mode intensity

The change in the intensity of the fully coordinated D$_2$O resonance for various coverages can be seen in the Figure 4.8. The corresponding peak in the crystalline ice is only visible if
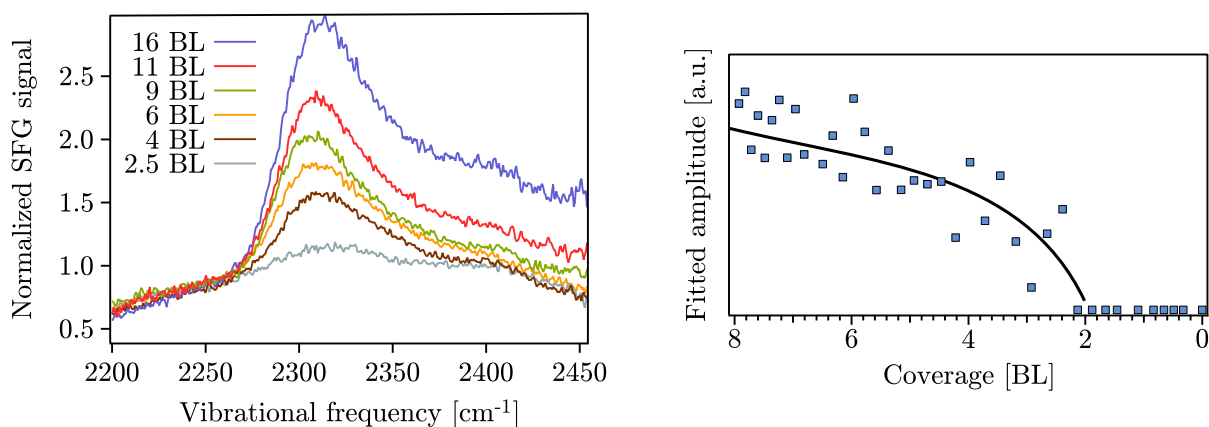
Figure 4.8.: Intensity and amplitude evolution of the fully coordinated OD stretch resonance. Left: Normalized SFG spectrum of amorphous ice is depicted for various coverages. The wing on the blue (right) side originates at least to some extent also from the partially coordinated mode. Right: Amplitude of the fully coordinated peak is extracted as a fit parameter from the SFG spectrum combined with a TDS measurement allowing to trace the actual water coverage. Note that the spectral intensity is not linearly proportional to the number of molecular oscillators and thus to the extracted amplitude ($I_q \propto A_q^2$). The black line is a guide to the eye.

---

[9]The term hydrophobic wetting layer may sound contradictory: It describes the unique property of the water adlayer on the Ru(0001) surface that wets the substrate, but the water–metal interaction leads to a structure that is very different from a typical hexagonal sheet in ice and thus the adsorption of further molecules on this wetting layer is less favorable than in the case of a 'normal' ice layer (see also the discussion in the following subsection).

experimental beam path is purged, from the wider feature in the amorphous ice just the red (left) wing can be observed if no purging is applied. With decreasing coverage the intensity of the resonance becomes gradually smaller and vanishes completely around 2 BL, whereas the strongest reduction of the resonant signal is recorded below 4 BL. Additionally, this behavior does not depend greatly on the ice modification.

This seemingly surprising result reflects the complexity of the investigated system. In the Section 1.1.3, the growth of crystalline D$_2$O layers on Ru(0001) obeying the Stranski–Krastanov mechanism has been introduced: If the water is dosed on this substrate, it first forms a closed, hydrophobic wetting layer and the consequently adsorbed molecules form clusters of various heights, keeping the first adlayer exposed up to a nominal coverage of several tens of multilayers. The most dramatic changes in this structure occur within the first 3–4 layers, where those formations mainly gain thickness [Kim07b, Haq07]. Further water layers contribute mostly to the height of these aggregates, nevertheless, the interfacial area still gradually increases. This structural consideration can explain the faster growing SFG signal at low coverages, as well as the increase in the SFG signal from the crystalline ice at larger coverages.

The structure of amorphous multilayers grown at low temperatures (below 60 K) is, however, different. They are believed to grow almost layer–by–layer for the first three bilayers on the Pt(111) surface [Kim06], but a higher roughness can be expected with increasing coverage due to the structural imperfections, probably a ballistic deposition process [Ste99] and also due to the Ostwald ripening (connected to the Gibbs–Thomson effect), leading to the preferential growth of larger structures created by random adsorption of the adsorbate molecules on the surface[10] [Das04]. This, again would lead to an increase in the SFG signal with growing layer thickness, whereas the larger surface area initially created by the closed layer could also explain the much larger resonant amplitude of the fully–coordinated mode in the amorphous case.

Even more intriguing is the disappearance of the fully coordinated mode below 2 BL. For 1 BL this resonance does not exist (see e.g. the assignment of the bilayer resonances in the reference [Thi84]), because assuming the standard bilayer structure as depicted e.g. in the Figure 1.10, the upper half of the molecules lacks coordination partners for hydrogen bonding from above and the lower oxygen plane from the bottom. The bond to the Ru(0001) surface can not mimic another water molecule. Moreover, the oxygen–oxygen distances, essentially determining the resulting OD stretch frequency are dictated mainly by the metal, which most probably expands the structure and leads to a shift of the resonance towards higher vibrational frequencies, where it could overlap with the partially coordinated species. In any case, as the coverage exceeds 1 BL, the appearance of the fully–coordinated mode is expected. Nevertheless, as it has been mentioned above, the wetting water layer is hydrophobic and the bonding to it not favorable for further D$_2$O molecules, which leads to the formation of the clusters on its surface, minimizing the contact area with the adlayer. At coverages below 3 BL the formed islands possess a low aspect ratio and thus the multilayers are preferentially stabilized by the weak interaction with the wetting layer rather than by the internal hydrogen bonding within the islands [Haq07]. Our result points exactly in this direction: if the first D$_2$O layer offered a possibility of the rather strong hydrogen bonding to further incoming water molecules, this structure would be hydrophilic and a layer–by–layer growth would be expected. The absence of the fully coordinated mode proves that this is not the case and that the D$_2$O molecules are formed only in thicker layers by interaction within the formed crystallites, resembling in the

---

[10]A further evidence for the rough structure can be found in our data presented at the very end of this Section: if we try to quench the vibrations of the interfacial D$_2$O molecules from the amorphous ice by coadsorbing H$_2$O, the amount of H$_2$O molecules needed to accomplish this is much larger (at least five times) than the equivalent of 1 BL. This strongly supports the rather high surface roughness in this case.

coordination the bulk ice structure.

Coverage dependence of the partially coordinated mode intensity

If the model of water multilayer on Ru(0001) discussed above is correct, the intensity (amplitude) evolution of the partially coordinated D$_2$O resonance with coverage is particularly interesting. This resonance namely should be visible nearly at all coverages and its vanishing would indicate either the detection limit of our setup, or the approximate coverage where the water molecules on the surface do not cluster and remain mostly adsorbed as monomers.

The partially coordinated OD stretch resonance is an unusually broad spectral feature (cf. Table 4.2). This is connected to the type of oscillators contributing to this mode: it is a characteristic oscillation not only of the well defined, coordinated OD bond within a molecule at the interface that exhibits the free OD vibration as well, but belongs also to many kinds of defects in the ice structure with a lower molecular coordination. As such, it is composed of many different modes[11] that, unfortunately, can not be distinguished experimentally. With decreasing coverage (and approaching 1 BL) the width of this resonance slightly increases, which can be understood as the influence of the metal that forces the altering of the ice structure and thus a formation of larger number of the reduced–coordination species. Interesting is the evolution of the resonant amplitudes depicted in the Figure 4.9. In both, amorphous and crystalline ice
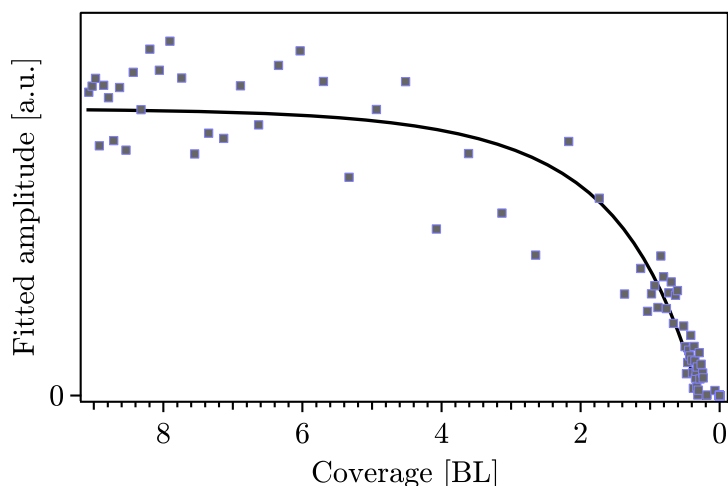
Figure 4.9.: Amplitude evolution of the partially coordinated OD stretch resonance. The black line is a guide to the eye.

the spectral intensity of the partially coordinated mode is nearly constant for coverages above 4 BL. Below this value a significant decrease can be observed, but the resonance is clearly present (with lower frequency of about 2450 cm^{-1}) also at coverages close to 0.25 BL. This would confirm the picture that the water molecules prefer to cluster on metal surfaces because the hydrogen bonding between them lowers the free energy of the system.

---

[11]Partial coordination itself does not indicate, which hydrogen bond is not saturated. The vibrational frequency of a water molecule with three coordination partners will differ from the frequency of a water molecule engaged in hydrogen bonding with only two D$_2$O molecules. Further, there is a subtle difference in whether the incomplete coordination occurs on the hydrogen or the oxygen end, i.e. whether the molecule is a hydrogen bond donor or acceptor. Based on these considerations, the molecules belonging to this class are often characterized as e.g. single–donors double–acceptors (with all permutations of single and double and void placeholder), which is useful to distinguish them in theoretical calculations [Dev01].

Again, consistent with the previously discussed data we observe the threshold of the amplitude growth at 4 BL, where the thickness of the water clusters does not grow significantly anymore, however, in this case the intensity of the mode does not grow significantly with the coverage. One way to explain this is a purely geometrical consideration: the signal that is observed stems mainly from the flat surface terraces rather than from the sides of the tower–like water structure. As the former sites grow very slowly, only a little increase in intensity is expected when the amount of D$_2$O molecules dosed is larger. If we take the structure of bulk ice as shown in the Figure 1.4 (see also the bottom panel of the Figure 1.15), assume its periodic repeating and then terminate it from the side, a defect analogous to the side of an ice tower is created. The partially coordinated oscillator can either be oriented such that it vibrates nearly perpendicular to the surface normal and is thus not visible in the SFG on a metal surface (see Section 3.1.3) or in a way that the dipole moment change can be projected to the surface normal, however, in this case the adjacent oscillators will cancel its contribution, as the OD directions are distributed randomly and the structure is centrosymmetric. Moreover, the same cancellation effect can be expected from the presence of neighboring clusters, as the system is symmetric in the plane parallel to the surface[12].

Coverage dependence and origin of the free OD mode intensity

If one is interested in resolving the structure of the complete wetting layer, a particularly useful vibrational resonance to look at in the OD stretching spectral part is the free OD vibration. Despite the indication from the fully coordinated mode that the first layer is hydrophobic, which means that there are not many bonds that can easily coordinate further D$_2$O molecules on top of the first layer (and a free OD pointing to the vacuum would be such a bond), there are several possibilities discussed above, how the wetting layer could be arranged. The free OD resonance is a very pronounced, narrow spectral feature, not significantly influenced by an interaction with other vibrational modes and can be therefore recognized with a high sensitivity (it also interferes constructively with the non–resonant part of the spectrum). In contrast, the D–down (or dangling O resonance) discovered and identified here is rather broad and overlapping with the partially coordinated peak, however, it can be clearly recognized due to its different phase. Moreover, in crystalline ice the partially coordinated peak appears at lower vibrational frequencies, which facilitates its identification even more (see Figure 4.7). Graphs in the Figure 4.10 show the experimental data of the coverage dependencies for both discussed resonances. Again, the signal from the free OD vibration rapidly decreases below 4 BL, being almost flat at large coverages. A similar behavior is observed for the dangling O resonance. This evolution is also common for both ice modifications. Consistent with the observations published earlier [Den03b], the intensity of the free OD resonance is zero at 1 BL. The fit indicates a rather low, but still existent amplitude of the D–down feature even slightly below this coverage, however, due to the high intensity in the overlapping, partially coordinated resonance and the shift of the former towards lower frequencies with decreasing coverage, this cannot be resolved reliably.

Structure of the water bilayer on Ru(0001)   Information obtained from these spectra is very valuable: first, we can show that the resonant frequency of the dangling O (D–down) structure

---

[12]If one considers the partially coordinated resonance as the resonance of water molecule having one free OD vibration and thus another OD end only partially coordinated, the latter will most probably point towards the bulk ice and be responsible for the molecular bonding. The direction 'towards the bulk' is perpendicular to the surface normal at a side of an ice tower and thus invisible, but parallel to the surface normal at the ice terrace and hence amplified.
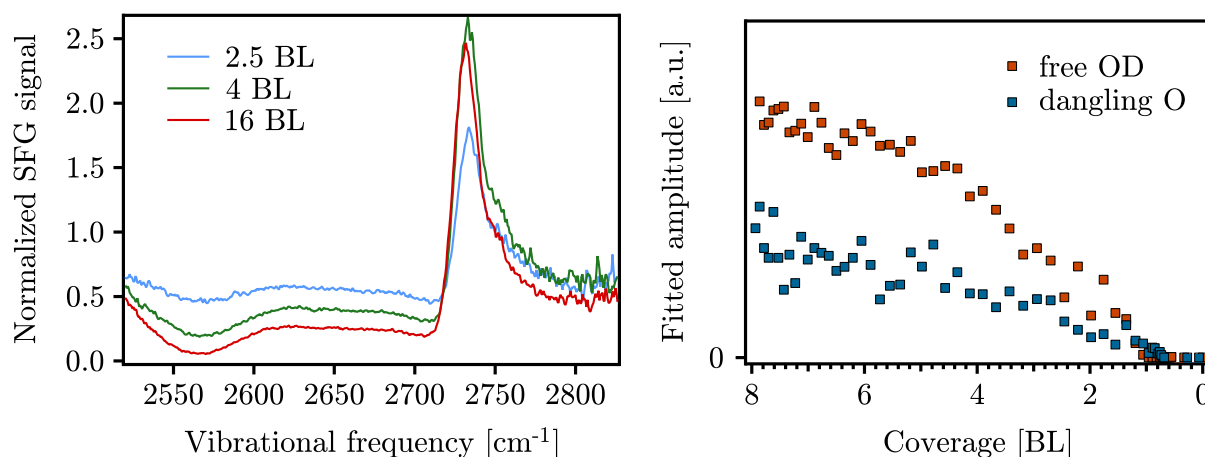
Figure 4.10.: Intensity and amplitude evolution of the free OD and the dangling O stretch resonance. Left: a series of SFG spectra for different amorphous ice coverages. Right: Decay of the amplitude of the free OD and dangling O resonance as a function of coverage in crystalline D_2O/Ru(0001). Data are extracted from the combined TDS and SFG study.

is different from that of the free OD mode and with decreasing coverage their frequencies do not converge, so that they cannot cancel each other even if present in the same ratio at the surface. One could argue against this consideration and assume that the D–down vibration gains exactly the vibrational frequency matching that of the free OD mode only if connected directly to the Ru(0001) surface. However, in such a case, this would have to be always visible in the SFG spectrum, as the symmetry of the system is also broken at the metal/ice interface. Nevertheless, as will be shown later, the resonance at $2730\,\mathrm{cm}^{-1}$ can be completely suppressed by dosing e.g. H_2O *on top* of the D_2O layer and thus it cannot originate from other than the ice/vacuum interface. This allows to definitively reject the mixed D–up and D–down bilayer structure from our considerations. Moreover, we have to discard any structure with D–up molecules as well, since this would be definitively observed in our spectra.

Is there then another structure of Ru(0001) wetting layer consistent with our observations? The molecular arrangement suggested recently by Haq et al. [Haq06, Hod09, Gal09] and displayed in Figure 4.11 seems to reproduce consistently all observations made on the D_2O/Ru(0001) system up to now. First, this geometry possesses the largest D_2O binding energy of all non–dissociatively adsorbed structures, which explains the wetting behavior best. Second, the calculated metal work function change almost exactly corresponds to the experimentally measured value, which is a requirement fulfilled only by a few other bilayer models. Further it is consistent with the He–atom scattering and the accessible LEED data. What is most important for our case, it explains the absence of the free OD vibration in either SFG and the RAIRS (reflection absorption infrared spectroscopy).

As can be seen in Figure 4.11, such a structure consists of hexagonal chains, whereas the structure (a) with long chains is energetically the most favorable. It is completely different from the standard bilayer model, but is only able to explain the hydrophobicity of the wetting layer, as this is can hardly occur in any of the ice–like structures (water and ice are generally hydrophilic). It does not contain fully coordinated species and the majority of the D_2O molecules is partially coordinated, consistent with our findings. The small fraction of the D–down bonds is very likely not detected for the reasons mentioned above, or below our detection limit due to the strong destructive interference with the resonant peak corresponding to the partially coordi-
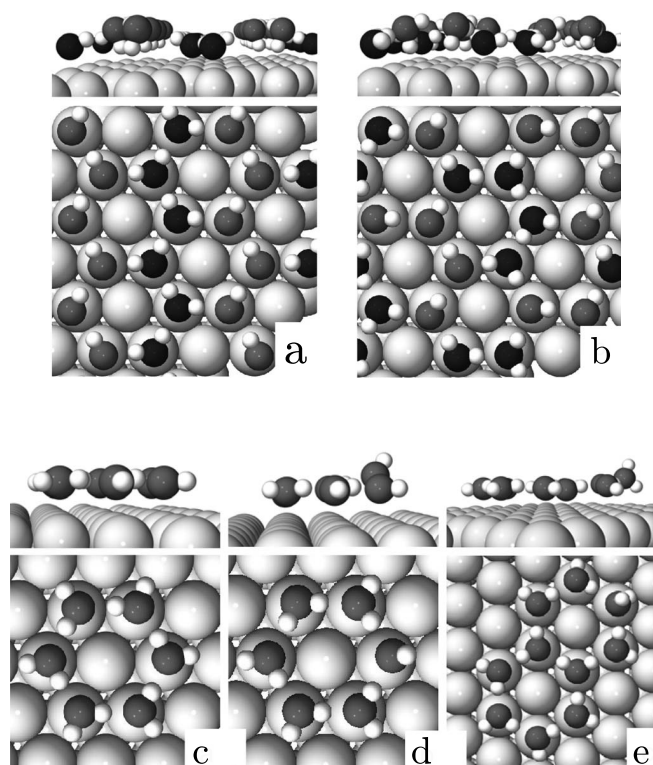
Figure 4.11.: A consistent model of the wetting D$_2$O layer on Ru(0001). In the top part a proposed geometry for the full bilayer consisting of hexagonal chains is shown (dark and gray shades represent a lower and a higher bilayer plane, respectively). As the coverage decreases, water hexamers are formed that possess no (or only a small fraction of) dangling OD bonds, but are composed almost entirely of partially coordinated D$_2$O molecules. Taken from [Haq06].

nated species (note the different phases in the Table 4.2). With coverage decreasing below 1 BL, the adlayer chains break down, forming hexagonal structures as can be also seen in the STM picture in Figure 1.13. These formations (especially the one depicted in Figure 4.11(c)) indeed do not contain dangling OD bonds anymore. Their binding energy is comparable, structures (c) and (e) (flat hexamer and double ring) exhibit slightly stronger bonding to the substrate than (d) (hexamer with enhanced hydrogen bonding).

With all these statements, the long–lasting controversy concerning the structure of ice bilayer and especially the contradictory results obtained from the previous SFG experiments could be successfully resolved. The theory (the structures in Figure 4.11 are supported by DFT, employing ultrasoft pseudopotentials for hydrogen bonding) and experiments are brought into accord, which indicates that for the one of the longest studied model systems for water–metal interaction finally our understanding reached a satisfying level.

Structure of the ice multilayers on Ru(0001): origin of the free OD vibrational mode The free OD vibration is a marker that can be used to evaluate and trace the structure of ice multilayers as well. The following investigations were motivated by the observation of its larger resonant amplitude in amorphous than in crystalline ice. Can the origin of the larger signal in the former case be found and if so, how does this enhance our knowledge?

A first reasonable assumption is based on the fact that the amorphous ice is known to be porous [Ste99]. The larger number of oscillators attributed to the larger amplitude could include those present in a pore, where the inversion symmetry is most likely broken, too. To test this hypothesis, one can prepare a sandwich water system: after dosing pure amorphous D$_2$O ice at low temperatures, H$_2$O gas is adsorbed on this sample (see Figure 4.12) and a SFG spectrum
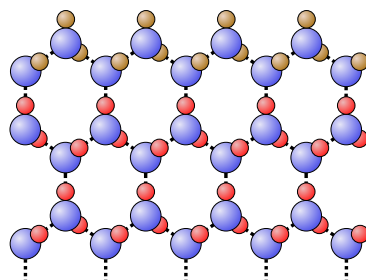
Figure 4.12.: A scheme of the free OD quenching experiment: on top of either amorphous or crystalline D$_2$O ice multilayer (deuterium atoms are filled by red), a certain amount of H$_2$O ice is dosed at low temperatures (hydrogens are filled green) and the free OD resonance is probed via SFG. The rather idealized structure in this scheme should represent both ice modifications.

is measured. As the H$_2$O stretch frequencies are significantly larger than those of D$_2$O, no signal from the surface species should be observed in the D$_2$O spectral region, as all of them are now coordinated by a H$_2$O molecule. This simple experiment produces interesting results. First, it is possible to quench the free OD vibration completely, as it is shown in Figure 4.13, which means that only the OD oscillators from the ice/vacuum interface contribute to the total
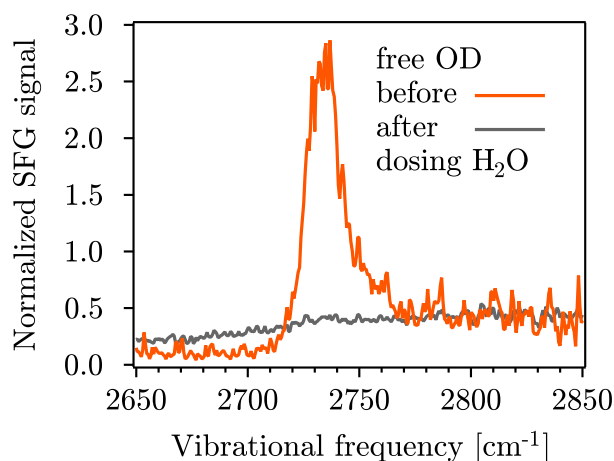
Figure 4.13.: A part of the SFG spectrum in the free OD region demonstrating the quenching of the resonant SFG signal intensity from ∼20 BL of amorphous ice (orange trace) upon dosing more than 6 BL of H$_2$O on top of this structure (gray trace).

signal. Indeed, the layers investigated in the present work are probably too thin (∼20 BL) to exhibit porosity [Kim06, Ste99]. Nevertheless, the amount of H$_2$O needed to accomplish the quenching is at least five times larger than it would correspond to one full bilayer. If a similar

experiment is performed with crystalline D$_2$O and amorphous H$_2$O overlayer[13], the quenching is still possible, however, clearly less ($\sim$3–4 layers) H$_2$O molecules are needed. A similar result can be achieved, if the rare gas (Xe) is used instead of H$_2$O, here, however, a full quenching cannot be accomplished probably due to a much lower desorption temperature (sensitive also to the actual adsorption site) that is easily reached upon irradiation with the visible and IR probing pulses.

The observation for the crystalline ice is readily understandable: the crystalline D$_2$O clusters possess a much larger surface area than a closed wetting layer and consequently the amount of water required to cover all surface sites will be larger than 1 BL. On the other hand, the contribution to the total SFG signal from the free OD oscillators located at the cluster sides is rather low due to their geometry (see the discussion above concerning the partially coordinated OD resonances at those sites), so it is not necessarily required that H$_2$O fills the gaps between the individual clusters completely. In any case, the number of coadsorbed H$_2$O molecules is only slightly higher than for a flat film on Ni(111) of comparable thickness [Cal92].

In contrast, amorphous ice is believed to grow layer–by–layer [Kim06, Haq07], so the only feasible explanation for the large amount of H$_2$O needed to quench the free OD signal is the existence of a very rough structure already at coverages of about 4 BL (even here more than 2 BL of H$_2$O need to be dosed). The possibility, that the increased number of H$_2$O molecules is a consequence of its preferential adsorption on already existing H$_2$O patches can be excluded based on the similar Xe–coadsorption results: at temperatures used in the experiment, the rare–gas is not able to form multilayers (it physisorbs at much lower temperatures of around 60 K [Sch93]) and possess an increased binding energy only to the water layer. The larger amount of H$_2$O molecules needed in the amorphous case to suppress the free OD resonance, is therefore an unambiguous proof of an extended surface area.

Unfortunately, we cannot obtain the information about the actual structure or mechanism leading to the amorphous surface roughening from our data. Nevertheless, with this experiment we confirm the conclusions made earlier, based on the observation of a coverage–dependence of the resonant amplitude, belonging to the fully coordinated resonance in amorphous ice (see also the discussion on page 137).

By investigating the behavior of the free OD resonance, we are able to reproduce many of the data known for ice and discussed in the Section 1.1 and additionally show that they are relevant for our metal supported system as well. If the sandwich system, schematically depicted in the Figure 4.12, is slowly heated (with a rate corresponding to $0.5\,\mathrm{K\,s^{-1}}$) and the spectra in the region around $2730\,\mathrm{cm^{-1}}$ recorded, one obtains a graph depicted in the Figure 4.14 that demonstrates all relevant processes in ice in the accessible temperature range in a very compact way. In the beginning (at 90 K), H$_2$O covers the D$_2$O ice layer so that no signal belonging to the free OD resonance can be detected. As the temperature increases, the glass transition is passed around 120 K. As the ice in this region forms the highly mobile 'water A' structure with enhanced molecular diffusivity, the water isotopologues intermix and the free OD mode becomes increasingly visible. Upon water crystallization, indicated by the shoulder in the TDS spectrum, the water crystallizes and becomes more compact rapidly, which leads to a drop in the SFG signal. Finally, upon reaching 1 BL, the observed vibrational signature vanishes, again reflecting a different structure of the ice, as discussed above.

---

[13]Preparing a crystalline H$_2$O overlayer is not possible, as at temperatures far below the phase transition those two isotopologues intermix via diffusion.
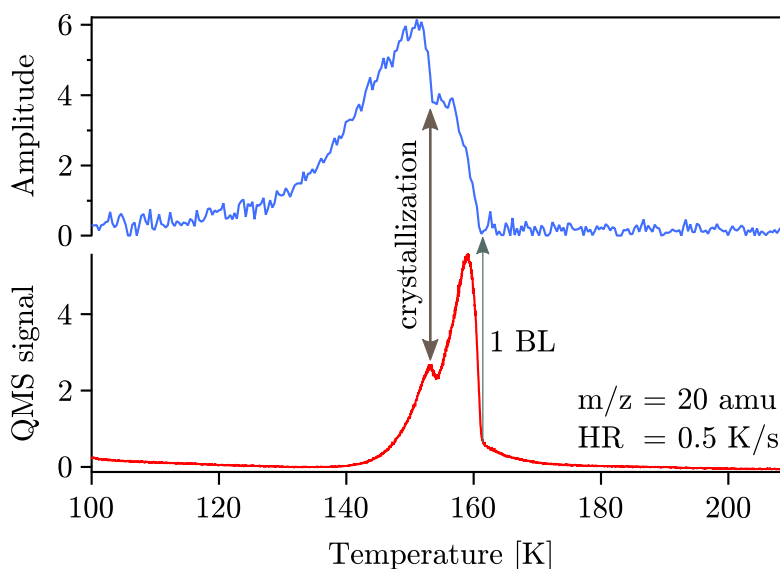
Figure 4.14.: A combined TDS and SFG study aimed to resolve the processes taking place in ice between 90–200 K on a molecular level. A sandwich system H$_2$O/D$_2$O/Ru(0001) is heated (the bottom panel shows the desorption trace as recorded in the TDS) and the evolution of the free OD amplitude extracted from the SFG data (top panel) observed. The glass transition accompanied high diffusivity of the water molecules can be observed (around 120 K), as well as the sharp phase change between the amorphous and crystalline phase. At a 1 BL coverage the free OD signal disappears. The slightly unequal levels in the free OD trace before and after the desorption are a consequence of the considerably changed non–resonant background in either case and can be regarded as noise.

These are convincing arguments that support the idea to investigate the response of the interfacial water molecules to a change in the environment or structure (not only) of the underlying substrate. Being inspired by the 2PPE results, showing a possibility to capture an *stable* electron on top of a crystalline D$_2$O ice on Ru(0001) (those are summarized in the Section 1.2.3), we were very interested to explore this phenomenon from the water molecule's point of view. What is the *structure* of the substrate that is capable to support an excess charge? The charm of this question led to the origin of the following Chapter.

4.2.3. Conclusions

In this Chapter we could resolve the long–lasting controversy concerning the structure of the ice layer in D$_2$O/Ru(0001), which is one of the longest studied model systems for water–metal interaction. Our contribution is essential in order to bring together the results obtained from the SFG spectroscopy and other experimental techniques.

In the structure of the wetting layer (and below) we could convincingly show the absence of OD stretching modes attributed to the molecular oscillators pointing towards the vacuum (free OD) *and* pointing towards the surface (dangling O, D–down). This confirms the wetting layer structure proposed by Haq et al. [Haq06], consisting of hexagonal chains and thus being significantly different from the classical bilayer derived from the bulk hexagonal ice.

By investigating the fully coordinated OD stretch vibration, we could further bring evidence for its *hydrophobicity*, manifesting itself in the surprisingly low coordination of the D$_2$O

molecules up to a nominal coverage of $\sim 2\,$BL.

From the evolution of the partially coordinated resonance we deduced a rather rough surface of D$_2$O ice on Ru(0001). We supported this finding by a combined SFG and TDS study of the 'sandwich' system H$_2$O/D$_2$O/Ru(0001).

We could show the remarkable difference between the *surfaces* of the amorphous and crystalline ice. Despite of the large amount of undercoordinated molecules at the ice/vacuum interface, its structure is not disordered and liquid–like as in many comparable cases, but at least at low temperatures the influence of the underlying ice substrate is shown to play a large role in determining the properties of the interfacial layer.

The latter finding was possible due to the advanced preparation procedure enabling us to prepare a smooth, crystalline ice, which was confirmed by the combined TDS and SFG experiment, showing a characteristic change in the spectra upon crystallization.

5. Vibrational response of ice to excess charge confinement

The following Chapter is by no means connected to alchemy, even though it tries to find the 'elixir of longevity' of the long–lived electron (see Section 1.2.3) and achieve the 'ultimate wisdom' at least what the stabilization processes, following the excess electron excitation on top of a thin ice layer, concerns. We employ an intrinsically *surface–sensitive* technique, SFG vibrational spectroscopy, to study the *surface* of ice, experiencing electron photoinjection from a metal substrate. As this newly discovered excited electronic state must be considerably delocalized *and* is limited to a certain pre-existent ice structure *and* the presence of the free charge obviously changes those 'electron traps', a study of the structural evolution of the interfacial D_2O layer along the stabilization process can significantly contribute to our knowledge about the electron localization phenomena.

The picture, we could gain from our data is discussed in the following way: after the experiment and its limitations are introduced, the *spectral* changes in the OD stretch region of ice are examined, together with the additional phenomena accompanying the electron localization at the ice surface. Several possible scenarios that could explain our observations are considered and tested. A microscopic insight is finally obtained by investigating the ultrafast dynamics of the confinement process and by comparing the excess charge stabilization in the H_2O and D_2O ice.

5.1. Long–lived excess electron confinement

In the previous Chapter, thin (up to 20 BL) D_2O layers on the Ru(0001) surface were characterized by means of the interface–sensitive SFG vibrational spectroscopy and the sensitivity of this method to the local structure on the ice surface was demonstrated. How does this structure change upon electron localization?

To answer this question, we enhance our setup used for the experiments discussed previously and employ an additional ultrashort UV beam[1] that is in spatial and temporal overlap with the visible and infrared pulses used to probe the vibrational response of the adsorbate. If the D_2O/Ru(0001) sample is irradiated by the UV light, the photons are absorbed in the metal, as ice is transparent in this wavelength range [Kob83]. The general scheme of this process is sketched in the Figure 5.1: The incoming light excites the metal electrons and they populate the unoccupied states above the Fermi level (E_F), most notably the horizontally delocalized first image potential state with the maximal probability amplitude above the ice surface (for more details refer to the Section 1.2.3). Most of the electrons decay back into the metal within a short time (after 500 fs there is no intensity in the peak belonging to the first IPS state as can be seen from the Figure 1.21), but some of them populate a lower–lying level, whose energy with respect to E_F considerably decreases with time (cf. the gray arrows in the Figure 5.1). The decay of the electron back into the metal is now hindered either by the poor wave function overlap with the metal states *and* by the absence of states in the bandgap of a crystalline solid

---

[1]Its wavelength is equal to 266 nm (4.66 eV) and the pulse is created in the non–collinear optical frequency tripler described in the Section 3.3.
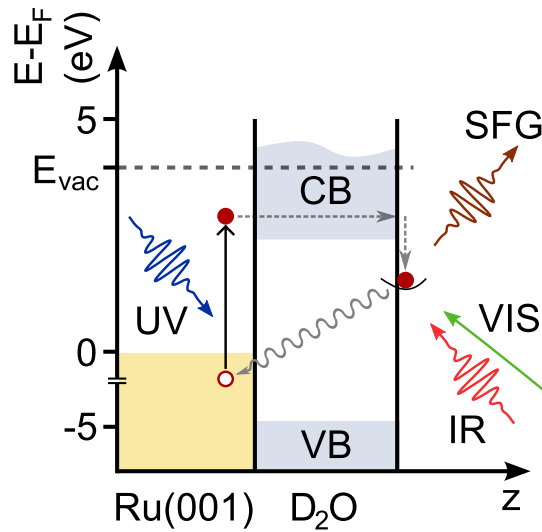
Figure 5.1.: A schematic illustration of the investigated phenomena. The goal of the presented experiment is to gain an insight into the mechanism of the extraordinarily strong electron stabilization caused by the D_2O molecules in the vicinity of the crystalline ice/vacuum interface. After an electron from the underlying metal is excited by the UV pump pulse, it is localized in a horizontally delocalized, unoccupied state at the ice surface. Water molecules reorient and screen this excess charge very efficiently, which lowers the energy of the populated level with respect to E_F. The mechanism of this screening is investigated by the interface–sensitive SFG vibrational spectroscopy.

(see Section 1.1.2), so only a slow radiative decay can proceed. For this reason, the lifetime of an electron at the ice/vacuum interface can reach several minutes[2]. This is the point, where the SFG vibrational spectroscopy can show its brilliance: as discussed earlier, the stable electronic state does not exist in the ice bulk, but the probability density of its wave function ($\langle\Psi^2\rangle$) is maximal at the ice/vacuum interface. This can be probed *in situ* by SFG, as the scheme in Figure 5.1 shows and by employing sufficiently short laser pulses, the dynamics of the stabilization process can be traced as well.

An important aspect of the measurement, not immediately clear from the simple scheme, is that the ice surface is always probed *in absence* of the electrons. This has two reasons: first, the probing visible light (800 nm; 1.55 eV) possess enough energy to excite the localized electron either into the conduction band of the ice, from where it can decay back into the metal very efficiently, or directly into the vacuum. Second, the number of excess charges that undergo localization is rather low[3], so that vast majority of sites present on ice surface does not experience any charge confinement. As the vibrational spectrum of ice arises from phonons (collective lattice vibrations) and not from the vibrations of individual molecules, such an isolated (and in every instant of the measurement rare) site can not be distinguished in the resulting SFG signal.

---

[2]Several minutes is the characteristic lifetime of e.g. phosphorescence as well, which is in a certain sense an analogous process. However, there the decay of the excited state (i.e. of a state above the Fermi level) is hindered by the quantum–mechanical selection rules, as the spin multiplicity of either state is different.

[3]The estimate, based on the fluence dependence of the intensity in the e_T peak in the 2PPE measurements is that per 10^3 surface D_2O molecules, there is only one trapping site with an appropriate structure, capable of electron stabilization [Ber09].
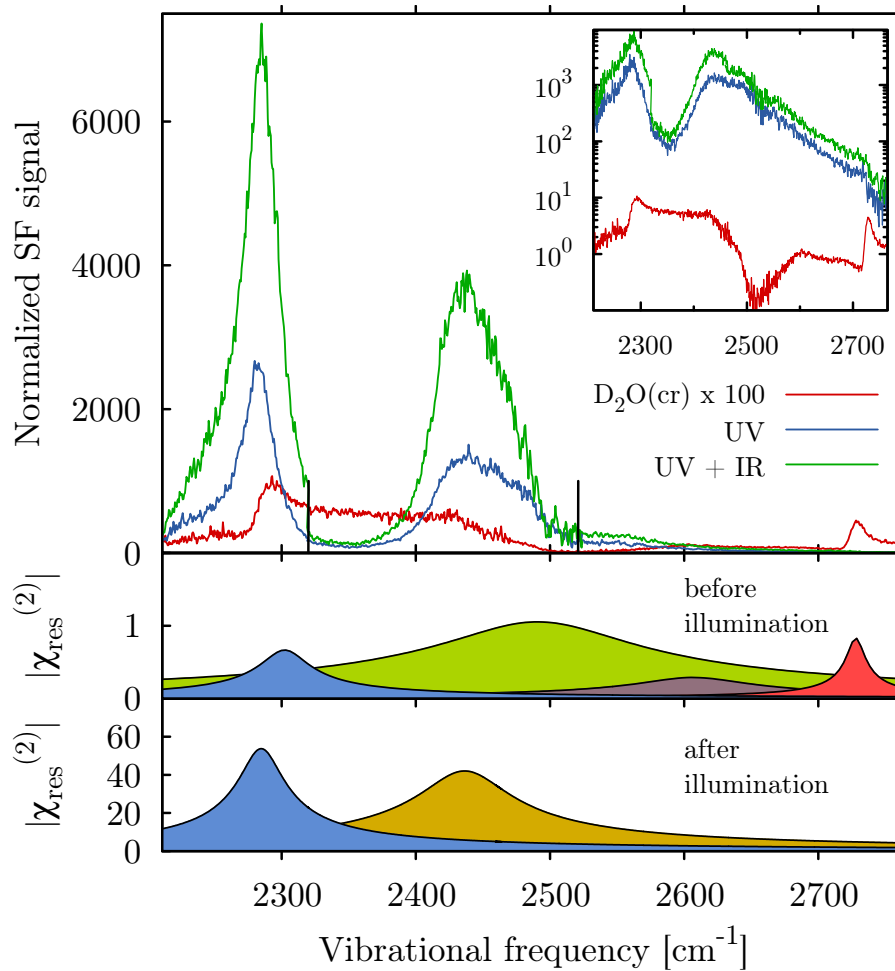
Figure 5.2.: Spectral changes in crystalline ice after UV illumination. In the top panel, a SFG spectrum of crystalline ice on Ru(0001), normalized to the incoming IR intensity is plotted (red trace; note the multiplication factor of 100). Upon UV irradiation, the SFG signal (intensity) is enhanced by a factor of $\sim 10^3$ (blue). If both UV and IR pulse temporally overlap on the sample, a further increase is observed (green). Inset shows the same spectra on a logarithmic scale, without a multiplication of the not illuminated spectrum. In the middle and bottom panel, a fit of Eq. 3.26 to the experimental data yields the vibrational bands for the crystalline ice and the ice after UV irradiation. Black vertical lines mark the boundaries between the three distinct spectral windows mappable by a single broadband IR pulse.

Electron localization: a water molecule's point of view

Having understood the excess charge localization from the 'electron's point of view' and being aware of the type of answer, the SFG vibrational spectroscopy can provide, we can look at the reaction of the water molecules to the electron confinement. Figure 5.2 displays the changes in the vibrational spectra of 10 BL crystalline ice after 20 min of UV illumination[4]. The red trace (note the multiplication by a factor of 10^2) represents the SFG spectrum of crystalline

---

[4]The overall UV fluence incident on the spot, where the SFG measurement is performed amounts to $\sim 1\,\mathrm{mJ/cm^2}$, however, due to the Gaussian profile of the employed laser beam, the total photon doses absorbed in various areas within the spot diameter differs considerably.

ice, analogous to that shown in the Figure 4.7. If the very same sample is irradiated by 4.66 eV photons, a dramatic increase in the SFG output signal is recorded (blue line). In contrast to the expectation that an excess charge localized at the ice/vacuum interface will change mainly the vibrational frequency or intensity of the free OD vibration, this is overwhelmed by the signal from the two adjacent peaks at $2285\,\mathrm{cm^{-1}}$ and $2435\,\mathrm{cm^{-1}}$ as can be clearly seen in the inset of the Figure 5.2. The newly formed peaks are extraordinary stable at temperatures below $100\,\mathrm{K}$ and the spectrum does not revert to the original state on timescales much longer than several hours.

Additionally, if the experiment is repeated with the ice sample of the same thickness and both, the UV and the resonant IR beam are on the sample during the whole time, even a larger intensity increase can be observed, as indicated by the green curve. Nevertheless, the peak positions remain the same, only the relative intensity of the vibrational modes depends on the IR frequency used and leads to an apparent discontinuity in the normalized SFG spectrum at the place, where two adjoining spectral windows are merged.

What does such a dramatic (and persistent) signal increase mean? It could be caused by an increased number of oscillators active in the SFG process, or by a much better alignment of molecular axes, so that vibrations formerly forbidden by the metal surface 'selection rule' (Section 3.1.3) become visible, or by dramatic changes in the structure of water, leading to a new, or strongly modified $\chi_{\mathrm{eff}}^{(2)}$ tensor. The latter could be even a water dissociation, leading to a presence of charged ions at the interface that could create a large electric field across the layer, so that nonlinear optical processes of different kind might occur (e.g. the Electric–Field Induced Second Harmonic generation (EFISH) [Ter62, Lee67, Dwo00]).

To discuss those possibilities, we need to gain a better understanding of the spectral response of the water layer. As a first step, one can try to fit the spectrum after UV irradiation to the model employed and described earlier. The resonant parameters obtained in this way are depicted in the bottom panel of the Figure 5.2 and listed in the Table 5.1. Due to the negligi-

OD resonance	$\omega\,[\mathrm{cm^{-1}}]$	A_q	$\phi_q\,[\pi]$	$\Gamma_q\,[\mathrm{cm^{-1}}]$
new resonance	2435	400	1.85	30
fully coordinated (symmetric, ν_1)	2285	300	0.90	15

Table 5.1.: Parameters of resonances in the SFG spectrum of crystalline ice after UV irradiation

ble signal from the non–resonant background, as compared to the resonant part, the fit offers reliable values only for the peak position, phase and the width, however, the estimate of the amplitude may vary ($\pm 10\,\%$), depending on small changes in the non–resonant amplitude A_{NR} that still lead to an excellent fit to the data. In any case, the intensity increase amounts to at least three orders of magnitude ($I_{\mathrm{SFG}} \propto |A_q|^2$).

As it could be expected from the rather long irradiation time between the initial and final spectrum in the Figure 5.2 mentioned earlier, the described changes are not instantaneous. If the SFG spectrum is measured together with the UV pumping beam on the sample (and hence slightly influenced by either beam as will be discussed later), one can trace the SFG signal buildup and follow the temporal evolution of the spectrum. This is best demonstrated by the Figure 5.3, showing the very fast growing two resonant amplitudes at vibrational frequencies listed in the Table 5.1. By the inspection of the data one can find that the essential changes in the spectrum involve only a slight shift of the vibrational mode at $2302\,\mathrm{cm^{-1}}$ in crystalline ice
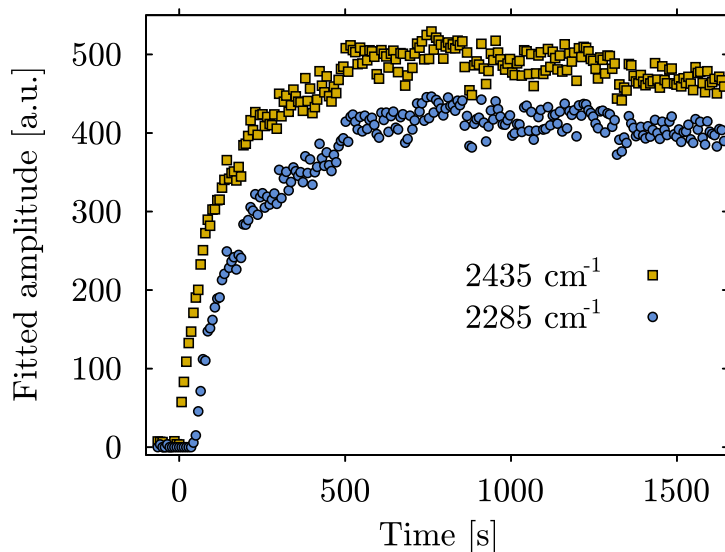
Figure 5.3.: Temporal evolution of the resonant amplitude (extracted from the data fit) for the vibrational modes at $2285\,\mathrm{cm}^{-1}$ and $2435\,\mathrm{cm}^{-1}$ during irradiation with $\sim 1\,\mathrm{mJ/cm}^2$ of $4.66\,\mathrm{eV}$ light. As IR and VIS light are present on the sample during the whole buildup time, numerical values from this graph should not be compared with the parameters in the Table 5.1.

to a lower frequency and its enhancement upon UV illumination. Along the buildup, another resonance at $2435\,\mathrm{cm}^{-1}$ becomes visible, nearly exactly copying the evolution of the former feature. Comparing its position to the available spectra of ice (Tables 1.1 to 1.3), it could belong either to the in–phase asymmetric, fully coordinated OD stretch (ν_3), or to the Fermi resonance between the symmetric, in–phase OD vibration (ν_1) and the overtone of the bending mode (ν_2). Even though the former can not be identified in the spectrum of the not irradiated crystalline ice[5], this assignment is more probable due to the different behavior of the resonances in some of the experiments discussed later (mainly the possibility to 'control' the buildup process and peak intensity by employing resonant IR pulses).

From seeing that the changes in the spectrum are of *resonant* nature at all stages, we can exclude additional nonlinear processes like EFISH from our considerations, as those should lead to an enhanced SFG yield, regardless of the IR wavelength. Furthermore, our spectra *after irradiation* show signatures of species characteristic more for the bulk ice, while the surface related vibrational modes do not encounter any enhancement. The shift in the vibrational frequency of the fully coordinated D_2O species towards lower values, as well as the slight narrowing of the corresponding peak are both indicative of a structure, where the hydrogen bonded network of the ice more resembles a perfectly aligned system of molecules with well defined distances, as it is rather in the ice volume than on the surface. The OD stretch frequency is namely a very sensitive measure for the hydrogen bond length [Fei04] and generally shows a decreasing trend with increasing water coordination [Del97, Buc07]. Is it possible that the SFG signal after UV irradiation is larger because the oscillators from the ice bulk contribute to the overall intensity?

---

[5]If a resonance at around $2430\,\mathrm{cm}^{-1}$ is enforced in the fit, its amplitude is very low and its inclusion does not further improve the fit quality.

Induced ferroelectricity in the D$_2$O ice   Consider a following scenario: if a sufficient amount of molecules screens the excess charge on the ice surface, their dipole moments might be aligned in its direction in a very efficient way by the phase transition from the hexagonal ice I$_h$ to the *ferroelectric* ice XI (see Section 1.1.2). This reorientation does not need to involve all the D$_2$O species, but just the number that is needed to create a suitable trap for the delocalized charges. A phase transition in the thin ice layers upon electron excitation is not an unusual process: it is observed also in other studies, e.g. the transition from the amorphous to crystalline phase is observed under similar conditions on graphite [Cha98].

If the dipole moments are aligned, the structure gains a net electric dipole moment, which is a similar process as the alignment of the magnetic domains in a ferromagnet. Such a water network is, however, not centrosymmetric anymore, so that the signal from the bulk can be indeed expected. The larger SFG signal would be thus caused by both, the molecular reorientation and by the larger amount of oscillators. Can such a behavior, even though fully consistent with our data and explaining the observations, be accepted? Can other experimental evidence put our hypothesis on a more solid ground? We shall find the answer to this question in the following Section.

5.1.1. Ferroelectric behavior of the water ice

After seeing the first SFG spectra and proposing the ferroelectric ordering of the ice layer as a response to the excess charge localization, the central challenge for this Section is to add more convincing arguments in favor of the net dipole alignment in the water layer and to discuss, how general can such a reaction be.

Maybe a good point to start with, is to introduce the nature of the ferroelectric ordering to be able to judge its feasibility. First, it should be noted, that this type of alignment does not affect the oxygen atoms ($\approx$ centers of mass) in the D$_2$O structure and thus the activation barrier of its formation is not large (obviously lower than that of crystallization or diffusion, setting on below 130 K). The only difference between the ices I$_h$ and XI consists of the unequal orientation distribution of the OD bonds connecting the hexagonal sheets of ice via hydrogen bonds. In ice I$_h$, the organization of those oscillators is random (although restricted by the ice rules), so that on average every ice layer exhibits an equal number of OD bonds pointing to the layer above and below and consequently possesses *no* net dipole moment. Ice XI, that is unstable under normal conditions, consists of almost identical hexagonal layers, but the OD resonances connecting them are all aligned in the same direction. This ordered structure could therefore be the thermodynamically stable form of ice at the low entropy and low pressure limit [Taj84] and as such is of considerable interest. Up to now, the only reliable method to create it in the laboratory is to dope an ice I$_h$ single crystal with OH$^-$ anions [Taj84, Jac95], which resembles our case in a way that the ordered structure is generated in a strong (local) voltage gradient, induced by the presence of the solvated ion[6]. Thin ice layers can also be grown (partially) ferroelectric on an appropriate substrate, like Pt(111), where the metal acts as a template for the proton–ordered bulk ice growth. The SFG experiments show a spectrum of H$_2$O adsorbed on this surface that (at larger thicknesses) very much resembles our spectrum of the D$_2$O after UV irradiation [Su98].

A characteristic sign of the ferroelectric ice structure would be a pronounced change in the

---

[6]The concentration of the alkali hydroxide (0.055–0.08 mol/dm^3) in the cited experiments is rather high and puts all water molecules less than six water molecules away from an ion [Cow99]. Nevertheless, it is believed that the role of the OH$^-$ ion is only to enhance the mobility of the D$_2$O molecules below 76 K, where the ice I$_h$ to ice XI phase transition takes place (it is kinetically inaccessible in a pure ice.

work function of the substrate metal, reflecting the net dipole moment created in the ice over-layer. To be able to measure it in the constrained geometry of the SFG chamber, the retarding field analyzer (RFA), described in detail in the Section 3.4 has been constructed and employed.

Work function changes upon ice ordering

To measure the work function under conditions of an SFG experiment is a particularly challenging task. As already discussed earlier, the classical methods (like e.g. a Kelvin probe, measuring the contact potential differences) can not be used mainly for two reasons:

(i) The change in the ice structure occurs only within a small region of the sample that is irradiated by the UV light (as can be checked by the SFG). Therefore the work function (Φ) of the *whole* sample contains no information about the ordering process. The preferred way is thus to measure the $\Delta\Phi$ only exactly at the point, where the irradiation occurs.

(ii) Optical access to the sample face during the complete buildup time is required. The optimal work function probe must be therefore able to measure the $\Delta\Phi$ remotely, without a contact with the surface and without an interference with the beam path designed to approach the sample under an intrinsically given, very flat angle.

One possibility to avoid both complications, is to map the kinetic energy distribution of electrons excited from the sample surface by the very same ultrashort UV pulse that induces the dipole moment reorientation in the ice layer. Unfortunately, its intensity is considerable and a precise measurement of the work function value is very inaccurate. The reason is the space charge in front of the sample, necessarily created by such intense pulses with low repetition rates. Even if the UV beam is attenuated close to the RFA detection limit, those effects can not be fully suppressed (see the discussion below). Nevertheless, despite of this experimental difficulty, such a measurement can provide valuable informations.

Figure 5.4 shows the kinetic energy distributions of the electrons arriving at the detector from the sample after the excitation. The measurement is performed before and after UV irradiation, whereas the first curve is taken at such a low pump beam intensity that no spectral changes are observed in the SFG spectra upon irradiation with this power on a timescale much longer than needed to complete the RFA measurement. The detected current (proportional to the integrated signal intensity from the channel electron multiplier) is plotted as a function of the retarding voltage on the analyzer grid, which is again proportional to the kinetic energy (E_{kin}) of the detected species, arriving parallel to the device axis. The curves are severely influenced by the space charge, as it is apparent from the shifted onset of the distribution curve: under ideal conditions namely, the electrons with the maximal E_{kin} (and thus detected at highest negative voltages) carry no information about the changed work function of the metal, but their energy only depends on the Φ_{detect} of the detector ($E_{\text{kin}}^{\text{max}} = h\nu - \Phi_{\text{detect}}$). As the latter value can not change during the experiment, both curves should start at the same retarding voltage. Knowing the photon energy of the exciting light (4.66 eV) and approximating the work function value of the detector grid with a tabulated value for the polycrystalline tungsten (4.55 eV [Lid07]), we can expect the first electrons leaving the sample after one–photon absorption with a kinetic energy of ≈ 0.1 eV (i.e. at a retarding voltage of -0.1 V). Due to the large work function of the detector (significantly larger than the work function of the water covered Ru(0001) surface), the electrons with low kinetic energies (close to zero) will arrive only at positive voltages, which is quite counterintuitive, as the electrons are indeed *retarded* by the *positive* potential that is put on the grid (although the actual potential with respect to the grounded sample is still negative
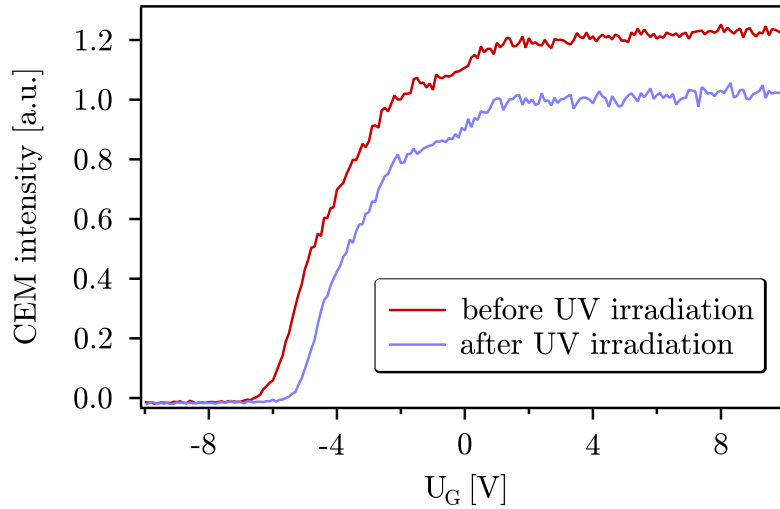
Figure 5.4.: Work function change in the crystalline ice on Ru(0001) upon UV irradiation as measured by the RFA. Plotted is the integrated intensity of the signal from the electron multiplier as a function of the retarding voltage. The graphs present raw data and are neither corrected for contact potential differences, nor for the different detection probability as explained in the text below.

or zero). The work function of Ru(0001) surface, covered by a crystalline water multilayer, is known (3.8 eV [Gah04]) and this implies that the kinetic energy distribution mapped in the experiment, yielding the dark red curve in Figure 5.4, should end at 0.8 V. This is apparently not the case – the curves are broader and shifted by further 4.66 eV towards higher energies. The former fact indicates the space charge, the latter one the reason, why it can not be avoided in our measurement: the low energy electrons generated in the one–photon photoemission are not detected at all, despite their orders of magnitude larger amount and instead, only electrons generated in the two–photon process are visible to our device. However, they naturally start to appear only at light intensities, where the direct photoemission has already generated a large electron cloud in front of the sample.

There is a number of reasons, why the low energy electrons are not detected and many of them are discussed in the Section 3.4.2. The probably most important is that they can be deflected much easier than the fast ones from their flight direction by an electric or magnetic field, whose presence in the SFG chamber can not be fully excluded, even though all separate contacts leading to all devices inside were properly grounded. Our setup also consists of three grids, allowing to employ the first one for attracting all charges by setting it to a large voltage (30 V), nevertheless, even then no distinguishable signal increase around 0 V (on the retarding grid) is observed.

What information bear the data depicted in the Figure 5.4 then? They show that if the D_2O/Ru(0001) system is left untouched and only the UV irradiation takes place between the two independent work function measurements, one can obviously detect *less* electrons and they possess *lower* energy with a *narrower* distribution after the molecular dipoles are aligned. All those effects are characteristic for less space charge. This unambiguously shows at least one fact: the work function of the system must *increase* upon irradiation, unfortunately, it is impossible to tell, how much. We can deduce the approximate value from earlier works – if the old 2PPE data is examined carefully, one can find a similar observation of the work function increase upon

UV illumination in the thesis of C. Gahl [Gah04], although not correctly interpreted and put in a quite different context. According to these results, changes of several tens of meV are to be expected.

Clearly, such a small work function difference is not compatible with an ordering of the whole ice layer, but this is also not expected. Ordering of a few percent of D_2O molecules is sufficient to produce a similar enhancement in the SFG signal as reported here and to account for comparable work function change [Ied98], which would fit to the number of electron traps estimated from the 2PPE data. If no *chemical* change takes place in the water layer upon illumination, this is a strong argument for the D_2O molecular alignment. In the next subsection, we therefore discuss the former option more thoroughly and evaluate its plausibility.

### Chemical stability of water upon UV illumination

It was mentioned earlier that water is transparent in the near UV and thus a direct light–induced dissociation is not probable, however, the system under investigation is more complex. Apart from a two photon absorption that might well excite the D_2O molecules to a state from where the OD bond breaking is feasible [Han90, Tho99], the excited electrons could interact with the water molecules and transfer substantial amount of energy, as will be discussed in the next Chapter, with the same result. Can we find some evidence for or against water dissociation in the SFG spectra?

Up to now, we considered the process responsible for the long living electronic state visible in the 2PPE measurements to be identical with the process investigated here, although a larger photon energy and beam intensities are employed in our work. We can test this assumption and obtain an important argument against e.g. the two–photon absorption in water itself: in the former work namely, no long–lived electronic state is observed in thin amorphous D_2O layers and only very thick layers provide a weaker signal comparable to that of crystalline ice. Simultaneously, samples 1 BL thick do not provide an electron confinement site probably due to their proximity (and thus large wave function overlap) to the metal. All those observations are consistently observed in the SFG as well: signal from 1 BL of D_2O on Ru(0001) does not change upon illumination and neither does the spectrum of thin amorphous layers (below ∼15 BL). The situation at larger amorphous ice thicknesses is shown in the Figure 5.5. In the top panel, the temporal evolution of the raw (not normalized to the IR intensity) SFG spectrum of 8 BL of crystalline ice is shown upon illumination with UV light (1 mJ/cm^2). The maximum IR intensity is concentrated in the region just below the free OD resonance at 2730 cm^{-1} and therefore only a wing of the giant signal increase can be observed, however, in this graph the free OD resonance can be seen more clearly. The apparent shift of this vibrational mode is in fact caused only by the increased intensity on the red side of the spectrum.

The picture is quite different in thick (20 BL) amorphous ice (bottom panel of Figure 5.5). The very same experimental conditions lead to a much slower intensity increase and the saturation level (photostationary state) that can be reached in this case is lower than that of the crystalline ice.

This all is not only consistent with the accessible 2PPE data, it is additionally a convincing argument that the *water intactness is not affected* neither *by the radiation*, nor *by the electrons* excited from the surface, even though they create a space charge in front of the sample under these experimental conditions. To test the compatibility of the SFG and 2PPE data, we even employed a nanosecond XeCl excimer laser, with the wavelength of 308 nm (4.03 eV) and observe analogous changes in our spectrum, albeit with a lower total intensity after illumination. Using this light source, any two photon process is extremely unlikely and the photon energy
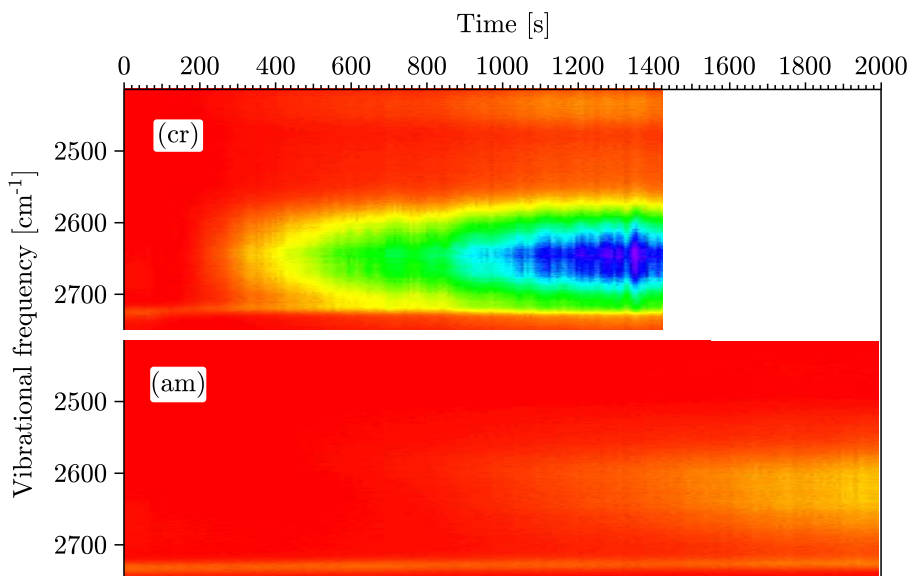
Figure 5.5.: Comparison of the buildup in the 20 BL of amorphous and 8 BL of crystalline D_2O layers on Ru(0001). The UV light starts to illuminate the sample after 71 s, which serves as an internal reference (e.g. to be able to normalize to the same IR intensity in all compared data sets).

matches the upper edge of the energies used in the former experiment. The similarity of the results affirms the assumption that the investigated process is the same[7].

Another scenario that involves bond breaking in the D_2O/Ru(0001) system, could postulate the water dissociation only after an interaction with the long–lived electron. However, a dissociation is not expected to be a reversible process, especially not in the water network that greatly facilitates the diffusion of the reaction products so that a recombination becomes improbable. Although it is not possible to reorient the ice layer completely back to the original state unless the temperatures are close to the desorption limit [Su98] (and thus the ferroelectric alignment is, to some extent and under our experimental conditions, an irreversible process, too), the process described here can be partly reverted by employing higher temperatures or (probably via the same mechanism) by irradiating the sample with the short and intense VIS laser pulses (stronger than usually used in the detection). In the latter way, the built–up SFG signal could be quenched to approximately 80 % of the maximum value and then enhanced again to nearly the same value by letting the UV pulse on the sample again. Such cycles can be repeated several times.

A further argument offer the thermal quenching experiments discussed more thoroughly later: if the sample is illuminated by the UV light at 55 K and after reaching the photostationary state annealed to a temperature below the desorption limit (particularly to temperatures in the

---

[7]The different intensities in the SFG signal at various wavelengths are most probably also compatible with the 2PPE data, showing an increase in the intensity of the e_T peak with increasing photon energy. Another factor represent the vastly different irradiation conditions upon illumination with an femtosecond UV pulse and with the output of the excimer. In the later part of this work, experiments with KrF excimer laser will be presented and even though the wavelength of this light source is close to the UV wavelength generated for our experiments in the tripler, for the reasons discussed there, the SFG intensity after the buildup with the nanosecond laser is always lower as compared to the ultrashort pulse induced SFG enhancement.

range between 110 and 140 K), the SFG signal is reduced significantly (to ~30 % of the photo-stationary value) as well. The original signal (as before the illumination) is reached again only at temperatures when the ice layer desorbs, but these are unfortunately not conditions directly comparable to the initial status. Adding to that, the TDS shows no sign of water dissociation, normally clearly visible as a high–temperature peak around 210 K, even not after a long UV illumination. It also shows (together with the SFG measurement) that the D_2O layers are not desorbing upon irradiation, and the dissociation is a process with a higher energy barrier than the desorption.

Summarizing all facts together, we exclude the possibility that the changes in the SFG spectra of crystalline ice after UV illumination are due to a photoinduced water dissociation mainly for two reasons: a two–photon absorption would necessarily induce a similar process in the amorphous ice, but for the layers with the same nominal thickness (up to 10 BL), no spectral change can be observed after illuminating the amorphous ice/Ru(0001). A dissociation induced by the long–lived excess charge can be discarded based on the (partial) reversibility of the process, leading to the SFG signal enhancement: the recombination probability of the defects in the ice network, created by a bond breaking, is expected to be very low and thus also the reversibility of a dissociation process should be considerably limited. So far, all observations are consistent and explicable by the ferroelectric ordering of the ice layer induced by the long–lived charges.

Is there a possibility, though, to induce the ordering in the amorphous ice as well and definitely exclude any dissociation scenario? One can think of stabilizing a charge in form of an anion at the amorphous ice surface: its field should have a similar effect on the D_2O molecular dipoles as a long–lived excess electron, but the reaction pathways in its presence should be different. For this purpose, we dose a small amount of the electron scavenger, $CFCl_3$, on top of the amorphous ice. After an electron excitation, the $CFCl_3$ molecules dissociate [Ryu06] and for a short time (until the Cl^- anionradical reacts with D_2O), they stabilize a negative charge at the ice surface. The response of the system seen in the SFG signal is depicted in the Figure 5.6: At 55 K, three samples are irradiated by the UV light: a pure, crystalline D_2O ice on Ru(0001) (blue rectangles), a crystalline sample prepared under identical conditions, but with a small amount (below 1 BL) of $CFCl_3$ adsorbed on top (gray rectangles) and amorphous sample of the same nominal thickness, again with the equal amount of $CFCl_3$ coadsorbed (red rectangles). In the first case, a smooth intensity increase is observed, similar to that described earlier. In both cases, where the electron scavenger is present on top of the ice layer, there is a jump in the intensity as soon as the first pulse reaches the sample. Nevertheless, while in the crystalline ice, the initial, fast increase is low and the buildup continues as without admolecules at the surface[8], the signal from the $CFCl_3$ covered ice is enhanced much more initially, and *decays* afterwards[9]. However, if the water dissociation would play a role in this process, we would expect that a *stable* photostationary state is reached as in both crystalline cases before.

In any case, the changes observed are only consistent with the ferroelectric ordering process, as described earlier: in the crystalline ice, the individual molecules are embedded in more saturated, stable hydrogen bonds. Therefore, the presence of an anion causes their *smaller*

---

[8]The lower intensity in the saturation can be explained by blocking a part of the sites, where electrons can be confined.

[9]Here, the different intensity at the maximum SFG signal is caused mainly by the lower ordering in the amorphous layer which leads to a lower intensity of the collective phonon modes responsible for the vibrational response of ice. In particular, the antisymmetric in–phase stretch (ν_3) is affected and its amplitude relative to the in–phase symmetric stretch (ν_1) smaller than in the crystalline case.
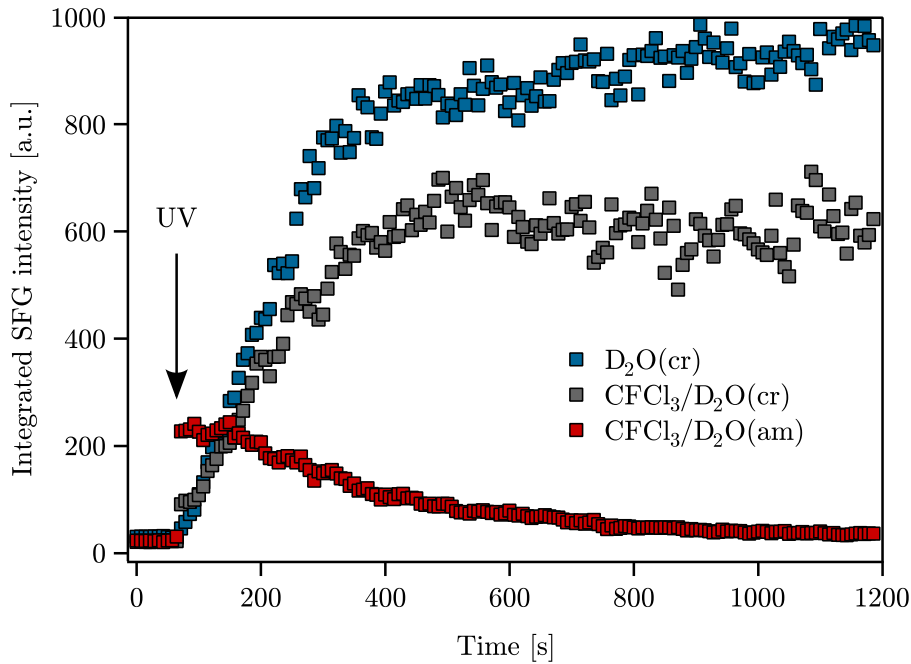
Figure 5.6.: Charge–induced SFG signal enhancement in the amorphous and crystalline ice covered by CFCl$_3$. Plotted is the integrated SFG intensity in the frequency region containing both growing resonances as a function of time, whereas the UV pulse is opened at 71 s, as marked by the black arrow. For details see text.

total reorientation in the first step (with first photons arriving, creating the Cl$^-$ anionradicals), as compared to the identical situation in the amorphous ice. After the anions are quenched by a reaction with neighboring D$_2$O molecules, electrons can be confined at the free sites in the crystalline ice and the buildup continues, although it is less efficient, because a part of the surface is definitively blocked by the admolecules. In amorphous ice, there are no species that could keep up the ordering after the decay of the anions, but the layer order is continuously revoked by the transient sample heating, induced by the intense ultrashort UV pulse. Additionally, as discussed earlier in the Section 1.2.3, the excess electrons in amorphous ice, with a lifetime of only several hundreds of femtoseconds, are not confined at the ice/vacuum interface, but populate the defects *inside* of the structure. As the defect distribution in ice is rather uniform, this yields a continuous changing, creation and disturbance of the dipole order. For thin amorphous layers, this is most probably the reason, why no change in the SFG spectrum is observed[10].

The current Section has introduced the most important experiments performed to probe the nature of the process following the UV illumination of thin D$_2$O layers adsorbed on the Ru(0001) surface. A close relationship to the processes investigated earlier by the 2PPE (see Section 1.2.3) was found and in the present study we could first explain those phenomena from the water molecule's point of view as a consequence of the ferroelectric ordering. This finding is able to explain a much wider variety of phenomena at different substrates[11]. We have also

---

[10]Moreover, the SFG is not sensitive to the centrosymmetric environments, as the oriented parts in the amorphous water layer, generated *around* an excess charge, certainly are.

[11]As an example, in ice on the Cu(111) surface, the lifetime of confined electrons is much shorter. Although this observation is hard to explain based on the electronic structure of the metal and the STM measurements reveal a similar growth of water on this surface (towers/clusters on top of the bare metal [Stä07a]) as in the Ru(0001)

shown that the ferroelectric ordering is not only a response of the water layer to an excess electron, but a similar effect can be expected in a wider class of charged particles. An analogous effect has been already observed on water surfaces containing ions of both polarities in previous investigations [Sch99, Jac95].

However, with these measurements the potential of the SFG method has by far not been exhausted. The following Section shows further experiments that allow to make conclusions about the *dynamics* and *mechanism* of the confinement process and hence provide an unique insight into the charge screening by D_2O molecules in our model system.

---

case, our result provides a hint why the stabilization process is different: The much smaller water–Cu(111) interaction (manifesting itself in the single peak in the TDS and a comparably small work function change) leads to a strong bonding within the closed D_2O network so that the formed crystallites in fact do not wet the metal layer. Nevertheless, it is this interaction with the metal that introduces a considerable strain into the ice structure – and thus defects that are mostly responsible for the orientation ability. The lack of this important channel in the more perfect network could explain its stiffness and low tendency towards the charge screening and stabilization.

5.2. Mechanism of the electron stabilization

In the previous part, the origin of the vibrational spectrum of ice has been attributed to the collective lattice motions, which means that we unfortunately can not distinguish a response of a *single* water molecule to the excess charge. This leads to the slow increase of the SFG signal that builds up as more and more oscillators are influenced and their *collective* motion becomes more feasible. Is there a possibility, though, to gain insight into the ultrafast dynamics of the reorientation process?

5.2.1. The IR assisted SFG signal enhancement

Influence of the IR wavelength on the SFG buildup

While discussing the first SFG spectrum (Figure 5.2) in the previous Section, the apparent discontinuity in the normalized SFG shape at the boundaries between two adjacent probing IR regions has been pointed out. They arise because the whole OD stretch spectrum of water can not be covered by a single broadband IR pulse, but more distinct spectral windows are scanned, each with quite different central IR frequency. However, the employed wavelength in the ultrashort infrared pulse evidently influences the resulting SFG signal. Therefore all the spectra up to now were taken either without the IR pulse on during the buildup process, or – if not possible – at a large delay between the UV and the IR pulse, so that their interference is minimal.

To demonstrate this effect, one can choose a spectral region (e.g. of the resonance at $2435 \, \text{cm}^{-1}$) and compare the result of the buildup process in this spectral window while inducing the dipole ordering in the water layer with temporally and spatially overlapping UV *and* IR beams of different frequencies. The result of such a measurement is summarized in the Figure 5.7. One
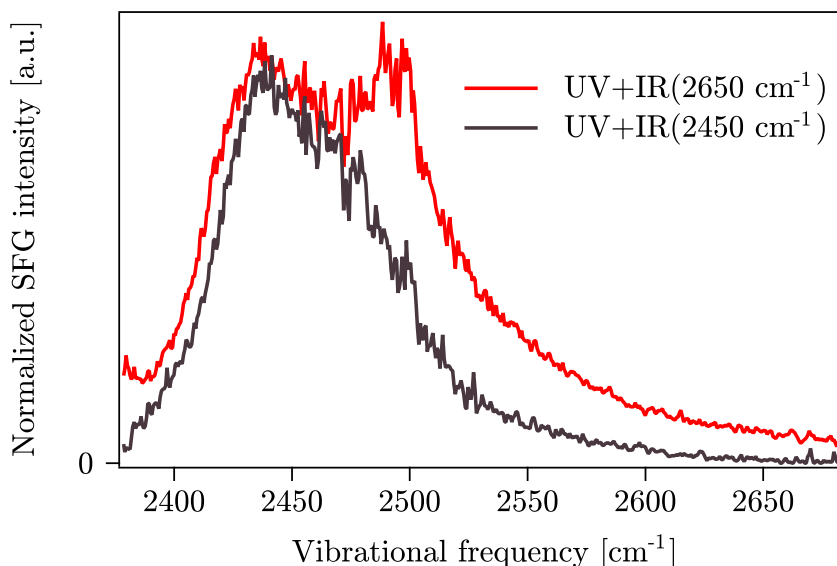
Figure 5.7.: Influence of the IR wavelength on the UV+IR induced buildup process. The SFG spectrum after irradiation with both (temporally and spatially) overlapping pulses is shown for two cases: when the IR wavelength matches the probing wavelength (dark curve) and when the infrared frequency employed during the buildup is higher than the frequency of the probing light. For details see text.

can clearly recognize the difference between the spectrum taken after illumination with the UV and the IR pulse matching the probing frequency and after an irradiation with the UV and an IR pulse shifted to larger frequencies: in the latter case the shoulder closer to the pumping frequency is much more pronounced. This indicates that we are able to actively influence the buildup process by employing additionally an IR pulse of a frequency in (or out of) the resonance with the resonance that should be enhanced (or attenuated) relative to the rest of the spectrum. The same picture can be obtained from the green curve in the Figure 5.2, showing the largest amplification of every vibrational mode when the probing IR light is in resonance with the same.

One experimental complicacy that should be mentioned here is the availability of only one coherent and intense IR source that has to be re–tuned between the pump and probe during the measurement. This experiment was only possible because of the high reproducibility of the set of parameters, repeatedly leading to a defined IR wavelength profile. Additionally, the shift of $\sim$200 cm^{-1} can be achieved by only a small change in the angles of the nonlinear media in the TOPAS, so that the temporal overlap is not lost while changing the frequency range back and forth.

Vibrational pre–excitation of water: a time resolved study

If the IR pulse has such a large influence on the SFG signal enhancement, it is possible that a vibrational pre–excitation can facilitate the D_2O reorientation and this is the reason for the additional increase in the SFG signal. The polarization of the ice layer induced by the IR pulse should show a limited lifetime, which can be tested by comparing the SFG signal buildup upon UV+IR irradiation, whereas a different time delay between those two pulses is employed and this is kept constant during the whole process. Figure 5.8 shows the dependence of the integrated SFG intensity in the photostationary state as a function of the UV–IR delay. The SFG spectrum was measured with an IR wavelength comprising both resonances visible in the enhanced SFG spectrum and the same was employed to co–induce the signal buildup. The visible beam has been only used at the end to check the saturation of the signal increase, although the quenching effect expected from its comparably small intensity should be negligible. The data show a considerable sensitivity of the SFG buildup to the UV–IR delay. However, the final SFG signal is only modified if both pulses (at least partially) overlap and the influence does not exceed their (mutual) cross–correlation. Evidently, to resolve the lifetime of the IR–induced polarization in ice lies beyond our experimental limit. Most probably, there is a very fast free induction decay process taking place, leading to an almost instantaneous fading of the IR induced polarization of the D_2O molecules[12].

---

[12]Another effect could seemingly explain our data as well: if, and only if the UV and IR pulses overlap, the total amount of electrons produced by the photoemission is larger than in the case, when they arrive separately (it is the same phenomenon that enables us to measure the cross–correlation between the IR and UV pulses). It could therefore also be assumed that the larger SFG intensity in the photostationary state is simply due to the larger amount of confined excess charges. However, the role of the IR pulse is not limited to a signal 'boost' – it is also responsible for the spectral changes that *can not* be explained by the increased amount of confined charges. A further argument delivers the measurement of the (UV–)fluence–dependence of the buildup process: with increasing fluence and thus the number of confined electrons, the SFG *intensity* in the photostationary state remains nearly constant and only the buildup *rate* changes significantly (if more electrons are injected on top of the water layer, the buildup process is accelerated, but we can not influence the *number* of water molecules that reorient, as this is given by the number of appropriate defect sites offering a stable trap for an excess charge). This is completely different in the measurement presented here: apart from the rate, the total *intensity* also changes dramatically. This could mean that the IR pre–excitation facilitates the reorientation of the species that would not be reoriented only upon UV irradiation (e.g. because of their distance to the excess charge or for
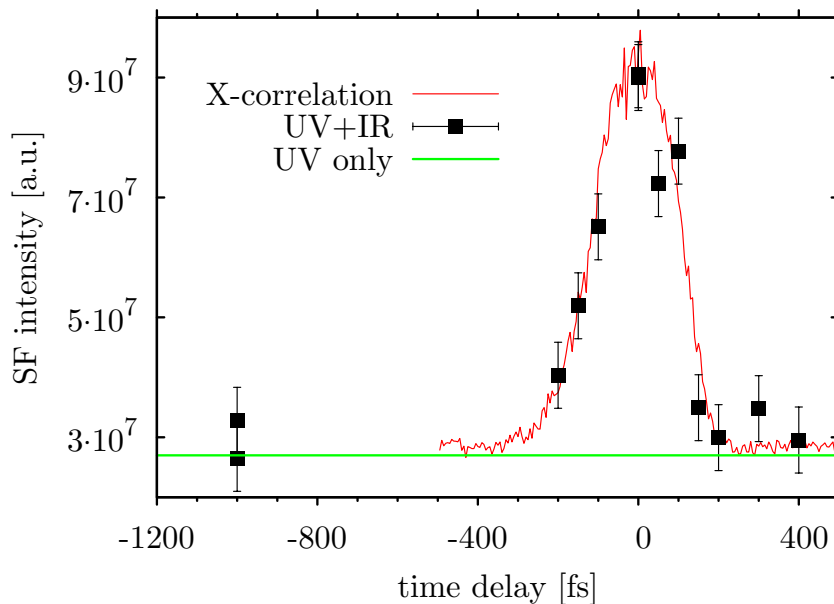
Figure 5.8.: Integrated SF intensity in the fully coordinated OD stretch vibrational region of ice as a function of time delay between the IR and the UV pulse (black rectangles). The green horizontal line indicates the integrated signal level obtained after irradiating the sample only with the UV light, the red curve is a cross–correlation between the two pulses. Positive (negative) delays stand for a pulse sequence IR (UV) prior to UV (IR).

There are indeed many indications that the vibrational dephasing occurs on a timescale comparable to the shortest achievable IR pulse length of our system ($\sim$130 fs) or even faster. The very strong coupling between the hydrogen–bonded molecules in a crystalline matrix explains this ultrafast dynamics below 100 fs (directly measured in the unpublished SFG work of our group) – a timescale that can be also understood as a consequence of the large anharmonicity of the hydrogen–bonded OD stretching mode [Ste01].

If any reorientational process can benefit from the ultrashort transient polarization discussed above, it has to be very fast as well. Flipping of the OD oscillators could provide a reasonable channel for such rapid changes[13]. To present a convincing argument in favor of this mechanism and to limit the number of possible other options, isotope resolved experiments have been performed. The results are displayed in the Figure 5.9. Despite of the relatively small molecular mass difference between H_2O and D_2O, the temporal evolution of the SFG spectra is significantly different in either isotopologue (much faster in the H_2O case). Based on this observation, the dipole realignment taking place in ice upon electron confinement cannot be connected to the movement of the center of mass of a D_2O molecule, but more probably involves the motion of D and H atoms, as the atomic mass difference between them is larger. This is exactly the process that is expected to take place in the phase transition from the ice I_h to ice XI.

---

another reason).

[13]A fast rotational movement (with no change in the center of mass) could also be considered in this context [Bar89].
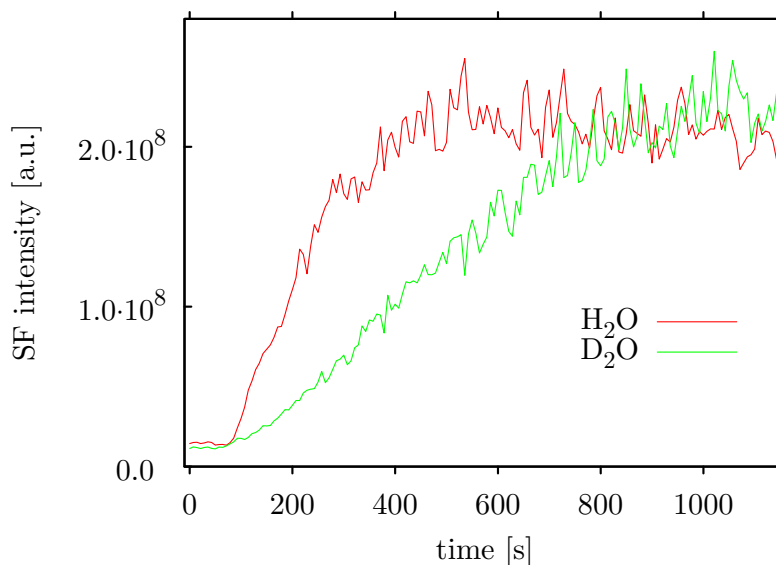
**Figure 5.9.:** Temporal evolution of the SFG signal of the two water isotopologues. The SFG vibrational spectra of H_2O and D_2O differ slightly in shape and intensity. Therefore in both cases the normalized SFG intensity in the vibrational region of fully coordinated OD(OH) oscillators is plotted as a function of the illumination time. The intensity of the employed UV light is the same in both cases.

Activation energy of the net dipole alignment in ice

Another important point in the discussion concerning the reorientation dynamics is the activation energy that a water molecule has to overcome to reorient and screen the excess charge. As all described processes take place even at temperatures around 55 K, the barrier should be sufficiently small. However, one has to take into account the not–negligible local heating induced by the pump and probe pulses.

This point has been emphasized many times before, but how important is actually the temperature of the sample and how does it influence the buildup of the SFG intensity upon UV illumination? To elucidate the influence of heat (deposited locally by the intense pulses, or contained in the different degrees of freedom that are activated at temperatures comparable to our working conditions, i.e. below 60 K), we have observed the SFG signal buildup at various sample temperatures. Up to 110 K, the overall enhancement does not show any temperature dependence, but as can be seen in the Figure 5.10, after this threshold, the SFG intensity in the photostationary state decreases with increasing temperature. Such a behavior is expected: the larger temperatures favor the ice I_h over the ice XI phase and a randomization of the OD bond directions is supported by unfreezing the degrees of freedom blocked in the 'colder' conditions. Nevertheless, one has to keep in mind that the process observed here is rather complex. If we neglect the influence of the IR pulse (coming with a great delay, so that this can be done safely) and the VIS light (of small intensity), the pulse mainly responsible for the growth seen is the UV. However, it can be expected that it in fact acts in two ways: it excites an electron into the ice layer and enforces its ordering *and* by heating the substrate it can support either the ferroelectric alignment in the presence of an electron or the random orientation of the D_2O molecules, if the negative charge is missing. As will be discussed later, either of those phenomena can become more dominant, depending on the experimental conditions. It is therefore hard
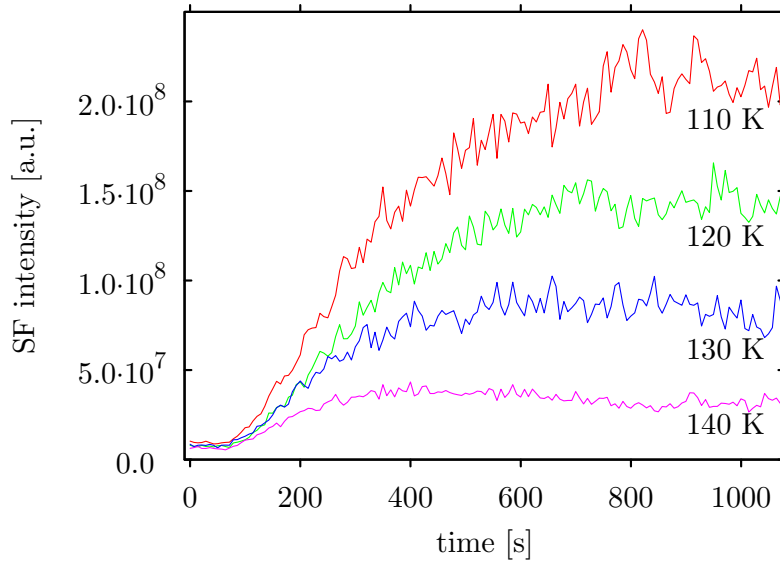
Figure 5.10.: The electron induced ferroelectric ice ordering is strongly dependent on temperature. The graph shows the integrated SFG signal during the illumination with UV pulses having a fluence of $\sim$0.8 mJ/cm^2 at different equilibrium sample temperatures.

to estimate the activation energy of the ordering transition from the measurement shown in the Figure 5.10.

On the other hand, one can make use of the fact, that at temperatures close to 100 K the two ice phases are close to equilibrium (phase transition) and approximate the activation barrier of the direct process with that of the reverse transformation. As we could show that the ferroelectric structure is less stable at higher temperatures, one can increase the sample temperature after a photostationary state is reached at 55 K. At different end temperatures, the decay rate and the final equilibrium level of the SFG signal will differ as well and considering an Arrhenius–like behavior one can estimate the activation energy of the ice XI $\rightarrow$ ice I$_h$ transition from the Arrhenius plot shown in the Figure 5.11 (the proportionality of the SFG signal to the square root of the number of oscillators is taken into account). Comparing the initial and final SF signal level reached at several different temperatures, the activation energy for the ice reorientation can be found and amounts to (25 ± 7) meV/molecule, which is consistent with the recent theoretical thermodynamic calculations [Joh98].
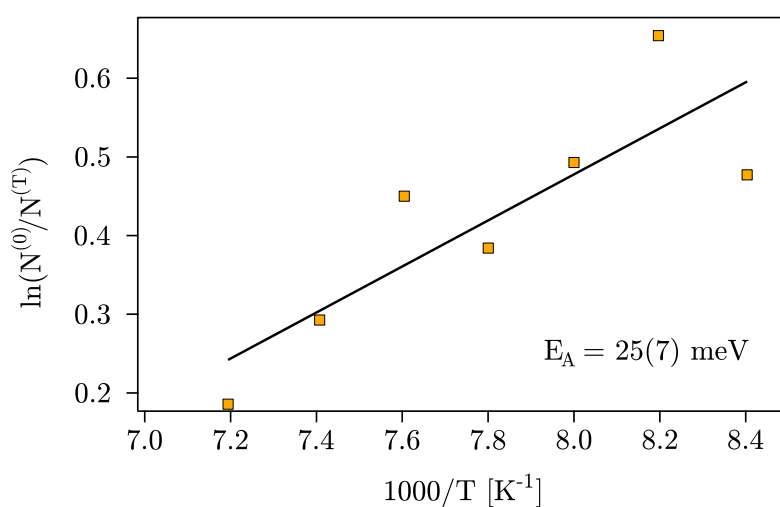
Figure 5.11.: An Arrhenius plot showing the temperature dependence of the photostationary SFG signal decay. After buildup at $55\,\mathrm{K}$ (up to saturation) the sample is heated to various temperatures and the decay of the signal is observed in very short SFG scans. The new equilibrium level at the elevated temperature is compared to the original (saturated) level at $55\,\mathrm{K}$ and their logarithmic ratio (after taking the square root of the intensity) is displayed on the y–axis. From the fit to the data, the approximate activation energy for ice reorientation is calculated.

5.3. Discussion

After the examination of the experimental data in the previous two Sections, the goal of this last part is to discuss the data in a more global picture, taking into account also the facts revealed by the two–photon photoemission results and offer a synthesis of the available information concerning the long–lived excess electron confinement in D_2O ice/Ru(0001).

Before a consistent picture of the phenomena observed in those works can be outlined, one point has to be mentioned: Despite of the high degree of complementarity and consistency between our work and [Bov09], our results are not completely identical, as they describe the same system from the water molecule's and the electron's point of view, respectively.

It has been stated before, that in the 2PPE spectra, the confined electron occupies an energy level denoted as e_T. Based on the threshold photon energy needed to populate it, it has been concluded, that the electrons reach this level by stabilization from a laterally delocalized image potential state located at $3.2\,eV$ above the Fermi level. Consequently, irradiating the crystalline sample with light of this wavelength should already lead to an accumulation of confined electrons (and thus to a buildup of the SFG signal) until a steady state between the population and bleaching is reached. Unfortunately, a light source of this frequency is not available in our setup. However, even if the D_2O/Ru(0001) system is exposed to $350\,nm$ ($3.54\,eV$) of Nd:YAG's 3rd harmonics, the SFG spectrum does not exhibit any distinguishable changes. The lowest photon energy at which we can observe an SFG intensity increase is $4.03\,eV$ ($308\,nm$ from a XeCl–excimer laser), whereas here the SFG intensity grows only by a factor of 3.

It is very difficult to compare such (in all aspects) different light sources, nevertheless, an excess charge localization was expected to occur upon illumination with lower energies as well. One possible explanation of this discrepancy lies in the *number* of confined electrons, created by the corresponding pulse. In the 2PPE spectra, the e_T peak intensity and hence the amount of confined electrons, grows rapidly with the photon energy used (and also beyond the energy of the first IPS). As the electron confinement in ice is dependent on a subtle balance between the localized state *population* and *depopulation* (bleaching), it is possible that in our intensity range the latter process is simply much more effective and a significantly larger amount of electrons has to be confined to be able to compete with the extremely efficient e_T state depletion.

Another factor might concern the different intensity in the nanosecond and the femtosecond laser pulse. The transient heating of the D_2O molecules upon irradiation can support their orientation in the external electric field imposed by the excess charge. The length of the pulses might therefore play an additional role, especially if the energy deposition is much faster (femtoseconds) of much slower (nanoseconds) than the heat diffusion in the system. As a result of this subtle equilibrium between the heat–supported ordering and disordering, the SFG intensity in the photostationary state obtained by the sample illumination with an excimer (KrF) laser is lower than with the femtosecond UV light of almost the same wavelength. The larger local heating upon sample illumination with different fluencies gives also rise to a slightly nonlinear fluence–dependence (power exponent of 1.6) of the orientation cross–section[14].

All other aspects investigated so far, however, offer a picture fully compliant with (and complementary to) the 2PPE data and in many cases provide an almost perfect possibility to understand the process on the microscopic level, which was not possible before.

---

[14]Although detailed examinations of this behavior were performed, the complexity of various independent phenomena contained there does not allow to draw any further conclusions from them. By using another light sources and by stretching the original UV light in several very thick glass plates we could, however, definitely exclude that the phenomenon under examination is a more–photon process.

Electron trapping in the amorphous ice on Ru(0001)

The short–lived electronic state in amorphous ice, as already discussed, is a consequence of the not negligible density of states in the bandgap of the amorphous solid. These states arise due to the structural imperfections and defects and the corresponding localization sites, possessing a better wavefunction overlap with the metal, are preferentially populated and depleted very fast ($\sim$400 fs). Although this lifetime is sufficient for D_2O reorientation as shown above, in thin layers the uniform defect distribution across the layer most probably hinders the net dipole alignment as new dipoles are recreated around every excess charge, canceling the same effect of their neighbors. Moreover, the absence of the signal in SFG could be explained also by the centrosymmetry of the 'solvation shells' and by the fact that a low amount of isolated, ordered molecules does not contribute to the *collective* phonon motion that is only visible in the vibrational spectrum of ice.

The seemingly strange phenomenon is the existence of the long–lived species (and of the corresponding SFG signature) in thick (more than 15 BL) amorphous layers. Explanations involving photoinduced crystallization (as on graphite [Cha98]) are not satisfactory, as the same effect would be expected in thin layers. Our result offers a much more elegant solution to this problem: Consider again the electrons localized for a short time in the uniformly distributed structural defects or irregularities. Every such 'trap' is populated with a probability that strongly depends on its spatial distance to the metal surface, as the wavefunction overlap with the metal surface states also decreases in this direction. Although this might not play such a large role for thin layers[15], in thicker layers a transient electric field gradient is created, as considerably more excess charges are present for a short time after the photoexcitation in layers close to the surface than in the layers further away. This causes the species in the upper layer to align their dipoles to a preferential direction, which again might create a good, horizontally delocalized electron confinement site. Consistent with this explanation is the much slower *rate* of the SFG signal buildup (the lifetime of the electrons in amorphous ice is considerably shorter, therefore the time for reorienting a certain amount of molecules is consequently longer) and also the lower SFG intensity in the photostationary state (only the upper layers can be reoriented and this process is continuously disturbed by the new electrons that recreate a new dipole alignment in the sample).

Electron trapping in the crystalline ice on Ru(0001)

The largest part of this Chapter was devoted to the electron localization in the crystalline ice. To the best of our knowledge, the experiment presented here is the first that describes a possibility to control the switching from the disordered to the ordered ice structure (and to a large extent also back) *without* using water contaminating molecules. Moreover, it could serve as a basis for the future IR or Raman spectroscopy studies of the vibrational signatures of pure and *perfect* crystalline ice.

Based on the rather small work function change upon ordering, one has to state that not all water molecules in the ice structure investigated here are aligned. For a ferroelectric ice/Pt(111), showing a slightly lower work function change, it was estimated that only about 0.2 % of molecules contribute to the overall net dipole moment [Ied98]. On the other hand, it still remains an open question whether the crystalline ice layers on metal surfaces are homogeneous, or composed of a mixture of several different phases of water [Nil10]. If the latter is the case,

---

[15]For the approximate thickness threshold refer to the coverage dependence of the SFG buildup in the crystalline ice (Figure 5.13).

it is possible that charges confined in such media can be responsible for a reorientation of a particular phase only (with a structure that already contains a preexisting electron trap). Then the small work function change could mean that upon UV illumination, only small ferroelectric *domains* are formed, which would explain the saturation of the SFG signal at such low total number of reoriented D_2O molecules. Such domains are then also spectroscopically accessible much better, which favors this picture more than a model containing isolated, preferentially oriented oscillators randomly distributed across the D_2O layer.

Resolving the electron confinement site in the crystalline ice

The work function increase discussed above could bear interesting consequences in resolving the actual electron confinement site. The sign of the work function change is indeed surprising: an increase usually indicates a creation of a dipole moment pointing preferentially towards the surface and not towards the ice/vacuum interface, where the excess electrons are believed to reside. Is the electron really localized at this interface also in our experiment?

To answer this question, we can block most of the available surface trapping sites with the Xe gas, adsorbed on top of the crystalline ice and inhibit the SFG buildup process if it, of course, is caused by the species localized at the ice/vacuum interface. Unfortunately, the lowest temperature achievable in our setup is not lower than $50\,K$ and therefore Xe layers are desorbing very fast under the local heating induced by the intense UV illumination. One way to circumvent this is to let a large $(1 \times 10^{-5}\,mbar)$ amount of Xe in the UHV chamber background, as this increases the Xe desorption temperature and acts as a continuously opened gas doser in front of the sample. The result of such a measurement is depicted in the Figure 5.12. Probably due
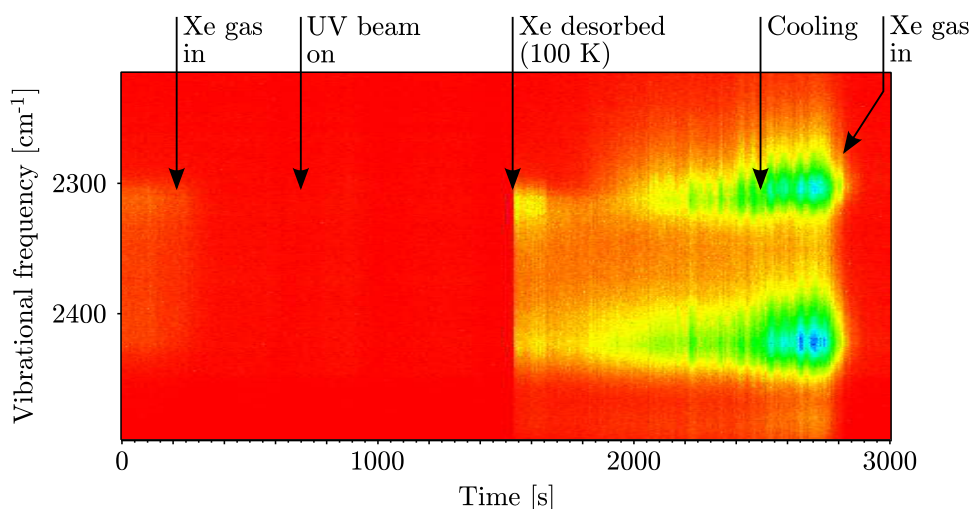
Figure 5.12.: The SFG buildup process in crystalline ice with the surface blocked by Xe adlayers. The spectrum shows the raw SFG spectrum in the region of both enhanced resonances and is not corrected for the incident IR intensity, as the (optical) conditions with Xe in the chamber are different.

to the different refractive index of the solid Xe adlayers (as compared to vacuum), the SFG signal from the D_2O surface vanishes upon the rare–gas adsorption. After no D_2O signature is visible in the spectrum anymore, the UV beam is allowed to reach the sample for a time that would be sufficient for the beam of this intensity to induce the SFG signal buildup up to the photostationary state. Then the temperature of the sample is increased above the Xe desorption

temperature at the elevated pressure (to $100\,K$ in this case). The characteristic signal of the un–irradiated D_2O surface is observed[16] and the spectral intensity starts to increase rapidly as if the layer was not illuminated before and the buildup has just started.

Clearly, this means that the net dipole ordering in the ice layer can be very effectively suppressed by blocking the *surface* sites and thus the ice/vacuum interface plays a key role in the excess charge stabilization.

If the electrons are localized at the ice surface and the work function of the $D_2O/Ru(0001)$ system is increased when these charges are screened, what is the actual confinement site of those species? It has been mentioned earlier that the ice on Ru(0001) grows by the Stranski—Krastanov mechanism in form of towers (clusters) on top of the first bilayer. An electron, stabilized at the ice surface can therefore either occupy a flat, horizontal ice terrace, or the vertical side of a cluster. The first case is not compatible with neither of our observations, but the second could explain them:

The ice towers, formed on top of the first D_2O bilayer, possess a thickness that does not correspond to the nominal thickness of the ice layer derived from a TDS spectrum, but are most probably much higher. The tunneling of an electron to the terrace of such a tower is therefore improbable. At the cluster sides, again, the confinement sites closer to the metal surface are populated with a higher probability (due to the better wave function overlap). This induces an ordering effect in the (thicker) layers 'above' the confined electron, so that they align their dipoles *to the metal surface* to screen it. As their amount is with a high probability larger than the amount of molecules 'below' the excess charge, the overall dipole moment change is positive. A further observation that confirms this scenario is the more precise measurement of the coverage–dependent work function change in the same system upon UV illumination performed by Gahl [Gah04]. There, the work function increases with increasing coverage and is almost zero to slightly negative for very small coverages. This is in a perfect agreement with the mechanism proposed here: the smaller the ice clusters bearing an electron are, the higher is the probability for an excess charge to be either confined at the ice terrace, or to be confined at the cluster side, but with an nearly equal amount of ice layers in either direction (up and down).

Spatial range of the confined–charge influence

The common ground of the previous discussions was the idea that D_2O molecules in ice stabilize an excess charge by a highly effective screening that is accomplished by their reorientation. As it is obvious from the magnitude of the SFG intensity increase (and other indications in the spectrum as discussed earlier), the alignment should involve more than one complete D_2O bilayer. But how large is the 'solvation shell' of an confined electron?

Unfortunately, this question we can not fully answer. Our measurements, however, can at least offer some indications to the spatial range of the confined–charge influence. To this end, the SFG intensity increase was observed and compared for ice layers on Ru(0001) of various thicknesses. A graph, showing the dependence of the signal intensity in the photostationary state on the nominal D_2O coverage is shown in the Figure 5.13. Two things are obvious from that picture: first, it confirms the conclusion made in the previous paragraph about the electron localization site. The SFG signal namely grows with the increasing coverage and at about $10\,BL$ it reaches a maximum level, but does not decay anymore – even not for coverages larger than $25\,BL$. If the electrons were confined only at the flat terraces on top of the water clusters as discussed

---

[16]Although with a slightly larger intensity, which is difficult to explain due to the numerous factors that are changed after the initial spectrum was taken.
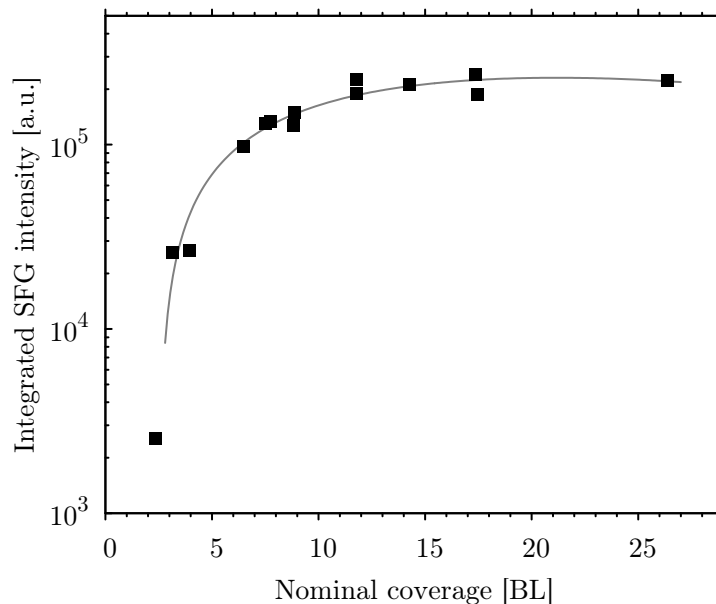
Figure 5.13.: Integrated SF intensity from ferroelectric ice sample after electron induced ordering vs. its nominal thickness. The frequency window around partially coordinated OD vibration is taken. The gray line is a guide to the eye.

earlier, those should become more and more inaccessible with increasing spatial distance from the surfce and thus a signal *decrease* would be expected.

The second aspect is the actual average height of an ice tower that is influenced by the presence of the excess electron. Due to the specific growth behavior of D_2O on Ru(0001), at the nominal coverage of 10 BL the actual average cluster thickness amounts to ~30 BL [Haq07], which is approximately 11 nm. This is a surprisingly high value and the image forces, contributing to the origin of an image potential state from where the electron can stabilize, are expected to be rather negligible at such a distance. Nevertheless, as this situation is very complex, one can only state that with a high probability the influence of an excess charge will extend beyond the first screening water layer, which is different e.g. from small ice clusters containing only several D_2O molecules. Simultaneously, a further–reaching dipole reordering in the subsurface layers is favored by the ice rules and minimizes the numbers of defects (and thus not saturated hydrogen bonds and strain) that would be considerable, if only the topmost layer would be dipole–aligned. A reasonable, but a very speculative guess from the most probable electron tunneling distance in the amorphous ice (~20–25 BL) would be still consistent with an ordering depth of up to ~5 BL.

Summary

Our experimental results show that the reason for the extraordinary long lifetime of electrons confined in crystalline ice on Ru(001) is the reorientation of water molecules resulting in a net dipole moment of the ice layer, that effectively screens trapped charges. In this stabilized state, the electrons can neither tunnel back into the metal, because after the confinement, additional activation energy is required for this process, nor can they decay into an state below the E_F, because no available unoccupied states between the Fermi level and the conduction band of ice are present in the crystalline phase. The new, ferroelectric alignment of D_2O molecules is very

stable with respect to time and to temperatures even above the phase transition and exhibits an dependence on the water isotopologue used. The net dipole reorientation leads to a rather small change in work function, which suggests the existence of ferroelectric domains created in ice upon illumination, offering exceptionally stable trapping sites. The different localization mechanism in amorphous ice does not allow an uniform ordering, therefore a similar confinement does not occur there. Nevertheless, long lived, stable species (anions like Cl^-) are able to cause similar structural changes, which suggests a net dipole ordering to be more general response of water to the charge localization.

6. Ultrafast energy transfer between Ru(0001) and D$_2$O – a desorption study

If the D$_2$O covered Ru(0001) substrate is excited by a sufficiently intense femtosecond laser pulse, the adsorbed molecules will leave the sample. The unresolved question remains on the surface: how was the energy from the laser pulse transferred into the adsorbate degrees of freedom? The following Chapter offers this insight into the *mechanism* of energy transfer between the Ru(0001) and the water adlayer. Presented are data for the desorption of the first, wetting D$_2$O layer that is most influenced by the vicinity of the metal. The interaction channels between the substrate and adsorbate are investigated and complement the presented work by showing how the energy – now in form of hot substrate electrons – can be transported in a different way than introduced in the Chapter before. The two–temperature model and frictional approach discussed earlier are used to model the data and their predictions qualitatively agree with the measured values. Implications for D$_2$O/Ru(0001) interaction obtained from this combined study are then discussed in the end.

6.1. Energetics of the laser–induced desorption

There is a lot of information about the Ru(0001)–D$_2$O system contained already in the TDS spectrum shown in Figure 4.6. Particularly interesting is the rough estimate of the activation energy for desorption (or the binding strength of a D$_2$O molecule to the metal surface) of about 0.49 eV that can be made using the Redhead formula. In the experiment introduced in this Chapter, we exploit femtosecond, 800 nm (1.5 eV) light pulses to induce the water desorption. As water does not absorb in the near IR, the energy is only deposited in the metal. This process that – in contrast to the TDS measurement – brings the different heat baths of the solid out of equilibrium is sketched in the Figure 6.1. As the photon energy used is larger than needed
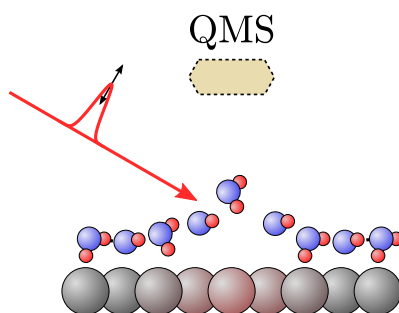
Figure 6.1.: A scheme of the laser–induced desorption measurement.

to desorb an individual water molecule, one could think of the simplest mechanism as being a single excitation of an electron into an antibonding orbital of D$_2$O, which would consequently lead to a desorption. If this applied, a process like DIMET could be automatically excluded and the interaction between the metal and adsorbed molecule would be reduced to an electron donor and acceptor, respectively.

6.1.1. Fluence dependence and desorption cross–section

To investigate whether more than one photon is involved in the desorption of one water molecule, the fluence dependence is probably the most suitable method: increasing the number of photons absorbed by the surface should lead to the same relative enhancement in the desorption yield in an one–photon process.

For this purpose, a sequence of pulses with the same fluence is sent onto the sample and the desorption yield measured as a function of photon dose (cf. Section 3.2.2). The measured yield decays with the increasing number of laser shots (and thus photons) reaching the sample, as the coverage is continuously depleted. For some representative fluences, such a decay curve is shown in Figure 6.2. In fact, the photoinduced desorption process closely resembles the first
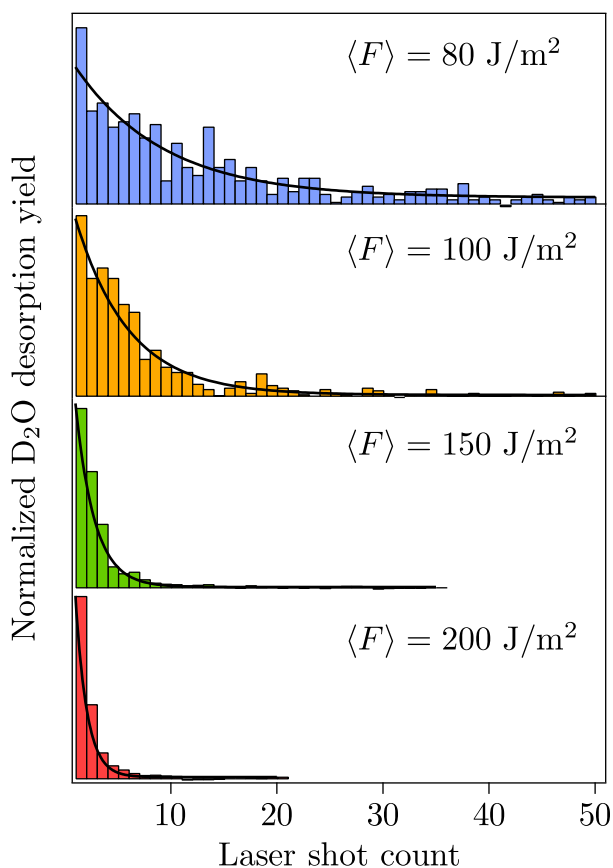
Figure 6.2.: Decay of the laser–induced D₂O desorption yield from Ru(0001) upon its illumination with various fluences.

order reaction type in chemical kinetics. Here, the species A (adsorbed molecule) transforms to another (B; free molecule) *without* an interaction with further reactants present in its vicinity. The rate is therefore only a function of the actual concentration of A: $r = -d[A]/dt = k[A]$, where r, k and $[A]$ denote the rate, rate constant and concentration of A, respectively. For the investigated surface process, in which the adsorbed molecules are intact and their interaction is limited, one can write a similar rate equation with the actual coverage (θ) instead of the concentration and a discretization not in the time, but in the absorbed photons count, N:

$$\frac{d\theta}{dN} = -\sigma\theta \qquad (6.1)$$

with σdN obviously determining the fraction of desorbed molecules after dN photons have excited the sample, i.e. the desorption probability P_{des}

$$dP_{des} = \sigma dN = -\frac{d\theta}{\theta} \tag{6.2}$$

In this expression, the proportionality constant σ is defined as the reaction cross–section. The decay curve is consequently obtained by integrating the Equation 6.1:

$$\theta = \theta_0 \, e^{-\sigma N} \tag{6.3}$$

For the given photon energy per area E_p in the pulse, one can express 6.3 in terms of absorbed fluence $(F = NE_p)$ after j pulses

$$\theta_j = \theta_0 e^{-\sigma F(j)/E_p} \quad \text{with} \quad F(j) = \sum_{n=1}^{j} F_n \tag{6.4}$$

As the fluence does not vary within the measurement yielding one decay–curve, the obtained data can be fitted by a single exponential function that immediately reveals the desorption probability as its exponent. Similarly straightforward is the estimation of the reaction cross–section – for various absorbed fluences its value is plotted in Figure 6.3[1].
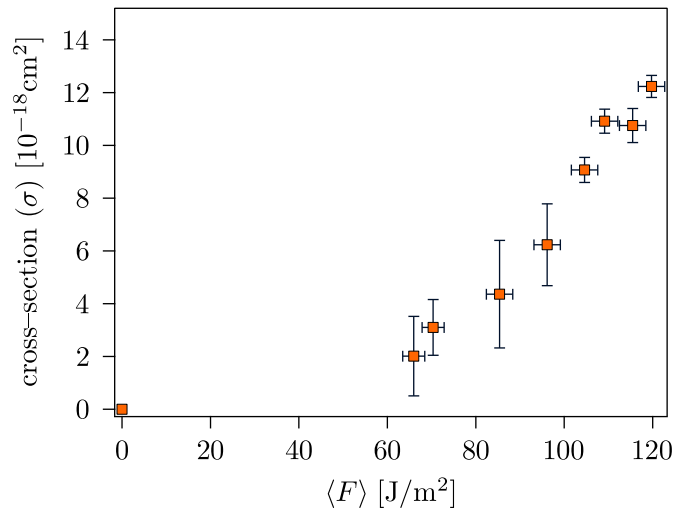
Figure 6.3.: Cross–section of the photoinduced D_2O desorption from the Ru(0001) surface as a function of the absorbed fluence.

It is important to note that even the non–associative desorption may resemble a second order process. This is the case, if the interaction between the adsorbed molecules is large, which might e.g. lead to coverage–dependent binding energies to the substrate, as it is observed in the CO/Ru(0001) system [Fun99]. In such a case the decay of the desorption yield is described by a function borrowed again from the chemical kinetics:

$$\frac{1}{\theta} = \frac{1}{\theta_0} + \sigma N \tag{6.5}$$

---

[1]It could be surprising that the cross–section is obviously changing with fluence, but as will be shown later, the desorption probability is not a linear function of absorbed fluence (or photon count) either, as the Equation 6.1 could suggest. This behavior is characteristic for nonlinear processes where, in general, a collective effect leads to a higher yield.

However, this model does not describe the decay data in our case and is introduced only for the sake of completeness.

A further information that can be extracted from the fit as a parameter is the desorption yield after one single (first) pulse. As this is calculated taking into account also the consequent pulses, its value is less prone to vary with the laser intensity fluctuations (cf. Section 3.2.2). It can be therefore used to characterize the amount of desorbing molecules from the sample with the best defined coverage (1 BL) and thus represents the observable that is most convenient to graph in the fluence–dependence evaluation. In the Figure 6.4, such a plot is shown, with x–
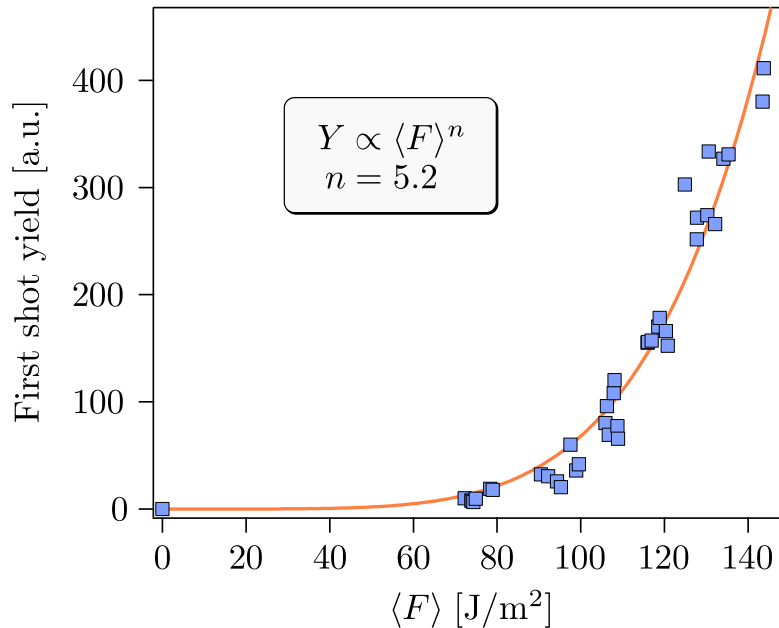
Figure 6.4.: Fluence dependence of the laser–induced D₂O desorption yield. The curve is a power law $(Y \propto \langle F \rangle^n)$ fit to the data. At higher photon doses per pulse the fluence dependence saturates, as most of the surface is already depleted in the first shot. For this reason data at fluences where the first shot yield exceeds 60 % are not taken into account and are not described by the fit function.

axis being the yield–weighted fluence $\langle F \rangle$ (introduced in Section 3.2.2). The strongly nonlinear exponent is consistent with a desorption mechanism induced by multiple transitions. However, this curve cannot be interpreted as an indicator of a purely electron mediated mechanism. If the desorption were phonon induced, the absorbed energy would indeed lead to a linearly proportional increase of metal substrate's temperature, if the dependence of the phonon heat capacity on the temperature is neglected. This approximation is valid especially for larger temperatures after the optical excitation, where the Dulong–Petit law is valid. Nevertheless, considering an Arrhenius–like desorption behavior, this clearly does not produce a linear increase of the reaction yield. As a consequence, both – a vibrationally assisted electronic desorption mechanism and a phonon mediated process are still consistent with the data presented up to now and further measurements are necessary to resolve the desorption mechanism.

6.1.2. Time–of–flight spectra and desorption energetics

The total desorption yield estimated in the preceding part represents the temporally integrated number of all D_2O molecules that have reached the mass spectrometer analyzer after the laser pulse excitation. Within the limited temporal resolution (and spatial restrictions) in the employed UHV chamber, we can measure the translational (kinetic) energy of the desorbing species from the time–of–flight spectra introduced in Section 3.2.2. A series of these data, again for various representative yield–weighted fluences is presented in the Figure 6.5. The best fit of the

$\langle F \rangle = 95 \text{ J/m}^2$
$\langle E \rangle / 2k_B = 1010 \text{ K}$

$\langle F \rangle = 130 \text{ J/m}^2$
$\langle E \rangle / 2k_B = 1140 \text{ K}$

$\langle F \rangle = 160 \text{ J/m}^2$
$\langle E \rangle / 2k_B = 1400 \text{ K}$

$\langle F \rangle = 210 \text{ J/m}^2$
$\langle E \rangle / 2k_B = 1500 \text{ K}$

$\langle F \rangle = 260 \text{ J/m}^2$
$\langle E \rangle / 2k_B = 1650 \text{ K}$

flight time [μs]
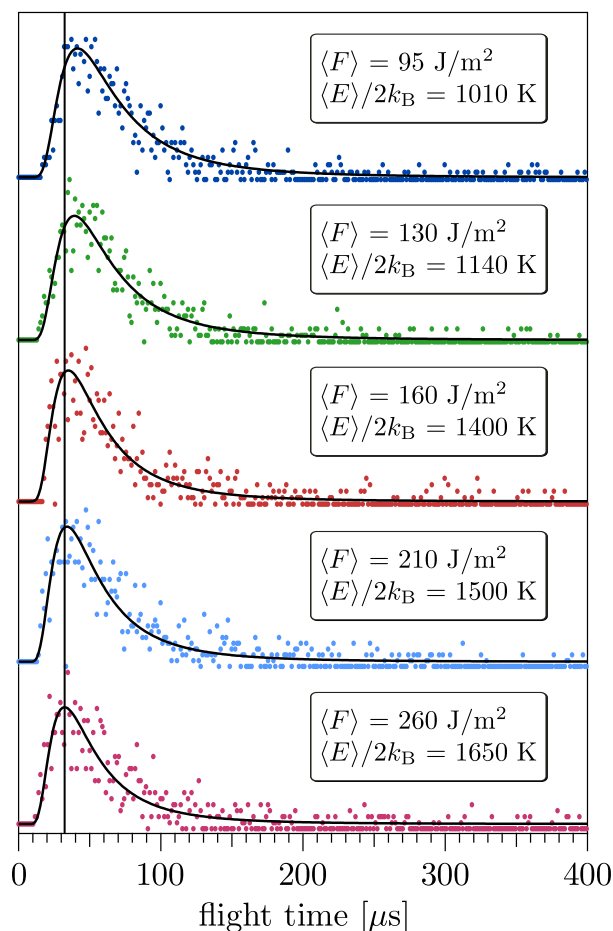
Figure 6.5.: A series of time–of–flight spectra of D_2O desorbing from Ru(0001) surface after a femtosecond laser excitation taken for different fluences. The data are described by a single Maxwell–Boltzmann distribution yielding one translational energy value (black fit curves). The vertical line placed at the maximum of the hottest distribution guides the eye and shows the shift in the velocities of particles desorbing at lower fluences.

data to the Maxwell–Boltzmann distribution (cf. Equation 3.21) yields then the translational energy that is commonly expressed as the mean translational temperature of the desorbing species and for this type of distribution can be obtained from the expression $T = \langle E_{\text{trans}} \rangle / 2k_B$. It is important to stress some aspects regarding the measurement conditions: Due to the spatial arrangement of the sample and the ionization volume of the QMS, only the desorption within a narrow angle close to the surface normal is measured. This geometrical factor is responsible for the artificially larger measured translational energy. The large fraction of the monolayer that

177

desorbs in almost each first shot makes namely the collision rate significant and the collision dynamics within the molecular cloud consequently leads to rejection of the slow particles from the flight direction parallel to the surface normal [Cow78].

Further, the D$_2$O molecules do not necessarily 'start' from the surface of a same temperature. After the excitation, some species might desorb before the thermal equilibrium in the system is reached and some even tens of picoseconds later, when the temperature of the sample is significantly lower, which would mean that the average temperatures obtained from the time–of–flight spectra are most probably underestimated. Although these effects might partially cancel each other, the resulting translational temperature has to be treated with care and cross–checked in every specific case, as it is done later in the present Chapter.

The values obtained for the translational temperatures range from ∼1000 to 1700 K. Considering the Gaussian shape of the spatial energy distribution in the exciting beam, the energy deposited in the beam center is much larger than the average, so that such extreme temperatures – if describing the pure lattice energy distribution – would probably lead to a local sample melting. As the electronic subsystem possess a much lower heat capacity, such temperatures can be easily achieved here. The large translational energies of desorbing D$_2$O molecules (cf. Figure 6.5) are thus the first indication that the laser–induced desorption process is influenced by the interaction between the hot metal electrons and the adsorbate.

6.2. Mechanism of the laser–induced desorption

Despite of the rather clear indication for the participation of the electronic subsystem in the laser–induced desorption process, a definitive answer to the question whether it plays a major role here, can be given only after a two–pulse correlation measurement that is reasonable to perform after the nonlinear fluence dependence has been observed[2]. Its experimental scheme (sketched in Figure 6.6) resembles the measurement of fluence dependence. However, in the
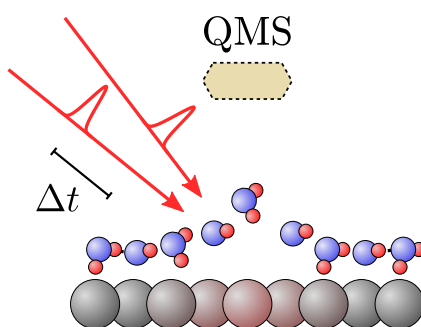
Figure 6.6.: A scheme of the two pulse correlation aimed to resolve the desorption mechanism. In contrast to the fluence dependence, the original pulse is divided into two parts that are delayed with respect to each other. Their intensities differ slightly (45:55) to facilitate the modeling of the data as will be discussed later.

fluence dependence *one* pulse is sent to the sample and the desorption yield is observed as a function of the *varying fluence* and in the two–pulse correlation a pulse of a certain *constant fluence* is divided into *two* parts and the reaction yield is recorded as a function of their *delay*. The main idea and details of the experiment, including the treatment of its limits, are described thoroughly in Section 1.3.3. The outcome of this measurement alone, however, might not give an explicit answer to our initial question about the energy transfer mechanism, therefore a modeling of the measured data based on the two–temperature model and frictional coupling is presented after the experimental results to finally offer a better insight into the desorption process.

6.2.1. Two–pulse correlation

If we employ two equally short pulses of slightly different intensity (45:55), delayed by a short time to induce desorption from the Ru(0001) surface covered with $1\,\mathrm{BL}\ D_2O$, the obtained yield as a function of the time delay is shown in the graph in Figure 6.7. What does this result mean and what are its indications for the desorption process? It is important to emphasize that this measurement does not provide a *direct* insight into the desorption mechanism, it is rather probing the dynamics of the energy transfer and exploits the (reasonable) assumption

---

[2]If the fluence dependence were linear ($\langle F \rangle^n$ with $n = 1$), the ratio between the yield obtained from two temporally widely separated and two overlapping pulses would be equal to unity, because

$$\frac{Y(2\langle F \rangle)}{2Y(\langle F \rangle)} = \frac{(2\langle F \rangle)^n}{2\langle F \rangle^n} = \frac{2^n}{2}$$

The correct ratio between the 'wings' and the maximum of the two–pulse correlation curve is an important indicator of common imperfections in the beam path like a not perfect spatial overlap or a beam self–focusing in the entrance window.
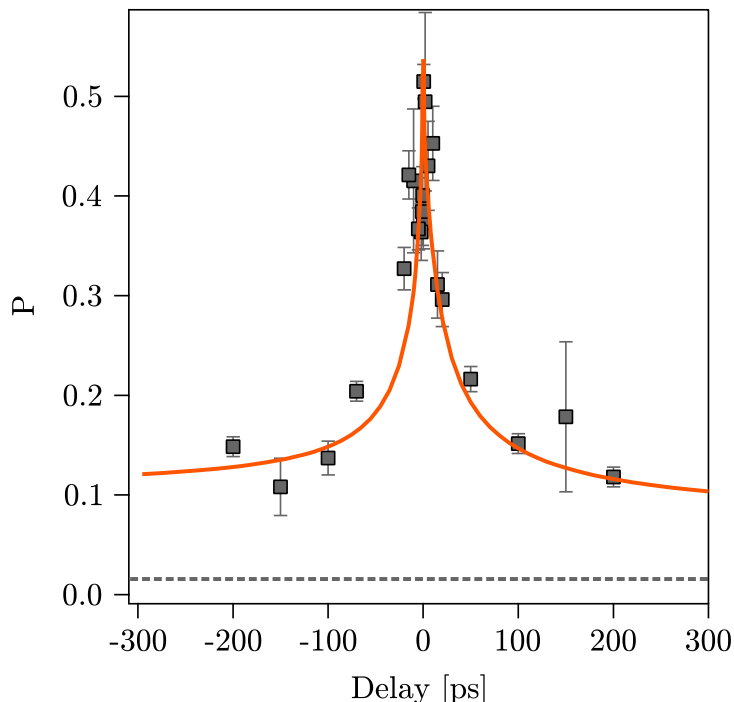
Figure 6.7.: Result of the two–pulse correlation measurement. Strong increase in reaction yield (and thus probability) is observed if the two pulses temporally overlap, however the width of the peak exceeds the electron–phonon equilibration time constant. The dashed line represents the desorption probability in a situation where the pulses are infinitely separated. The line simulating the yield evolution serves to guide the eye. The delay convention is chosen such that at negative delays the pulse with the lower intensity arrives first.

that electron dynamics are much faster than that of the lattice. If we focus on the peak width, we find

$$\text{FWHM} \approx 30 \, \text{ps}$$

which is much larger than the electron–phonon equilibration time. In other words, the second pulse in the simple sequence used in this investigation benefits from the elevated temperature of the system left after the first excitation even on a time scale where the temperatures of the electron and phonon subsystem are equal. The time is apparently too long for a purely electron mediated process.

One of the intrinsic problems in the D$_2$O/Ru(0001) system is the very low activation energy of the desorption process – the binding strength is only negligibly larger than the strength of the hydrogen bonds as discussed earlier (Section 4.2). As a consequence (shown later in a more detail), even 300 ps after the excitation the surface temperature is about 100 K higher than the desorption temperature estimated from a TDS spectrum. This greatly widens the two–pulse correlation curve. Even in the case of a strong coupling of the adsorbate to the substrate's electron heat bath, a simple 'rule of thumb' stating that processes with a two–pulse correlation wider than 5 ps cannot be (only) electron mediated definitely does not apply[3]. The only appropriate way to examine the underlying process is thus to model the surface

---

[3]This typical value has been derived considering the electron–phonon equilibration time that is about 1.6 ps in Ru(0001) [Fun99, Wag06].

temperatures via the two–temperature model and extract the coupling strengths between the different heat baths using the frictional approach and finding the model parameters that show the best correspondence to the measured data.

6.2.2. Modeling the laser induced D$_2$O desorption

The model aimed to describe the measured the data is described in detail in Sections 1.3.2 and 1.3.3. Using the material properties of ruthenium one can calculate the temperature (energy) evolution in the electron and phonon subsystem in this solid and consider their coupling to the adsorbate, which is expressed by the friction coefficients $\eta_{el} = 1/\tau_{el}$ and $\eta_{ph} = 1/\tau_{ph}$. The temperature of the adsorbate heat bath is then calculated from the equation $dT_{ads}/dt = \eta_{el}(T_{el}-T_{ads})+\eta_{ph}(T_{ph}-T_{ads})$. The desorption rate is expressed by an Arrhenius–like expression with the exponential prefactor in the Kramer's low–friction limit

$$\nu = (\eta_{el} + \eta_{ph})E_{ads}/k_B T_{ads} \qquad (6.6)$$

Integrating the rate over time we obtain the *absolute* yield, i.e. the desorption probability for a given fluence and pulse sequence as discussed above. It is important to note that this approach is a rather crude approximation: the rate of the process was originally made independent of the actual presence of the desorbing species and therefore the time integral over the Arrhenius–like expression 1.38 is in fact divergent for higher temperatures kept over long times. One has to be aware of this fact especially when modeling desorption with a high first shot yield, where this behavior, leading to an apparent desorption from a depleted surface has to be taken into account. The easiest way to introduce a parametrization of the rate, so that its integral will correspond to the actually measured yield is to include a further fit parameter into our model that effectively acts as a scaling of the exponential prefactor defined in the Equation 6.6. Such a modified theory can be than compared to the situation where this modification is not considered and the match to the data can be evaluated. As the value of ν obtained in this way must be consistent with our TDS data, we do have a further independent check of the obtained parameters.

In the following, four possible desorption scenarios are modeled and their agreement with experimental results is discussed.

A purely electron mediated desorption scenario   A desorption mediated only by a coupling of the adsorbate to the electronic subsystem of the solid could be possible considering the high translational energies of desorbing D$_2$O molecules, however, it seems to be unlikely due to the broad two–pulse correlation (2PC). Modeling this situation yields a series of graphs and parameters shown in Figure 6.8. The model is very sensitive to coupling strengths and adsorption energies, so both parameters can be determined with an excellent precision. In this scenario, the E_{ads} is with 0.55 eV slightly higher than the value obtained from the TDS analysis, which is the consequence of the rather large transient temperatures reached by coupling to the electronic subsystem that enhance the yield considerably, if the binding strength is low. On the other hand, the large coupling constant (small coupling time; $\tau_{el} = 0.45$ ps) accounts for the appropriate height of the two–pulse correlation curve, measured from the base level where the desorption takes place even if the pulses are widely (more than 100 ps) separated.

It is apparent that in this scenario the 2PC is not described well and the modelled curve is too narrow. From the knowledge of the temperature and rate evolution, we can extract a mean
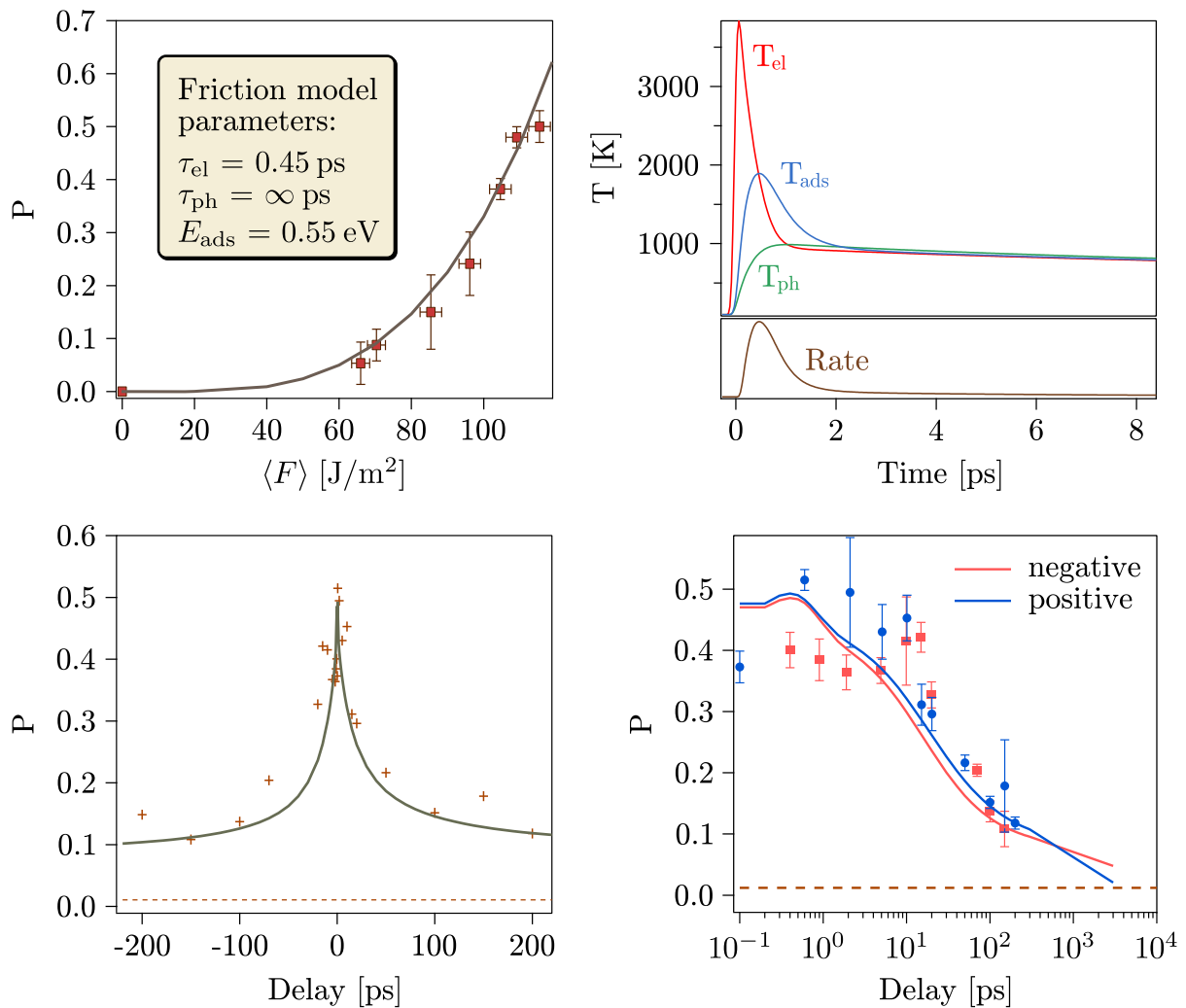
Figure 6.8.: Modeling results for purely electron mediated desorption scenario. Solid lines represent the model curves obtained by optimization of the frictional coupling parameters (here τ_{el} and E_{ads}) to achieve the best possible overlap with the measured data. The top right panel displays the temperature evolution of either subsystem after excitation with a single pulse of the same intensity that is used (and divided) in the two–pulse correlation.

translational temperature of the desorbing molecules by weighting the transient temperatures with desorption rate (rate–weighted adsorbate temperature):

$$T_{ads}^{RW} = \frac{\int R(t)\, T_{ads}(t) dt}{\int R(t) dt} \tag{6.7}$$

For lower fluences its value is strongly overestimated, as will be discussed later in a more detail.

If the exponential prefactor is parametrized, the width of the 2PC curve can be increased, however, the electron–adsorbate coupling time has to be increased considerably and the correction essentially leads to an adsorbate temperature evolution that closely follows the phonon temperatures and thus offers no improvement to the model. The translational temperatures are in this case way too low to describe the time–of–flight distributions correctly.

A purely phonon mediated desorption scenario To look at the problem from the other side, we investigate the situation where only phonons play the role in the laser–induced desorption. The corresponding data fits are depicted in Figure 6.9. The adsorption energy in this case must
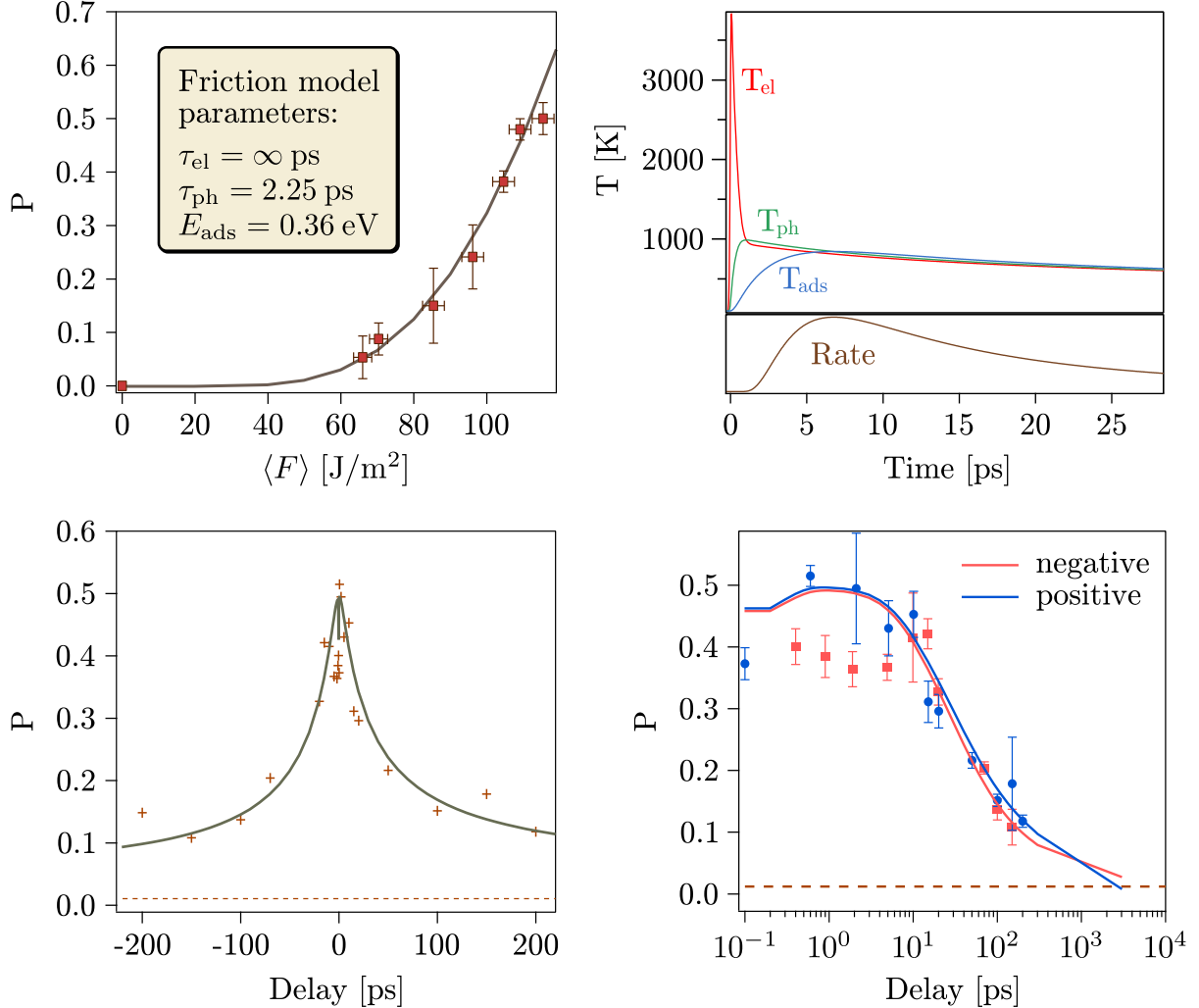
Figure 6.9.: Modeling results for purely phonon mediated desorption scenario. The graphs show the same data as in the graphics before, but now the solid lines are determined by the adsorbate–phonon coupling strength ($1/\tau_{\text{ph}}$) and a different adsorption energy.

be set to a very low value, $0.36\,\text{eV}$, and the reason is analogous to the one named before: the coupling to the phonons leads to a much lower transient adsorbate temperature and hence to a low rate, which can be only increased to describe the data if the activation energy in the Arrhenius–like expression 1.38 is lowered. In fact, such a low value is far from consistent with the TDS estimate using realistic values for ν (see also discussion at the end of this Section). The coupling to the phononic heat bath is also quite large and is necessary to explain the amplitude of the relative desorption–yield increase around $\Delta t = 0$.

Despite of the very efficient coupling to the phononic subsystem, the predicted 2PC curve is too wide and not fully consistent with the data. Our measurement shows a slight asymmetry in the 2PC curve, caused by the different light intensity contained in the employed pulses. In a phonon mediated process, however, this curve is nearly perfectly symmetric, as the phonons

react only slowly on the excitation and also due to their higher heat capacity (and inefficient transport mechanisms) store the energy for a much longer time than electrons.

On the other hand, the fluence dependence can be descirbed much better in this scenario than if purely electron mediation is assumed. The adsorbate temperature after excitation remains rather low, it does not significantly exceed the phonon temperature at any stage, which leads to a slow desorption rate spread over an exceptionally long time. Translational energies obtained here are strongly underestimated if compared to the experimental time–of–flight results.

The main problem of this scenario – the low adsorption energy predicted – can not be removed if the reaction rate is parametrized by a constant factor. The only achievable improvement is the narrowing of the 2PC curve that requires an unphysically fast coupling between the adsorbate and the phononic heat bath.

A desorption scenario including coupling to both heat baths As neither of the 'pure' models can offer a satisfactory result that would match the experimental data, one has to conclude that a process involving both heat baths at Ru(0001) surface must be active. Figure 6.10 displays this situation from the viewpoint of the parameter optimization. The best overlap is achieved for a configuration that resembles the electron mediated process, although the two–pulse correlation is predicted wider due to the opened phononic energy transfer channel, which is a significant improvement. Both, high adsorption energy and adsorbate temperature are 'inherited' from the electron mediated process and indeed, the coupling to this subsystem is almost five times larger than to phonons. Translational energies are very similar to that case as well.

Although the data are reproduced to a reasonable degree, much better consistency can be achieved, if the rate constant is modified by a constant factor of $k = 0.5$ (i.e. the modeled yield reduced to $1/2$) as it is shown in Figure 6.11. The adsorption energy matches the value expected based on the simple analysis of the TDS data. The stronger coupling of the adsorbate to phonons and a slightly weaker friction coefficient corresponding to the interaction with the electronic heat bath allows to reproduce the width of the 2PC as well as the shape of the fluence dependence with physically reasonable coupling times. The adsorbate temperature reaches an intermediate value between the phononic and electronic limit and hence describes the translational energy distribution best, as can be seen in Figure 6.12. It important to note that the data points presented there are plotted with error bars corresponding to the statistical deviations from the corresponding average values and might be systematically lower either due to the difficulty to estimate the exact place where the ionization of the molecules takes place in the ionization volume[4], or due to the error in estimating the flight time in the quadrupole system. A further interesting observation is connected to the height of the 2PC 'wings' and to the low adsorption energy of D$_2$O on Ru(0001): the obtained yield in fact desorbs as in two steps, including a fast and intense one that lasts up to $\sim$2 ps after the optical excitation and a slow component of low rate active several hundred picoseconds until the surface temperature below 175 K is reached. The fraction of desorbed molecules in either of these steps is nearly equal.

The optimized parameters obtained for each model are summarized in Table 6.1. The modeled attempt frequencies $\nu_{\text{mod}}^{\text{RW}}$ are calculated from the data shown before (assuming the Kramers low–friction limit and thus Equation 6.6 applies) and can be checked for consistency with the

---

[4]This has to be determined very exactly, as the total flight distance between the sample surface and the QMS is only about 55 mm and enters the Maxwell–Boltzmann fit equation quadratically. An error of 1 mm in the measured distance yields a difference in translational temperatures of about 80 K in the fast velocity distributions (i.e. at large fluences).
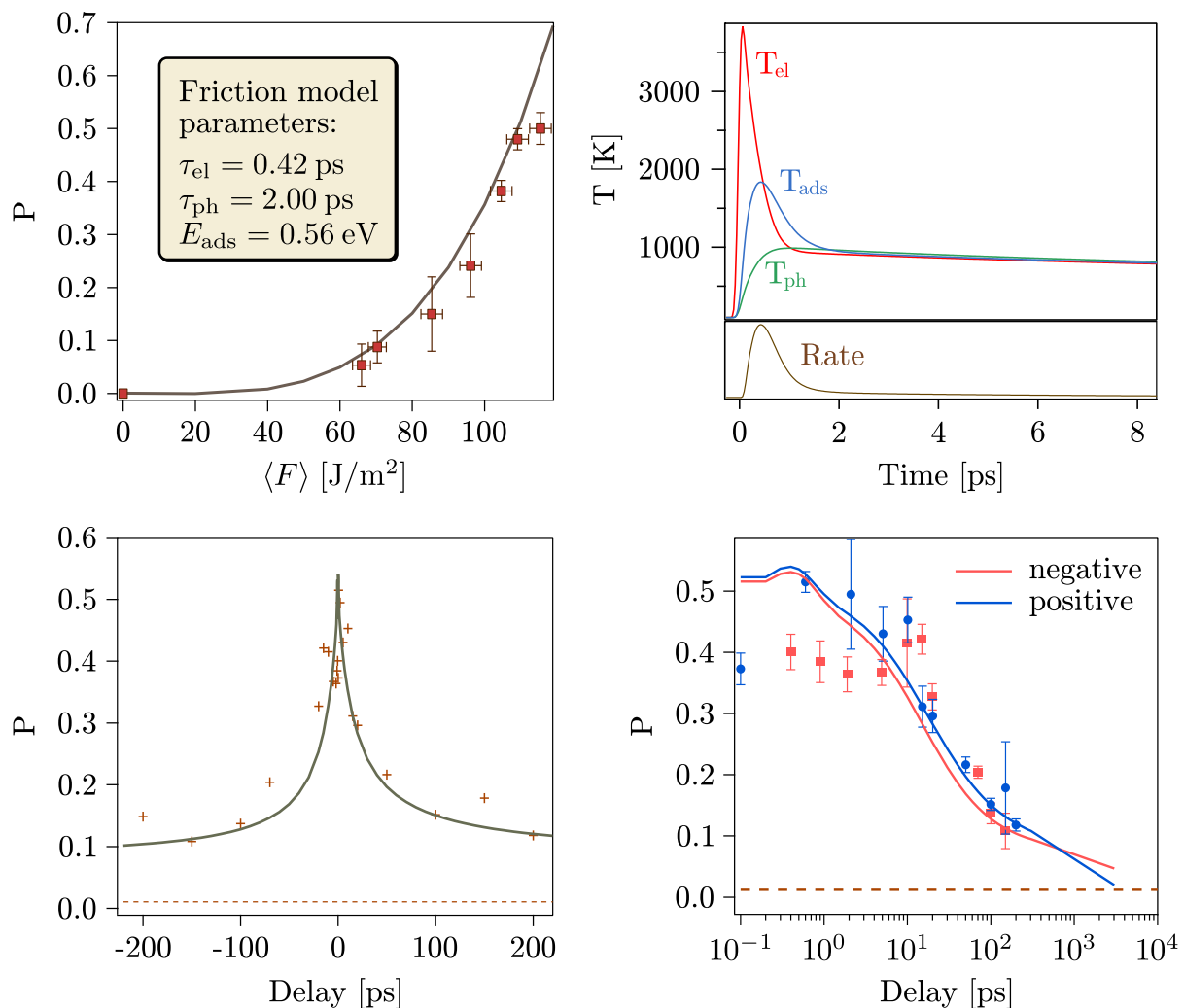
Figure 6.10.: Modeling results for a desorption scenario including electron and phonon mediation. The coupling constants to both heat baths and adsorption energy are optimized to achieve the closest possible match between the model and the measurement.

values obtained from the TDS spectrum using the Redhead formula (Equation 3.16). The correctness of the adsorption energy predicted by the corresponding model is supposed as well. Such a comparison is a very useful cross–check based only on the known temperature at which the desorption rate measured in the TDS reaches its maximum and independent on the friction model. The results are listed in the Table 6.2. Again, the phonon mediated scenario shows the worst consistency, predicting a value for the attempt frequency three orders of magnitude different from the semi–experimentally determined one. Values for purely electron and unmodified combined mechanism differ also a lot from their corresponding cross–references. Interestingly the agreement in the situation where the reaction rate is parametrized and both energy transfer channels opened simultaneously, the agreement is excellent (identical within the error bars), if one considers the parameter factor 2. One can state that the last modeled situation exhibits the best self–consistency and considering the further indications as well represents the most probable reaction mechanism.
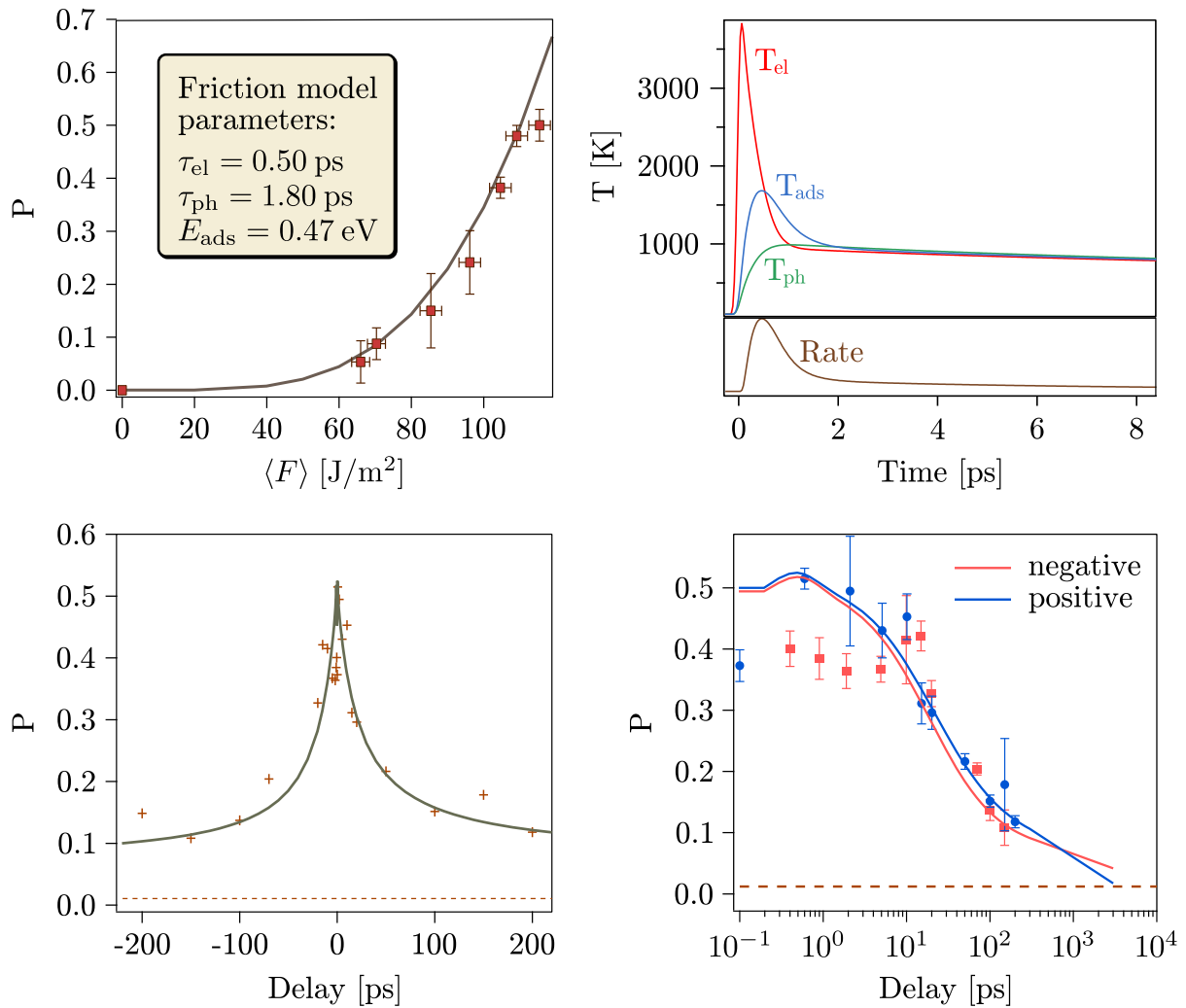
Figure 6.11.: Modeling results for a desorption scenario including electron and phonon mediation and modified rate expression. The coupling constants to both heat baths, the adsorption energy and the rate parameter are optimized to achieve the closest possible match between the model and the measurement.

modeled scenario	E_{ads} [eV]	τ_{el} [ps]	τ_{ph} [ps]	Y_{exp}/Y_{mod}	ν_{mod}^{RW} [s^{-1}]
purely electron mediated	0.55	0.45	∞	1	1×10^{13}
purely phonon mediated	0.36	∞	2.25	1	3×10^{12}
electron and phonon mediated	0.56	0.42	2.00	1	2×10^{12}
modified theory	0.47	0.5	1.8	2	1×10^{12}

Table 6.1.: Optimized coupling parameters in the examined laser–induced desorption scenarios.
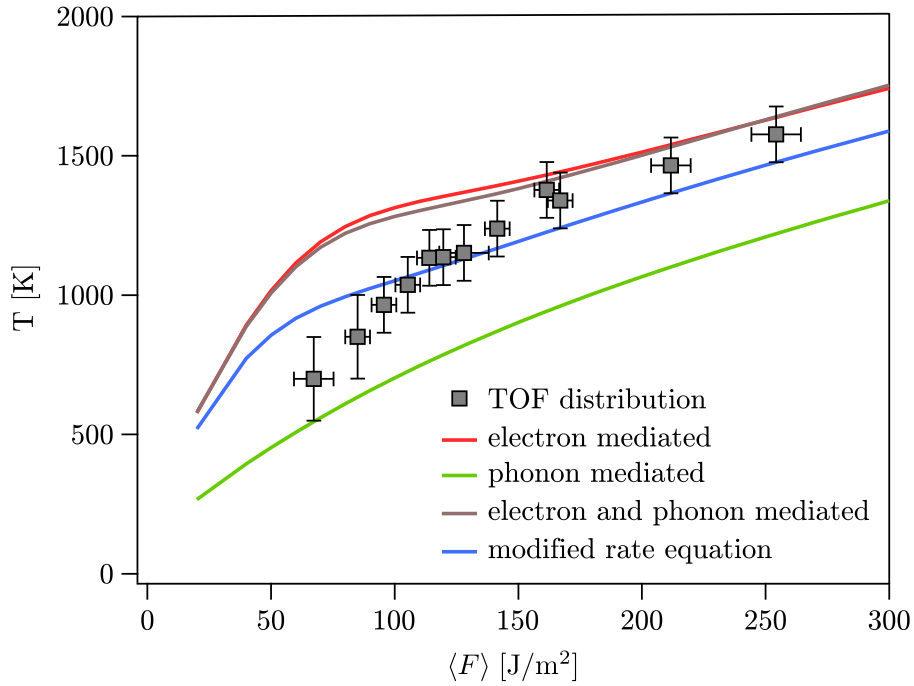
Figure 6.12.: Translational temperatures obtained from the rate–weighted modeled transient adsorbate temperature in different discussed models and from the time–of–flight distribution. The trend clearly shows especially the inability of the purely phonon–mediated scenario to describe the experimental observables.

modeled scenario	$\nu_{\mathrm{mod}}^{\mathrm{RW}}\ [\mathrm{s}^{-1}]$	ν_{TDS}
purely electron mediated	1×10^{13}	7.5×10^{14}
purely phonon mediated	3×10^{12}	2.5×10^{9}
electron and phonon mediated	2×10^{12}	1.4×10^{15}
modified theory	1×10^{12}	3.7×10^{12}

Table 6.2.: Comparison between the attempt frequencies calculated from the friction model and calculated using the same parameters from the Redhead formula.

6.3. Discussion

An important conclusion regarding the mechanism of the laser–induced desorption has been made based on the modeling of the experimental data by the two–temperature and friction model discussed earlier. Details about its reliability and limits have been also mentioned before, here only some points should be briefly noted that are relevant for its outcome and the results interpreted in more detail.

It is known that the simple two–temperature model tends to overestimate the temperatures of both, electronic and phononic heat bath, the former one being much stronger affected [Lis04]. As already mentioned, this systematic error will rapidly decrease with fluence (and be rather negligible at the fluences leading to desorption), nevertheless, one could expect the electron heat bath is in reality slightly colder than calculated. If this applies, the model would artificially favor the adsorbate–phonon coupling more than the other evaluated energy transfer channel in our case. The already high friction coefficient η_{el} would be increased (and/or analogously η_{ph} decreased) and support the *non–adiabatic* desorption dynamics even more.

Together with the highly nonlinear fluence dependence, this means that a DIMET mechanism most probably leads to the D_2O desorption from the Ru(0001) surface. Taking the typical vibrational period of the Ru–OD$_2$ bond that amounts to ~ 85 fs [Thi87], the electron bath–adsorbate coupling time corresponds to slightly more than 5 periods of the vibrational mode, whose excitation is most probably responsible for the desorption. Such a consideration confirms the obtained coupling constant as a reasonable value, compatible with the physical process it should represent.

It is interesting to observe that apparently all energy transferred to the adsorbate is stored exclusively in the translational degree of freedom, as the translational energies of the desorbing species are equal to the predictions of the one–dimensional two temperature model. This could mean that the barriers for vibrational[5] or rotational excitations of water on the surface are much higher and/or those motions do not (significantly) facilitate the desorption process.

To corroborate our findings, theoretical input would be very welcome, as the friction coefficients can be also calculated theoretically from first principles [Lun05]. Further experimental evidence for a DIMET mechanism could be obtained from a laser–induced desorption dynamics measurement on the isotope substituted $D_2^{18}O/Ru(0001)$ system, where the heavier mass of the molecule should change the behavior of the system, if the energy transfer from electronic heat bath to the adsorbate prevails. The reason for the expected isotope effect is the short energy transfer time that determines the temporal length of a single energy transfer step. As could be shown in the Figure 1.25, the vibrational excitation of a molecule is crucially dependent on the movement of the molecular coordinates on the excited PES within a short time period. Heavier species will be accelerated less, which leads to a less efficient vibrational excitation of the electronic ground state and thus lower desorption probabilities in the same amount of DIMET cycles.

A further question that might arise concerns the applicability of the proposed mechanism of the laser–induced desorption to the desorption in thermal equilibrium. Could the mechanism in reality depend on the temperature of the system and can only one scenario explain the desorption under all experimental conditions? One argument has already been given before (see page 63): although the temperature of the electronic heat bath in equilibrium is much lower than if the bath is excited with an intense light pulse, its energy distribution still contains

---

[5]Of course, with the exception of the abovementioned vibration along the surface normal that leads directly to the desorption with no energy stored in the internal degrees of freedom.

species with comparably high temperatures that can drive a process similar to that investigated here. Considering the typical time–scale ratio for laser induced desorption (1 ps) and desorption in equilibrium (1 s) and the ratio in number of species with a given high energy (e.g. 3000 K), one can conclude that the desorption prerequisites are indeed comparable.

Another factor that enhances the applicability of our desorption mechanism is the observed proportion between the desorption yield during the ultrashort time when the electron temperature is large and the yield obtained during the long time in equilibrium at temperatures still high enough for phonons to drive a desorption. Apparently, in the almost 1 ns available to phonons possessing enough energy to induce the desorption of the whole D_2O layer, this does not take place and the desorption rate is very low. This indicates that even at temperatures much lower than transiently induced by the laser pulses the electronically induced desorption channel is at least comparable to its phonon induced counterpart.

The results presented here can serve as a starting point for further investigations of water desorption. As an example, experiments have been performed utilizing the time–resolved SFG spectroscopy to investigate the vibrational changes in the desorbing water molecules at the time delay corresponding to the predicted maximal desorption rate. As the water shows no free OD signal at a coverage below 1 BL, its appearance was expected in the fraction of molecules leaving the surface. Unfortunately, due to the low signal produced by a small fraction of reoriented molecules we were not able observe this phenomena within the whole reasonable time–delay window. A further difficulties were the rather high desorption yield and the repetition rate of the laser system (needed to record the SFG spectra with an acceptable signal–to–noise ratio). To force at least 5 % of the molecules to desorb in every shot (still leading to a rather poor signal), a fluence is needed that depletes the surface completely after less than 0.05 s. In the employed setup the possibility do re–dose the water molecules with this speed in a defined way was not implemented and a drastic increase of the D_2O background pressure could influence the desorption behavior (and the measured signal) considerably.

In summary, we have found that *non–adiabatic* coupling of the electronic subsystem of the metal into the adsorbate degrees of freedom is responsible for laser–induced desorption of D_2O from a Ru(0001) surface. The energy is coupled primarily into the translational degree of freedom of the desorbing molecule and the coupling most probably follows the DIMET mechanism. The combination of the two–temperature and the friction model can describe the observed data well and reveals the coupling strengths between the adsorbate and either of the subsystems of the metal. The electron–adsorbate coupling time is consistent with the DIMET mechanism as it is comparable to several vibrational periods of the metal–adsorbate vibration that is most probably responsible for the desorption process.

7. Summary

A metallic catalyst used in water splitting, an important chemical process utilizing the heterogeneous charge transfer and the charge stabilization at the supported ice surface, an ice particle in the atmosphere that mediates reactions we can understand and from which we can benefit. There is still a long way to go to reach these goals. But three important steps towards this dream have been made in this thesis, providing an insight into the charge and energy transfer processes in the model system $D_2O/Ru(0001)$.

The stabilization mechanism of the extraordinary long–lived excess electron at the ice/vacuum interface was found: The heterogeneous charge transfer between the Ru(0001) metal surface and a D_2O overlayer was studied previously in our group [Bov09]. In this pioneering work, the exceptionally long lifetime of excess charges excited from the metal into the ice layer was discovered and the stabilization of the corresponding electronic state was described. The processes taking place in the ice layer and leading to this confinement were, however, unknown. The present work contributes to our knowledge by investigating the vibrational response of water layer to the electron localization and shows the importance of the local environment created by the D_2O molecules in the excess charge stabilization process.

The electrons are injected into the ice layer from the Ru(0001) substrate that is photoexcited by the UV (4.66 eV) laser beam. Crystalline ice supported on the Ru(0001) surface exhibits dramatic changes in its SFG vibrational spectrum after the electron localization. A tremendous intensity enhancement, mainly of the resonant frequencies belonging to the fully coordinated, bulk D_2O species, is observed, whereas the surface–related vibrational signatures are overwhelmed by these intense spectral features and are not recognizable anymore. Nonetheless, not only the type of oscillators appearing in the SFG spectrum is indicative of an effect, in which the ice interior plays a role. If crystalline ice samples of different thickness are prepared, the total intensity enhancement upon illumination dramatically increases up to a coverage of $\sim$10 BL and this increase is much larger than expected from the slightly higher surface area exposed in the ice films of this size.

The changes in the SFG spectrum are not instantaneous. Depending on the laser fluence used, the original SFG spectrum of the crystalline ice surface is altered until a stationary state is reached. This happens on a minute timescale, typically 5–15 minutes for the laser fluences used in the present work. This behavior is not affected by the sample temperature, if kept below 100 K and the same, extraordinarily large SFG intensity can be detected even hours after the initial UV excitation. Excess charges that were initially confined at the ice/vacuum interface must have decayed during this time, but most probably the long–lived state is depopulated much earlier by the probing visible pulse (1.5 eV; in absence of the UV pulse), which excites the localized electrons either above the vacuum level or into the conduction band of the ice, from where they can decay back into the metal easily.

The excess charge is localized predominantly at the crystalline ice/vacuum interface, as can be shown by an experiment, where Xe gas is co–adsorbed on top of the crystalline ice layer and nearly completely blocks the signal growth. Our results show that to screen the excess

electrons from the metal surface, the D_2O molecules undergo a partial *ferroelectric ordering*. Such a process is comparable with the phase transition between the ices I_h and XI, although the amplitude of the work function change along this process indicates that a rather small fraction of D_2O species reorients. This is, however, in agreement with the theoretical models that assume a limited number of surface sites that are preformed in a way to facilitate the molecular alignment and that are supportive of electron localization [Bov09]. Only in the consequent step – after the excitation of the excess charges – those electron traps become increasingly stable via molecular realignment under the influence of the free charge field, which explains the significant energy shift of the corresponding electronic state. Once the energy of the localized electron is below that of the ice conduction band, the tunneling into the metal is hindered by the absence of states in the bandgap of a crystalline solid, so that a radiative decay is the prevalent depopulation channel and the lifetime of such a species is significantly enhanced.

In a way to exclude water dissociation or another chemical process taking place in the water layer, one can investigate amorphous ice layers at the same surface. As no signal increase in layers of comparable thickness as in the crystalline ice discussed above is observed, chemical changes have to be discarded. Even for thicker amorphous layers, where a comparably small amount of long–lived electrons was detected by the photoemission experiments, only a weak intensity increase can be recorded.

Due to the relatively large number of structural defects in the volume of the amorphous D_2O modification, the electron localization occurs in its bulk. Here, the screening possibilities are limited (and mutually canceled), resulting in a much shorter excess electron lifetime and no effect on the SFG spectrum. The short lifetime is also a consequence of the not–negligible density of states in the bandgap of the amorphous solid. The defects further away from the surface are, however, populated with lower probability, which might lead to a charge gradient across a thicker layer of amorphous ice after the electrons are photoexcited. This in turn could explain the molecular reorientation observed in the corresponding SFG spectrum.

The ferroelectric alignment of ice appears to be a more general response of D_2O molecules to charge confinement: if a small amount of an electron scavenger ($CFCl_3$) is adsorbed on top of the amorphous ice layer, the SFG spectrum immediately after the photoexcitation resembles the response of crystalline ice after electron stabilization. In the reaction of $CFCl_3$ with the excess charge, Cl^- anion radicals are formed and could be responsible for the D_2O reorientation. Since Cl^- ions are not further recreated in the course of the irradiation, at low temperatures the initially large bulk SFG signal decays, probably due to a consequent reaction with water or neighboring ions. Such a stabilization of fluorochlorocarbons and their dissociation products might be of great importance for atmospheric processes leading to ozone depletion.

The mechanism of the D_2O reorientation in ice at temperatures below $60\,K$ can be elucidated based on the fact that a vibrational excitation with the probing pulse apparently supports the molecular realignment. The total SFG signal increase is much larger if the pump UV light temporally overlaps with the probing IR beam. However, due to the strong coupling between the hydrogen bonded D_2O molecules in ice, the transient polarization induced by the latter pulse decays on timescales shorter than our experimental resolution (the length of the IR pulse is about $\sim150\,fs$). Such a fast process can hardly involve a center–of–mass movement. This was proven by observing the SFG signal increase in thick, crystalline H_2O and D_2O layers. The discovered large isotope effect is not explicable by the mass difference between the whole molecules, it is rather indicative of a reorientation pathway via an OD (OH) flip, which is a very common event in the defect–rich, Ru(0001)–supported ice structure. Its activation energy can be found by evaluating the slow decay of the enhanced SFG signal taking place above $110\,K$ and amounts to $(25 \pm 7)\,meV/molecule$.

Surprisingly large is the range of influence of the localized charge. Up to a nominal coverage of 10 BL the total (integrated) signal in saturation increases. From this coverage on, it stays nearly constant. Due to the specific growth of D_2O layers of Ru(0001), this corresponds to water clusters on average 30 BL (11 nm) high that are still experiencing a rather strong excess charge field. Together with other observations, this allows us to make conclusions about the electron confinement site: at least for thicker clusters (>3 BL nominal coverage) the excess charges are confined predominantly at the vertical sides of the water clusters.

An important difference between the *surface* of crystalline and amorphous ice was discovered: The periodicity, characteristic for the structure of ice bulk, is interrupted at the ice/vacuum interface. The large number of undercoordinated D_2O molecules naturally attempts to increase the number of hydrogen bonds they engage [Wit99, Buc98], which leads to a significant disorder in the upper layers that seems to be frozen below 200 K [Wei02]. Of large interest is the question, whether such a disordered surface structure reflects the order or disorder of the underlying layers and if the ice film is very thin, how is its structure influenced by the interaction with the metal.

The D_2O bond to the Ru(0001) surface is very strong and exceeds the strength of the hydrogen bonding in ice, as can be best seen from the corresponding TDS spectrum, showing a separate desorption peak for the first, wetting D_2O layer at temperatures above the sublimation point of a water multilayer. For a long time though, the structure of this adlayer was considered to be ice–like, although with nearly planar geometry of the hexagonal ice sheets [Thi81, Men02b]. Only recently, the D_2O wetting layer on Ru(0001) was found to be hydrophobic and the formation of clusters with a relatively large height (to avoid the contact with the first layer) was proposed to be the preferred way of crystalline D_2O layers to grow [Haq07]. A model consisting of flat, hexagonal ice chains has been suggested to theoretically explain the spectroscopic data available for this system [Haq06]. In the present work, experimental evidence for its validity is be offered. For the traditional, ice–like wetting layer, OD oscillators should be observed pointing either freely towards the vacuum or towards the metal. Although both are recorded in the spectra of crystalline (and amorphous) ice above 1 BL (the latter vibrating towards the underlying ice sheet), both disappear below this limit. Even though a specific case, in which both kinds of OD vibrations (towards vacuum and towards the metal) possess the same vibrational frequency and are present in a nearly equal amount could explain the signal vanishing due to their mutual cancellation [Men05], H_2O coadsorption experiments, selectively quenching the OD vibration towards the vacuum do not find any similarly pronounced opposite vibration.

Of equal significance are the two other surface–related vibrations. The large number of partially coordinated species and the absence of the fully coordinated species at coverages below 1 BL demonstrates the excellent agreement with the abovementioned model even for submonolayer coverages. Additionally, the evolution of the fully coordinated resonance with increasing layer thickness substantiates the meaning of the hydrophobicity of the water layer: at coverages up to 2 BL the hydrogen bonding between the wetting layer and the consequently grown ice sheets is significantly limited. The signature for the fully coordinated resonance in the SFG spectra arises only above ∼2 BL, where first clusters, forming extensive internal hydrogen bonds are formed. The growth of the amplitude of this resonance for thicker amorphous layers is, together with other arguments, indicative of a considerable roughness of the amorphous ice surface.

The surfaces of thicker crystalline and amorphous ice films are influenced by the underlying water layers and show signatures characteristic for the corresponding modification. The largest

difference is in the amount of partially coordinated D_2O species that is larger in the amorphous case and appears at higher vibrational frequency than their crystalline counterpart, which is a sign of a lower overall coordination. In any chemical or physical process e.g. in the atmosphere, in the interstellar space, where the ice surface at low temperatures might play a role, these distinct differences might be of significant importance.

Energy transfer mechanism between the Ru(0001) surface and the water adlayer has been resolved   The simple chemical reaction, in which the bond between the metal and the adsorbed D_2O molecule is broken was studied. To be able to investigate the electron and phonon heat bath influence separately, the system was brought out of equilibrium with an intense, ultrashort laser pulse. Upon excitation, the Fermi–Dirac population distribution of the excited electrons can be transiently characterized by a temperature close to 4000 K (far above the melting point of the substrate) for a pulse of fluence typically used in the present work. In contrast, the temperature of the lattice increases on a longer timescale and does not exceed 1000 K at any instant of time. The reaction yield is found to depend nonlinearly on the absorbed laser fluence and the translational energy of the desorbing species reaches values above 1000 K, which is significantly higher than the equilibrium D_2O desorption temperature (175 K). Simultaneously, it is higher than the temperature of the phonon heat bath, both indicative of an energy transfer mechanism different from the coupling of the lattice vibrations to the adsorbate's degrees of freedom.

The role of phonons and hot electrons in the energy transfer between the Ru(0001) surface and the adsorbed water layer can be derived from a two–pulse correlation measurement. Modeling the correlation between the desorption yield and the transient temperatures achieved upon irradiation with a pulse sequence consisting of two, variably delayed pulses reveals a significant participation of the hot substrate electrons in the energy transfer process, even though the width of this correlation exceeds the typical electron–phonon equilibration time. The reason for the latter lies probably in the fact that the lattice vibrations are excited above the water desorption temperature for a considerably long time. The best fit to our data offers a model with following parameters:

$$E_{ads} = 0.47 \text{ eV}$$
$$\tau_{el} = 0.5 \text{ ps}$$
$$\tau_{ph} = 1.8 \text{ ps}$$

showing that the coupling of the adsorbate to the hot electrons is a much more effective energy transfer channel. The time constants τ_{el} and τ_{ph} namely reflect the timescales of the energy transfer and the activation energy E_{ads} the desorption barrier, assuming the desorption is a simple, first order process. The proposed scenario is self–consistent and agrees also with other available experimental indications, particularly with the results of the TDS spectra analysis. The underlying non–adiabatic coupling is best described by the DIMET (desorption induced by multiple electronic transitions) picture, whereas the coupling time τ_{el} corresponds to slightly more than 5 vibrational periods of the water molecule along the reaction coordinate. A higher–lying, unoccupied antibonding orbital could in principle provide an effective, repulsive potential energy surface that would lead to the molecular desorption, however, a further theoretical investigation of this process is required and would be welcome to clarify this point.

In the present work, the microscopic understanding of the energy and charge transfer between the supporting metal surface (Ru(0001)) and the thin adsorbed D_2O film was obtained

and important contributions to our knowledge regarding the interfacial structure of ice was made. Non–adiabatic energy transfer mechanisms and the actual structure of ice – considerably influenced by the metal surface – play a decisive role in these processes and are a key to the understanding of more complex phenomena in nature or technology.

A. Determining molecular orientation using SFG spectroscopy

To emphasize the versatility, uniqueness and power of the SFG method, the possibility to exploit it to determine the molecular orientation on the surface is presented. Although not possible on metal surfaces (due to the 'metal surface selection rule' and vanishing IR intensity for an s–polarized beam as discussed in the Section 3.1.3), this direct insight into the average arrangement of molecular axes is particularly interesting property of SFG spectroscopy.

The Figure 3.3 in Section 3.1.2 already introduced the geometry of the SFG setup, here its part is again offered as Figure A.1: The full solution of Maxwell equations for the SFG process
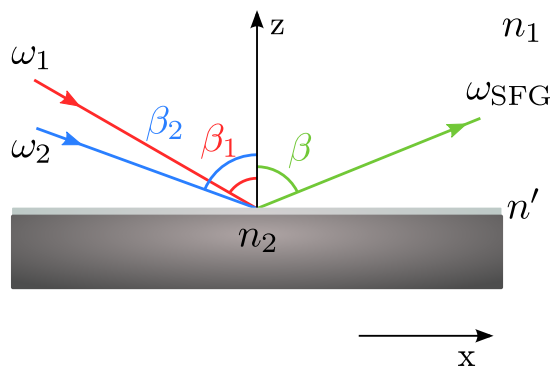
Figure A.1.: A typical geometry of an SFG setup. The three media in contact are characterized by refractive indices n_1, n', n_2.

yields (cf. Equation 3.9) [Zhu99]

$$I_{\mathrm{SFG}} = \frac{8\pi^3 \omega_{\mathrm{SFG}}^2}{c^3 n_1(\omega_{\mathrm{SFG}}) n_1(\omega_1) n_1(\omega_2) \cos^2 \beta} \left| \boldsymbol{\chi}_{\mathrm{eff}}^{(2)} \right|^2 I_1(\omega_1) I_2(\omega_2) \tag{A.1}$$

where $n(\omega) = \sqrt{\epsilon(\omega)}$ is the refractive index in medium 1 at frequency ω, c is the speed of light in vacuum. As can be seen, the prefactor does not contain any information related to microscopic properties of the layer, they are only included in the susceptibility tensor $\boldsymbol{\chi}_{\mathrm{eff}}^{(2)}$. What does this value mean? It was shown before that it is in a close relation to the angular average of the second–order nonlinear polarizability of individual molecules adsorbed on a surface (cf. Equation 3.11):

$$\boldsymbol{\chi}_{\mathrm{R}}^{(2)} = \frac{N}{\epsilon_0} \langle \boldsymbol{\beta} \rangle \tag{A.2}$$

The principle of adsorbate geometry estimation therefore essentially relies on the reconstruction of the important parts of the original, not averaged $\boldsymbol{\chi}^{(2)}$ tensor.

In general, every surface geometry is first defined by the three laboratory axes (x, y, z), conventionally chosen in a way that z is parallel to the surface normal (see Figure A.1). For a

generic molecule one can expect a different polarizability along either axis, whereas the axes x and y are interchangeable as the molecular layer is usually isotropic in this plane. This reduces the number of independent (third rank) tensor components $\chi^{(2)}_{xyz}$. If the particular case of ice with hexagonal symmetry is considered, most of the 27 tensor elements vanish identically. Remaining four elements are[1] $\chi^{(2)}_{zzz}$, $\chi^{(2)}_{xzx} = \chi^{(2)}_{yzy}$, $\chi^{(2)}_{xxz} = \chi^{(2)}_{yyz}$ and $\chi^{(2)}_{zxx} = \chi^{(2)}_{zyy}$ [Boy03, Rok04]. We investigate the surface with laser pulses that are either s or p polarized, the former probing the axis x (or y) in the laboratory frame, the latter probing axis z. The actual electric field experienced by the molecules in the layer can be calculated using diagonal elements of the Fresnel matrix so that the effective $\chi^{(2)}_q$ component for the resonance q and for a polarization combination expressed in the parentheses in the order of decreasing frequency (SFG, VIS, IR) is [Wei02]:

$$\chi^{(2)}_{q,\mathrm{eff}}(\mathrm{SSP}) = L_{yy}(\omega_\mathrm{SFG})L_{yy}(\omega_\mathrm{VIS})L_{zz}(\omega_\mathrm{IR})\sin(\beta_\mathrm{IR})\chi^{(2)}_{q,yyz} \tag{A.3}$$

$$\chi^{(2)}_{q,\mathrm{eff}}(\mathrm{SPS}) = L_{yy}(\omega_\mathrm{SFG})L_{zz}(\omega_\mathrm{VIS})L_{yy}(\omega_\mathrm{IR})\sin(\beta_\mathrm{VIS})\chi^{(2)}_{q,yzy} \tag{A.4}$$

$$\chi^{(2)}_{q,\mathrm{eff}}(\mathrm{PSS}) = L_{zz}(\omega_\mathrm{SFG})L_{yy}(\omega_\mathrm{VIS})L_{yy}(\omega_\mathrm{IR})\sin(\beta_\mathrm{SFG})\chi^{(2)}_{q,zyy} \tag{A.5}$$

$$\begin{aligned}
\chi^{(2)}_{q,\mathrm{eff}}(\mathrm{PPP}) = &- L_{xx}(\omega_\mathrm{SFG})L_{xx}(\omega_\mathrm{VIS})L_{zz}(\omega_\mathrm{IR})\cos(\beta_\mathrm{SFG})\cos(\beta_\mathrm{VIS})\sin(\beta_\mathrm{IR})\chi^{(2)}_{q,yyz} \\
&- L_{xx}(\omega_\mathrm{SFG})L_{zz}(\omega_\mathrm{VIS})L_{xx}(\omega_\mathrm{IR})\cos(\beta_\mathrm{SFG})\sin(\beta_\mathrm{VIS})\cos(\beta_\mathrm{IR})\chi^{(2)}_{q,yzy} \\
&+ L_{zz}(\omega_\mathrm{SFG})L_{xx}(\omega_\mathrm{VIS})L_{xx}(\omega_\mathrm{IR})\sin(\beta_\mathrm{SFG})\cos(\beta_\mathrm{VIS})\cos(\beta_\mathrm{IR})\chi^{(2)}_{q,zyy} \\
&+ L_{zz}(\omega_\mathrm{SFG})L_{zz}(\omega_\mathrm{VIS})L_{zz}(\omega_\mathrm{IR})\sin(\beta_\mathrm{SFG})\sin(\beta_\mathrm{VIS})\sin(\beta_\mathrm{IR})\chi^{(2)}_{q,zzz} \tag{A.6}
\end{aligned}$$

with Fresnel matrix elements [Zhu99]

$$L_{xx}(\omega) = \frac{2n_1(\omega)\cos\gamma}{n_1(\omega)\cos\gamma + n_2(\omega)\cos\beta_\mathrm{SFG}} \tag{A.7}$$

$$L_{yy}(\omega) = \frac{2n_1(\omega)\cos\beta_\mathrm{SFG}}{n_1(\omega)\cos\beta_\mathrm{SFG} + n_2(\omega)\cos\gamma} \tag{A.8}$$

$$L_{zz}(\omega) = \frac{2n_2(\omega)\cos\beta_\mathrm{SFG}}{n_1(\omega)\cos\gamma + n_2(\omega)\cos\beta_\mathrm{SFG}}\left(\frac{n_1(\omega)}{n'(\omega)}\right)^2 \tag{A.9}$$

Here the refracted angle γ is obtained from

$$n_1(\omega)\sin\beta_\mathrm{SFG} = n_2(\omega)\sin\gamma \tag{A.10}$$

and usually the refractive index n' of the thin layer is approximated with the macroscopic refractive index of the bulk adsorbate.

So far we have shown that the microscopic observable, hyperpolarizability, can be accessed in the SFG experiment and its different components are probed in the laboratory frame by changing the polarization of the incident light and detecting a selected polarization of the SF output. However, we are more interested in molecular orientation than to the projection of different components of molecular polarizability into the axes of the laboratory frame. Therefore one has to transform the laboratory coordinates (x, y, z) into the molecular coordinates (α, β, γ).

As an example for this procedure, we take a simplistic model for D_2O (taking into account especially the free OD vibration), where its symmetry is reduced to cylindrical with polarization change along the bond axis, as indicated by the Equation 3.12 (see Figure A.2). The molecular

---

[1]The same is valid for all isotropic surfaces
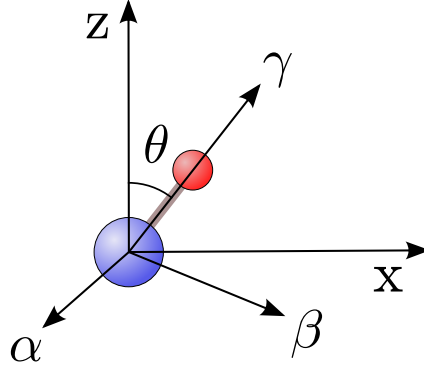
Figure A.2.: Molecular orientation in the laboratory frame.

axis γ can be chosen to follow the O–D direction at angle θ with respect to the laboratory z axis. The transformation between the two axial systems can be, in general, expressed as a product of rotation matrices

$$\chi_{ijk}^{(2)} = \boldsymbol{R}_i \boldsymbol{R}_j \boldsymbol{R}_k \chi_{\alpha\beta\gamma}^{(2)} \tag{A.11}$$

for Euler angles ϕ, η, θ they have the form [Hir92]

$$\boldsymbol{R}_i = \begin{pmatrix} \cos\phi & \sin\phi & 0 \\ -\sin\phi & \cos\phi & 0 \\ 0 & 0 & 1 \end{pmatrix} \tag{A.12}$$

$$\boldsymbol{R}_j = \begin{pmatrix} \cos\eta & 0 & -\sin\eta \\ 0 & 1 & 0 \\ \sin\eta & 0 & \cos\eta \end{pmatrix} \tag{A.13}$$

$$\boldsymbol{R}_j = \begin{pmatrix} \cos\theta & \sin\theta & 0 \\ -\sin\theta & \cos\theta & 0 \\ 0 & 0 & 1 \end{pmatrix} \tag{A.14}$$

From these transformations follows for our simple case obviously possessing only a component parallel and perpendicular to the OD bond [Du93, She89]

$$\chi_{q,yyz}^{(2)} = \frac{1}{2\epsilon_0} N_s \alpha_{\gamma\gamma\gamma}^{(2)} [\langle \sin^2\theta \cos\theta \rangle (1-r) + 2r\langle \cos\theta \rangle] \tag{A.15}$$

$$\chi_{q,yzy}^{(2)} = \frac{1}{2\epsilon_0} N_s \alpha_{\gamma\gamma\gamma}^{(2)} [\langle \sin^2\theta \cos\theta \rangle (1-r)] \tag{A.16}$$

$$\chi_{q,zyy}^{(2)} = \frac{1}{2\epsilon_0} N_s \alpha_{\gamma\gamma\gamma}^{(2)} [\langle \sin^2\theta \cos\theta \rangle] \tag{A.17}$$

$$\chi_{q,zzz}^{(2)} = \frac{1}{\epsilon_0} N_s \alpha_{\gamma\gamma\gamma}^{(2)} [\langle \cos^3\theta \rangle] \tag{A.18}$$

with $\alpha_{\gamma\gamma\gamma}^{(2)}$ being the hyperpolarizability along the OD axis and r being the hyperpolarizability ratio ($r = \alpha_\perp/\alpha_\parallel$) that can be either obtained from fitting the SFG spectra [Wei02] or is known e.g. from Raman spectra of water in this particular case case [Du93].

In the analysis, the amplitude A_q of the free OD resonance for all polarizations (if possible and not vanishing) would be extracted and its value could be set to the $\chi_{q,\text{eff}}^{(2)}$. Using Equations A.3 to A.6 the left side of A.15 to A.18 is determined. The ratio of e.g. the first two (measured in

SSP and SSP polarization configuration) yields then an explicit formula to calculate the angle θ between the surface normal and the (angularly averaged) OD bond axis direction.

B. Abbreviations

2PC   Two–pulse correlation

2PPE   Two–photon photoemission

AES   Auger electron spectroscopy

ASW   Amorphous solid water

BBO β–BaB$_2$O$_4$

BL   Bilayer

BOA   Born–Oppenheimer approximation

CB   Conduction band

CEM   Channel electron multiplier

DFG   Difference frequency generation

DFT   Density functional theory

DIET   Desorption induced by electronic transition

DIMET   Desorption induced by multiple electronic transitions

E_F Fermi level

EFISH   Electric–field induced second harmonic generation

ESH   Electron bombardment heating

e_T Trapped electron (spectral signature)

FWHM   Full width at half maximum

hcp   hexagonal close–packed

HOMO   Highest occupied molecular orbital

I_c Cubic structure of ice I

I_h Hexagonal structure of ice I

ICCD   Intensified charge–coupled device

IR   Infrared

IPS   Image potential state

LCAO	Linear combination of atomic orbitals
LEED	Low energy electron diffraction
LUMO	Lowest unoccupied molecular orbital
ML	Monolayer
NLO	Nonlinear optics
NRB	Non–resonant background
OPA	Optical parametric amplification
OPG	Optical parametric generation
OPO	Optical parametric oscillator
PES	Potential energy surface
PS	Photoelectron spectroscopy
QMS	Quadrupol mass spectrometer
RFA	Retarding–field analyzer
SF	Sum–frequency
SFG	Sum–frequency generation
SHG	Second harmonic generation
T_{des}	Desorption temperature
TDS	Thermal desorption spectroscopy
Ti:sapphire	Titanium (Ti_3^+) doped sapphire (Al_2O_3) crystal
TOPAS	Travelling-wave optical parametric amplifier of superfluorescence
UHV	Ultrahigh vacuum
UV	Ultraviolet
VB	Valence band
VDE	Vertical detachment energy
VIS	Visible
Nd:YAG	Solid–state laser with neodymium–doped yttrium aluminium garnet ($\text{Nd:Y}_3\text{Al}_5\text{O}_{12}$) as the lasing medium
Nd:YLF	Solid–state laser with neodymium–doped lithium yttrium fluoride (Nd:YLiF_4) as the lasing medium

Bibliography

[Ada66] A. W. Adamson and L. M. Dormant. *Adsorption of nitrogen on ice at 78 K*. J. Am. Chem. Soc., **88**, (1966) 2055.

[All87] P. B. Allen. *Theory of thermal relaxation of electrons in metals*. Phys. Rev. Lett., **59**, (1987) 1460.

[All00] H. C. Allen, E. A. Raymond and G. L. Richmond. *Non–linear vibrational sum frequency spectroscopy of atmospherically relevant molecules at aqueous solution surfaces*. Current Opinion in Colloid & Interface Science, **5**, (2000) 74.

[And04] K. Andersson, A. Nikitin, L. G. M. Pettersson, A. Nilsson and H. Ogasawara. *Water dissociation on Ru(001): an activated process*. Phys. Rev. Lett., **93**, (2004) 196101.

[And05] I. Andrianov, T. Klamroth, P. Saalfrank, U. Bovensiepen, C. Gahl and M. Wolf. *Quantum theoretical study of electron solvation dynamics in ice layers on a Cu(111) surface*. J. Chem. Phys., **122**(23), (2005) 234710.

[Ani74] S. I. Anisimov, B. L. Kapeliovich and T. L. Perelman. *Electron emission from metal surfaces exposed to ultrashort laser pulses*. Sov. Phys.–JETP, **39**, (1974) 375.

[Ant80] P. R. Antoniewicz. *Model for electron– and photon–stimulated desorption*. Phys. Rev. B, **21**, (1980) 3811.

[Arm62] J. A. Armstrong, N. Bloembergen, J. Ducuing and P. S. Pershan. *Interactions between light waves in a nonlinear dielectric*. Phys. Rev., **127**, (1962) 1918.

[Arm96] D. J. Armstrong, W. J. Alford, T. D. Raymond and A. V. Smith. *Absolute measurement of the effective nonlinearities of KTP and BBO crystals by optical parametric amplification*. Applied Optics, **35**, (1996) 2032.

[Arn10] H. Arnolds and M. Bonn. *Ultrafast surface vibrational dynamics*. Surf. Sci. Reports, **65**, (2010) 45.

[Ash76] N. W. Ashcroft and N. D. Mermin. *Solid state physics* (Harcourt College Publishers), 1976.

[Ayo97] P. Ayotte and M. A. Johnson. *Electronic absorption spectra of size–selected hydrated electron clusters: $(H_2O)_n^-$, n=6–50*. J. Chem. Phys., **106**, (1997) 811.

[Bac98] S. Backus, C. G. Durfee, M. M. Murnane and H. C. Kapteyn. *High power ultrafast lasers*. Rev. Sci. Instrum., **69**, (1998) 1207.

[Bac04] E. H. G. Backus, M. L. Grecea, A. W. Kleyn and M. Bonn. *Surface crystallization of amorphous solid water*. Phys. Rev. Lett., **92**(23), (2004) 236101.

[Bac07] E. H. G. Backus, M. L. Grecea, A. W. Kleyn and M. Bonn. *Ultrafast electron–induced desorption of water from nanometer amorphous solid water films.* J. Phys. Chem. B, **111**, (2007) 6141.

[Bad85] P. Bado and M. Bouvier. *Multikilohertz Pockels cell driver.* Rev. Sci. Instrum., **56**, (1985) 1744.

[Bai91] C. D. Bain, P. B. Davies, T. H. Ong, R. N. Ward and M. A. Brown. *Quantitative analysis of monolayer composition by sum-frequency vibrational spectroscopy.* Langmuir, **7**, (1991) 1563.

[Bai95] C. D. Bain. *Sum-frequency vibrational spectroscopy of the solid/liquid interface.* J. Chem. Soc., Faraday Trans., **91**, (1995) 1281.

[Bal97] A. Baltuška, Z. Wei, M. S. Pshenichnikov and D. A. Wiersma. *Optical pulse compression to* 5 fs *at a* 1 MHz *repetition rate.* Optics Letters, **22**, (1997) 102.

[Bal05] F. Baletto, C. Cavazzoni and S. Scandolo. *Surface trapped excess electrons on ice.* Phys. Rev. Lett., **95**, (2005) 176801.

[Bar87] R. N. Barnett, U. Landman, C. L. Cleveland and J. Jortner. *Surface states of excess electrons on water clusters.* Phys. Rev. Lett., **59**, (1987) 811.

[Bar88] R. N. Barnett, U. Landman, C. L. Cleveland and J. Jortner. *Electron localization in water clusters. II. Surface and internal states.* J. Chem. Phys., **88**, (1988) 4429.

[Bar89] R. B. Barnett, U. Landman and A. Nitzan. *Relaxation dynamics following transition of solvated electrons.* J. Chem. Phys., **90**, (1989) 4413.

[Bas62a] M. Bass, P. A. Franken, A. E. Hill, C. W. Peters and G. Weinreich. *Optical mixing.* Phys. Rev. Lett., **8**, (1962) 18.

[Bas62b] M. Bass, P. A. Franken, J. F. Ward and G. Weinreich. *Optical rectification.* Phys. Rev. Lett., **9**, (1962) 446.

[Bel00] M. A. Belkin, T. A. Kulakov, K.-H. Ernst, L. Yan and Y. R. Shen. *Sum–frequency vibrational spectroscopy on chiral liquids: A novel technique to probe molecular chirality.* Phys. Rev. Lett., **85**, (2000) 4474.

[Bel01] M. A. Belkin, S. H. Han, X. Wei and Y. R. Shen. *Sum–frequency generation in chiral liquids near electronic resonance.* Phys. Rev. Lett., **87**, (2001) 113001.

[Ben56] W. S. Benedict, N. Gailar and E. K. Plyler. *Rotation–vibration spectra of deuterated water vapor.* J. Chem. Phys., **24**, (1956) 1139.

[Ber33] J. D. Bernal and R. H. Fowler. *A theory of water and ionic solution, with particular reference to hydrogen and hydroxyl ions.* J. Chem. Phys., **1**, (1933) 515.

[Ber64] J. E. Bertie and E. Whalley. *Infrared spectra of ices Ih and Ic in the range 4000 to 350 cm^{-1}.* J. Chem. Phys., **40**, (1964) 1637.

[Ber69] J. E. Bertie, H. J. Labbe and E. Whalley. *Absorptivity of ice I in the range* 4000 – 30 cm^{-1}. J. Chem. Phys., **50**, (1969) 4501.

[Ber00] W. Berthold, U. Höfer, P. Feulner and D. Menzel. *Influence of Xe adlayer morphology and electronic structure on image–potential state lifetimes of Ru(0001).* Chem. Phys., **251**, (2000) 123.

[Ber04] W. Berthold, F. Rebentrost, P. Feulner and U. Höfer. *Influence of Ar, Kr, and Xe layers on the energies and lifetimes of image–potential states on Cu(100).* Appl. Phys. A, **78**, (2004) 131.

[Ber09] M. Bertin, M. Meyer, J. Stähler, C. Gahl, M. Wolf and U. Bovensiepen. *Reactivity of water–electron complexes on crystalline ice surfaces.* Faraday Discuss., **141**, (2009) 293.

[Bir58] A. J. Birch and H. Smith. *Reduction by metal–amine solutions: applications in synthesis and determination of structure.* Q. Rev. Chem. Soc., **12**, (1958) 17.

[Bje52] N. Bjerrum. *Structure and properties of ice.* Science, **11**, (1952) 385.

[Bla58] M. Blackman and N. D. Lisgarten. *Electron diffraction investigations into the cubic and other structural forms of ice.* Advances in Physics, **7**(26), (1958) 189.

[Blo62] N. Bloembergen and P. S. Pershan. *Light waves at the boundary of nonlinear media.* Phys. Rev., **128**, (1962) 606.

[Bon75] R. Bonifacio and L. A. Lugiato. *Cooperative radiation processes in two–level systems: Superfluorescence.* Phys. Rev. A, **11**, (1975) 1507.

[Bon99] M. Bonn, S. Funk, C. Hess, D. N. Denzler, C. Stampfl, M. Scheffler, M. Wolf and G. Ertl. *Phonon- versus electron-mediated desorption and oxidation of CO on Ru(0001).* Science, **285**, (1999) 1042.

[Bon00a] M. Bonn, D. N. Denzler, S. Funk, M. Wolf, S.-S. Wellershoff and J. Hohlfeld. *Ultrafast electron dynamics at metal surfaces: Competition between electron–phonon coupling and hot–electron transport.* Phys. Rev. B, **61**, (2000) 1101.

[Bon00b] M. Bonn, C. Hess, S. Funk, J. H. Miners, B. N. J. Persson, M. Wolf and G. Ertl. *Femtosecond surface vibrational spectroscopy of CO adsorbed on Ru(001) during desorption.* Phys. Rev. Lett., **84**, (2000) 4653.

[Bon01] M. Bonn, C. Hess, J. H. Miners, T. F. Heinz, H. J. Bakker and M. Cho. *Novel surface vibrational spectroscopy: infrared–infrared–visible sum–frequency generation.* Phys. Rev. Lett., **86**, (2001) 1566.

[Bon05] M. Bonn, H. Ueba and M. Wolf. *Theory of sum-frequency generation spectroscopy of adsorbed molecules using the density matrix method – broadband vibrational sum-frequency generation and applications.* J. Phys.: Condens. Matter, **17**, (2005) S201.

[Bor20] M. Born and V. Fock. *Beweis des Adiabatensatzes.* Zeitschrift für Physik A: Hadrons and Nuclei, **51**(3–4), (1920) 165.

[Bor27] M. Born and R. Oppenheimer. *Zur Quantentheorie der Molekeln.* Annalen der Physik, **84(389)**, (1927) 457.

[Bor75] M. Born and E. Wolf. *Principles of optics* (Pergamon Press), 1975.

[Bos09] S. K. Bose. *Electron–phonon coupling and spin fluctuations in 3d and 4d transition metals: implications for superconductivity and its pressure dependence.* J. Phys.: Cond. Matter, **21**, (2009) 025602.

[Böt99] A. Böttcher and H. Niehus. *Formation of subsurface oxygen at Ru(0001).* J. Chem. Phys., **110**, (1999) 3186.

[Bov05a] U. Bovensiepen. *Ultrafast electron transfer, localization and solvation at ice–metal interfaces: Correlation of structure and dynamics.* Prog. Surf. Sci., **78**, (2005) 87.

[Bov05b] U. Bovensiepen, C. Gahl, J. Stähler, P. Loukakos and M. Wolf. *Femtosecond dynamics of electron transfer, localization, and solvation processes at the ice–metal interface.* Isr. J. Chem., **45**, (2005) 171.

[Bov05c] U. Bovensiepen, C. Gahl, J. Stähler and M. Wolf. *Ultrafast electron dynamics in amorphous and crystalline D_2O layers on Ru(001).* Surf. Sci., **584**, (2005) 90.

[Bov09] U. Bovensiepen, C. Gahl, J. Stähler, M. Bockstedte, M. Meyer, F. Baletto, S. Scandolo, X.-Y. Zhu, A. Rubio and M. Wolf. *A dynamic landscape from femtoseconds to minutes for excess electrons at ice-metal interfaces.* J. Phys. Chem. C, **113**, (2009) 979.

[Boy03] R. W. Boyd. *Nonlinear optics* (Academic press), 2nd edition, 2003.

[Bra95] M. Brandbyge, P. Hedegård, T. F. Heinz, J. A. Misewich and D. M. Newns. *Electronically driven adsorbate excitation mechanism in femtosecond–pulse laser desorption.* Phys. Rev. B, **52**, (1995) 6042.

[Bra97] J. Braun, K. L. Kostov, G. Witte, L. Surnev, J. G. Skofronick, S. A. Safron and C. Wöll. *Surface phonon dispersion curves for a hexagonally close packed metal surface: Ru(0001).* Surf. Sci., **372**, (1997) 132.

[Bra98] J. Braun, A. Glebov, A. P. Graham, A. Menzel and J. P. Toennies. *Structure and phonons of the ice surface.* Phys. Rev. Lett., **80**, (1998) 2638.

[Bra99] S. T. Bramwell. *Condensed–matter science: Ferroelectric ice.* Nature, **397**, (1999) 212.

[Bra00] T. Brabec and F. Krausz. *Intense few–cycle laser fields: Frontiers of nonlinear optics.* Rev. Mod. Phys., **72**, (2000) 545.

[Bro87] S. D. Brorson, J. G. Fujimoto and E. P. Ippen. *Femtosecond electronic heat–transport dynamics in thin gold films.* Phys. Rev. Lett., **59**, (1987) 1962.

[Bro90] S. D. Brorson, A. Kazeroonian, J. S. Moodera, D. W. Face, T. K. Cheng, E. P. Ippen, M. S. Dresselhaus and G. Dresselhaus. *Femtosecond room–temperature measurement of the electron–phonon coupling constant λ in metallic superconductors.* Phys. Rev. Lett., **64**, (1990) 2172.

[Bro96] D. E. Brown, S. M. George, C. Huang, E. K. L. Wong, K. B. Rider, R. S. Smith and B. D. Kay. *H_2O condensation coefficient and refractive index for vapor-deposited ice from molecular beam and optical interference measurements.* J. Phys. Chem., **100**, (1996) 4988.

[Buc96] V. Buch, L. Delzeit, C. Blackledge and J. P. Devlin. *Structure of the ice nanocrystal surface from simulated versus experimental spectra of adsorbed CF_4*. J. Phys. Chem., **100**, (1996) 3732.

[Buc98] V. Buch, P. Sandler and J. Sadlej. *Simulations of H_2O solid, liquid, and clusters, with an emphasis on ferroelectric ordering transition in hexagonal ice*. J. Phys. Chem. B, **102**, (1998) 8641.

[Buc99] V. Buch and J. P. Devlin. *A new interpretation of the OH–stretch spectrum of ice*. J. Chem. Phys., **110**, (1999) 3437.

[Buc01] M. Buck and M. Himmelhaus. *Vibrational spectroscopy of interfaces by infrared-visible sum frequency generation*. J. Vac. Sci. Technol. A, **19**, (2001) 2717.

[Buc05] V. Buch. *Molecular structure and OH–stretch spectra of liquid water surface*. J. Phys. Chem. B, **109**, (2005) 17771.

[Buc07] V. Buch, T. Tarbuck, G. L. Richmond, H. Groenzin, I. Li and M. J. Shultz. *Sum frequency generation surface spectra of ice, water, and acid solution investigated by an exciton model*. J. Chem. Phys., **127**, (2007) 204710.

[Bud91] F. Budde, T. F. Heinz, M. M. T. Loy, J. A. Misewich, F. de Rougemont and H. Zacharias. *Femtosecond time–resolved measurement of desorption*. Phys. Rev. Lett., **66**, (1991) 3024.

[Bud93] F. Budde, T. F. Heinz, A. Kalamarides, M. M. T. Loy and J. A. Misewich. *Vibrational distributions in desorption induced by femtosecond laser pulses: coupling of adsorbate vibration to substrate electronic excitation*. Surf. Sci., **283**, (1993) 143.

[Bur35] E. F. Burton and W. F. Oliver. *The crystal structure of ice at low temperatures*. Proc. R. Soc. Lond. A, **153**, (1935) 166.

[But77] W. H. Butler. *Electron–phonon coupling in the transition metals: Electronic aspects*. Phys. Rev. B, **15**, (1977) 5267.

[Bye68] R. L. Byer and S. E. Harris. *Power and bandwidth of spontaneous parametric emission*. Phys. Rev., **168**, (1968) 1064.

[Cah03] D. Cahen and A. Kahn. *Electron energetics at surfaces and interfaces: concepts and experiments*. Adv. Mater., **15**, (2003) 271.

[Cal92] B. W. Callen, K. Griffiths and P. R. Norton. *Observation of free hydroxyl groups on the surface of ultra thin ice layers on Ni(110)*. Surf. Sci., **261**, (1992) L44.

[Cha98] D. Chakarov and B. Kasemo. *Photoinduced crystallization of amorphous ice films on graphite*. Phys. Rev. Lett., **81**(23), (1998) 5181.

[Che81] C. K. Chen, A. R. B. de Castro and Y. R. Shen. *Surface-enhanced second-harmonic generation*. Phys. Rev. Lett., **42**, (1981) 145.

[Che02] Z. Chen, Y. R. Shen and G. A. Somorjai. *Studies of polymer surfaces by sum frequency generation vibrational spectroscopy*. Annual Review Physical Chemistry, **53**, (2002) 437.

Bibliography

[Cho04] K. C. Chou, S. Westerberg, Y. R. Shen, P. N. Ross and G. A. Somorjai. *Probing the charge-transfer state of CO on Pt(111) by two-dimensional infrared-visible sum frequency generation spectroscopy.* Phys. Rev. B, **69**, (2004) 153413.

[Cho05] E.-M. Choi, Y.-H. Yoon, S. Lee and H. Kang. *Freezing transition of interfacial water at room temperature under electric fields.* Phys. Rev. Lett., **95**, (2005) 085701.

[Cla04] C. Clay, S. Haq and A. Hodgson. *Intact and dissociative adsorption of water on Ru(0001).* Chem. Phys. Lett., **388**, (2004) 89.

[Cla05] C. Clay and A. Hodgson. *Water and mixed OH/water adsorption at close packed metal surfaces.* Current opinion in solid state and materials science, **9**, (2005) 11.

[Clo73] S. A. Clough, Y. Beers, G. P. Klein and L. S. Rothman. *Dipole moment of water from Stark measurements of H_2O, HDO, and D_2O.* J. Chem. Phys., **59**, (1973) 2254.

[Coe06] J. V. Coe, S. T. Arnold, J. G. Eaton, G. H. Lee and K. H. Bowen. *Photoelectron spectra of hydrated electron clusters: Fitting line shapes and grouping isomers.* J. Chem. Phys., **125**, (2006) 014315.

[Cow78] J. P. Cowin, D. J. Auerbach, C. Becker and L. Wharton. *Measurement of fast desorption kinetics of D_2 from tungsten by laser induced thermal desorption.* Surf. Sci., **78**, (1978) 545.

[Cow99] J. P. Cowin and M. J. Iedema. *Reply to comment on "Ferroelectricity in water ice".* J. Phys. Chem. B, **103**, (1999) 8194.

[Cro77] A. Crossley and D. A. King. *Infrared spectra for CO isotopes chemisorbed on Pt (111): Evidence for strong absorbate coupling interactions.* Surf. Sci., **68**, (1977) 528.

[Cro96] R. A. Crowell and D. M. Bartels. *Multiphoton ionization of liquid water with 3.0 5.0 eV photons.* J. Phys. Chem., **100**, (1996) 17940.

[Cub67] G. Cubiotti and R. Geracitano. *Ferroelectric behaviour of cubic ice.* Phys. Lett., **24**, (1967) 179.

[d'A75] E. G. d'Agliano, P. Kumar, W. Schaich and H. Suhl. *Brownian motion model of the interactions between chemical species and metallic electrons: Bootstrap derivation and parameter evaluation.* Phys. Rev. B, **11**, (1975) 2122.

[Dah00] D. A. Dahl. SIMION *for the personal computer in reflection.* International Journal of Mass Spectrometry, **200**, (2000) 3.

[Dan93] R. Danielius, A. Piskarskas, A. Stabinis, G. P. Banfi, P. Di Trapani and R. Righini. *Traveling–wave parametric generation of widely tunable, highly coherent femtosecond light pulses.* J. Opt. Soc. Am. B, **10**, (1993) 2222.

[Das89] J. G. Dash. *Surface melting.* Contemporary Physics, **30**, (1989) 89.

[Das04] J. L. Daschbach, B. M. Peden, R. S. Smith and B. D. Kay. *Adsorption, desorption, and clustering of H_2O on Pt(111).* J. Chem. Phys., **120**, (2004) 1516.

[De 84] L. J. De Koning and N. M. M. Nibbering. *Formation of the long–lived $H_2O^- \cdot$ ion in the gas phase.* J. Am. Chem. Soc., **106**, (1984) 7971.

[Dec89] A. A. Deckert, J. L. Brand, M. V. Arena and S. M. George. *Surface diffusion of carbon monoxide on Ru(001) studied using laser-induced thermal desorption.* Surf. Sci., **208**, (1989) 441.

[Ded81] P. H. Dederichs, H. Schober and D. J. Sellmyer. *Phonon states of elements. Electron states and Fermi surfaces of alloys.* In *Landolt–Börnstein,* group III, volume 13a (Springer–Verlag Berlin), 1981.

[Del95] S. Deliwala, R. J. Finlay, J. R. Goldman, T. H. Her, W. D. Mieher and E. Mazur. *Surface femtochemistry of O_2 and CO on Pt(111).* Chem. Phys. Lett., **242**, (1995) 617.

[Del97] L. Delzeit, J. P. Devlin and V. Buch. *Structural relaxation rates near the ice surface: Basis for separation of the surface and subsurface spectra.* J. Chem. Phys., **107**, (1997) 3726.

[Dem08] W. Demtröder. *Laser spectroscopy* (Springer Verlag Berlin Heidelberg), 2008.

[Den64] O. Dengel, U. Eckener, H. Plitz and N. Riehl. *Ferroelectric behaviour of ice.* Phys. Lett., **9**, (1964) 291.

[Den99] D. N. Denzler. *Untersuchungen zur Ultrakurzzeitdynamik photostimulierter Oberflächenreaktionen und der Energierelaxation in Metallen.* Master's thesis, FU Berlin, 1999.

[Den03a] D. N. Denzler. *Zur ultraschnellen Reaktionsdynamik von Wasserstoff und Grenzflächenstruktur von Wasser auf der Ru(001)–Oberfläche.* Ph.D. thesis, FU Berlin, 2003.

[Den03b] D. N. Denzler, C. Hess, R. Dudek, S. Wagner, C. Frischkorn, M. Wolf and G. Ertl. *Interfacial structure of water on Ru(001) investigated by vibrational spectroscopy.* Chem. Phys. Lett., **376**, (2003) 618.

[Den03c] D. N. Denzler, S. Wagner, M. Wolf and G. Ertl. *Isotope effects in the thermal desorption of water from Ru(001).* Surf. Sci., **532-535**, (2003) 113.

[Dev90a] J. P. Devlin. *Vibrational modes of amorphous ice: bending mode frequencies for isotopically decoupled H_2O and HOD at 90 K.* J. Molecular Structure, **224**, (1990) 33.

[Dev90b] J. P. Devlin. *Vibrational spectra and point defect activities of icy solids and gas phase clusters.* Int. Rev. Phys. Chem., **9**, (1990) 29.

[Dev95] J. P. Devlin and V. Buch. *Surface of ice as viewed from combined spectroscopic and computer modeling studies.* J. Phys. Chem., **99**, (1995) 16534.

[Dev01] J. P. Devlin, J. Sadlej and V. Buch. *Infrared spectra of large H_2O clusters: new understanding of the elusive bending mode of ice.* J. Phys. Chem. A, **105**, (2001) 974.

[Dic54] R. H. Dicke. *Coherence in spontaneous radiation processes.* Phys. Rev., **93**, (1954) 99.

[Doe82] D. L. Doering and T. E. Madey. *The adsorption of water on clean and oxygen–dosed Ru(001).* Surf. Sci., **123**, (1982) 305.

[Doh00] Z. Dohnálek, G. A. Kimmel, R. L. Ciolli, K. P. Stevenson, R. S. Smith and B. D. Kay. *The effect of the underlying substrate on the crystallization kinetics of dense amorphous solid water films.* J. Chem. Phys., **112**, (2000) 5932.

[Dok08] A. M. Dokter and H. J. Bakker. *Transient absorption of vibrationally excited ice Ih.* J. Chem. Phys., **128**, (2008) 024502.

[Du93] Q. Du, R. Superfine, E. Freysz and Y. R. Shen. *Vibrational spectroscopy of water at the vapor/water interface.* Phys. Rev. Lett., **70**, (1993) 2313.

[Du07] Y. Du, E. Price and D. M. Bartels. *Solvated electron spectrum in supercooled water and ice.* Chem. Phys. Lett., **438**, (2007) 234.

[Dub08] D. Y. Dubov and A. A. Vostrikov. *Ordering of molecular dipole moments in a nanosized water cluster.* JETP Letters, **88**, (2008) 674.

[Dwo00] R. Dworczak and D. Kieslinger. *Electric field induced second harmonic generation (EFISH) experiments in the swivel cell: New aspects of an established method.* Physical Chemistry Chemical Physics, **2**, (2000) 5057.

[Dzu05] J. Dzubiella and J.-P. Hansen. *Electric-field-controlled water and ion permeation of a hydrophobic nanopore.* J. Chem. Phys., **122**, (2005) 234706.

[Ech78] P. M. Echenique and J. B. Pendry. *The existence and detection of Rydberg states at surfaces.* J. Phys. C, **11**, (1978) 2065.

[Ech86] P. Echenique and J. Pendry. *Electron–hole pair contributions to the effective mass of electrons at surfaces.* Surf. Sci., **166**, (1986) 69.

[Ech04] P. M. Echenique, R. Berndt, E. V. Chulkov, T. Fausterd, A. Goldmanne and U. Höfer. *Decay of electronic excitations at metal surfaces.* Surf. Sci. Reports, **52**, (2004) 219.

[Eim87] D. Eimerl, L. Davis, S. Velsko, E. K. Graham and A. Zalkin. *Optical, mechanical, and thermal properties of barium borate.* J. Appl. Phys., **62**, (1987) 1968.

[Eng96] I. Engquist and B. Liedberg. D_2O *ice on controlled wettability self–assembled alkanethiolate monolayers: cluster formation and substrate–adsorbate interaction.* J. Phys. Chem., **100**, (1996) 20089.

[Ert94] G. Ertl. *Reactions at well–defined surfaces.* Surf. Sci., **299–300**, (1994) 742.

[Fan61] U. Fano. *Effects of configuration interaction on intensities and phase shifts.* Phys. Rev., **124**, (1961) 1866.

[Fan92] W. S. Fann, R. Storz, H. W. K. Tom and J. Bokor. *Electron thermalization in gold.* Phys. Rev. B, **46**, (1992) 13592.

[Fan09] Y. Fan, X. Chen, L. Yang, P. S. Cremer and Y. Q. Gao. *On the structure of water at the aqueous/air interface.* J. Phys. Chem. B, **113**, (2009) 11672.

[Far59] M. Faraday. *Note on regelation.* Proc. R. Soc. Lond. A, **10**, (1859) 440.

[Far05] N. S. Faradzhev, K. L. Kostov, P. Feulner, T. E. Madey and D. Menzel. *Stability of water monolayers on Ru(0001): Thermal and electronically induced dissociation.* Chem. Phys. Lett., **415**, (2005) 165.

[Fei02]   P. J. Feibelman. *Partial dissociation of water on Ru(0001)*. Science, **295**, (2002) 99.

[Fei03]   P. J. Feibelman. *Vibrations of water adlayer on Ru(0001)*. Phys. Rev. B, **67**, (2003) 35421.

[Fei04]   P. J. Feibelman. *What the stretch frequency spectrum of $D_2O/Ru(0001)$ does and does not mean*. Chem. Phys. Lett., **389**, (2004) 92.

[Fei05a] P. J. Feibelman. *Using Ar adsorption to estimate the van der Waals contribution to the wetting of Ru(0001)*. Phys. Rev. B, **72**, (2005) 113405.

[Fei05b] P. J. Feibelman. *A wetting layer breaks the ice rules*. Chem. Phys. Lett., **410**, (2005) 120.

[Fer31]   E. Fermi. *Über den Ramaneffekt des Kohlendioxyds*. Zeitschrift für Physik, **71**(3–4), (1931) 250.

[Feu80]   P. Feulner and D. Menzel. *Simple ways to improve flash desorption measurements from single–crystal surfaces*. J. Vac. Sci. Technol., **17**, (1980) 662.

[Fin02]   J. L. Finney, A. Hallbrucker, I. Kohl, A. K. Soper and D. T. Bowron. *Structures of high and low density amorphous ice by neutron diffraction*. Phys. Rev. Lett., **88**, (2002) 225503.

[Fis80]   G. B. Fisher and J. L. Gland. *The interaction of water with the Pt(111) surface*. Surf. Sci., **94**, (1980) 446.

[Fis95]   M. Fisher and J. P. Devlin. *Defect activity in amorphous ice from isotopic exchange data: insight into the glass transition*. J. Phys. Chem., **99**, (1995) 11584.

[Fle08]   J. I. Flege, J. Hrbek and P. Sutter. *Structural imaging of surface oxidation and oxidation catalysis on Ru(0001)*. Phys. Rev. B, **78**, (2008) 165407.

[Fra61]   P. A. Franken, A. E. Hill, C. W. Peters and G. Weinreich. *Generation of optical harmonics*. Phys. Rev. Lett., **7**, (1961) 118.

[Fra63]   P. A. Franken and J. F. Ward. *Optical harmonics and nonlinear phenomena*. Rev. Mod. Phys., **35**, (1963) 23.

[Fra01]   G. Franzese, G. Malescio, A. Skibinsky, S. V. Buldyrev and H. E. Stanley. *Generic mechanism for generating a liquid–liquid phase transition*. Nature, **409**, (2001) 692.

[Fre95]   P. M. W. French. *The generation of ultrashort laser pulses*. Rep. Prog. Phys., **58**, (1995) 169.

[Fri06]   C. Frischkorn and M. Wolf. *Femtochemistry at metal surfaces: nonadiabatic reaction dynamics*. Chem. Rev., **106**, (2006) 4207.

[Fri08]   C. Frischkorn. *Ultrafast reaction dynamics of the associative hydrogen desorption from Ru(001)*. J. Phys.: Condens. Matter, **20**, (2008) 313002.

[Fu97]   Q. Fu, F. Seier, S. K. Gayen and R. R. Alfano. *High–average–power kilohertz–repetition–rate sub–100–fs Ti:sapphire amplifier system*. Optics Letters, **22**, (1997) 712.

[Fun99] S. Funk. *Ultraschnelle Reaktionsdynamik an Oberflächen: Desorption und Oxidation von CO auf Ru(001) induziert durch Femtosekunden–Laserpulse.* Ph.D. thesis, FU Berlin, 1999.

[Gah00] C. Gahl, K. Ishioka, Q. Zhong, A. Hotzel and M. Wolf. *Structure and dynamics of excited electronic states at the adsorbate/metal interface: $C_6F_6/Cu(111)$.* Faraday Discuss., **117**, (2000) 191.

[Gah02] C. Gahl, U. Bovensiepen, C. Frischkorn and M. Wolf. *Ultrafast dynamics of electron localization and solvation in ice layers on Cu(111).* Phys. Rev. Lett., **89**, (2002) 107402.

[Gah04] C. Gahl. *Elektronentransfer- und Solvatisierungsdynamik in Eis adsorbiert auf Metalloberflächen.* Ph.D. thesis, Freie Universität Berlin, 2004.

[Gal09] M. Gallagher, A. Omer, G. R. Darling and A. Hodgson. *Order and disorder in the wetting layer on Ru(0001).* Faraday Discuss., **141**, (2009) 231.

[Gan06] W. Gan, D. Wu, Z. Zhang, R.-R. Feng and H.-F. Wang. *Polarization and experimental configuration analyses of sum frequency generation vibrational spectra, structure, and orientational motion of the air/water interface.* J. Chem. Phys., **124**, (2006) 114705.

[Ge98] N.-H. Ge, C. M. Wong, R. L. L. Jr., J. D. McNeill, K. J. Gaffney and C. B. Harris. *Femtosecond dynamics of electron localization at interfaces.* Science, **279**, (1998) 202.

[Ger01] B. Gergen, H. Nienhaus, W. H. Weinberg and E. W. McFarland. *Chemically induced electronic excitations at metal surfaces.* Science, **294**, (2001) 2521.

[Gio65a] J. A. Giordmaine. *Nonlinear optical properties of liquids.* Phys. Rev., **138**, (1965) A1599.

[Gio65b] J. A. Giordmaine and R. C. Miller. *Tunable coherent parametric oscillation in $LiNbO_3$ at optical frequencies.* Phys. Rev. Lett., **14**, (1965) 973.

[Gra99] A. P. Graham, A. Menzel and J. P. Toennies. *Adsorption of fluoroform CHF_3 on ice Ih(0001): Structure and vibrations.* J. Chem. Phys., **111**, (1999) 1169.

[Gre66] R. G. Greenler. *Infrared study of adsorbed molecules on metal surfaces by reflection techniques.* J. Chem. Phys., **44**, (1966) 310.

[Gre97] T. Greber. *Charge–transfer induced particle emission in gas surface reactions.* Surf. Sci. Reports, **28**, (1997) 1.

[Gro92] R. H. M. Groeneveld, R. Sprik and A. Lagendijk. *Effect of a nonthermal electron distribution on the electron-phonon energy relaxation process in noble metals.* Phys. Rev. B, **45**, (1992) 5079.

[Gro95] R. H. M. Groeneveld, R. Sprik and A. Lagendijk. *Femtosecond spectroscopy of electron–electron and electron–phonon energy relaxation in Ag and Au.* Phys. Rev. B, **51**, (1995) 11433.

[Gro07] H. Groenzin, I. Li, V. Buch and M. J. Shultz. *The single-crystal, basal face of ice Ih investigated with sum frequency generation.* J. Chem. Phys., **127**, (2007) 214502.

[GS88]   P. Guyot-Sionnest and Y. R. Shen. *Bulk contribution in surface second–harmonic generation.* Phys. Rev. B, **38**, (1988) 7985.

[Ham04] N. I. Hammer, J.-W. Shin, J. M. Headrick, E. G. Diken, J. R. Roscioli, G. H. Weddle and M. A. Johnson. *How do small water clusters bind an excess electron?* Science, **306**, (2004) 675.

[Han90] P. Han and D. M. Bartels. *H/D isotope effects in water radiolysis. 2. Dissociation of electronically excited water.* J. Phys. Chem., **94**, (1990) 5824.

[Haq02] S. Haq, J. Harnett and A. Hodgson. *Growth of thin crystalline ice films on Pt(111).* Surf. Sci., **505**, (2002) 171.

[Haq06] S. Haq, C. Clay, G. R. Darling, G. Zimbitas and A. Hodgson. *Growth of intact water ice on Ru(0001) between* 140 *and* 160 K*: Experiment and density–functional theory calculations.* Phys. Rev. B, **73**, (2006) 115414.

[Haq07] S. Haq and A. Hodgson. *Multilayer growth and wetting of Ru(0001).* J. Phys. Chem. C, **111**, (2007) 5946.

[Har62] E. J. Hart and J. W. Boag. *Absorption spectrum of the hydrated electron in water and in aqueous solutions.* J. Am. Chem. Soc., **84**, (1962) 4090.

[Har67] S. E. Harris, M. K. Oshman and R. L. Byer. *Observation of tunable optical parametric fluorescence.* Phys. Rev. Lett., **18**, (1967) 732.

[Har03] J. Harnett, S. Haq and A. Hodgson. *Electron induced restructuring of crystalline ice adsorbed on Pt(111).* Surf. Sci., **528**, (2003) 15.

[Hei99] R. Heid, K.-P. Bohnen and W. Reichardt. *Ab initio phonon spectra from a supercell approach.* Physica B: Cond. Matter, **263–264**, (1999) 432.

[Hei00] R. Heid, L. Pintschovius, W. Reichardt and K.-P. Bohnen. *Anomalous lattice dynamics of ruthenium.* Phys. Rev. B, **61**, (2000) 12059.

[Hel94] G. Held and D. Menzel. *The structure of the $p(\sqrt{3} \times \sqrt{3})R30°$ bilayer of D_2O on Ru(001).* Surf. Sci., **316**, (1994) 92.

[Hel95a] G. Held and D. Menzel. *Isotope effects in structure and kinetics of water adsorbates on Ru(001).* Surf. Sci., **327**, (1995) 301.

[Hel95b] G. Held and D. Menzel. *Structural isotope effect in water bilayers adsorbed on Ru(001).* Phys. Rev. Lett., **74**, (1995) 4221.

[Hen79] H. G. E. Hentschel. *The ferroelectric transition in hexagonal ice Ih.* Molecular Physics, **38**(2), (1979) 401.

[Hen02] M. A. Henderson. *The interaction of water with solid surfaces: fundamental aspects revisited.* Surf. Sci. Reports, **46**, (2002) 1.

[Her06] J. M. Herbert and M. Head-Gordon. *First-principles, quantum–mechanical simulations of electron solvation by a water cluster.* Proc. Natl. Acad. Sci. USA, **103**, (2006) 14282.

[Hes02] C. Hess, M. Wolf, S. Roke and M. Bonn. *Femtosecond time–resolved vibrational SFG spectroscopy of CO/Ru(001)*. Surf. Sci., **502–503**, (2002) 304.

[HG95] M. Head-Gordon and J. C. Tully. *Molecular dynamics with electronic frictions*. J. Chem. Phys., **103**, (1995) 10137.

[Him83] F. J. Himpsel. *Angle–resolved measurements of the photoemission of electrons in the study of solids*. Advances in Physics, **32**, (1983) 1.

[Hir92] C. Hirose, N. Akamatsu and K. Domen. *Formulas for the analysis of the surface SFG spectrum and transformation coefficients of cartesian SFG tensor components*. Applied Spectroscopy, **46**, (1992) 1051.

[Hod09] A. Hodgson and S. Haq. *Water adsorption and the wetting of metal surfaces*. Surf. Sci. Reports, **64**(9), (2009) 381 .

[Hoh00] J. Hohlfeld, S.-S. Wellershoff, J. Güdde, U. Conrad, V. Jähnke and E. Matthias. *Electron and lattice dynamics following optical excitation of metals*. Chem. Phys., **251**, (2000) 237.

[Hol91] S. Holloway and J. K. Norskov. *Bonding at surfaces* (Liverpool University Press), 1991.

[Hot74] H. Hotop, T. A. Patterson and W. C. Lineberger. *High resolution photodetachment study of OH^- and OD^- in the threshold region* 7000–6450 Å. J. Chem. Phys., **60**, (1974) 1806.

[Hua94] J. Y. Huang and Y. R. Shen. *Theory of doubly resonant infrared-visible sum-frequency and difference-frequency generation from adsorbed molecules*. Phys. Rev. A, **49**, (1994) 3973.

[Hun87] J. H. Hunt, P. Guyot-Sionnest and Y. R. Shen. *Observation of C–H stretch vibrations of monolayers of molecules optical sum–frequency generation*. Chem. Phys. Lett., **133**, (1987) 189.

[Ied98] M. J. Iedema, M. J. Dresser, D. L. Doering, J. B. Rowland, W. P. Hess, A. A. Tsekouras and J. P. Cowin. *Ferroelectricity in water ice*. J. Phys. Chem. B, **102**, (1998) 9203.

[Jac95] S. M. Jackson and R. W. Whitworth. *Evidence for ferroelectric ordering of ice Ih*. J. Chem. Phys., **103**, (1995) 7647.

[Jac97] S. M. Jackson, V. M. Nield, R. W. Whitworth, M. Oguro and C. C. Wilson. *Single-crystal neutron diffraction studies of the structure of ice XI*. J. Phys. Chem. B, **101**, (1997) 6142.

[Jak09] K. Jakobi. *SpringerMaterials - The Landolt-Börnstein Database* (Springer), 2009.

[Jam07] T. James, D. J. Wales and J. H. Rojas. *Energy landscapes for water clusters in a uniform electric field*. J. Chem. Phys., **126**, (2007) 054506.

[Jen94] P. Jenniskens and D. F. Blake. *Structural transitions in amorphous water ice and astrophysical implications*. Science, **265**, (1994) 753.

[Jen96] P. Jenniskens and D. F. Blake. *Crystallization of amorphous water ice in the solar system*. Astrophys. J., **473**, (1996) 1104.

[Jen97] P. Jenniskens, S. F. Banham, D. F. Blake and M. R. S. McCoustra. *Liquid water in the domain of cubic crystalline ice* I_c. J. Chem. Phys., **107**, (1997) 1232.

[Jep75] O. Jepsen, O. K. Andersen and A. R. Mackintosh. *Electronic structure of hcp transition metals.* Phys. Rev. B, **12**, (1975) 3084.

[Joh98] G. P. Johari. *An interpretation for the thermodynamic features of ice Ih—ice XI transformation.* J. Chem. Phys., **109**, (1998) 9543.

[Jor04] K. D. Jordan. *A fresh look at electron hydration.* Science, **306**, (2004) 618.

[Jou79] F.-Y. Jou and G. R. Freeman. *Temperature and isotope effects on the shape of the optical absorption spectrum of solvated electrons in water.* J. Phys. Chem., **83**, (1979) 2383.

[Kag57] M. I. Kaganov, I. M. Lifshitz and L. V. Tanatarov. *Relaxation between electrons and the crystalline lattice.* Sov. Phys.–JETP, **4**, (1957) 173.

[Kan98] A. P. Kanavin, I. V. Smetanin, V. A. Isakov, Y. V. Afanasiev, B. N. Chichkov, B. Wellegehausen, S. Nolte, C. Momma and A. Tünnermann. *Heat transport in metals irradiated by ultrashort laser pulses.* Phys. Rev. B, **57**, (1998) 14698.

[Kaw72] S. Kawada. *Dielectric dispersion and phase transition of KOH doped ice.* J. Phys. Soc. Jpn., **32**, (1972) 1442.

[Kaw97] S. Kawada, R. G. Jin and M. Abo. *Dielectric properties and 110 K anomalies in KOH– and HCl–doped ice single crystals.* J. Phys. Chem. B, **101**, (1997) 6223.

[Kev81] L. Kevan. *Solvated electron structure in glassy matrices.* Acc. Chem. Res., **14**, (1981) 138.

[Kim97] J. Kim, J. M. Park, K. S. Oh, J. Y. Lee, S. Lee and K. S. Kim. *Structure, vertical electron–detachment energy, and O–H stretching frequencies of $e + (H_2O)_{12}$.* J. Chem. Phys., **106**, (1997) 10207.

[Kim99] J. Kim, S. B. Suh and K. S. Kim. *Water dimer to pentamer with an excess electron: Ab initio study.* J. Chem. Phys., **111**, (1999) 10077.

[Kim05] G. A. Kimmel, N. G. Petrik, Z. Dohnalek and B. D. Kay. *Crystalline ice growth on Pt(111): Observation of a hydrophobic water monolayer.* Phys. Rev. Lett., **95**, (2005) 166102.

[Kim06] G. A. Kimmel, G. P. Nikolay, Z. Dohnalek and B. D. Kay. *Layer-by-layer growth of thin amorphous solid water films on Pt(111) and Pd(111).* J. Chem. Phys., **125**, (2006) 044713.

[Kim07a] J.-H. Kim, Y.-K. Kim and H. Kang. *Interaction of NaF, NaCl, and NaBr with amorphous ice films. Salt dissolution and ion separation at the ice surface.* J. Phys. Chem. C, **111**, (2007) 8030.

[Kim07b] G. A. Kimmel, N. G. Petrik, Z. Dohnalek and B. D. Kay. *Crystalline ice growth on Pt(111) and Pd(111): nonwetting growth on a hydrophobic water monolayer.* J. Chem. Phys., **126**, (2007) 114702.

[Kin75] D. A. King. *Thermal desorption from metal surfaces: A review.* Surf. Sci., **47**, (1975) 384.

[Kit96] C. Kittel. *Introduction to solid state physics* (John Wiley & Sons, Inc.), 1996.

[Kle03] R. S. Klein, G. E. Kugel, A. Maillard, A. Sifi and K. Polgár. *Absolute non–linear optical coefficients measurements of BBO single crystal and determination of angular acceptance by second harmonic generation.* Optical Materials, **22**, (2003) 163.

[Kob83] K. Kobayashi. *Optical spectra and electronic structure of ice.* J. Phys. Chem., **87**, (1983) 4317.

[Koe03] W. Koechner and M. Bass. *Solid–state lasers* (Springer Verlag New York, Inc.), 2003.

[Koh00] I. Kohl, E. Mayer and A. Hallbrucker. *The glassy water–cubic ice system: a comparative study by X–ray diffraction and differential scanning calorimetry.* Physical Chemistry Chemical Physics, **2**, (2000) 1579.

[Kon06] T. Kondo, S. Mae, H. S. Kato and M. Kawai. *Morphological change of D_2O layers on Ru(0001) probed with He atom scattering.* Surf. Sci., **600**, (2006) 3570.

[Kon07] T. Kondo, H. S. Kato, M. Bonn and M. Kawai. *Deposition and crystallization studies of thin amorphous solid water films on Ru(0001) and on CO-precovered Ru(0001).* J. Chem. Phys., **127**, (2007) 094703.

[Koo34] T. Koopmans. *Über die Zuordnung von Wellenfunktionen und Eigenwerten zu den einzelnen Elektronen eines Atoms.* Physica, **1**, (1934) 104.

[Kos92] K. L. Kostov, H. Rauscher and D. Menzel. *Adsorption of CO on oxygen-covered Ru(001).* Surf. Sci., **278**, (1992) 62.

[Kra08] C. A. Kraus. *Solutions of metals in non–metallic solvents: Material effects accompanying the passage of an electrical current through solutions of metals in liquid ammonia, migration experiments.* J. Am. Chem. Soc., **30**, (1908) 1323.

[Kra09] F. Krausz and M. Ivanov. *Attosecond physics.* Rev. Mod. Phys., **81**, (2009) 163.

[Kro92] G.-J. Kroes. *Surface melting of the (0001) face of TIP4P ice.* Surf. Sci., **275**(3), (1992) 365.

[Kub02] J. Kubota, A. Wada, K. Domen and S. S. Kano. *Transient responses of SFG spectra of D_2O ice/CO/Pt(111) interface with irradiation of ultra-short NIR pump pulses.* Chem. Phys. Lett., **362**, (2002) 476.

[Kuh08] W. F. Kuhs and M. S. Lehmann. *The structure of ice–Ih.* Water science reviews, **2**, (2008) 1.

[Kus97] H. Kusanagi. *Infrared spectra of water isotopes (H_2O, HDO, and D_2O molecules) in hydrophobic polyvinylidene fluoride.* Chem. Lett., **26**, (1997) 683.

[Kwi05] S. Kwiet, D. E. Starr, A. Grujic, M. Wolf and A. Hotzel. *Femtosecond laser induced desorption of water from silver nanoparticles.* Appl. Phys. B, **80**, (2005) 115.

[Lee67] C. H. Lee, R. K. Chang and N. Bloembergen. *Nonlinear electroreflectance in silicon and silver.* Phys. Rev. Lett., **18**, (1967) 167.

[Lee91] G. H. Lee, S. T. Arnold, J. G. Eaton, H. W. Sarkas, K. H. Bowen, C. Ludewigt and H. Haberland. *Negative ion photoelectron spectroscopy of solvated electron cluster anions, $(H_2O)_n^-$ and $(NH_3)_n^-$.* Zeitschrift für Physik D – Atoms, Molecules and Clusters, **20**, (1991) 9.

[Leh99] L. Lehr, M. T. Zanni, C. Frischkorn, R. Weinkauf and D. M. Neumark. *Electron solvation in finite systems: femtosecond dynamics of iodide·(water)$_n$ anion clusters.* Science, **284**, (1999) 635.

[Lid07] D. R. Lide, ed. *CRC Handbook of chemistry and physics* (CRC Press), 88th edition edition, 2007.

[Lin06] J. Lindner, A.-N. Unterreiner and P. Vöhringer. *Femtosecond relaxation dynamics of solvated electrons in liquid ammonia.* ChemPhysChem, **7**(2), (2006) 363.

[Lis04] M. Lisowski, P. A. Loukakos, U. Bovensiepen, J. Stähler, C. Gahl and M. Wolf. *Ultrafast dynamics of electron thermalization, cooling and transport effects in Ru(001).* Appl. Phys. A, **78**, (2004) 165.

[Lis06] M. J. Lisowski. *Elektronen– und Magnetisierungsdynamik in Metallen untersucht mit zeitaufgelöster Photoemission.* Ph.D. thesis, FU Berlin, 2006.

[Liu94] H. Liu, J. Yao and A. Puri. *Second and third harmonic generation in BBO by femtosecond Ti:sapphire laser pulses.* Optics Communications, **109**, (1994) 139.

[Liu06] W.-T. Liu, L. Zhang and Y. R. Shen. *Interfacial structures of methanol: water mixtures at a hydrophobic interface probed by sum-frequency vibrational spectroscopy.* J. Chem. Phys., **125**, (2006) 144711.

[Liu10] W.-T. Liu and Y. R. Shen. *Sum–frequency spectroscopy on bulk and surface phonons of noncentrosymmetric crystals.* Annalen der Physik, **n/a.**, (2010) 1.

[Löb97] J. Löbau and K. Wolfrum. *Sum-frequency spectroscopy in total internal reflection geometry: signal enhancement and access to molecular properties.* J. Opt. Soc. Am. B, **14**, (1997) 2505.

[Loe06] T. Loerting and N. Giovambattista. *Amorphous ices: experiments and numerical simulations.* J. Phys.: Condens. Matter, **18**(50), (2006) R919.

[Lof03] P. Lofgren, P. Ahlstrom, J. Lausma, B. Kasemo and D. Chakarov. *Crystallization kinetics of thin amorphous water films on surfaces.* Langmuir, **19**, (2003) 265.

[Lon90] F. H. Long, H. Lu and K. B. Eisenthal. *Femtosecond studies of the presolvated electron: An excited state of the solvated electron?* Phys. Rev. Lett., **64**(12), (1990) 1469.

[Lu10] Q.-B. Lu. *Cosmic–ray–driven electron–induced reactions of halogenated molecules adsorbed on ice surfaces: Implications for atmospheric ozone depletion and global climate change.* Phys. Rep., **487**, (2010) 141.

[Lud01] R. Ludwig. *Water: From clusters to the bulk.* Angewandte Chemie International Edition, **40**, (2001) 1808.

[Lud04] V. Ludwig, K. Coutinho and S. Canuto. *Sequential classical–quantum description of the absorption spectrum of the hydrated electron.* Phys. Rev. B, **70**, (2004) 214110.

[Lun05] A. C. Luntz and M. Persson. *How adiabatic is activated adsorption/associative desorption?* J. Chem. Phys., **123**, (2005) 074704.

[Lun06] A. C. Luntz, M. Persson, S. Wagner, C. Frischkorn and M. Wolf. *Femtosecond laser induced associative desorption of H_2 from Ru(0001): Comparison of "first principles" theory with experiment.* J. Chem. Phys., **124**, (2006) 244702.

[Ma09] L. Ma, K. Majer, F. Chirot and B. von Issendorff. *Low temperature photoelectron spectra of water cluster anions.* J. Chem. Phys., **131**, (2009) 144303.

[Mad75] T. E. Madey, H. A. Engelhardt and D. Menzel. *Adsorption of oxygen and oxidation of CO on the Ruthenium (001) surface.* Surf. Sci., **48**, (1975) 304.

[Mad77] T. E. Madey and J. T. Yates. *Evidence for the conformation of H_2O adsorbed on Ru(001).* Chem. Phys. Lett., **51**, (1977) 77.

[Mad07] Á. Madarász, P. J. Rossky and L. Turi. *Excess electron relaxation dynamics at water/air interfaces.* J. Chem. Phys., **126**, (2007) 234707.

[Mad09] Á. Madarász, P. J. Rossky and L. Turi. *Interior– and surface–bound excess electron states in large water cluster anions.* J. Chem. Phys., **130**, (2009) 124319.

[Mae10] K. Maeda and K. Domen. *Photocatalytic water splitting: Recent progress and future challenges.* J. Phys. Chem. Lett., **1**, (2010) 2655.

[Mak94] G. Makov and A. Nitzan. *Solvation and ionization near a dielectric surface.* J. Phys. Chem., **98**, (1994) 3459.

[Mal87] M. S. Malcuit, J. J. Maki, D. J. Simkin and R. W. Boyd. *Transition from superfluorescence to amplified spontaneous emission.* Phys. Rev. Lett., **59**, (1987) 1189.

[Mal09] G. Malenkov. *Liquid water and ices: understanding the structure and physical properties.* J. Phys.: Condens. Matter, **21**, (2009) 283101.

[Mar99] W. Marbach, A. N. Asaad and P. Krebs. *Optical absorption of solvated electrons in water and tetrahydrofuran/water mixtures.* J. Phys. Chem. A, **103**, (1999) 28.

[Mar02] D. C. Marinica, C. Ramseyer, A. G. Borisov, D. Teillet-Billy, J. P. Gauyacq, W. Berthold, P. Feulner and U. Höfer. *Effect of an atomically thin dielectric film on the surface electron dynamics: Image–potential states in the Ar/Cu(100) system.* Phys. Rev. Lett., **89**, (2002) 046802.

[Mar10] O. Marsalek, F. Uhlig, T. Frigato, B. Schmidt and P. Jungwirth. *Dynamics of electron localization in warm versus cold water clusters.* Phys. Rev. Lett., **105**, (2010) 043002.

[Mat95] N. Materer, U. Starke, A. Barbieri, M. A. van Hove, G. A. Somorjai, G. J. Kroes and C. Minot. *Molecular surface structure of a low-temperature ice Ih(0001) crystal.* J. Phys. Chem., **99**, (1995) 6267.

[Mat03] B. Mate, A. Medialdea, M. A. Moreno, R. Escribano and V. J. Herrero. *Experimental studies of amorphous and polycrystalline ice films using* FT–RAIRS. J. Phys. Chem. B, **107**, (2003) 11098.

[Mat05] G. Materzanini, G. F. Tantardini, P. J. D. Lindan and P. Saalfrank. *Water adsorption at metal surfaces: A first–principles study of the* $p(\sqrt{3} \times \sqrt{3})R30°$ H_2O *bilayer on Ru(0001).* Phys. Rev. B, **71**(15), (2005) 155414.

[McG78] R. McGraw, W. G. Madden, M. S. Bergren, S. A. Rice and M. G. Sceats. *A theoretical study fo the OH stretching region of the vibrational spectrum of ice* I_h. J. Chem. Phys., **69**, (1978) 3483.

[McG06] J. A. McGuire and Y. R. Shen. *Ultrafast vibrational dynamics at water interfaces.* Science, **313**, (2006) 1945.

[McM68] W. L. McMillan. *Transition temperature of strong–coupled superconductors.* Phys. Rev., **167**, (1968) 331.

[Men02a] S. Meng, L. F. Xu, E. G. Wang and S. Gao. *Vibrational recognition of hydrogen–bonded water networks on a metal surface.* Phys. Rev. Lett., **89**, (2002) 176104.

[Men02b] D. Menzel. *Water on a metal surface.* Science, **295**, (2002) 58.

[Men04] S. Meng, E. G. Wang and S. Gao. *Water adsorption on metal surfaces: A general picture from density functional theory studies.* Phys. Rev. B, **69**, (2004) 195404.

[Men05] S. Meng, E. G. Wang, C. Frischkorn, M. Wolf and S. Gao. *Consistent picture for the wetting structure of water/Ru(0001).* Chem. Phys. Lett., **402**, (2005) 384.

[Met00] U. Metka, M. G. Schweitzer, H. R. Volpp and J. Wolfrum. *In-situ detection of NO chemisorbed on platinum using infrared-visible sum-frequency generation (SFG).* Zeitschrift für physikalische Chemie, **214**(Part 6), (2000) 865.

[Mey08] M. Meyer, J. Stähler, D. O. Kusmierek, M. Wolf and U. Bovensiepen. *Determination of the electron's solvation site on* $D_2O/Cu(111)$ *using Xe overlayers and femtosecond photoelectron spectroscopy.* Physical Chemistry Chemical Physics, **10**, (2008) 4932.

[Mic03] A. Michaelides, A. Alavi and D. A. King. *Different surface chemistries of water on Ru0001: From monomer adsorption to partially dissociated bilayers.* J. Am. Chem. Soc., **125**, (2003) 2746.

[Mic06] A. Michaelides. *Density functional theory simulations of water–metal interfaces: waltzing waters, a novel* $2D$ *ice phase, and more.* Appl. Phys. A, **85**, (2006) 415.

[Mid65] J. E. Midwinter and J. Warner. *The effects of phase matching method and of uniaxial crystal symmetry on the polar distribution of second–order non–linear optical polarization.* Brit. J. Appl. Phys., **16**, (1965) 1135.

[Mik86] W. Mikenda. *Stretching frequency versus bond distance correlation of* $O{-}D(H)\ldots Y$ *(Y = N, O, S, Se, Cl, Br, I) hydrogen bonds in solid hydrates.* Journal of Molecular Structure, **147**, (1986) 1.

[Mil87] J. B. Miller, H. R. Siddiqui, S. M. Gates, J. N. Russel, J. T. Yates, J. C. Tully and M. J. Cardillo. *Extraction of kinetic parameters in temperature programmed desorption: A comparison of methods.* J. Chem. Phys., **87**, (1987) 6725.

[Mir98] P. B. Miranda, L. Xu, Y. R. Shen and M. Salmeron. *Icelike water monolayer adsorbed on mica at room temperature.* Phys. Rev. Lett., **81**, (1998) 5876.

[Mir99] P. B. Miranda and Y. R. Shen. *Liquid interfaces: A study by sum–frequency vibrational spectroscopy.* J. Phys. Chem. B, **103**, (1999) 3292.

[Mis92] J. A. Misewich, T. F. Heinz and D. M. Newns. *Desorption induced by multiple electronic transitions.* Phys. Rev. Lett., **68**, (1992) 3737.

[Mis95] J. A. Misewich, T. F. Heinz, P. Weingard and A. Kalamarides. *Laser spectroscopy and photochemistry on metal surfaces* (World Scientific, Singapore), 1995.

[Mit04] S. Mitlin and K. T. Leung. *Temporal evolution of an ultrathin, noncrystalline ice deposit at crystallization near 160 K studied by FTIR reflection–absorption spectroscopy.* Can. J. Chem., **82**, (2004) 978.

[Mon10] A. Monmayrant, S. Weber and B. Chatel. *A newcomer's guide to ultrashort pulse shaping and characterization.* J. Phys. B: At. Mol. Opt. Phys., **43**, (2010) 103001.

[Mor99] U. Morgner, F. X. Kärtner, S. H. Cho, Y. Chen, H. A. Haus, J. G. Fujimoto, E. P. Ippen, V. Scheuer, G. Angelow and T. Tschudi. *Sub–two–cycle pulses from a Kerr–lens mode–locked Ti:sapphire laser.* Optics Letters, **24**, (1999) 411.

[Mor06] A. Morita. *Improved computation of sum frequency generation spectrum of the surface of water.* J. Phys. Chem. B, **110**, (2006) 3158.

[Mou86] P. F. Moulton. *Spectroscopic and laser characteristics of $Ti:Al_2O_3$.* J. Opt. Soc. Am. B, **3**(1), (1986) 125.

[Mus82] R. G. Musket, W. McLean, C. A. Colmenares, D. M. Makowiecki and W. J. Siekhaus. *Preparation of atomically clean surfaces of selected elements: A review.* Appl. Surf. Sci., **10**, (1982) 143.

[Nak99] M. Nakamura, Y. Shingaya and M. Ito. *The vibrational spectra of water cluster molecules on Pt(111) surface at 20 K.* Chem. Phys. Lett., **309**, (1999) 123.

[Nan00] N. Nandi, K. Bhattacharyya and B. Bagchi. *Dielectric relaxation and solvation dynamics of water in complex chemical and biological systems.* Chem. Rev., **100**, (2000) 2013.

[Nar76] A. H. Narten, C. G. Venkatesh and S. A. Rice. *Diffraction pattern and structure of amorphous solid water at 10 and 77 K.* J. Chem. Phys., **64**, (1976) 1106.

[New69] D. M. Newns. *Self–consistent model of hydrogen chemisorption.* Phys. Rev., **178**, (1969) 1123.

[New83] G. H. C. New. *The generation of ultrashort laser pulses.* Rep. Prog. Phys., **46**, (1983) 877.

[New91] D. M. Newns, T. F. Heinz and J. A. Misewich. *Desorption by femtosecond laser pulses: an electron–hole effect?* Prog. Theor. Phys. Supplement, **106**, (1991) 411.

[Nie45] A. H. Nielsen and Y. T. Yao. *The analysis of the vibration–rotation band ω_3 for $C^{12}O_2^{16}$ and $C^{13}O_2^{16}$.* Phys. Rev., **68**, (1945) 173.

[Nik91] D. N. Nikogosyan. *Beta–barium borate (BBO) – A review of its properties and applications.* Appl. Phys. A, **52**, (1991) 359.

[Nil02] A. Nilsson. *Applications of core level spectroscopy to adsorbates.* Journal of Electron Spectroscopy and Related Phenomena, **126**, (2002) 3.

[Nil10] A. Nilsson, D. Nordlund, I. Waluyo, N. Huang, H. Ogasawara, S. Kaya, U. Bergmann, L.-A. Näslund, H. Öström, P. Wernet, K. J. Andersson, T. Schiros and L. G. M. Pettersson. *X–ray absorption spectroscopy and X–ray Raman scattering of water and ice; an experimental view.* Journal of Electron Spectroscopy and Related Phenomena, **177**, (2010) 99.

[Nor09] D. Nordlund, H. Ogasawara, K. J. Andersson, M. Tatarkhanov, M. Salmeron, L. G. M. Pettersson and A. Nilsson. *Sensitivity of x-ray absorption spectroscopy to hydrogen bond topology.* Phys. Rev. B, **80**(23), (2009) 233404.

[Ock58] N. Ockman. *The infra–red and Raman spectra of ice.* Advances in Physics, **7**(26), (1958) 199.

[Oga94] H. Ogasawara, J. Yoshinobua and M. Kawai. *Water adsorption on Pt(111): from isolated molecule to three–dimensional cluster.* Chem. Phys. Lett., **231**, (1994) 188.

[Oga97] H. Ogasawara, J. Yoshinobu and M. Kawai. *Direct observation of the molecular interaction between chemisorbed CO and water overlayer on Pt(111).* Surf. Sci., **386**, (1997) 73.

[Oga99] H. Ogasawara, J. Yoshinobu and M. Kawai. *Clustering behavior of water (D_2O) on Pt(111).* J. Chem. Phys., **111**, (1999) 7003.

[Oga02] H. Ogasawara, B. Brena, D. Nordlund, M. Nyberg, A. Pelmenschikov, L. G. M. Pettersson and A. Nilsson. *Structure and bonding of water on Pt(111).* Phys. Rev. Lett., **89**, (2002) 276102.

[Ond05] K. Onda, B. Li, J. Zhao, K. D. Jordan, J. Yang and H. Petek. *Wet electrons at the $H_2O/TiO_2(110)$ surface.* Science, **308**, (2005) 1154.

[Ost05] V. Ostroverkhov, G. A. Waychunas and Y. R. Shen. *New information on water interfacial structure revealed by phase-sensitive surface spectroscopy.* Phys. Rev. Lett., **94**, (2005) 46102.

[Ows58] P. G. Owston. *The structure of ice–I, as determined by x–ray and neutron diffraction analysis.* Advances in Physics, **7**(26), (1958) 171.

[Pai04] D. H. Paik, I.-R. Lee, D.-S. Yang, J. S. Baskin and A. H. Zewail. *Electrons in finite–sized water cavities: hydration dynamics observed in real time.* Science, **306**, (2004) 672.

Bibliography

[Pal98] E. D. Palik, ed. *Handbook of optical constants of solids*, volume 3 (Academic Press), 1998.

[Pan09] S. Pandelov, B. M. Pilles, J. C. Werhahn and H. Iglev. *Time-resolved dynamics of the OH stretching vibration in aqueous NaCl hydrate.* J. Phys. Chem. A, **113**, (2009) 10184.

[Par00] S.-C. Park, T. Pradeep and H. Kang. *Ionic dissociation at NaCl on frozen water.* J. Chem. Phys., **113**, (2000) 9373.

[Pau35] L. Pauling. *The structure and entropy of ice and of other crystals with some randomness of atomic arrangement.* J. Am. Chem. Soc., **57**, (1935) 2680.

[Pet95] A. V. Petukhov. *Sum–frequency generation on isotropic surfaces: General phenomenology and microscopic theory for jellium surfaces.* Phys. Rev. B, **52**, (1995) 16901.

[Pet98] H. Petek and S. Ogawa. *Femtosecond time–resolved two–photon photoemission studies of electron dynamics in metals.* Progress in Surface Science, **56**, (1998) 239.

[Pet99] V. F. Petrenko and R. W. Whitworth. *Physics of ice* (Oxford University Press Inc., New York), 1999.

[Pfn83] H. Pfnür, P. Feulner and D. Menzel. *The influence of adsorbate interactions on kinetics and equilibrium for CO on Ru(001). II. Desorption kinetics and equilibrium.* J. Chem. Phys., **79**, (1983) 4613.

[Pin66] D. Pines and P. Nozières. *The theory of quantum liquids.* Advanced Book Classics (Benjamin, New York), 1966.

[Pol70] G. W. Poling. *Infrared reflection studies of metal surfaces.* J. Colloid Interface Sci., **34**, (1970) 365.

[Pre97] W. H. Press, S. A. Teukolsky, W. T. Vetterling and B. P. Flannery. *Numerical recipes in C* (Cambridge University Press), 2 edition, 1997.

[Pry92] J. A. Prybyla, H. W. K. Tom and G. D. Aumiller. *Femtosecond time–resolved surface reaction: Desorption of CO from Cu(111) in < 325 fsec.* Phys. Rev. Lett., **68**, (1992) 503.

[Pui03] S. R. Puisto, T. J. Lerotholi, G. Held and D. Menzel. *A refined LEED analysis of water on Ru(0001): an experimental test of the partial dissociation model.* Surf. Rev. and Lett., **10**(2–3), (2003) 487.

[Ran89] W. Ranke. *Low temperature adsorption and condensation of O_2, H_2O and NO on Pt(111), studied by core level and valence band photoemission.* Surf. Sci., **209**, (1989) 57.

[Ran04] H. Rangwalla and A. Dhinojwala. *Probing hidden polymeric interfaces using IR–visible sum–frequency generation spectroscopy.* The Journal of Adhesion, **80**, (2004) 37.

[Rao77] R. R. Rao and A. Ramanand. *Lattice dynamics, thermal expansion, and bulk modulus of ruthenium.* J. Low. Temp. Phys., **27**(5–6), (1977) 837.

[Ras29] F. Rasetti. *Raman effect in gases.* Nature, **123**(3093), (1929) 205.

[Ras02] M. B. Raschke, M. Hayashi, S. H. Lin and Y. R. Shen. *Doubly-resonant sum-frequency generation spectroscopy for surface studies.* Chem. Phys. Lett., **359**, (2002) 367.

[Ras04] M. B. Raschke and Y. R. Shen. *Nonlinear optical spectroscopy of solid interfaces.* Current opinion in solid state and materials science, **8**, (2004) 343.

[Ray02] E. A. Raymond, T. L. Tarbuck and G. L. Richmond. *Isotopic dilution studies of the vapor/water interface as investigated by vibrational sum–frequency spectroscopy.* J. Phys. Chem. B, **106**, (2002) 2817.

[Ray03] E. A. Raymond, T. L. Tarbuck, M. G. Brown and G. L. Richmond. *Hydrogen–bonding interactions at the vapor/water interface investigated by vibrational sum–frequency spectroscopy of $HOD/H_2O/D_2O$ mixtures and molecular dynamics simulations.* J. Phys. Chem. B, **107**, (2003) 546.

[Red62] P. A. Redhead. *Thermal desorption of gases.* Vacuum, **12**, (1962) 203.

[Ree70] W. Reese and W. L. Johnson. *Low–temperature specific heat of ruthenium.* Phys. Rev. B, **2**, (1970) 2972.

[Reh71] N. E. Rehler and J. H. Eberly. *Superradiance.* Phys. Rev. A, **3**, (1971) 1735.

[Ric02] G. L. Richmond. *Molecular bonding and interactions at aqueous surfaces as probed by vibrational sum frequency spectroscopy.* Chem. Rev., **102**, (2002) 2693.

[Ric05] S. W. Rick. *Simulations of proton order and disorder in ice Ih.* J. Chem. Phys., **122**, (2005) 094504.

[Rin93] J. Ringling, O. Kittelmann, F. Noack, G. Korn and J. Squier. *Tunable femtosecond pulses in the near vacuum ultraviolet generated by frequency conversion of amplified Ti:sapphire laser pulses.* Optics Letters, **18**, (1993) 2035.

[Rit77] G. Ritzhaupt and J. P. Devlin. *Infrared spectrum of D_2O vibrationally decoupled in glassy H_2O.* J. Chem. Phys., **67**, (1977) 4779.

[Rit78] G. Ritzhaupt, C. Thornton and J. P. Devlin. *Infrared spectrum of D_2O vibrationally decoupled in H_2O ice I_c.* Chem. Phys. Lett., **59**, (1978) 420.

[Rob71] C. W. Robertson and D. Williams. *Lambert absorption coefficients of water in the infrared.* J. Opt. Soc. Am., **61**, (1971) 1316.

[Rok04] S. Roke. *New light on hidden surfaces.* Ph.D. thesis, Universiteit Leiden, 2004.

[Rom95] L. Romm, T. Livneh and M. Asscher. *Collision-induced desorption of water from Ru(001).* J. Chem. Soc. Faraday Trans., **91**, (1995) 3655.

[Ros06] J. R. Roscioli, N. I. Hammer and M. A. Johnson. *Infrared spectroscopy of water cluster anions, $(H_2O)^-_{n=3-24}$ in the HOH bending region: Persistence of the double H–bond acceptor (AA) water molecule in the excess electron binding site of the class I isomers.* J. Phys. Chem. A, **110**, (2006) 7517.

[Row95] B. Rowland, N. S. Kadagathur, J. P. Devlin, V. Buch, T. Feldman and M. J. Wojcik. *Infrared spectra of ice surfaces and assignment of surface–localized modes from simulated spectra of cubic ice.* J. Chem. Phys., **102**, (1995) 8328.

[Rua04] C.-Y. Ruan, V. A. Lobastov, F. Vigliotti, S. Chen and A. H. Zewail. *Ultrafast electron crystallography of interfacial water.* Science, **304**, (2004) 80.

[Ryu06] S. Ryu, J. Chang, H. Kwon and S. K. Kim. *Dynamics of solvated electron transfer in thin ice film leading to a large enhancement in photodissociation of $CFCl_3$.* J. Am. Chem. Soc., **128**, (2006) 3500.

[Sad99] J. Sadlej, V. Buch, J. K. Kazimirski and U. Buck. *Theoretical study of structure and spectra of cage clusters $(H_2O)_n$, $n = 7–10$.* J. Phys. Chem. A, **103**, (1999) 4933.

[Sad02] V. Sadtchenko, G. E. Ewin, D. R. Nutt and A. J. Stone. *Instability of ice films.* Langmuir, **18**, (2002) 4632.

[Sag10] D. M. Sagar, C. D. Bain and J. R. R. Verlet. *Hydrated electrons at the water/air interface.* J. Am. Chem. Soc., **132**, (2010) 6917.

[San89] B. A. Sanborn, P. B. Allen and D. A. Papaconstantopoulos. *Empirical electron–phonon coupling constants and anisotropic electrical resistivity in hcp metals.* Phys. Rev. B, **40**, (1989) 6037.

[Sch74] W. Schulze and D. M. Kolb. *Density and refractive index of solid layers of noble gases and sulphur hexafluoride.* J. Chem. Soc. Faraday Trans., **70**, (1974) 1098.

[Sch77] J. R. Scherer and R. G. Snyder. *Raman intensities of single crystal ice I_h.* J. Chem. Phys., **67**, (1977) 4794.

[Sch87] J. Schnitker and P. J. Rossky. *Quantum simulation study of the hydrated electron.* J. Chem. Phys., **86**, (1987) 3471.

[Sch88] J. Schnitker, K. Motakabbir, P. J. Rossky and R. A. Friesner. *A priori calculation of the optical absorption spectrum of the hydrated electron.* Phys. Rev. Lett., **60**, (1988) 456.

[Sch93] H. Schlichting and D. Menzel. *Techniques for attainment, control and calibration of cryogenic temperatures at small single-crystal samples under ultrahigh vacuum.* Rev. Sci. Instrum., **64**, (1993) 2013.

[Sch94] J. E. Schaff and J. T. Roberts. *Structure sensitivity in the surface chemistry of ice: acetone adsorption on amorphous and crystalline ice films.* J. Phys. Chem., **98**, (1994) 6900.

[Sch99] C. Schnitzer, S. Baldelli, D. J. Campbell and M. J. Shultz. *Sum frequency generation of O–H vibrations on the surface of H_2O/HNO_3 solutions and liquid HNO_3.* J. Phys. Chem. A, **103**, (1999) 6383.

[Sch00] C. Schnitzer, S. Baldelli and M. J. Shultz. *Sum frequency generation of water on NaCl, $NaNO_3$, $KHSO_4$, HCl, HNO_3, and H_2SO_4 aqueous solutions.* J. Phys. Chem. B, **104**, (2000) 585.

[Sch10]   T. Schiros, K. J. Andersson, L. G. M. Pettersson, A. Nilsson and H. Ogasawara. *Chemical bonding of water to metal surfaces studied with core–level spectroscopies.* Journal of Electron Spectroscopy and Related Phenomena, **177**, (2010) 85.

[She84]   Y. R. Shen. *The principles of nonlinear optics* (Wiley & Sons, New York), 1984.

[She89]   Y. R. Shen. *Surface properties probed by second-harmonic and sum-frequency generation.* Nature, **337**, (1989) 519.

[She96]   Y. R. Shen. *A few selected applications of surface nonlinear optical spectroscopy.* Proc. Natl. Acad. Sci. USA, **93**, (1996) 12104.

[She01]   Y. R. Shen. *Exploring new opportunities with sum–frequency nonlinear optical spectroscopy.* Pure Appl. Chem., **73**, (2001) 1589.

[She06]   Y. R. Shen and V. Ostroverkhov. *Sum frequency vibrational spectroscopy on water interfaces: polar orientation of water molecules at interfaces.* Chem. Rev., **106**, (2006) 1140.

[Shi08]   T. K. Shimizu, A. Mugarza, J. I. Cerdá, M. Heyde, Y. Qi, U. D. Schwarz, D. F. Ogletree and M. Salmeron. *Surface species formed by the adsorption and dissociation of water molecules on a Ru(0001) surface containing a small coverage of carbon atoms studied by scanning tunneling microscopy.* J. Phys. Chem. C, **112**, (2008) 7445.

[Shu02]   M. J. Shultz, S. Baldelli, C. Schnitzer and D. Simonelli. *Aqueous solution/air interfaces probed with sum frequency generation spectroscopy.* J. Phys. Chem. B, **106**, (2002) 5313.

[Sie10a]   K. R. Siefermann and B. Abel. *Ion chemistry mediated by water networks.* Science, **327**, (2010) 280.

[Sie10b]   K. R. Siefermann, Y. Liu, E. Lugovoy, O. Link, M. Faubel, U. Buck, B. Winter and B. Abel. *Binding energies, lifetimes and implications of bulk and interface solvated electrons in water.* Nature Chemistry, **2**, (2010) 274.

[Sin68]   A. C. Sinnock and B. L. Smith. *Dielectric properties of the solified inert gases.* Phys. Lett. A, **28**, (1968) 22.

[Smi81]   H. G. Smith and N. Wakabayashi. *Phonon anomalies and superconductivity in the hcp metals, Tc, Re, and Ru.* Solid State Communications, **39**, (1981) 371.

[Smi96]   R. S. Smith, C. Huang, E. K. L. Wong and B. D. Kay. *Desorption and crystallization kinetics in nanoscale thin films of amorphous water ice.* Surf. Sci., **367**, (1996) L13.

[Smi97]   R. S. Smith, C. Huang and B. D. Kay. *Evidence for molecular translational diffusion during the crystallization of amorphous solid water.* J. Phys. Chem. B, **101**, (1997) 6123.

[Smi99]   R. S. Smith and B. D. Kay. *The existence of supercooled liquid water at 150 K.* Nature, **398**, (1999) 788.

[Smi07]   M. Smits, A. Ghosh, M. Sterrer, M. Müller and M. Bonn. *Ultrafast vibrational energy transfer between surface and bulk water at the air-water interface.* Phys. Rev. Lett., **98**, (2007) 098302.

[Sob07] A. L. Sobolewski and W. Domcke. *Computational studies of aqueous-phase photochemistry and the hydrated electron in finite-size clusters.* Physical Chemistry Chemical Physics, **9**, (2007) 3818.

[Sol90] S. Solomon. *Progress towards a quantitative understanding of Antarctic ozone depletion.* Nature, **347**, (1990) 347.

[Stä06] J. Stähler, C. Gahl, U. Bovensiepen and M. Wolf. *Ultrafast electron dynamics at ice–metal interfaces: competition between heterogeneous electron transfer and solvation.* J. Phys. Chem. B, **110**, (2006) 9637.

[Stä07a] A. J. Stähler. *Freezing hot electrons.* Ph.D. thesis, Freie Universität Berlin, 2007.

[Stä07b] J. Stähler, M. Mehlhorn, U. Bovensiepen, M. Meyer, D. O. Kusmierek, K. Morgenstern and M. Wolf. *Impact of ice structure on ultrafast electron dynamics in D_2O clusters on Cu(111).* Phys. Rev. Lett., **98**, (2007) 206105.

[Stä07c] J. Stähler, M. Meyer, X. Y. Zhu, U. Bovensiepen and M. Wolf. *Dynamics of electron transfer at polar molecule–metal interfaces: the role of thermally activated tunnelling.* New Journal of Physics, **9**, (2007) 394.

[Stä08] J. Stähler, U. Bovensiepen, M. Meyer and M. Wolf. *A surface science approach to ultrafast electron transfer and solvation dynamics at interfaces.* Chem. Soc. Rev., **37**, (2008) 2180.

[Ste99] K. P. Stevenson, G. A. Kimmel, Z. Dohnalek, R. S. Smith and B. D. Kay. *Controlling the morphology of amorphous solid water.* Science, **283**, (1999) 1505.

[Ste01] J. Stenger, D. Madsen, P. Hamm, E. T. J. Nibbering and T. Elsaesser. *Ultrafast vibrational dephasing of liquid water.* Phys. Rev. Lett., **87**, (2001) 027401.

[Str96] L. M. Struck, L. J. Richter, S. A. Buntin, R. R. Cavanagh and J. C. Stephenson. *Femtosecond laser–induced desorption of CO from Cu(100): comparison of theory and experiment.* Phys. Rev. Lett., **77**, (1996) 4576.

[Su98] X. Su, L. Lianos, Y. R. Shen and G. A. Somorjai. *Surface–induced ferroelectric ice on Pt(111).* Phys. Rev. Lett., **80**, (1998) 1533.

[Suh00] S. B. Suh, H. M. Lee, J. Kim, J. Y. Lee and K. S. Kim. *Vibrational spectra and electron detachment energy of the anionic water hexamer.* J. Chem. Phys., **113**, (2000) 5273.

[Sut99] D. H. Sutter, G. Steinmeyer, L. Gallmann, N. Matuschek, F. Morier-Genoud, U. Keller, V. Scheuer, G. Angelow and T. Tschudi. *Semiconductor saturable–absorber mirror assisted Kerr–lens mode–locked Ti:sapphire laser producing pulses in the two–cycle regime.* Optics Letters, **24**, (1999) 631.

[Svi96] I. M. Svishchev and P. G. Kusalik. *Electrofreezing of liquid water: a microscopic perspective.* J. Am. Chem. Soc., **118**, (1996) 649.

[Sym76] M. C. R. Symons. *Solutions of metals: solvated electrons.* Chem. Soc. Rev., **5**, (1976) 337.

[Tad00] A. Tadjeddine. *Spectroscopic investigation of surfaces and interfaces by using infrared–visible sum and difference frequency generation.* Surf. Rev. and Lett., **7**, (2000) 423.

[Taj84] Y. Tajima, T. Matsuo and H. Suga. *Calorimetric study of phase transition in hexagonal ice doped with alkali hydroxides.* J. Phys. Chem. Solids, **45**, (1984) 1135.

[Ter62] R. W. Terhune, P. D. Maker and C. M. Savage. *Optical harmonic generation in calcite.* Phys. Rev. Lett., **8**(10), (1962) 404.

[Thi81] P. A. Thiel, F. M. Hoffmann and W. H. Weinberg. *Monolayer and multilayer adsorption of water on Ru(001).* J. Chem. Phys., **75**, (1981) 5556.

[Thi84] P. A. Thiel, R. A. DePaola and F. M. Hoffmann. *The vibrational spectra of chemisorbed molecular clusters: H_2O on Ru(001).* J. Chem. Phys., **80**, (1984) 5326.

[Thi87] P. A. Thiel and T. E. Madey. *The interaction of water with solid surfaces: fundamental aspects.* Surf. Sci. Reports, **7**, (1987) 211.

[Tho99] C. L. Thomsen, D. Madsen, S. R. Keiding, J. Thogersen and O. Christiansen. *Two–photon dissociation and ionization of liquid water studied by femtosecond transient absorption spectroscopy.* Phys. Rev. Lett., **110**, (1999) 3453.

[Tom96] E. Tomkova. *TDS spectra analysis.* Surf. Sci., **351**, (1996) 309.

[Tra07] F. Traeger, D. Langenberg, Y. K. Gao and C. Wöll. *Water on a close–packed Ru surface: A high–order commensurate adlayer with a high sensitivity towards electron beam damage.* Phys. Rev. B, **76**, (2007) 33410.

[Tul80] J. C. Tully. *Theories of the dynamics of inelastic and reactive processes at surfaces.* Annual Review Physical Chemistry, **31**, (1980) 319.

[Tul81] J. C. Tully. *Dynamics of gas–surface interactions: Thermal desorption of Ar and Xe from platinum.* Surf. Sci., **111**, (1981) 461.

[Tul93] J. C. Tully, M. Gomez and M. Head-Gordon. *Electronic and phonon mechanisms of vibrational relaxation: CO on Cu(100).* J. Vac. Sci. Technol. A, **11**, (1993) 1914.

[Tul00] J. C. Tully. *Chemical dynamics at metal surfaces.* Annual Review Physical Chemistry, **51**, (2000) 153.

[Tur05a] L. Turi, W.-S. Sheu and P. J. Rossky. *Characterization of excess electrons in water–cluster anions by quantum simulations.* Science, **309**, (2005) 914.

[Tur05b] L. Turi, W.-S. Sheu and P. J. Rossky. *Response to comment on "Characterization of excess electrons in water–cluster anions by quantum simulations".* Science, **310**, (2005) 1769.

[Tur06] L. Turi, Á. Madarász and P. J. Rossky. *Excess electron localization sites in neutral water clusters.* J. Chem. Phys., **125**, (2006) 014308.

[Unt02a] H. Unterhalt. *Summenfrequenzerzeugungsspektroskopie an Platin– und Palladiummodellkatalysatoren.* Ph.D. thesis, FU Berlin, 2002.

[Unt02b] H. Unterhalt, G. Rupprechter and H.-J. Freund. *Vibrational sum frequency spectroscopy on Pd(111) and supported Pd nanoparticles: CO adsorption from ultrahigh vacuum to atmospheric pressure.* J. Phys. Chem. B, **106**, (2002) 356.

[Vai90] G. Vaillancourt, T. B. Norris, J. S. Coe, P. Bado and G. A. Mourou. *Operation of a 1–kHz pulse–pumped Ti:sapphire regenerative amplifier*. Optics Letters, **15**, (1990) 317.

[vdH98] E. van der Ham. *Sum–frequency generation at interfaces: a study employing the FELIX free–electron laser*. Ph.D. thesis, Rijksuniversiteit te Leiden, 1998.

[Ver98] T. Verbiest, S. Van Elshocht, M. Kauranen, L. Hellemans, J. Snauwaert, C. Nuckolls, T. J. Katz and A. Persoons. *Strong enhancement of nonlinear optical properties through supramolecular chirality*. Science, **282**, (1998) 913.

[Ver05a] J. R. R. Verlet, A. E. Bragg, A. Kammrath, O. Cheshnovsky and D. M. Neumark. *Comment on "Characterization of excess electrons in water–cluster anions by quantum simulations"*. Science, **310**, (2005) 1769.

[Ver05b] J. R. R. Verlet, A. E. Bragg, A. Kammrath, O. Cheshnovsky and D. M. Neumark. *Observation of large water–cluster anions with surface–bound excess electrons*. Science, **307**, (2005) 93.

[Vid05] F. Vidal and A. Tadjeddine. *Sum-frequency generation spectroscopy of interfaces*. Rep. Prog. Phys., **68**, (2005) 1095.

[Wag06] S. Wagner. *State- and time-resolved investigations of energy transfer mechanisms in femtosecond-laser induced associative desorption*. Ph.D. thesis, Freie Universität Berlin, 2006.

[Wal06] D. S. Walker, D. K. Hore and G. L. Richmond. *Understanding the population, coordination, and orientation of water species contributing to the nonlinear optical spectroscopy of the vapor–water interface through molecular dynamics simulations*. J. Phys. Chem. B, **110**, (2006) 20451.

[Wal08] I. Waluyo, D. Nordlund, L.-Å. Näslund, H. Ogasawara, L. Pettersson and A. Nilsson. *Spectroscopic evidence for the formation of 3–D crystallites during isothermal heating of amorphous ice on Pt(111)*. Surf. Sci., **602**, (2008) 2004.

[Wan05] H.-F. Wang, W. Gan, R. Lu, Y. Rao and B.-H. Wu. *Quantitative spectral and orientational analysis in surface sum frequency generation vibrational spectroscopy (SFG–VS)*. Int. Rev. Phys. Chem., **24**(2), (2005) 191.

[Was92] M. R. Wasielewski. *Photoinduced electron transfer in supramolecular systems for artificial photosynthesis*. Chem. Rev., **92**, (1992) 435.

[Wat01] M. R. Watry, M. G. Brown and G. L. Richmond. *Probing molecular structure at liquid surfaces with vibrational sum frequency spectroscopy*. Applied Spectroscopy, **55**, (2001) 321A.

[Wei01a] X. Wei and Y. R. Shen. *Motional effect in surface sum–frequency vibrational spectroscopy*. Phys. Rev. Lett., **86**, (2001) 4799.

[Wei01b] X. Wei, P. B. Miranda and Y. R. Shen. *Surface vibrational spectroscopic study of surface melting of ice*. Phys. Rev. Lett., **86**, (2001) 1554.

[Wei02] X. Wei, P. B. Miranda, C. Zhang and Y. R. Shen. *Sum–frequency spectroscopic studies of ice interfaces*. Phys. Rev. B, **66**, (2002) 085401.

[Wei04] J. Weissenrieder, A. Mikkelsen, J. N. Andersen, P. J. Feibelman and G. Held. *Experimental evidence for a partially dissociated water bilayer on Ru(0001)*. Phys. Rev. Lett., **93**, (2004) 196102.

[Wer04] P. Wernet, D. Nordlund, U. Bergmann, M. Cavalleri, M. Odelius, H. Ogasawara, L. A. Näslund, T. K. Hirsch, L. Ojamäe, P. Glatzel, L. G. M. Pettersson and A. Nilsson. *The structure of the first coordination shell in liquid water*. Science, **304**, (2004) 995.

[Wey64] W. Weyl. *Ueber Metallammonium-Verbindungen*. Annalen der Physik, **197**, (1864) 601.

[Wha77] E. Whalley. *A detailed assignment of the O–H stretching bands of ice I*. Can. J. Chem., **55**, (1977) 3429.

[Whi99] R. W. Whitworth. *Comment on "Ferroelectricity in water ice"*. J. Phys. Chem. B, **103**, (1999) 8192.

[Wit99] H. Witek and V. Buch. *Structure of ice multilayers on metals*. J. Chem. Phys., **110**, (1999) 3168.

[Wod04] A. M. Wodtke, J. C. Tully and D. J. Auerbach. *Electronically non–adiabatic interactions of molecules at metal surfaces: Can we trust the Born–Oppenheimer approximation for surface chemistry?* Int. Rev. Phys. Chem., **23**(4), (2004) 513.

[Woj93] M. J. Wojcik, V. Buch and J. P. Devlin. *Spectra of isotopic ice mixtures*. J. Chem. Phys., **99**, (1993) 2332.

[Woj02] M. J. Wojcik, K. Szczeponek and S. Ikeda. *Theoretical study of the OH/OD stretching regions of the vibrational spectra of ice Ih*. J. Chem. Phys., **117**, (2002) 9850.

[Won75] P. T. T. Wong and E. Whalley. *Optical spectra of orientationally disordered crystal. V. Raman spectrum of ice Ih in the range* 4000–350 cm^{-1}. J. Chem. Phys., **62**, (1975) 2418.

[Wor04] G. A. Worth and L. S. Cederbaum. *Beyond Born–Oppenheimer: Molecular dynamics through a conical intersection*. Annual Review Physical Chemistry, **55**, (2004) 127.

[Wou97] S. Woutersen, U. Emmerichs and H. J. Bakker. *Femtosecond mid-IR pump–probe spectroscopy of liquid water: Evidence for a two–component structure*. Science, **278**, (1997) 658.

[Wyn94] K. Wynne, G. D. Reid and R. M. Hochstrasser. *Regenerative amplification of* 30–fs *pulses in Ti:sapphire at* 5 kHz. Optics Letters, **19**, (1994) 895.

[Yam09] T. Yamauchi, K. Mine, A. Nakashima, A. Izumi and A. Namiki. *Crystallization of* D_2O *thin films on Ru(001) surfaces*. Appl. Surf. Sci., **256**, (2009) 1124.

[Yat87] J. T. Yates and T. E. Madey. *Vibrational spectroscopy of molecules on surfaces* (Plenum Press, New York), 1987.

[Yat97] J. T. Yates. *Experimental innovations in surface science: A guide to practical laboratory methods and instruments* (Springer, Berlin), 1997.

[Yok98]   K. Yokoyama, C. Silva, D. H. Son, P. K. Walhout and P. F. Barbara. *Detailed investigation of the femtosecond pump–probe spectroscopy of the hydrated electron.* J. Phys. Chem. A, **102**, (1998) 6957.

[Zac09]   J. Zacharias. *Untersuchungen an Eis auf Ruthenium nach UV–Photoanregung.* Master's thesis, FU Berlin, 2009.

[Zal98]   R. Zallen. *The physics of amorphous solids* (Wiley classics library edition), 1998.

[Zan04]   R. Zangi and A. E. Mark. *Electrofreezing of confined water.* J. Chem. Phys., **120**, (2004) 7123.

[Zha90]   Q. Zhang and V. Buch. *Computational study of formation dynamics and structure of amorphous ice condensates.* J. Chem. Phys., **92**, (1990) 5004.

[Zha06]   J. Zhao, B. Li, K. Onda, M. Feng and H. Petek. *Solvated electrons on metal oxide surfaces.* Chem. Rev., **106**, (2006) 4402.

[Zhe06]   E. A. Zheligovskaya and G. G. Malenkov. *Crystalline water ices.* Russian Chemical Reviews, **75**(1), (2006) 57.

[Zhu87]   X. D. Zhu, H. Suhr and Y. R. Shen. *Surface vibrational spectroscopy by infrared-visible sum frequency generation.* Phys. Rev. B, **35**(6), (1987) 3047.

[Zhu99]   X. Zhuang, P. B. Miranda, D. Kim and Y. R. Shen. *Mapping molecular orientation and conformation at interfaces by surface nonlinear optics.* Phys. Rev. B, **59**, (1999) 12632.

[Zim60]   J. M. Ziman. *Electrons and phonons* (Oxford University Press), 1960.

[Zim94]   F. M. Zimmermann and W. Ho. *Velocity distributions of photochemically desorbed molecules.* J. Chem. Phys., **100**, (1994) 7700.

[Zim95]   F. M. Zimmermann and W. Ho. *State resolved studies of photochemical dynamics at surfaces.* Surf. Sci. Reports, **22**, (1995) 127.

Publications

This thesis

Juraj Bdžoch, Martin Wolf and Christian Frischkorn.
Molecular vibrational response of ice layers after ultrashort–laser excitation of metal surfaces
Ultrafast Phenomena XVII, ISBN–13: 978–0–19–976837–0 (in press)

Juraj Bdžoch, Marcel Krenz, Martin Wolf and Christian Frischkorn.
Vibrational response of ice to long–living excess electron localization
submitted to Journal of Physical Chemistry C

Juraj Bdžoch, Christian Frischkorn and Martin Wolf.
Interfacial structure of a metal–supported water layer: A $D_2O/Ru(0001)$ case study
in preparation

Juraj Bdžoch, Christian Frischkorn and Martin Wolf.
Ultrafast energy transfer dynamics and mechanism during D_2O desorption from Ru(0001) surface
in preparation

Earlier work

Michal Žitňan, Vojtech Szöcs, Marián Janek, Ignác Bugár, Juraj Bdžoch, Tibor Palszegi, Gabriele Link and Dušan Velič.
Fluorescence dynamics of coumarin C522 on reduced–charge montmorillonite in aqueous dispersion
Langmuir, **25**, 6800–6807 (2009)

Danksagung

Ist es ein unerforschtes Kraftfeld, das an die Menschen wirkt und die viele außergewöhnlich begabte und nette Personen an bestimmten Orten konzentriert? Ich bin mir nicht sicher, dass sich die Soziologie mit solchen stark nichtlinearen und die Zentrosymmetrie brechenden Phänomenen beschäftigt – in jedem Fall möchte ich in diesem letzten Kapitel darüber berichten, eine solche seltene Raumzeitkoordinate gefunden zu haben.

Ich durfte in der Arbeitsgruppe von Herrn Professor Martin Wolf forschen und hier meine Doktorarbeit verfassen. Ich danke ihm sehr für seine offene Art und stete Diskussionsbereitschaft. Die langen Gespräche mit ihm waren sehr motivierend, seine Fragen immer gut gestellt, seine Ratschläge und breites theoretisches und experimentelles Wissen unschätzbar. Seine Persönliche Größe beweist auch der Fakt, dass er mir immer noch den Gruss erwidert, obwohl ich die altberühmte kreisfreie Goldschlägerstadt Schwabach nach Oberfranken (Sie lesen richtig!) versetzt habe.

Herr Professor Nikolaus Schwentner hat sich meiner Dissertation als Zweitgutachter angenommen. Sein Interesse an dieser Arbeit hat mich sehr ermutigt und seine kritischen Fragen haben mich zum Überdenken einiger Aspekte in unserer Messungen gebracht. Als ich einem Channeltron in unserer Kammer das zumutete, wovon sich in jedem elektrischem Bauelement vor Schreck sofort alle Spins aufrichten, haben wir von ihm gleich vier unbenutzte Ersatzgeräte zur Auswahl bekommen.

Gleich am Anfang war ich in das Büro von Christian Frischkorn eingezogen und er hat sich vorbildlich um mein Subprojekt gekümmert. In ihm hatte ich den ersten Ansprechpartner und viele meiner verrückten Ideen musste er zuerst ertragen. Ich habe viel von ihm gelernt und schätze seinen Umgang und Respekt vor den Mitmenschen besonders hoch. Diese Eigenschaft ist außerdem ausgesprochen konstant und ändert sich auch dann nicht, wenn man einen ultradünnen, speziell geschnittenen BBO Kristall auf die 'übliche Art und Weise' reinigt und dabei eher wenig Glück hat.

Immer wenn ich den dampfenden Kaffeebecher auf dem TOPAS gesichtet habe, konnte ich mich darauf verlassen, aus dem Labor zwar nicht vor Mitternacht zu gehen, dafür aber mit meistens noch nie zuvor erreichten Laserleistung und Stabilität. Es ist schwer zu sagen, ob es die magischen Hände oder der Humor und Ausstrahlung von Marcel Krenz waren, die das kalte Stück aus Metall, Glas und 'Edelsteinen' zum neuem Leben auferweckten. In jedem Fall aber kannte er dessen Geheimsprache viel besser als jeder andere. Sein Einsatz war immer riesig, deswegen tun mir auch die unzähligen, meinetwegen verpassten Züge aufrichtig Leid.

Sehr dankbar bin ich auch für den Menschen Philipp Giese, mit dem wir während einer kurzen Phase an dem gleichem Projekt gearbeitet haben. In den Laborbüchern aus dieser Zeit befinden sich sowohl grosse Buchstaben des experimentellen Erfolges, als auch halbe Sätze der Enttäuschung. In den ganzen Jahren der Alleinarbeit waren die genannten Monate sehr erfrischend und positiv anders und so manches frustrierendes lies sich viel besser tragen.

Viel gelernt habe ich auch von Jan Zacharias, einem Diplomstudenten, der – im positiven Sinne – besonders hohe Ansprüche an sich und seine Arbeit hat. Für die Programme, die er während seiner Zeit in unserer Arbeitsgruppe geschrieben hat, habe ich ihm sehr oft insgeheim gedankt.

Curriculum vitae

Der Lebenslauf ist in der Online–Version aus Gründen des Datenschutzes nicht enthalten.